Manufacturing deviations in Hydrofoils and their impact on performance.

Investigating the Manufacturing deviations of the Nacra 17 Hydrofoil and their impact on performance.

Master of Science Thesis

Timo van Maarschalkerweerd

Delft University of Technology

TU Delft

Manufacturing deviations in Hydrofoils and their impact on performance.

Investigating the Manufacturing deviations of the Nacra 17 Hydrofoil and their impact on performance.

by

Timo van Maarschalkerweerd

to obtain the degree of Master of Science

at the Delft University of Technology,

Student number:	4441958	
Thesis committee:	Prof. ir. C. Dransfeld,	TU Delft, supervisor
	Dr. ir. O.k. Bergsma,	TU Delft
	Dr. ir. D.A.M De Tavernier	Tu Delft

Cover:	Dutch olympic team sailing the Nacra 17, image made by Sailing Energy
Style:	TU Delft Report Style

An electronic version of this thesis is available at `http://repository.tudelft.nl/`.

TU Delft

Preface

This literature study will be the last report that I will deliver in my time at the Technical University of Delft. My decision to study aerospace was influenced by the America's Cup boat that started flying two years earlier. During my studies, I focused more and more on the aerospace sector. I joined the Stratos IV dream team to design a rocket. With this project, my interest in structures was formed. During the structure master class, I met Clemens Dransfeld. Clemens Dransfeld presented himself with his work on composite structures for the America's Cup, although the boats he worked on were older than those that first caught my interest. His presentation showed the possibilities for an aerospace structural engineer in the marine industry. Through Clemens, I finally closed the circle by investigating sailboats during my thesis.

This thesis was started because of the interest of the Olympic team in better understanding their underwater appendages. The trainer, Coen, was eager to find out if optimisations could be found in the underwater appendages. The Italian team has been dominant in the Nacra 17 fleet and there were rumours that it had to do with their appendages. It was finally decided that I should analyse their daggerboards. The daggerboards are a restricted item by the class organisation and cannot be adjusted. They are supposed to be identical. The fact that there is a significant difference between the hydrofoils sparks curiosity about where these differences originate. The presence of these differences in identical parts broadens the reach of this thesis. The hydrofoil is making an appearance again. By identifying why they differ and what effect some differences can have, it can help all hydrofoil designs. This can help streamline production and design. Making hydrofoils faster, easier to control, and cheaper to make, thus improving the benefits of hydrofoils in general.

This report aims to offer a comprehensive overview of the key areas of interest pertaining to hydrofoils, catering to individuals with a vested interest in this field, and possessing a foundational understanding of engineering principles. Whether you are an aspiring engineer, a naval architect, or a passionate enthusiast fascinated by hydrofoil technology, this report seeks to provide valuable insights and analysis. By delving into the intricate dynamics of hydrofoil design, performance optimisation, and the underlying factors influencing their efficiency, this report aims to deepen your understanding and contribute to the advancement of hydrofoil knowledge.

I want to thank Clemens Dransfeld and Otto Bergsma for all the support during this research. They shared the excitement of the topic and provided great guidance to structure the large project that this has turned out to be. I want to thank Maarten Sikkema, who provided a lot of insight in hydrofoil developments and practical tips on how to approach the different problems. The majority of this research was conducted in the presence of Roosa Joensuu while studying in Room NB2.44. Finally, I want to thank Alex Ashworth Brigs for providing a lot of help during this thesis. As a researcher at the Olympic centre, he was both a person of contact as a sparring partner to brainstorm ideas about the investigation in hydrofoils. At the end of the project, he even helped me escape the thesis to go (Wing) foiling myself.

Timo van Maarschalkerweerd
Delft, September 2023

Abstract

The Nacra 17 is a foiling catamaran selected to compete in the 2024 Olympic Games. The Nacra 17 is a one-design class, which requires all equipment to be identical. The Dutch Olympic team found through testing the bending stiffness that there is a slight difference in how each of their hydrofoils performed. The question was asked: What are the manufacturing deviations in the Nacra 17 hydrofoils and how do they impact the performance?

This research aims to answer the previously stated question. The 3D scanned hydrofoils validated that there is indeed a measurable difference in shape between the different hydrofoils of the Olympic team. A successful method was proposed that automatically extracts 2D profile section properties from the point-cloud data of a 3D scanned hydrofoil. This method used a rough orientation using the profile plotted in polar coordinates. The mean camber line could be extracted using the Voronoi vertex points and the offset of the profile surface. The resulting data set was fitted using non-periodic cubic B-spline curves. This produced a curve for the mean camber line and the thickness profile.

Comparison of profile properties resulted in the conclusion that profile thickness (y_t) could show that the two female mould halves were probably spaced differently for the different hydrofoils by a standard deviation of 0.0669 mm at a thickness of 22.6 mm. Differences are found in the maximum thickness location (x_t), Leading edge radius (r_{le}), maximum camber (y_c) and its location (x_c).

However, the differences in lift over drag for the different hydrofoils are minimal. The size of the drag bucket did not differ more than 0.1 of the lift coefficient (c_l) for the same drag coefficient. With the exception of in general one section that presented an early separation. The specific profile showing early separation changes along the span, not allowing for the generalisation for the complete hydrofoil. It shows that the curvature at the leading edge of the profile is critical for the performance of the Nacra hydrofoil.

Knowing which part of the profile shape is critical. Companies can take this area into account when designing the production process for the next hydrofoil, and the Olympic team can focus on maintaining these areas of the hydrofoil. Allowing the best preparation to be competitive at the next Olympic games.

Contents

List of Figures

List of Tables

Nomenclature

List of Abbreviations

.step	File type: Standard for the Exchange of Product model data
.stl	File type: Stereolithography
AOA	Angle Of Attack
BB	Port or the left side of a boat when observed from behind
CAD	Computer Aided Design
CFD	Computational Fluid Dynamics
CT scan	Computed Tomography scan
DIC	Digital Image Correlation
FFT	Fast Fourier Transform
FOV	Field Of View
FRP	Fibre Reinforced Composite
FSI	Fluid Structure Interaction
GPS	Global positioning system
IR	light in the infrared electromagnetic spectrum
NACA	National Advisory committee for aeronautics
SB	Starboard or the right side of a boat when observed from behind
SST	Shear Stress Transport
TU Delft	Delft University of Technology
VPP	Velocity Prediction Programme
X-ray	Electromagnetic radiation with a wavelength of 10 picometers to 10 nanometers

List Greek Symbols

α	Angle of attack	deg°
κ	Curvature of a line	$\frac{1}{m}$
μ	Dynamic viscosity	$\frac{N}{m^2}s$
ν	Kinameticviscosity	$\frac{m^2}{s}$
σ	Caviation Number	–
θ_c	Camber line slope	rad

List Latin Symbols

$\boldsymbol{D}$	Data matrix	–
$\boldsymbol{R}$	Rotation matrix	–
ρ	Density	$\frac{kg}{m^3}$
$\vec{R}$	Transformation Vector	–
c	Chord length	–
C_D	Wing Drag coefficient	–
c_d	Profile Drag coefficient	–
c_f	Profile Friction coefficient	–
C_L	Wing Lift coefficient	–
c_l	Profile Lift coefficient	–
C_M	Wing Moment coefficient for three-dimensional bodies	–
C_m	Profile Moment coefficient	–
c_p	Pressure coefficient	–
$d_{Z_{te}}$	Trailing edge thickness	–
e_a	Constant measurement error for the 3D scanner	mm
e_b	Constant measurement error for the 3D scanner	$\frac{\text{mm}}{\text{m}}$
e_{SD}	Squared error for the New spline curve	–

F_c	Chord Froude Number	–
f_c	Focal Length	m
F_h	Immersion height Froude Number	–
h	Height	m
$N(u)$	Normal vector	–
N_{crit}	Critical Amplification factor	–
P	Pressure	$\frac{N}{m^2}$
$P(u)$	Curve	–
P_v	A fluid vapour Pressure	$\frac{N}{m^2}$
r	Radius	–
u	Arc length of a spline spanning from 0 to 1	–
w	Width	m
x	The x direction or Chordwise direction	m
x_c	Maximum Camber location	$\frac{x}{c}$
X_k	Data Point k in two dimensional space	–
x_t	Maximum Thickness location	$\frac{x}{c}$
x_{tr}	Flow transition location along the chord	$\frac{x}{c}$
y	The y direction or Thickness direction	–
y_c	Maximum Camber Thickness	$\frac{y}{c}$
$y_c(x)$	Profile Camber line function over x	–
y_t	Maximum Thickness	$\frac{y}{c}$
$y_t(x)$	Profile Thickness function over x	–
D	Drag	N
g	Gravitational acceleration	$9.81\frac{m}{s^2}$
L	Lift	N
M	Moment	N

Re	Reynolds Number	–
S	Area Span	m^2
s	seconds	sec
V	Velocity	$\frac{m}{s}$

List of Subscripts

∞	The free stream values
$_A$	Catia Coordinate system 1
$_B$	Catia Coordinate system 2
$_C$	Final Section Coordinate system
$_D$	New spline Curve
$_p$	Profile Curve
$_{bot}$	lower surface
$_{le}$	Leading edge
$_{te}$	Trailing edge
$_{top}$	upper surface

1

Introduction

"Have you ever dreamed of flying? The feeling of floating in the air with no noise, completely silent, and not a worry in the world? The wind rushing by your face as you average speeds of 20-to-30 knots? The ability to explore the ocean or island you're staying on? Well let me tell you, this is the feeling of foiling. as said by LeRoy [10].

A hydrofoil is a wing submerged in water with the primary function of lifting (the boat) out of the water. When the speed increases, the lifting force increases until the water craft is lifted out of the water. When only the hydrofoil is submerged the resistance decreases significantly. This results in improved efficiency and speed. "It's quite a breakdown or disrupting of the old physics laws in sailing" Ian Burns, Performance Manger Oracle Team USA 2014 [11].

Hydrofoils themselves are not a new invention. Their development can be traced back to Enrico Forlanini's successful use of hydrofoils in 1906, nearly 49 years before the emergence of the first foiling sailing boat (Figure 1.1) in 1955 [12]. Throughout the twentieth century, hydrofoil boats underwent further advancements and explorations of their potential. Popular Mechanics even mentioned hydrofoiling sailboats as early as 1956 [13]. Hydrofoiling for pleasure water crafts experienced its rise around 2013 when the America's Cup introduced foiling catamarans [14].

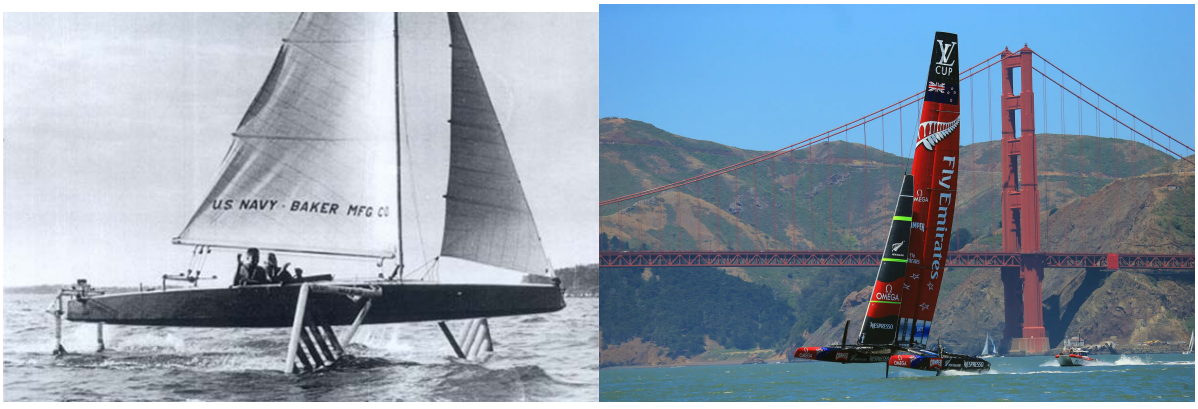

(a) The Monitor build by Gordon Baker [14] **(b)** An 2013 America's Cup boat [15]

Figure 1.1: An example of hydrofoil sailing yachts

The America's Cup race featuring 72-foot (22m) catamarans (Figure 1.1b) showed the possibility of foiling sailing yachts. Following this race, the desire to "fly" on the water led to the widespread adoption of foiling in various (wind-powered) water sports.

Foiling founds its introduction in the Olympic games at Tokyo 2020, with the Foiling configuration of the Nacra 17 [16]. With the pressure to perform in the Olympics. Research has started by independent parties into identifying how these boats can be optimised.

The Dutch Olympic Nacra 17 team sought assistance from TU Delft to gain insight into what could affect the hydrofoils of a Nacra 17. They discovered that a foil that is rigid in the spanwise bending direction yields higher performance. To make the most of the hydrofoils in the 2024 Olympics, an understanding of their function is necessary. The team found that there is a disparity in stiffness, and thus performance, between the hydrofoils. Measurements carried out by the Nacra 17 class organisation [17] revealed a difference in thickness between different hydrofoils. The thickness variations of the new hydrofoil boards were similar to those of the boards owned by different teams, indicating that the sailors did not have a significant influence in the results.

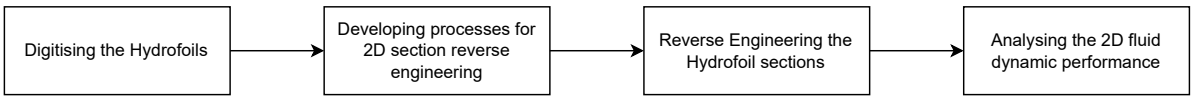

Figure 1.2: The different steps of research performed in this thesis in order to answer the research question.

The report is divided into four sections. These sections are visualised in Figure 1.2. Each section is divided into the following parts: method, results, and discussion. These parts are presented together.

The first section ,*Digitisation of the Nacra 17 Hydrofoil*, will investigate the digitisation of a hydrofoil. With the necessary background and method presented in chapter 4. The results of the digitisation are presented in chapter 8. The hypotheses presented in the methods are validated in the discussion (chapter 12).

With the hydrofoils digitised, a method needs to be found to accurately process the results for further analysis. These methods are researched in *Research Method Validation for 2D Section Processing*. The method (chapter 5) will present the different proposed methods. These methods are tested in the results (chapter 9). The best method is identified in chapter 13, the discussion chapter.

Using the methods proposed in the previous step, the difference in geometry can be identified in *Geometric deviation analysis*. The final method of processing the hydrofoils is discussed in chapter 6. The differences between the hydrofoils can finally be analysed in chapter 10. With the results, the hypothesis stated in the methods can be challenged in chapter 14.

The impact of geometric variations will be analysed in *2D section hydrodynamic analysis*. The method of this analysis is described first in chapter 7. Using the analysis of Xfoil, the differences in fluid dynamic performance are presented in the results chapter (chapter 15). Using these results, the impact can be defined by challenging the hypotheses in the discussion (chapter 15).

The conclusions of each step will be summarised in the final conclusion.

I

Background

2

State-Of-Art

The Dutch Olympic team discovered that the Nacra 17 hydrofoils had varying levels of bending stiffness. It was observed that the hydrofoil with the highest bending stiffness was the most successful. During a measurement session organised by the Nacra 17 class organisation, discrepancies in shape were noticed. These discrepancies are already present in brand new hydrofoils, showing that the manufacturing impacts the shape. With these two discoveries, the team consulted the TU Delft to explore the differences between the Nacra 17 hydrofoils.

Manufacturing The manufacturing process used to make Nacra hydrofoils was explained by the builder &DNA composites [18]. The &DNA hydrofoils are build from pre impregnated carbon composite woven sheets (plies) that are cut using an automatic cutting machine. These plies are then laid up by hand in two female moulds. The Nacra 17 hydrofoils consist of two compartments separated by the main compartment, with a vacuum bag in each compartment according to [19]. With the carbon fibre built up in the correct order, the two mould halves are closed, and the part is cured in an autoclave (pressurised oven).

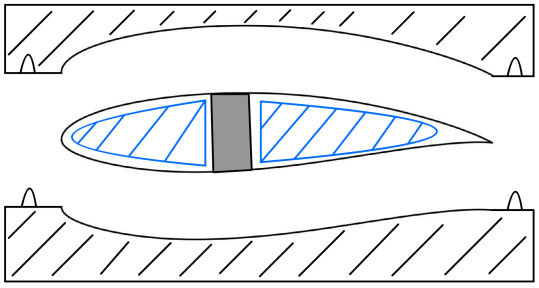

Figure 2.1: 2D representation of the two mould halves (top and bottom) with the hydrofoil in between. The Blue area shows the internal vacuum bag and the grey area the internal spar. The thicknesses of the different components are not to scale.

The different manufacturing errors that could occur during the production of composite parts are summarised in Potter [20]. In the separate literature review written for this project (found in Appendix E), the moulding process was identified as the critical production step that influences the differences in shape between the hydrofoils. The fact that this production step can affect performance is highlighted by the research of Brient et al. [21]. They showed a difference in performance due to the machining direction and quality of the moulds used for production.

Reverse Engineering For the manufacturing variations to be identified and compared between the hydrofoils. Hydrofoils need to be digitised and reversed engineered in order to make a comparison. Reverse engineering of foil shapes is applied in the research of gas turbine blades. Khameneifar [22] showed in his Ph.D. thesis a method for reverse engineering 3D point cloud data of turbine blades using

closed non-periodic B-spline curves fitted by finding the closest neighbourhood points. The resulting papers in his thesis highlight profile Reconstruction [23] and an improvement in his orientation method [24]. The problem of fitting a spline to a noisy data set was solved differently by Li et al. [1]. In their paper, an energy minimisation was used to filter the data set. This energy minimisation used large values of the curvature to exclude points that are not along the presumed surface. Li et al. [1] identified the mean camber line of the turbine blades by inscribed circles within the profile.

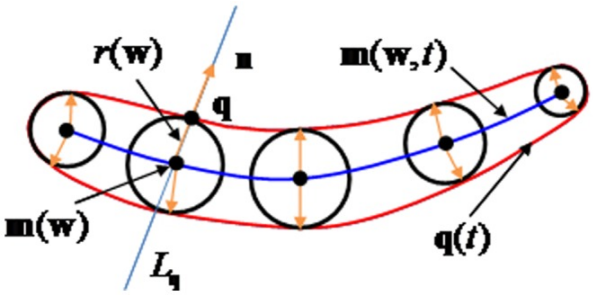

Figure 2.2: Showing the method of inscribed circles as proposed by Li et al. [1]

The 2D foil shapes are often described by the maximum thickness and maximum mean camber location. These parameters could be extracted using aerofoil parameterisation methods. While a large number of different parameterisation methods are devised, the following two methods use the shape parameters directly. These are the well-known methods, according to [25], called Parsec, and the version Bezier-Parsec developed by Derksen and Rogalsky [26]. These models require the leading and trailing edges to be located on the x axis.

Fluid dynamic analysis Analysing the effect of differences in shape parameters is a well-developed study within aerodynamics. With Schrenk [27] identifying the impact of profile thickness on profile drag that led to the systematic series of aerofoils developed by the National Advisory Committee for Aeronautics (NACA)[28], now known as NASA. These sections were analysed in detail by Abbott and Doenhoff [29]. In the book "*Theory of wing sections: including a summary of airfoil data*" Doenhoff described the impact of each parameter on the lift and drag for different Reynolds numbers.

The same kind of analysis was performed by Hoerner in: "*Fluid-dynamic drag : practical information on aerodynamic drag and hydro- dynamic resistance.*"Hoerner [30]. In his book, the differences between hydro- and aerodynamics are given. Hydrodynamics differentiates itself from aerodynamics, mainly due to free surface effects, ventilation, and cavitation. The impact of the free surface effects is explained by Hoerner in the previously mentioned book and his other book: "*Some Characteristics of Spray and Ventilation*"Hoerner [31]. The effects of the free surface are also explained by Molland and Turnock [32] in "*"Chapter 4 - Hydrofoils"* in the book "*Marine Rudders, Hydrofoils and Control Surfaces (Second Edition)*".

Cavitation is the formation of air bubbles because the water changes phase as an effect of low pressure as explained by Morch [33]. The effect of cavition only occurs in the speed range between 45 and 50 knots according to Carlton [7]. This is far above the estimated maximum speed of 35 knots for the Nacra 17.

The ventilation of surface-piercing hydrofoils is extensively researched by Yin Lu Young summarised in the paper: "*Ventilation of Lifting Bodies: Review of the Physics and Discussion of Scaling Effects*"Young et al. [34]. The effect of ventilation is possible due to a region of separated flow. Within aerodynamics, Micheal Selig investigated the aerofoil design preventing laminar separation bubbles to form on the surface [35–37] with the concepts clearly explained in his lecture notes Selig [9].

The most common computational 2D fluid dynamic model used in the industry is Xfoil, designed by Drela [38]. This programme provided an improvement in the boundary formulation from its predecessor: Profil by Eppler and Somers [39]. Fluid dynamics research is currently performed using Computational Fluid Dynamics (CFD). While Xfoil uses a simplified model of the physical systems and can only calculate 2D flow, CFD approximate the movement of the different air particles. This allows for more complex

flow analysis. However, Xfoil is still the preferred tool for first estimations and optimisations according to Bergmann et al. [40]. For the 2D case, a minimal loss of accuracy is observed while the analysis is performed in significantly less time.

Research in to the Nacra 17 Some research is done specifically for the Nacra 17. These are the analysis of the control stability of a small hydrofoiling boat by Bagué [41], the generation of a Velocity Prediction Programme by Graf et al. [42], and fluid-structure interaction by Marimon Giovannetti et al. [43].

The first study by Alec Baque [41, 44], analysed the practically identical boat, the ”Goodall Design Foiling Viper”. In the analysis, a 3D model of the boat was used to analyse the dynamic stability of a hydrofoiling sailing boat using CFD. In the study Bagué et al. [44], it was concluded that the boat was both statically and dynamically stable.

The second study designed a Velocity Prediction Programme (VPP) in collaboration with the German Sailors Association, as written by Graf et al. [42]. A VPP predicts the speed potential of a sailing yacht by finding the equilibrium of all the forces that act on the boat. The adjustable parameters of the boat are optimised for each wind direction and speed. The goal of the VPP is to find an optimised set of trim parameters and show the speed potential of the boat. The trim parameters analysed in the paper by Graf et al. [42], are those of the daggerboard rake, the rudder rake, the rudder angle, the heel angle, and the platform trim. CFD analysis was again used to analyse the performance of the foils with the assumption that the foil is rigid.

The third paper investigates fluid structure interactions (FSI) for the daggerboard. In the paper from Marimon Giovannetti et al. [43], the interaction between the water and the resulting mechanical deformation is investigated. The foil deflection was measured in a cavitation tunnel using digital image correlation (DIC) to calculate the strains and deflection. For computational analysis, the foil was scanned using a 3D scanner with a volumetric accuracy of 0.1 + 0.3 mm/m. After comparing the results, they found a discrepancy between the actual deflection and the calculated deflection using the computer model. They attributed this change to the incorrect internal geometry and the estimated torsional rigidity. The error in angle of attack (AOA) was estimated to be an increase of 1.6 degrees at the tip. Resulting in higher lift than predicted.

Conclusion The literature highlighted in this State-of-Art identifies the different research areas needed to investigate manufacturing deviations in the Nacra 17 hydrofoils. Manufacturing deviations can be identified by reverse engineering the shape in 2D sections. The differences between the hydrofoils can be translated to the different shape parameters of a 2D profile. The shape parameters are widely used to analyse the fluid dynamic performance of a given profile.

For the analysis of the profile, the lift drag and laminar separation are of interest in the comparison. These properties can be calculated for the different hydrofoils using the programme XFoil. This will allow for the analysis of a larger number of 2D sections for a comparison.

The final areas of interest are the fluid-structure interaction and the generation of a VPP. Fluid-structure interactions can connect the differences in shape and stiffness of the different hydrofoils to obtain a complete picture of the differences in the hydrofoils due to manufacturing deviations. The VPP could identify the difference in speed and sailing angles due to the variation in shape between the different hydrofoils.

3

Defining the Research direction

3.1. Research Scope

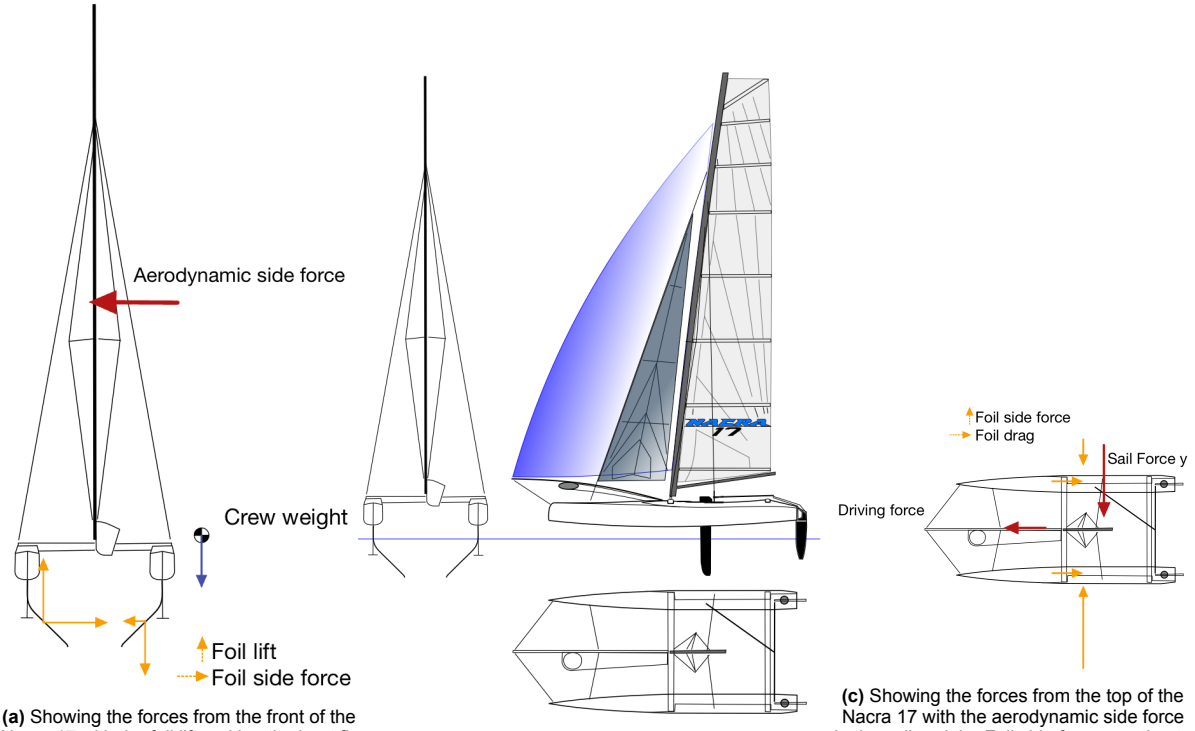

(a) Showing the forces from the front of the Nacra 17 with the foil lift making the boat fly and reacting against the sail side force.

(b) Schematic representation of the Nacra 17.

(c) Showing the forces from the top of the Nacra 17 with the aerodynamic side force in the sail and the Foil side force reacting to this force.

Figure 3.1: The schematic representation of the Nacra 17 showing that the Foil needs to counter act the side force and that the upwind hydrofoil can create downward force to counter act the moment from the sails.

The Nacra 17 is a foiling catamaran, as depicted in Figure 3.1b. A catamaran is a boat with two hulls, distinguishing it from monohulls (one hull) and trimarans (three hulls). "*Foiling*" refers to the ability of the boat to fully lift all the hulls out of the water at specific wind angles and speeds. This is one of the three possible modes with the hull floating on the water as: *"displacement mode"*, and the hull(s) skimming over the water as: *"planing mode"*. The Nacra 17 class is a one-design class and is selected to be one of the disciplines at the 2024 Olympic Games. With the one-design status, all parts are meant to be identical. Parts can only be bought from selected dealers, and each part needs a certification sticker

to prove that it is a genuine part. The goal of a one-design class is to reduce development cost and maintain a competitive sailing fleet where anyone can compete for the win.

This thesis focusses on the main dagger boards (hydrofoils) of the Nacra 17. The daggerboards are non-weighted boards that prevent a sailing boat from going sideways. The z-shaped daggerboards will be called hydrofoils from now on. Some specifications of the boat are given below:

- Depth: 1.71 m [19]
- Width: 0.7 m [19]
- Chord length: 197 mm [19]
- Chord Thickness: 25 mm [19]
- Boat weight: 173 kg [45]
- Ideal crew weight: 135 kg [46]
- Relative righting moment: 754 kg*m [46]
- Approximate lift-off speed: 10 knots (5.14m/s)
- Approximate maximum speed: 35 knots (18m/s)

Figure 3.2: The Pipestrel alpha trainer aircraft with a maximum takeoff weight of 550 kg and a minimum stall speed of 43 knots [47].

In some situations, only a small section of the hydrofoil is submerged. In these situations, the full righting moment of 754 kg is applied on this small section of submerged hydrofoil. With the boat being 2.59 metres wide [46]. The foil needs to produce more than 580 kg of lift. This is about the lift the wings of a small 2 person aircraft like the Pipistrel in Figure 3.2 needs to produce with a fraction of the size. It is not hard to imagine that the hydrofoils need to be strong and stiff to withstand this load and not bend significantly. The weight should be minimised to reduce the required lift for flight. The generation of lift by the hydrofoil is also comparable to how the lift on an aircraft is generated. Two uncompressed fluids can be compared using the Reynolds number (Equation 3.1). The Reynolds number is calculated using Equation 3.1. With flow speed (V), chord length (l) and kinematic viscosity (ν). Using the same Reynolds, the foil can be compared or analysed.

$$Re = \frac{Vl}{\nu} \tag{3.1}$$

The Reynolds numbers in which the Nacra 17 operates are very comparable to the Cessna 172. With the Nacra 17 operating in Reynolds numbers up to 3.5 milion in 20 degree water at 35 knots. When converting these numbers to a warm day of 20 degrees. A Cessna, with a wing chord of 1.47 m is flying at 73 knots for the same Reynolds number. This is well above the stall speed of 42 knots. This will give an indication as to what type of aerodynamics needs to be considered when analysing the Nacra hydrofoils.

For the research, the Olympic team gave limited access to their six hydrofoils that they are currently using. These will thus be the hydrofoils that will be used in the analysis. The Team does travel around the

world, visiting the different regatta's. This requires good coordination to determine when the hydrofoils can be used for analysis.

The tools that can be used for any research are limited to what is available at the TUdelft. It is decided at an early stage that CFD analysis would not be used in the analysis. This was decided because of the large number of sections from the hydrofoil and the lack of experience of the author with these tools.

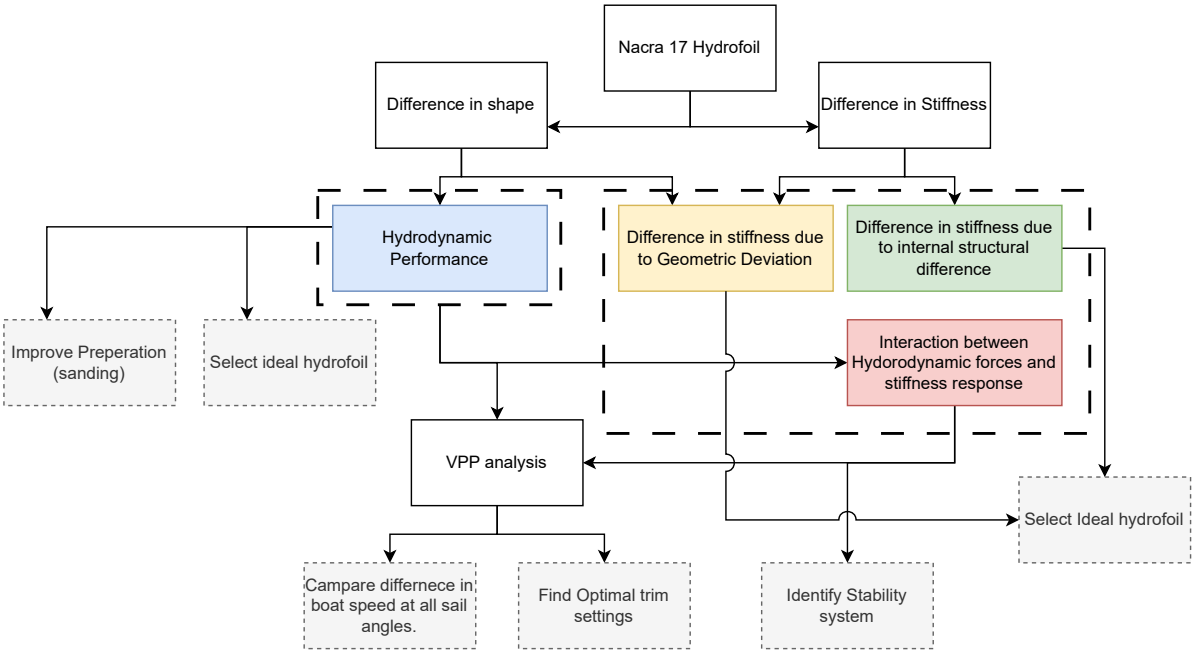

Figure 3.3: The Road map of the area's that can be investigated with the Nacra 17 hydrofoils.

From the State-of-Art (chapter 2), it became clear that the final research of the Nacra 17 hydrofoil would focus on: Optimising a Velocity Prediction Programme (VPP) of the Nacra 17, and Identifying the Control Stability of the Boat. Due to limited resources, it will not be able to perform these two analyses. Therefore, the steps towards this goal will be considered. The research steps required to reach these two results are shown in Figure 3.3. For these areas of research, a basis of understanding on the working of the hydrofoils is necessary. There may be two areas that are different in the Nacra 17 hydrofoils due to manufacturing. These are the shape and stiffness. The shape can affect the hydrodynamic performance and the stiffness. Stiffness is affected by geometry, internal structure, and fibre orientations. Hydrodynamics and stiffness analysis can be brought together in fluid-structure interactions. Therefore, these can be used to identify the stability of the boat. The hydrofoils can twist and bend while loaded in the water, and this twist will affect the load. This creates an unstable system with a positive correlation between the two (twisting up creates a higher angle of attack, which generates more lift). A stable system is achieved when torsion and load are negatively correlated. Knowledge of the stability with each hydrofoil. The team can choose the most suitable hydrofoil to use in the upcoming regattas.

The Velocity Prediction Programme is one of the possible outcomes for research in the Nacra 17. This VPP takes all the boat's performance data and creates a diagram showing the highest possible speeds in all wind directions. To create this diagram the different trim settings, small adjustments that can be made to the boats systems, are optimised for a given wind angle and speed. These trim settings can be used while sailing to optimise boat performance. Using a VPP, the actual difference in performance can be expressed in boat speed.

The VPP generates more accurate solutions with better data. Thus, creating a good data set containing the Hydrodynamic Performance Data for the different hydrofoils would be needed to gain understanding. Both areas of research are far beyond the scope of this master thesis. Thus, a direction needs to be chosen between the following. Hydrodynamic performance, difference in stiffness due to geometry, and difference in stiffness due to the internal structural. The different tests that can be performed in each area are highlighted in Figure 3.4.

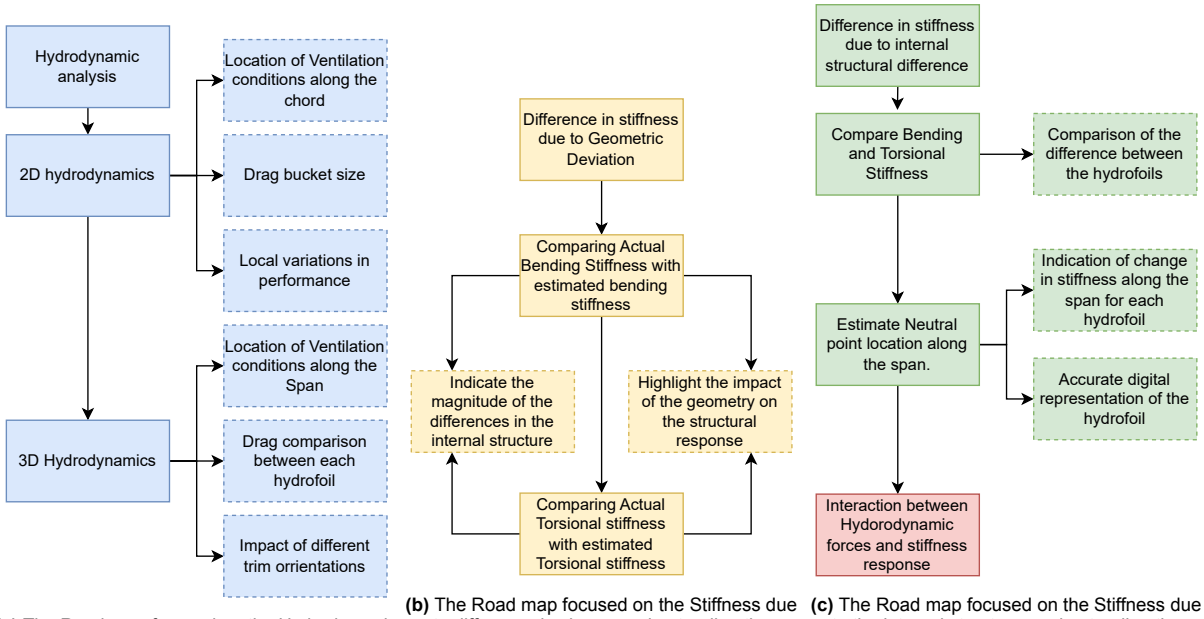

(a) The Road map focused on the Hydrodynamic analysis with increasing the complexity by understanding the local differences before analysing the Full hydrofoil.

(b) The Road map focused on the Stiffness due to difference in shape, understanding the difference in stiffness between the hydrofoil and how the moulding in production affects the hydrofoil.

(c) The Road map focused on the Stiffness due to the internal structure, understanding the difference in stiffness between the hydrofoil and how other production processes affect the hydrofoil performance.

Figure 3.4: The different area's of interest identified from the Nacra 17 hydrofoil, expanded into smaller steps that show the road map of what the research can take.

The stiffness resulting from the geometry (Figure 3.4b) would primarily validate that the assumption is correct. If the stiffness is mainly affected by the internal geometry, this direction would not produce usable results. For the internal structure (Figure 3.4c), the differences between the hydrofoils can be compared. First, the overall bending and torsional stiffness must be identified. After these are measured, the structure needs to be reverse-engineered. The current assumption would be that the bending and torsional stiffness deviate from the direction of the fibres or from a change in location of the mid-spar in the foil. The mid-spar is a beam that connects the upper and lower surfaces of the hydrofoil, (probably) in the middle of the chord along the full span. These effects can be analysed when the neutral point of the hydrofoil is calculated along the span. The neutral point is defined as the point where, if a load is applied to the neutral point, only a bending moment is created. It is contrary to intuition that this point is not in the middle of the structure. In the case of a C beam, this point is located outside of the structure. When the neutral point is found, the exact orientation of the fibres and geometry are not needed to create a digital version of the hydrofoil. With a structural model of the hydrofoil, the hydrodynamic forces can be applied. This will identify the stability of each hydrofoil.

Although this is a very interesting research direction, it has limited benefits to the Olympic team. The team only has a limited number of hydrofoils. The sample size is small. It is not feasible to test a wider range of hydrofoils and pick the best-performing set. The final direction of research would provide some immediate benefit to the sailors. This direction is the hydrodynamic analysis (Figure 3.4c).

The hydrodynamic analysis can be divided into two different areas. These are 2D and 3D hydrodynamics. The 2D hydrodynamics would analyse the 2D cross section of the hydrofoil. The analysis of these sections can identify the impact of specific deviations present between the hydrofoils. These details will become lost when the complete hydrofoil is observed. 2D section analysis can identify the impact of shape differences on drag, drag bucket size, and (laminar) separation that could induce ventilation.

3D hydrodynamics uses the calculation of the 2D sections to generate a 3D model of the hydrofoil. This 3D model can indicate the final difference in performance between the different hydrofoils. The 3D analysis can analyse the impact of different orientations of the hydrofoil. These different orientations can be the angle of the hydrofoil forward or backward, and the rotation around its axis (toe in/out). These analyses can help the team find the best trim settings while sailing.

3.2. Research Definition

The Research question that can be formulated from the State of Art is:

What are the manufacturing deviations of the Nacra 17 hydrofoil and how much do they affect performance?

In order to answer this question. The research question must be divided into several research questions. The first sub-question is focused on the feasibility of measuring the manufacturing deviations in the Nacra 17 hydrofoils stating:

Q.1 Can a 2 m spanning hydrofoil be accurately digitised to make a comparison between different geometric variations? The successful digitisation of the hydrofoil follows up to the next sub-question identifying the best method to reconstruct the profile sections in order to make a comparison.

Q.2 What methods can accurately reconstruct the 2D section profiles parameters of the digitised Nacra 17 hydrofoils?

The third sub-question focusses on the documentation on magnitude and cause of the differences in geometry between the different hydrofoils.

Q.3 Which 2D profile parameters can be linked to a manufacturing process to show the magnitude of the difference variations in this process produced?

The final sub-question links the hydrodynamic analysis to ***Q.4 Can a 2 m spanning hydrofoil be accurately digitised to make a comparison between different geometric variations?***

The subsequent hypotheses are then formulated as follows:

H. 1 The Creaform HandyScan Black provides the necessary accuracy at high measurement speeds in order to digitise all hydrofoils in a timely matter.
- 1.1 The differences between the hydrofoil are greater than 0.1226 mm as calculated in equation (4.2)
- 1.2 The hydrofoil varies in shape along the span, requiring a scan of the complete surface
- 1.3 The sanded resin layer provides a good measurement surface without the need for extra pre-processing for the scan

H. 2 The Data can be processed using python with a accuracy higher as the differences observed in the hydrofoil sections.
- 2.1 The Leading and trailing edges can be found consistently by using the raw data set.
- 2.2 The camber line can be extracted from the profile data
- 2.3 The Profile can be accurately approximated by applying a low pass filter on the data.
- 2.4 The profile can be accurately approximated using a B-spline function for the Camber line and the thickness profile.

H. 3 Manufacturing defects can be identified by the differences in the shape parameters of the different hydrofoil sections.
- 3.1 The profile thickness can be an indicator for improper mould closure.
- 3.2 The polynomial camber line can indicate a miss alignment of the mould halves
- 3.3 A correlation can be found between the different parameters that could indicate improper mould closure or miss alignment.

H. 4 There is a difference in the hydrodynamic performance between the different hydrofoils.
- 4.1 The difference in shape affect the location where ventilation can occur.
- 4.2 The biggest impact on the performance is influenced by the leading edge radius.
- 4.3 The high pressure side of the profile presents separated flow at positive angles of attack.

II

Methodologies

4

Digitisation of the Nacra 17 Hydrofoil: Method

(a) The Nacra 17 hydrofoil laying on its side.

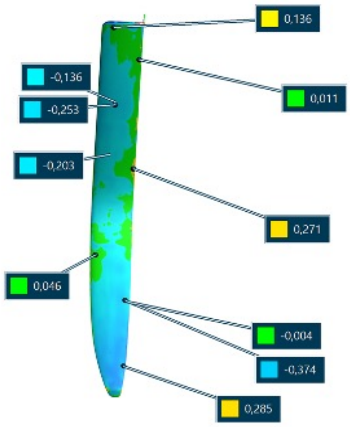

(b) The Nacra 17 hydrofoil laying on its side with the differences in geometry highlighted by the difference in colour.

Figure 4.1: An example of the visual variations on the Nacra 17 hydrofoil.

By just looking at the hydrofoils they appear to be identical. Only differences that can be observed are different scratches. Apart from the scratches, there is no observable difference. This shows the need for a measurement technique that is able to observe the small differences in geometry.

The differences in the hydrofoil are expected to be due to small misalignments in the mould. With pinched fibres and the resin run out on the leading edge (Figure 6.2b), the part requires manual sanding before it can be sold. This manual sanding is a variable process that changes over the span of the hydrofoil. The entire span of the hydrofoil needs to be examined, as the differences can thus change. The hydrodynamic performance will be evaluated with the Xfoil programme. Xfoil allows for a fast comparison between different geometries. This programme can isolate the different sections to show

specific problems with the shape. Without using a computer, the hydrofoil can be tested in a wind tunnel or towing tank. Both options require the whole foil to be analysed in one way. This might show a difference, but will not identify why there is a difference. The programme XFoil requires a set of points in a text document that represent a cross-section of the hydrofoil for the analysis.

This leads to the following requirements. High precision is needed to detect small differences. The cross-section of the hydrofoil needs to be examined at a number of different locations to capture a range of shapes that are present on the hydrofoils. A digital representation of the hydrofoil is needed for further analysis.

Requirements:

1. High precision.
2. Large number of 2D sections.
3. Digital format.

Assumptions:

- Lesser detail for the whole foil is preferred *over* high detail for a select set of cross-sections.
- The sanded resin layer is opaque enough for the 3D scanner to produce a precise measurement.

In order to digitise the hydrofoils, the Creaform Handyscan Black 3D scanner from civil engineering provided the best fit to the requirement set. An overview of the theory behind digitisation will be provided in section 4.1. The digitisation process will be explained in section 4.2. The results of the digitisation process will be elaborated upon in chapter 8 with the discussion in chapter 12.

Hypothesis 1: ***The Creaform HandyScan Black provides the necessary accuracy at high measurement speeds in order to digitise all hydrofoils in a timely matter.***

H. 1.1: *The differences between the hydrofoil are greater than 0.1226 mm as calculated in equation* (4.2)
H. 1.2: *The hydrofoil varies in shape along the span, requiring a scan of the complete surface*
H. 1.3: *The sanded resin layer provides a good measurement surface without the need for extra pre-processing for the scan*

4.1. Theory

The following section will cover the theory needed to minimise the loss between the actual hydrofoil and the digital model. First, the reverse engineering method will be discussed to identify the best suited 3D scanner (subsection 4.1.1). The two suitable 3D scanners available for this project will be compared in Appendix G. This section will cover the principles of how the 3D scanner will digitise the hydrofoils. The different file types that can be exported will be covered briefly (subsection 4.1.3. The file system that does not affect the measurement data will be identified.

4.1.1. Reverse Engineering

Getting a digital model of an existing object can be called *Reverse Engineering*. There are a large number of different measuring methods that allow for reverse engineering. The first dividing method is contact or non-contact methods. Contact methods use a probe that follows the surface. With the location of the probe known, the surface geometry can be extrapolated from this data. In the book "*Reverse engineering: an industrial perspective*", Raja and Fernandes [48] identified the benefits of contact methods with respect to non-contact methods to be its:

a) high accuracy,

b) (Relative) low cost,

c) insensitivity to color and reflectivity, and

d) the ability to measure deep pockets and slots.

This is accompanied by the disadvantages of:

a) very slow data collection,

b) inability to accurately measure soft objects due to the distortion of the surface by the probe, and

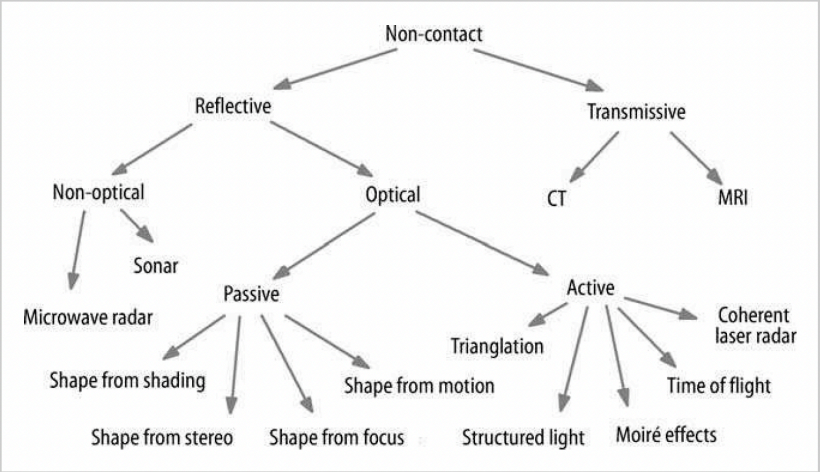

Figure 4.2: Non-contact method hardware classification [48].

Non-contact methods add high measurement speeds that allow for the digitisation of large volumes. This is necessary for the digitisation of the hydrofoils because the whole surface needs to be measured, as explained in the introduction. The resin of the hydrofoils are affecting the measurment results of the non-contact measurements. Most scanners will not be able to scan (see) transparent materials.

When considering non-contact measurement methods, there are a large number of techniques that can be used. A summary of the different methods is given in Figure 4.2. From these measurement techniques, triangulation was identified to be the most promising method.

4.1.2. 3D scanner specification

(a) A comparable scanner to the FAROBLu HD Quantum^{E} FARO [49].

(b) The Creaform HandySCAN BLACK while scanning an helicopter blade OLDBAC [50].

Figure 4.3: The 3D scanner types available at the university at the time of writing.

At the University there are two 3D scanners that use laser-triangulation and are accessible to the author. These scanners are the Creaform HandySCAN BLACK and the FAROBLu HD Quantum^{E} with a 2.5 meter arm. Both scanners use laser triangulation to measure the distance to the object. The difference between these scanners is their spatial awareness. The Faro scanner uses the movement of the arm to identify its position in space. Creaform scanners use markers and photogrammetry to identify its

position in space. A more detailed explanation of the orientation method used by the Creaform scanner will be given in subsubsection 4.1.2.

There are a couple of important specifications that can be compared to identify the suitability of the scanner. The most important hardware specifications for a good result are: **a)** accuracy **b)** volumetric accuracy **c)** measurement resolution **d)** mesh resolution. For different optical scanners, the measurement rate might be an important parameter to keep in mind. Scanners that use lasers are usually fast enough so that this is not a problem. The HandySCAN has a measurement rate of 800,000 measurements/s [51]. The Faro arm measures at a rate of 600,000 points per second. The measurement rate for these scanners depends mostly on the support computer and the measurement conditions. At a very high measurement rate, the operator does not have to worry about moving the scanner too fast to scan the part. The downside would be the large file sizes that are generated at high scan rates. These are limited by the supporting PC's working and storage memory.

The *accuracy* of the scanner references the repeatability of a distance measurement. Creaform used ISO 17025 based on the VDI/VDE 2634 part 3 standard to find the probing error on tractable spheres. The Faro arm is measured using ISO 10360-8 Annex D. While scanning a part, the scanning sensor is moved around the profile to observe the whole surface.

The accuracy of the whole part is denoted by the *volumetric accuracy*. The faro arm uses very accurate position sensors in the joints of each arm. This allows for volumetric accuracy that is independent of part size. It is important to properly calibrate the arm with the measurement base to ensure that the stated accuracy is achieved. The Creaform scanner uses small infrared (IR) reflectors to identify the position of the scanner with respect to the part. Therefore, this volumetric accuracy is therefore dependent on the part size. The volumetric accuracy is calculated with (Equation 4.1) a constant (e_a) and a variable (e_b) accuracy scaled by length (l). The constant accuracy for the HandySCAN is 0.020 mm and the variable accuracy 0.060mm. This can be improved with MaxSHOT. MaxSHOT™Elite can only scan the reference markers, but will scan these markers with a higher accuracy of $e_b = 0.015mm/m$ as given by the data sheet in section G.1. The volumetric accuracy of the HandySCAN when measuring the Nacra hydrofoil is given in Equation 4.2

$$\text{Volumetric accuracy} = e_a + e_b l \tag{4.1}$$

$$\text{Volumetric accuracy} = 0.02 + 0.06 * 1.71 \text{ (span in m)} \approx .1226 \text{ mm} \tag{4.2}$$

The next specification is the resolution. The *measurement resolution* is defined by the number of measurement points. This resolution does not dictate the final resolution of the scan data. This is defined by the mesh resolution. The mesh resolution filters out the measurement noise outside the date and produces the average distance of a number of measurement points. The averaged point creates the point cloud that represents the part's surface.

Using the data in Table 4.1 it can be concluded that the specifications of both scanners are very close. The Creaform scanner shows a better mesh resolution compared to the faro. The Faro scanner needed to be moved to accommodate the large size of the hydrofoils. This would increase the Volumetric accuracy error, or required a large time investment for calibrating the scanner. The Creaform scanner was possible to be operated by students and did not require a technician to be present, increasing the availability of the scanner.

Table 4.1: Applicable 3D scanners available at the university

	HandySCAN BLACK [52]	FAROBlu HD Quantum^E 2.5m [53]
single shot accuracy	0.035 mm	0.075 mm
Volumetric accuracy	0.020 mm + 0.060 mm/m	0.075 mm
measurement resolution	0.025 mm	0.04 mm
mesh resolution	0.1 mm	0.16 mm
recommended part size	0.05m - 4m	<2.5m

Distance measurements

The HandySCAN Black uses laser triangulation to measure the distance from the object. The scanner uses 7 laser lines [1] with many measurement points per line. For each measurement point, triangulation is used to determine the distance to the object. The combination of all these points will produce the measurement area. By moving the scanner around, the part can be digitised.

In order to use laser triangulation, a camera and a laser device are needed, and the desired object is needed. For one laser line, a single unknown point is measured. A schematic representation of the scanner is given in Figure 4.4b. The different terminology is shown in Figure 4.4a. The given variables are coloured green. The red variables are unknown and need to be calculated. The blue value can be given or needs to be calculated using the Field Of View (FOV). The value Z will be the variable that is needed for digitisation.

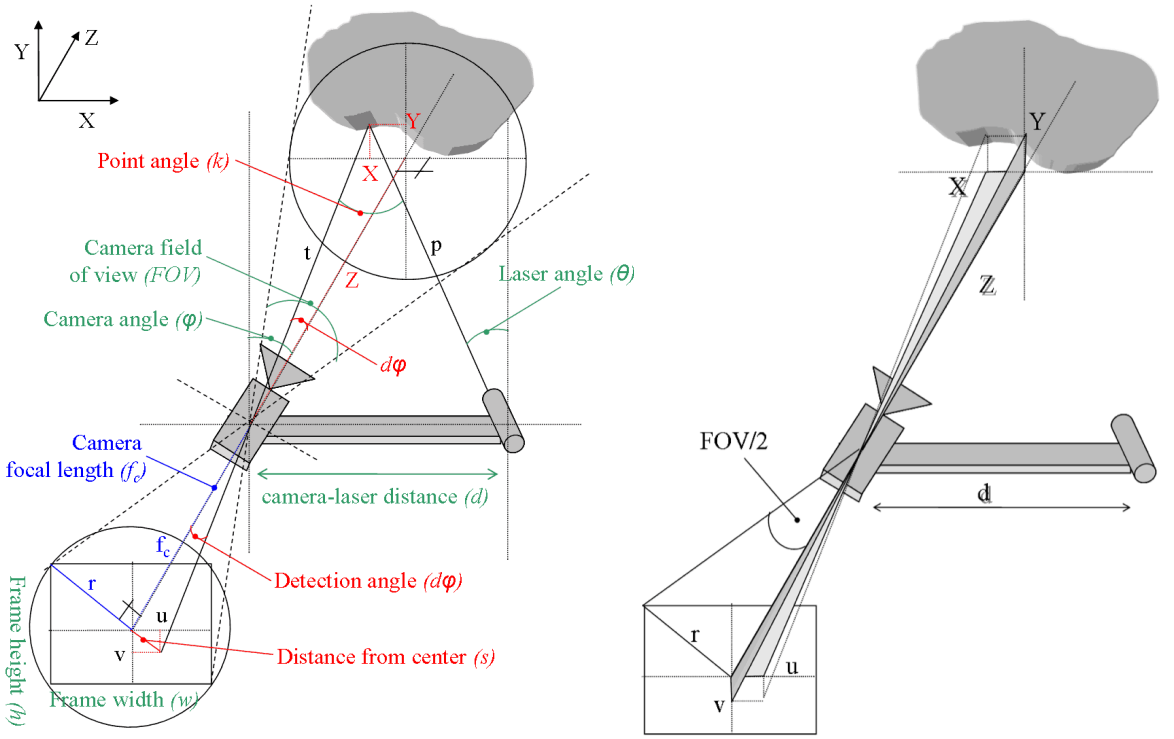

(a) The basic principle of laser triangulation in order to find the distance to a point on av=n object [54]

(b) Laser triangulation and identifying the location in X, Y and Z [54]

Figure 4.4: Overview of the principles of laser triangulation

The focal length and field of view are related by Equation 4.3.

$$\tan\left(\frac{FOV}{2}\right) = \frac{r}{f_c} \tag{4.3}$$

In these equations the FOV is the camera field of view. The r is the maximum distance from the centre. The height and width of the frame are given by h and w. The radius and frame dimensions are related as shown in Equation 4.4.

$$(2r)^2 = w^2 + h^2 \tag{4.4}$$

Using these two equations the focal length (f_c) can be calculated by substituting r and rearranging both equations to Equation 4.5

[1] See the spec-sheet in section G.1

$$f_c = \frac{\sqrt{w^2 + h^2}}{2 \tan\left(\frac{FOV}{2}\right)} \tag{4.5}$$

The length of the laser beam reflection from the surface to the camera is given by t. The variable t can be calculated using the law of sines (Equation 4.6).

$$\frac{a}{\sin(A)} = \frac{b}{\sin(B)} = \frac{c}{\sin(C)} = 2R \tag{4.6}$$

By filling in the angles and distances of the problem, the law of sines is changed into Equation 4.7.

$$\frac{d}{\sin(k)} = \frac{p}{\sin(\frac{\pi}{2} - \varphi + d\varphi)} = \frac{t}{\sin(\frac{\pi}{2} - \theta)} = 2R \tag{4.7}$$

The reason is that the laser beam forms a triangle. The following geometric problem can be calculated using the principle that the sum of all angles of a triangle is equal to π. The sum of all angles is there equal to pi as seen in Equation 4.8

$$k + (\frac{\pi}{2} - \varphi + d\varphi) + (\frac{\pi}{2} - \theta) = \pi \tag{4.8}$$

When solving for k in Equation 4.8 the following definition for k is found, as seen in Equation 4.9.

$$k = \varphi + \theta - d\varphi \tag{4.9}$$

Using Equation 4.9 and Equation 4.7 the equation can be rewritten to be a function of t and thus find the distance of the object to the camera in Equation 4.11.

$$\frac{d}{\sin k} = \frac{t}{\sin(\frac{\pi}{2} - \theta} \tag{4.10}$$

$$t = d\frac{\sin(\frac{\pi}{2} - \theta}{\sin(\varphi + \theta - d\varphi} \tag{4.11}$$

The variable $d\varphi$ is still unknown and can be calculated by Equation 4.12:

$$d\varphi = \arctan(\frac{s}{f_c}) = \arctan(\frac{\sqrt{u^2 + v^2}}{f_c}) \tag{4.12}$$

With the definition for $d\varphi$, t can be calculated and the distance to the object is known.

An easier method to calculate Z would be to use the X, Y, and Z coordinates of the detection point. Using Figure 4.4b, Equation 4.12 can be rewritten for u and v to obtain the following equations:

$$d\varphi_u = \arctan(\frac{u}{f_c}) \tag{4.13}$$

$$d\varphi_v = \arctan(\frac{v}{f_c}) \tag{4.14}$$

From the geometry it can be deduced that:

$$Z = \cos(d\varphi)t\varphi \tag{4.15}$$

By substituting Equation 4.11 into the equation for Z.

$$Z = d\frac{\cos(d\varphi)\sin(\frac{\pi}{2})}{\sin(\varphi + \theta - \varphi)} \tag{4.16}$$

X and Y can be calculated using the geometric principle that the angles on both sides of an intersection of the same line are equal in Equation 4.16. The detection angles for v (4.14) and u (4.13) can be rewritten using Equation 4.16.

$$d\varphi_x = d\varphi_u \Rightarrow \arctan(\frac{X}{Z}) = \arctan(\frac{u}{f_c} \Rightarrow X = Z\frac{u}{f_c} \tag{4.17}$$

$$d\varphi_y = d\varphi_v \Rightarrow \arctan(\frac{Y}{Z}) = \arctan(\frac{v}{f_c} \Rightarrow Y = Z\frac{v}{f_c} \tag{4.18}$$

With Z being the only unknown variable, the distance to the object can now be calculated.

These calculations assume an ideal situation of only one beam. As stated before, the scanner uses 7 lines each containing a large number of measurement lasers. The measurement speed is therefore greatly increased over one single point.

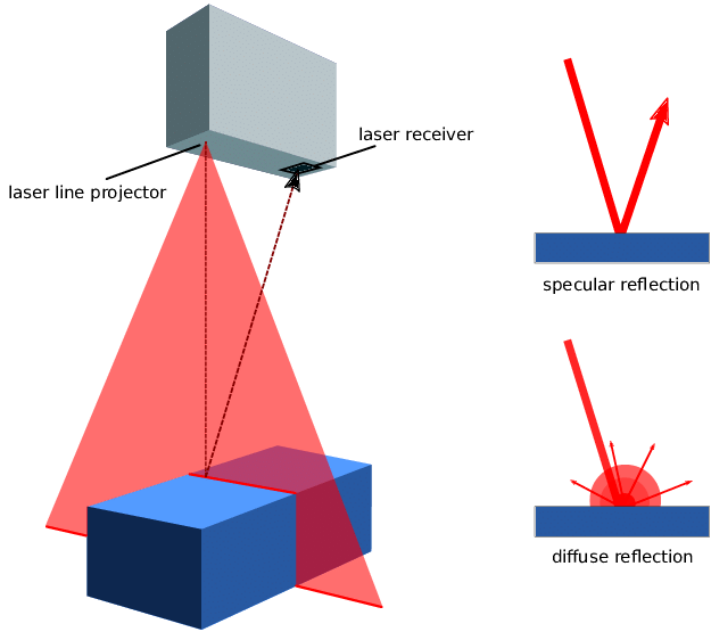

Figure 4.5: The different reflections from a matt surface finish and a reflective surface finish [55].

There are some outside influences that affect the accuracy of laser triangulation. As stated in subsection 4.1.1, non-contact methods are sensitive to surface colour, opacity, and reflectivity. The HandySCAN uses blue lasers for triangulation. Blue objects are thus hard or impossible to scan without preparation. This preparation entails the coating of the surface with a reflective matt finish[2]. This matt finish can aid with scanning of transparent and reflective surfaces. The reflective surface would seem to be the ideal surface for triangulation. This would be the case with an infinite resolution of the scanning sensor. For finite-resolution sensors, a range of reflected light results in better accuracy. Different reflective surface reflection can be seen in Figure 4.5. The gradual reflection of a matt surface provides a wider range of data from which the distance can be estimated.

The final impact on the scanner is the ambient light. With a light room or a dark surface, the intensity of the laser compared to the surrounding room is less. This makes the identification of the laser reflections hard. The result would be to increase the laser light strength and increase the number of measurements per second to achieve the same scan speed observed by the operator. The increase of the shutter

[2]More information can be found: Paul Motley. *HOW TO SCAN DARK, SHINY, OR CLEAR SURFACES WITH A 3D SCANNER [WITH VIDEO DEMO]*. Mar. 19, 2021. URL: `https://gomeasure3d.com/blog/scan-dark-shiny-clear-surfaces-3d-scanner-video-demo/` (visited on 07/14/2023).

speed gives her more data every second. This could be a problem when scanning large parts at high resolutions.

Spatial Orientation

The HandySCAN uses stereo photography to spatially orient the scanner with the object. The two camera's on each side are encircled by LED's that transmit an ultra-violet light. This light is reflected by the position markers placed on the measurement surface. The orientation of the scanner can be used to determine the location of the scanner.

Triangulation is used to determine the distance from the scanner to the marker. The schematic setup is shown in Figure 4.6c. In the example, the epipolar theoretical framework is used to calculate the position X. This is the distance to 1 point. In order to create a full 3D spatial orientation, more points are needed.

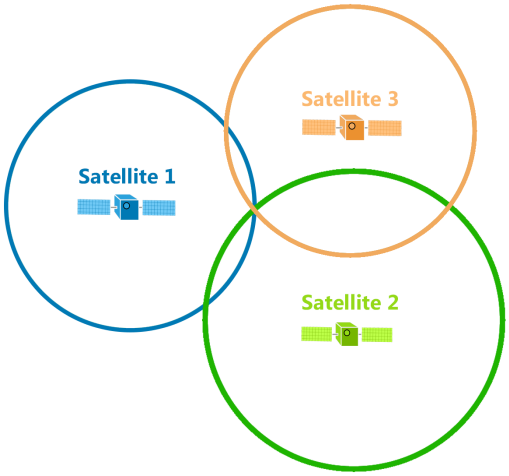

(a) Trilation of 3 satilites in 2D [57].

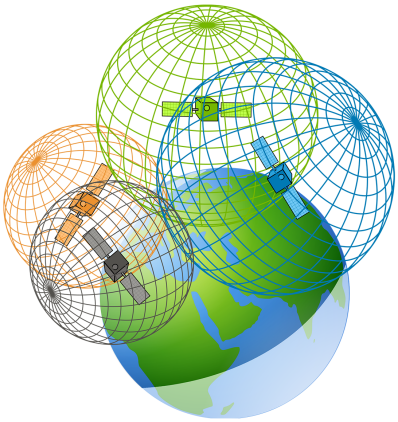

(b) Trilation of 4 satilites in 3D [57].

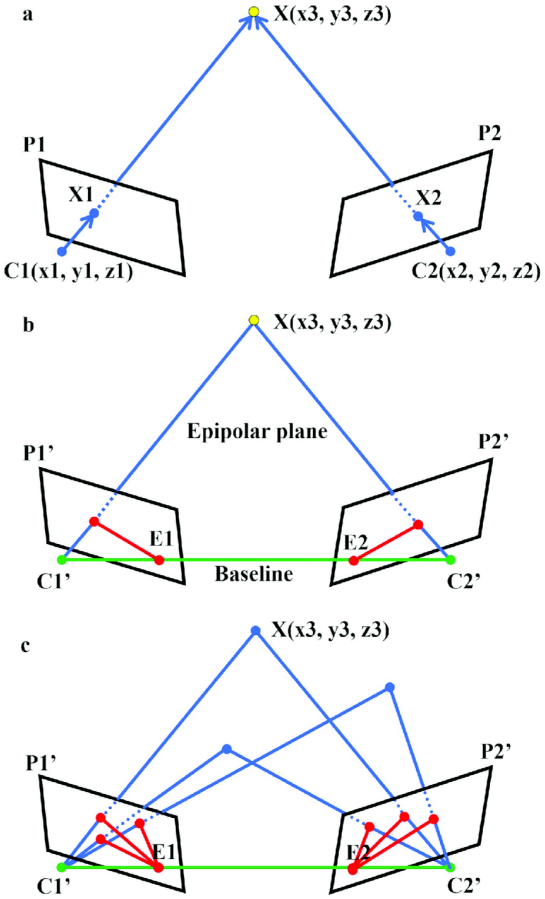

(c) 3D determination of the target position relative to cameras using epipolar geometry [58].

Figure 4.6: Stereo vision spatial orientation concepts

The orientation in space is very similar to the method that the Global Positioning System (GPS) uses for the spatial orientation. As Figure 4.6a shows that 3 different sources are needed to create a constraint location in 2D. Translating the problem to 3D shows a collection of spheres, as shown in Figure 4.6b. These 4 spheres have only one point where all intersect. That is, the position of the scanner. This position will always have a small error. This error is reduced with an increase in the number of position markers.

Markers are placed by humans. This results in a semi-random spacing of each collection of markers. Using this principle, the scanner knows which set of markers it is looking at. This is the final variable in spatial positioning with respect to geometry.

4.1.3. Filesystems

There are several different file types that can be exported by VXelements according to the brochure in section G.1. The different file systems are explained in section A.1. From these descriptions: `.stl` and `.step` are identified to be the most suitable file types. The point cloud data can be exported without compression to the STL file. The file in Catia will thus be of the same quality as the scan data. The step file can be used for normal geometries. This includes planes, lines, and volumes. STEP can be imported by Catia as well, allowing for the use of both programmes.

4.2. Methodology

4.2.1. Hydrofoil measurement preparations

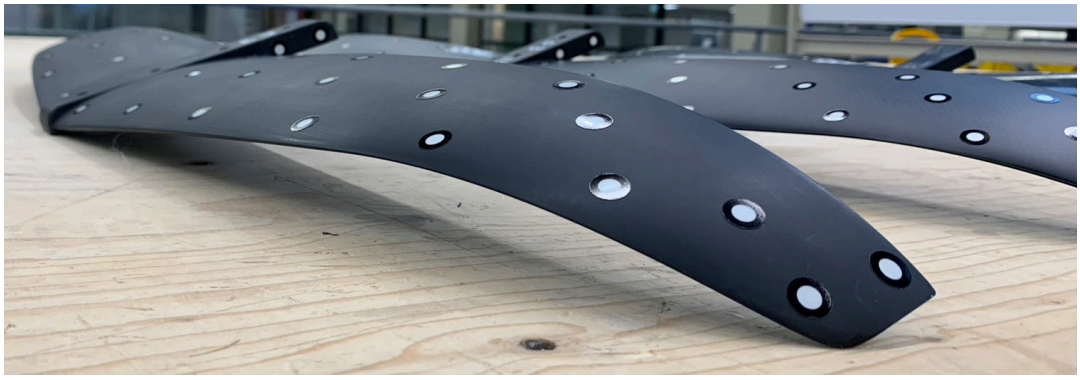

Figure 4.7: A wind surf hydrofoil with the measurement markers applied

The Creaform Handyscan uses small markers that are used for spatial orientations. Targets need to be placed in a random manner. This helps to identify the scanners spatial orientation using the principle of triangulation. The dots should be placed between 2 and 10 cm apart, according to the user manual [59]. The placement needs to be in such a manner that the dots can be connected and there are no isolated groups. A good example of these markers can be seen in Figure 4.7. The scanner needs a minimum of 3 targets to identify its position. Near the leading and trailing edges, the number of markers should increase to maintain this number of markers around the high curvature.

The curve of the leading edge and the trailing edge is still too high to transition to the other side. For this reason, plates with markers are glued to the foil. These plates can be seen from the edge and maintain the 3 makers for the orientation as seen in Figure 4.8a. This ability to transition to the other side helps with the accuracy of the leading and trailing edges, as they can be measured straight on.

4.2.2. Test Setup

The reliance of the 3D scanner on the markers allows a less restricted measurement setup. This resulted in the measurement setup shown in Figure 4.8b. The hydrofoil is held by two bolts in a steel beam while supported by a wooden post on the ground.

As long as the markers stay in the same place with respect to each other, the hydrofoil measurement will not be affected. In the first scans some of these plates moved. This resulted in an offset of the two sides of the foil intersecting at the leading and trailing edges, or a ghost foil appearing in the data. This problem was solved by starting the scan at the tip of the foil. The wooden post (figures 4.8a and 4.8b) did not move during the scan and provided a good reference point to start the scan.

(a) Measurement setup from the side showing the wooden post and the bolts in the steel beam.

(b) Showing the marker placement on the hydrofoil with the marker plates glued on top of the surface.

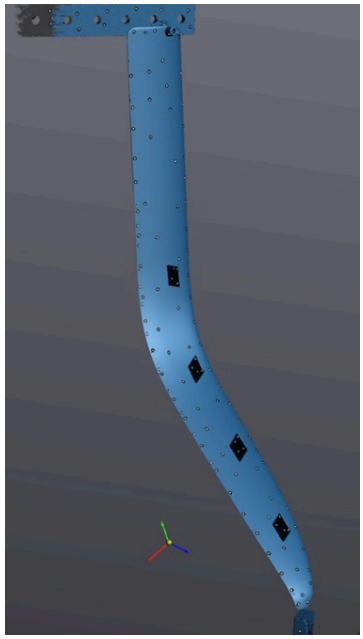

(c) Showing the Visual representation of the 3D scanner while scanning the hydrofoil. The green markers are in the correct measurement range and are used for triangulation.

Figure 4.8: The hydrofoil measurement setup used for the digitisation of the Nacra hydrofoils using two supports to hold the hydrofoil in place.

Table 4.2: The Scanner settings for each hydrofoil.

Foil code	Boat Side	Shutter speed [ms]	Resolution [mm]
ZS00531	Starboard	0.61	0.5
ZS00544	Port	0.61	0.5
ZS00696	Port	0.61	0.4
ZS00664	Port	0.63	0.4
ZS00691	Starboard	0.72	0.5
ZS00663	Starboard	0.61	0.4

The scanner used a number of different settings that could be changed for each scan. The settings that where changed are: the shutter speed and the resolution. The shutter and resolution were refined during the measurements. The minimum resolution is highly dependent on the operator and the computer used for the measurement. The measurement data are stored in the video memory of the computer. Increasing the resolution means that more data is collected and the video memory fills up before the part is successfully scanned. Reducing the shutter speed could allow more scan time before the data set becomes too big. Reducing the shutter speed could affect the scanners ability to gather data.

This results in the programme crashing and losing the whole scan. With a skilled operator the shutter speed can be reduced, resulting in lower measurement speed. This reduces the data rate, allowing for more time to scan the part. At a reduced shutter speed, the scanner has more difficulty finding the markers and scanning the part. It requires the operator to move very slowly and stay in the optimal measurement distance. Scan quality can be aided by reducing light in the environment. A darker room showed a better result at lower shutter speeds. The level of light was not a factor that could be controlled by the operator at the time of measurement.

During the hydrofoil scanning, the operator needs to move the scanner along the part to scan the surface. The scanner should be held within a specified distance range from the surface. This distance is communicated to the operator using colours. A light on top of the scanner changes from blue (far away), green (just right), to red (close by), depending on how far it is from the part.

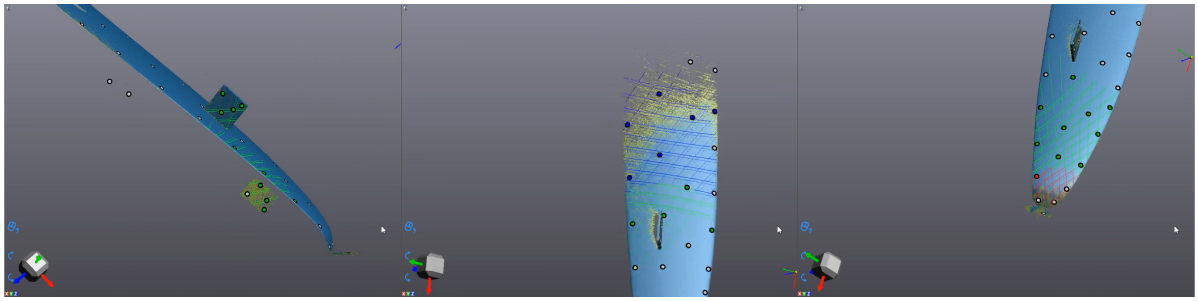

(a) Scan showing the utility of the wooden plates.

(b) Scan showing blue colour indicating that the scanner is to far away.

(c) Scan showing red indicating that the scanner is to close to measure.

Figure 4.9: Showing screen shots of the hydrofoil while it is being measured.

This light can be seen in figure 4.8b at the top of the scanner, showing blue. These colours are shown in more detail on the connected computer. The computer colours both the scanning lines, as well as the markers, to show the correct distance to the surface. Figure 4.9b, shows the blue lines and markers indicating that that part is too far from the scanner. While, figure 4.9c, shows the red lines and markers indicating that the specific part is too close to the scanner. When scanning the part, the operator uses these colours to position the scanner in the correct position. Figure 4.9a shows the effect of the wooden plates glued to the surface. Both plates show green markers that indicate a good measurement. Using the four markers on the plate on the opposite side, the scanner can be rotated to start scanning the opposite surface. Without these plates there could not be made a connection between the two sides of the hydrofoil.

The light blue surface, shown in both images, indicates the scanned surface. While the yellow indicates a partially scanned surface. These indicators are used to identify if the part is fully scanned or that certain areas need more attention.

4.2.3. Processing the foils in VXelements

Ones the all the hydrofoils were digitised. The data files needed to be processed using the integrated programme: VXelements (Figure 4.10a). The hydrofoils needed to be processed by: 1. removing the mounting beam. 2. removing the marking plates and support 3. finalising the scan (removing the tracking markers) 4. filling the holes in the model

The mounting beam was removed by placing a clipping plane perpendicular to the beam surface. This surface can be selected by creating a plane using the three markers shown in Figure 4.10b. This plane could be offset to remove all objects that are on one side of this plane. This method works to remove the base of a part. The screws, plates and support post at the tip are still present in the model. These must be manually removed. The best way to remove these parts is to use a brush selection tool. Selecting the base of the foreign objects using the brush tool and removing the selection isolates the objects from the foil. These isolated parts can be removed by selecting all the geometries attached to the foil and deleting all the other geometries. With only the hydrofoil left, the part can be finalised. Finalisation updates the mesh and removes the tracking markers. The last step is to use the automatic tool to fill all the holes in the mesh, which can be seen in Figure 4.10c.

The hydrofoil was processed within VXelements. It is transported to Catia for alignment of the different hydrofoils. The files are saved as an STL file. This file maintains the resolution as close to the measurement resolution as possible. The STL files are named using the following naming convention starting with `Narca_Foil` followed by the identification code of the foil. This identification code contains two letters and five numbers. This is followed by the shutter speed that was used for the scan. `SH0-61`, is a shutter speed of 0.61 ms. For a shutter speed of 0.74 the code would be: `SH0-74`. The resolution (`Res0-40`) is the next value. This is the mesh resolution that is set at 0.40 mm. After resolution, the side of the board is noted with SB (starboard/right side of the boat observed from the back) and BB (port/left side of the boat observed from the back). The VXmodel and STL state the progression in the

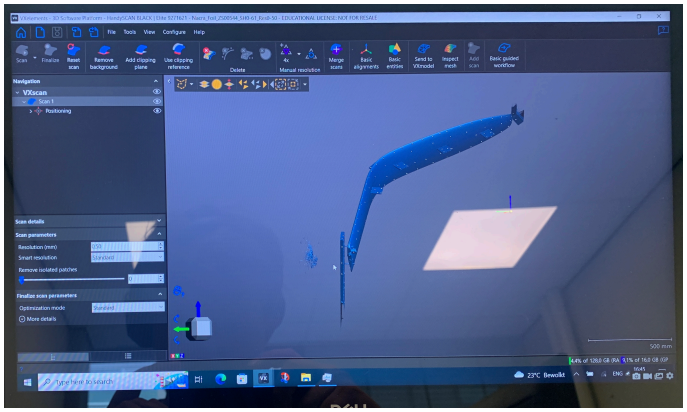

(a) Screen shot of VXelements.

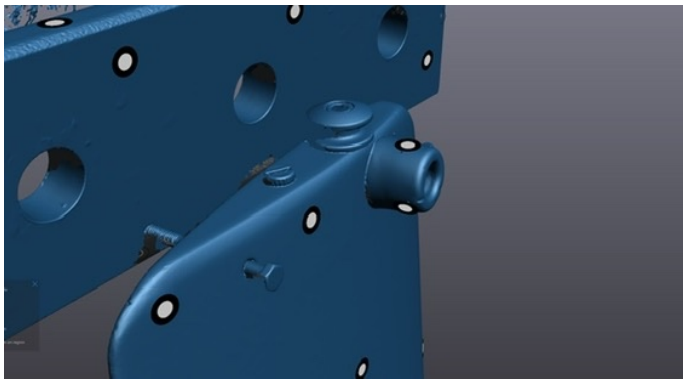

(b) The top of the hydrofoil after scanning.

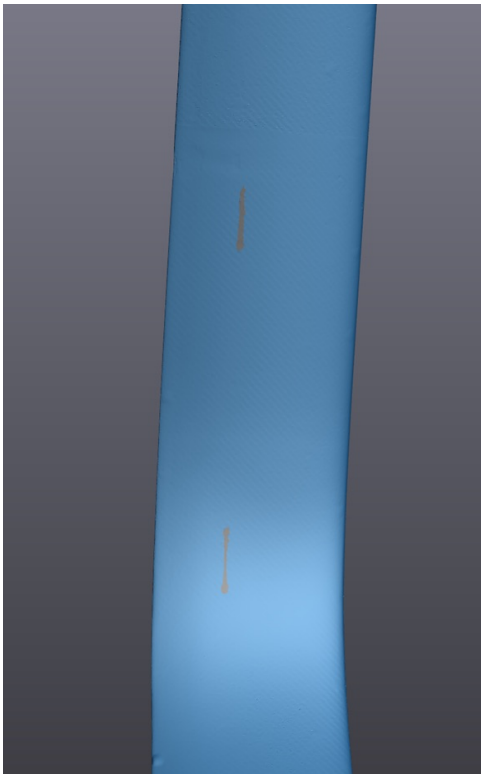

(c) Holes in the surface after finalisation.

Figure 4.10: VXelement processing stages

post-processing with VXmodel the final save file in VXelements and STL the file system. This naming scheme results in the following file name: "`Nacra_Foil_ZS00691_SH1-72_Res0-50_SB_VXmodel_STL.stl`".

4.2.4. Catia processing

With the foil scans processed in VXelements. STL files are aligned to the same coordinate system and sliced into sections using Catia VI. These sections are exported to be analysed using Python scripts. This analysis will be discussed in chapter 5. The environments that are used in Catia are highlighted in bold before the paragraph. To aid the understanding of this process in Catia, several images are placed in the Appendix showing the location of the different functions.

Digitized Shape Preparation The first foil (ZS00531) is imported from Catia, in the *digitised shape preparation* environment. The first action would be to save the file and name the geometrical set according to the set naming scheme. After saving the part, the mesh is repaired using *mesh pathologies* (figure A.1).

Digitize Shape to Surface With the imported foil, the coordinate system needs to be aligned. The first step is to create planes on the hydrofoil using *3D primitive Recognition* (Figure A.2). This can create a plane at the top of the hydrofoil. The next plane is aligned using the thick trailing edge at the top of the hydrofoil. The final plane is aligned with the middle of the leading edge and the middle of the trailing edge. This plane should follow the leading and trailing edge, up to the elbow. These planes can be used to align the hydrofoil with the global coordinate system using *fast align* (Figure A.3). Save the file.

Freestyle Shape design With the hydrofoil aligned to the coordinate system. Steps can be taken to produce the cross-sections of the hydrofoils. The cross sections need to be aligned with the profile

thickness and thus follow the hydrofoil curvature. This curvature is captured by manually fitting a line along the trailing edge of the hydrofoil. This line is created with the function: *3D curve* (Figure A.4). This curve is finally projected on the plane perpendicular to the trailing edge. Save the file.

Part Design On the curve, a set of points is repeated 50 times with even spacing. On each point, a plane is placed with the curve normal to the plane and constrained by the point. The same procedure is repeated to place a local coordinate system at the point. The coordinate system is required to rotate the cross sections in Python in the next step. Save the file.

Digitized Shape Preparation A new *geometrical set*(Figure A.6) and is named ”Scans”. Within this set, planer sections are created in every plane along the hydrofoil using *Planer section* (Figure A.5). Save the file.

This finalise the steps for the first hydrofoil. The other hydrofoils can now be added to this file and aligned with the first hydrofoil. Before importing the new file, a new geometric set must be created using: *geometrical set*(Figure A.6). This set should be named according to the file naming scheme.

The hydrofoil can be imported into the geometrical set within the Digitised Shape Preparation environment. The hydrofoil file should be named using the foil code. Save the file.

The new hydrofoil will likely be placed in a random orientation with respect to the first hydrofoil. This placement depends on where the scanner started scanning the hydrofoil. This requires the hydrofoil to be roughly placed along the original hydrofoil. This can be achieved with the rotation and translation functions under the *standard* tab.

Depending on which hydrofoil was used for the initial setup, some hydrofoils will be a mirrored version. The ZS00531 hydrofoil was used for the initial setup, and this is a Starboard side hydrofoil. The port-side hydrofoils need to be mirrored through the x and z plane. This will create a starboard version of the port hydrofoil. Save the file now before continuing. This is especially important in the alignment steps, as these will take between 30 min and up to 2-3 hours depending on the computer.

The hydrofoil will be aligned twice. The first time *Fast Alignment* (Figure A.3) is used with a limited selection of the hydrofoil. This limted selection is made by deactivating parts of the mesh using the *activate* function located next to *Fast Alignment*. Only the tip and the root need to be active for this first alignment. After the alignment is finished, safe the file.

The complete mesh should be activated again. Now the *Best Fit Alignment* option should be used. This is found in the drop down menu of *Fast Alignment*. After the alignment is finished, safe the file.

The hydrofoil can now be compared with the original hydrofoil. This comparison is made using *Deviation Analysis*. This is the coloured block seen in Figure A.3. Save the file.

With the hydrofoil aligned to the original hydrofoil. The planer section needs to be made. This is the same procedure as described above. These last steps are repeated until all hydrofoils are aligned in Catia.

The data will now be exported to be processed further using Python. The first part to be exported is the set of coordinate systems along the span-wise spline. These are exported as a single digitised file (Figure A.7). The file with all coordinate systems need to be named `axissytems.txt`. The planer sections are exported next. Planar sections are exported using the file-naming scheme followed by `__(section number)`. This will result in the following file name:
`Nacra_Foil_ZS00531_SH0-61_Res0-50_SB_VXmodel-section__18.asc_fmt`. This concludes the processing in Catia.

4.2.5. 3D scanner accuracy test method

In order to find the real accuracy of the 3D scanner, a known shape was used to test the accuracy of the scanner. The shape used was a thin metal strip. This thin metal strip will test the accuracy of measuring a thin plate using wooden plates to capture both sides. The experiments were conducted by Alex Ashworth Briggs.

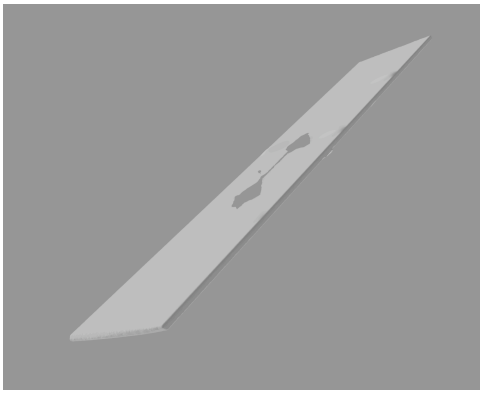

Figure 4.11: Thin metal strip used for scanner accuracy test

The metal strip was clamped to a table. The markers and wooden plates are applied in the same manner as that performed on the hydrofoils. This plate was scanned with Creaform HandySCAN black at a resolution of 0.4 mm and a shutter speed of 0.63 ms. Using the volumetric accuracy given in equations (4.1) and (4.2) and a length of approximately 2212 mm, the volumetric accuracy is given as 0.026 mm. Manual width measurements are performed using a Vernier with a resolution of 0.05 mm. The thickness of the plate is measured with a micrometre with a resolution of 0.01 mm.

5

Research Method Validation for 2D Section Processing: Method

The point data obtained from the 3D scan data need to be processed. But the data are now unstructured, it needs to be orientated, and made suitable for the analysis in Xfoil. The shape parameters of the hydrofoil can be extracted to observe how these change between the foils and throughout the hydrofoil. For orientation, it is important to identify the front (leading edge) and back (trailing edge) of the sections. In the methods, there are a number of ways that could be used to find these specific points. Using these points, the section can be rotated and translated to the correct position. This position is defined by Xfoil. Xfoil needs the leading edge to be at the origin of the coordinate system. The x- and y coordinate should start at the top of the trailing edge and go around to foil to finish at the bottom part of the trailing edge. The section should be scaled by the chord so that the chord length is equal to one.

Hypothesis 2: ***The Data can be processed using python with a accuracy higher as the differences observed in the hydrofoil sections.***

- **H. 2.1:** *The Leading and trailing edges can be found consistently by using the raw data set.*
  - **H. 2.1.1:** *The leading and trailing edge are the data points placed furthest apart using the Nacra data set.*
  - **H. 2.1.2:** *The minimum x-axis value will be at the leading edge location.*
  - **H. 2.1.3:** *The y values cross the x-axis at the leading edge.*
  - **H. 2.1.4:** *The leading edge is positioned on the maximum value of the first derivative using the Nacra data set.*
  - **H. 2.1.5:** *The leading edge is located at the point of maximum curvature of the profile using the Nacra data set.*
  - **H. 2.1.6:** *The leading and trailing edges are the points with the largest radius when transformed to polar coordinates.*
- **H. 2.2:** *The camber line can be extracted from the profile data*
  - **H. 2.2.1:** *The intersection of the offset of the profile surface inward is placed on the camber line and results in a reliable data set.*
  - **H. 2.2.2:** *The voronoi vertex points from the profile data are located on the camber line and result in a reliable data set.*
  - **H. 2.2.3:** *A polynomial function of degree 9 can accurately predict the Camber line using the appropriate data set.*
  - **H. 2.2.4:** *A B-spline with 5 knots can accurately predict the Camber line using the appropriate data set*
- **H. 2.3:** *The Profile can be accurately approximated by applying a low pass filter on the data.*
- **H. 2.4:** *The profile can be accurately approximated using a B-spline function for the Camber line and the thickness profile.*

5.1. Theory

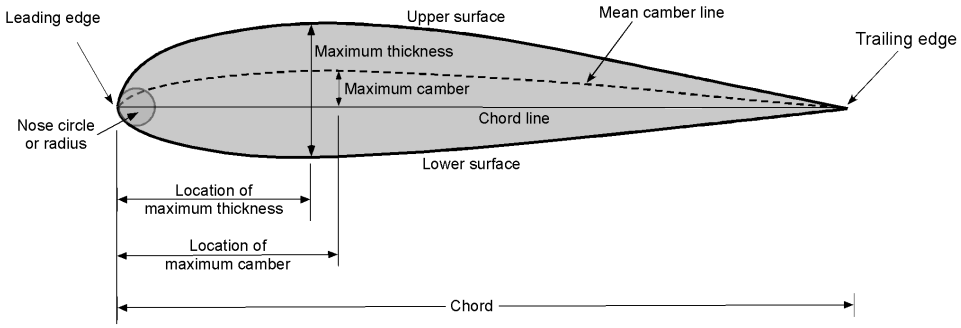

Figure 5.1: The different terminologies for a 2D Section with the profile maximum thickness (y_t) and its location (x_t), the maximum camber (y_c) and its location (x_c), leading edge (le),and trailing edge (te). The x axis is defined at the Chord line and the y axis is the thickness [60].

The 2D profiles in fluid dynamics use the name scheme shown in Figure 5.1. The leading edge is defined as "*The edge of a moving object that reaches a point in space or time ahead of the rest of the object*"-Crane [61]. The leading edge is this the most forward point, as seen from the flow. This is usually accompanied by the point farthest away from the trailing edge. When the maximum camber increases, this statement might not be correct anymore. The leading edge is usually the point at the highest curvature or the lowest radius. This is called the radius of the leading edge.

The trailing edge is the opposite of the leading edge. It is placed on the other side of the profile from the leading edge. The trailing edge often ends in a sharp tip. If this is not the case, the distance between the upper and lower surfaces is defined as the trailing edge thickness.

The mean camber line is the middle between the upper and lower surface. It will always intersect with the exterior surface at the leading and trailing edge.

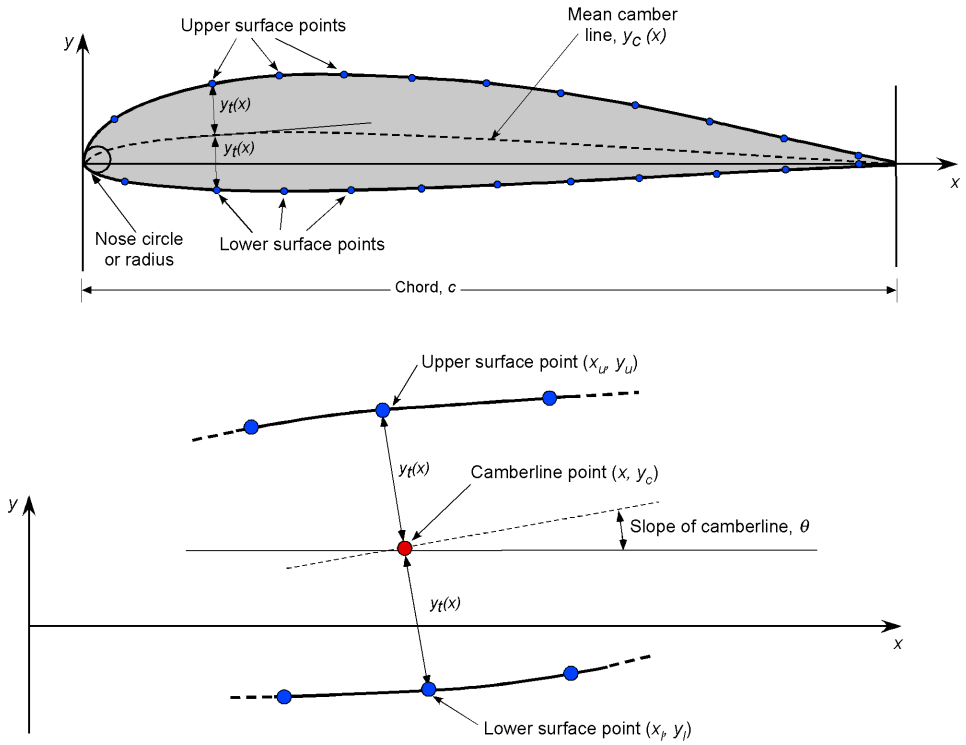

Figure 5.2: The construction of the profile is plotted perpendicular to the camber line with at a distance defined by function ($y_t(x)$) [60].

The profile thickness is defined from the camber line as shown in Figure 5.2. The upper profile coordinates are given by equations (5.2) and (5.3) and the lower profile is given by equations (5.4) and (5.5) with the slope given by Equation 5.1. The camber and thickness function can be seen in Figure 5.3.

$$\theta_c = \arctan \frac{dy_c}{dx_c} \tag{5.1}$$

$$x_u = x + y_t(x) * \sin\theta_c \tag{5.2}$$

$$y_u = y_c(x) - y_t(x) * \cos\theta_c \tag{5.3}$$

$$x_l = x - y_t(x) * \sin\theta_c \tag{5.4}$$

$$y_l = y_c(x) + y_t(x) * \cos\theta_c \tag{5.5}$$

The thickness is often defined as a function of x ($y_t(x)$). This results in all profiles ending either in a sharp point or with a trailing edge at a right angle. When the trailing edge is a sharp point, this is called a closed trailing edge (closed-TE). The opposite is the open trailing edge, which is usually accompanied by the width of the opening. It is clear that the upper and lower surfaces of a real aerofoil are slightly spaced as a result of physical limitations. The designed profile is cut by a small amount at the trailing edge to achieve this small thickness.

The orientation of the profile is important for the further analysis of the profile sections. Profiles are characterised by the maximum thickness and maximum camber as a percentage of the chord. With an incorrect alignment or chord length, these values will be distorted. Although the impact on these parameters will be relatively low. The fluid dynamic analysis is very sensitive to small errors in the orientation.

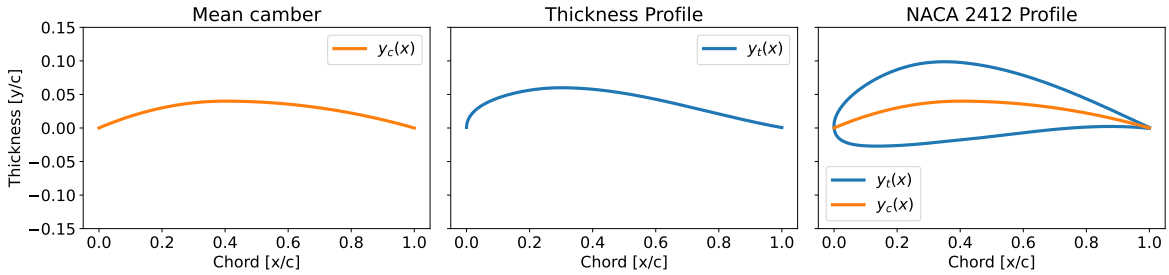

Figure 5.3: Showing the construction of the NACA 2412, with the mean camber line function on the left, the thickness profile in the middle and the combination of the two on the right.

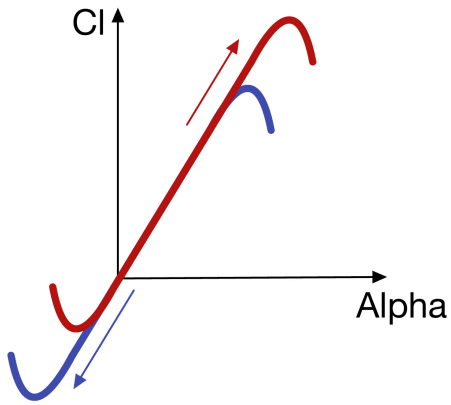

Figure 5.4: The shift of the lift over alpha curve when the profile is rotated incorrectly, the maximum lift coefficient will increase shift up or down.

If the profile is not orientated correctly, there is a difference in the angle of attack between the different sections. The result can be seen in Figure 5.4. The lift coefficient will change due to the difference in the initial orientation. This shift will also be observed in all other results of fluid dynamic analysis.

5.2. Methodology

This section will explain the different methods that were considered for the comparison between the hydrofoils. To compare the hydrofoil sections, good alignment is needed. This alignment of the hydrofoil needs to be performed by the programme automatically due to the large number of hydrofoil sections. The hydrofoils need to be placed in a specific orientation, and they need to be analysed with Xfoil in a latter stage. The alignment will be covered in subsection 5.2.1.

The resulting hydrofoils showed large variations in the Xfoil results when using the raw data. This shows the necessity of smoothing the data in order to obtain comparable results. It is very important that the shape of the hydrofoil is maintained. These methods are explained in subsection 5.2.3.

5.2.1. Alignment using the Profile data

Furthest points method

The aerofoil can be seen as an ellipse. The leading and trailing edges would be the two large curved areas. The middle of these two curves are the furthest distance two points in an ellipse can be. This can be converted to the aerofoil, where the leading and trailing edges are the points furthest apart. This analogy becomes less accurate as the camber of the profile increases. With this curvature, a different set of points could be closer.

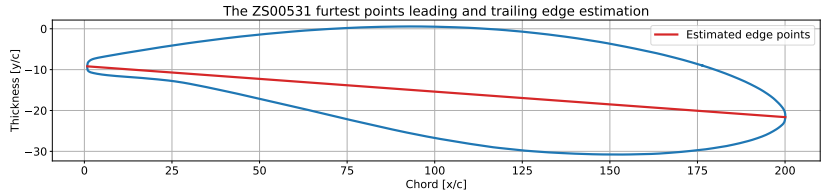

Figure 5.5: The chord line for a cross section using furthest points

The input is the set of translated points that are exported by Catia. This hydrofoil is now defined by the local coordinate system defined in Catia. The code to find the distance is given in Listing 5.1.

The distances between the points are calculated using the two-dimensional Euclidean distance as shown in Equation 5.6, with scipy's spatial distance function[1].

$$d(p,q) = \sqrt{(q_x - p_x)^2 + (q_y - p_y)^2} \tag{5.6}$$

The distance function produces a one-dimensional array. This is transformed into an nXn matrix, with n being the number of points in the profile, using the scipy squareform function[2]. From this matrix, the chord length is given as the maximum value. The leading edge and trailing edge are the index points of this maximum value. The index is found by obtaining the location of the maximum value and using numpy's unravel_index [3] to get the index locations in original array shape. These indices are the leading and trailing edge. The resulting chord line will look like Figure 5.5.

Listing 5.1: Finding the furtest distance

```
data_raw_cr_n = np.flip(data_raw_cr.T,axis =1)
pointsdist = sci_spat.distance.squareform(sci_spat.distance.pdist(data_raw_cr_n.T))
# square matrix containg the distance between any two points on the airfoil.
chordleng = np.max(pointsdist)
# getting the chord lenght, defined as the largest distance between the leading and trailing
    edge
I = np.unravel_index(np.argmax(pointsdist),pointsdist.shape)
#indecies of the leading and trailing edge
idlead, idtrai =I[data_raw_cr_n[0][list(I)].argmin()], I[data_raw_cr_n[0][list(I)].argmax()]
```

X and Y axis intersections

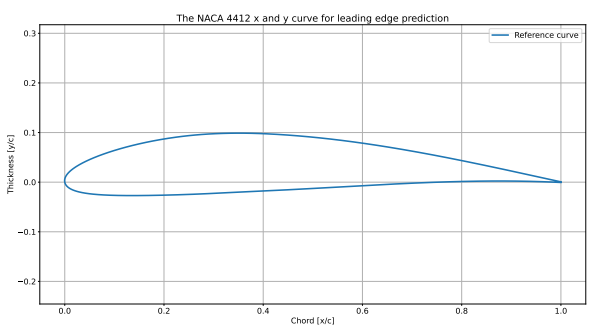

(a) The corresponding NACA 4412 profile

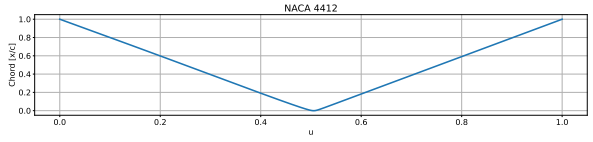

(b) The x axis plotted over variable u

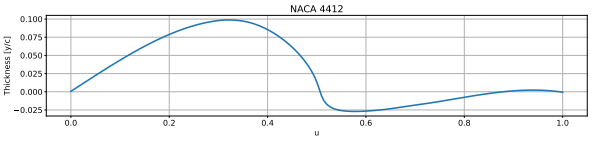

(c) The y axis plotted over variable u

Figure 5.6: A comparison between a normal and noisy data set for using the derivatives to find the leading edge

[1] scipy.spatial.distance.pdist:`https://docs.scipy.org/doc/scipy/reference/generated/scipy.spatial.distance.pdist.html`, (visited on: 07/17/2023)

[2] scipy.spatial.distance.squareform:`https://docs.scipy.org/doc/scipy/reference/generated/scipy.spatial.distance.squareform.html`, (visited on: 07/17/2023)

[3] numpy.unravel_index:`https://numpy.org/doc/stable/reference/generated/numpy.unravel_index.html`, (visited on: 07/17/2023)

The x- and y-arrays can show the leading edge and trailing edge of the hydrofoil. As the points are a continuous line in a circle, the x-axis contains a maximum and a minimum. These maximums can be used to define the edges. The x and y arrays are plotted over u, which spans from 0 to 1. The x-axis looks like Figure 5.6b. While the y-axis looks like Figure 5.6c. The leading edge would be the minimum value of x. The leading edge can also be defined by the y-axis. When y is equal to zero (or the minimum of the absolute of y), that should be the leading edge.

These methods could be very dependent on the foil orientation and position. This is tested by rotating and translating a known shape and observing the change in leading edge location. The translation subtracts 0.05 of the y-axis moving the hydrofoil down. This translation affects the estimation using the y-axis.

The part is rotated -60 degrees around the origin. This rotation affects the estimation using the x-axis. Equation 5.7 shows the rotation formula. The F_r would be the new array of rotated coordinates, x and y the original data set, and theta the rotation.

$$F_r = \begin{bmatrix} x_0, y_0 \\ x_1, y_1 \\ \vdots, \vdots \\ x_{n-1}, y_{n-1} \\ x_n, y_n \end{bmatrix}^T \cdot \begin{bmatrix} \cos\gamma, -\sin\gamma \\ \sin\gamma, \cos\gamma \end{bmatrix} \tag{5.7}$$

First derivative or Curvature of the profile

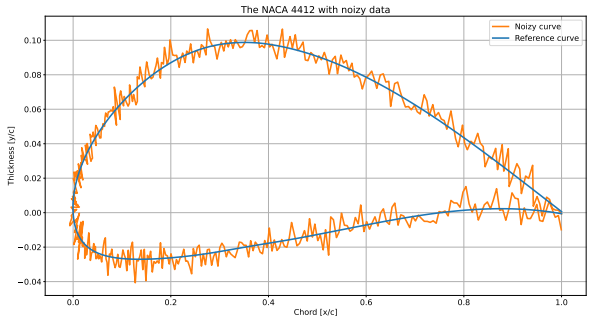

(a) The corresponding NACA 4412 profile with a profile with normally distributed noise with a deviation of 0.005 x/c

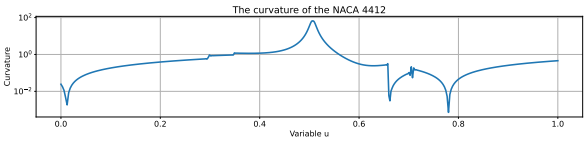

(b) The curvature plotted over variable u

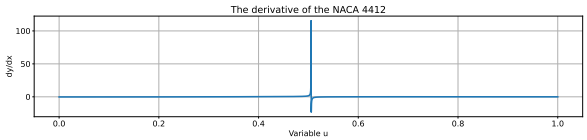

(c) The derivative plotted over variable u

Figure 5.7: Showing the first derivative and curvature of a NACA 4412 foil section.

The leading edge is the point with the highest curvature of the hydrofoil. The leading edge could thus be found by the derivative of the line curvature. A representative B-spline is first created to extract the derivatives of the curve. This B-spline was created using scipy's splprep function [4]. The derivative of the spline is obtained using scipy's splev[5] function. This function returns the derivatives $\frac{dy}{du}$ and $\frac{dx}{du}$. The derivative $\frac{dy}{dx}$ is calculated using Equation 5.8. The derivative of a NACA 4412 foil section can be seen in Figure 5.7c.

$$\frac{dy}{dx} = \frac{\frac{dy}{du}}{\frac{dx}{du}} \tag{5.8}$$

[4] scipy.interpolate.splprep:`https://docs.scipy.org/doc/scipy/reference/generated/scipy.interpolate.splprep.html`, (visited on: 07/18/2023)

[5] scipy.interpolate.splev:`https://docs.scipy.org/doc/scipy/reference/generated/scipy.interpolate.splev.html`, (visited on: 07/18/2023)

The peak observed in Figure 5.7c at u = 0.5, shows the leading edge. Curvature can also be obtained from this spline. The profile curvature is calculated using Equation 5.9, with (κ) the curvature.

$$\kappa = \frac{\frac{dx}{du}\frac{d^2y}{du^2} - \frac{dy}{du}\frac{d^2x}{du^2}}{\left(\frac{dx}{du}^2 + \frac{dy}{du}^2\right)^{\frac{3}{2}}} \tag{5.9}$$

When plotted over u, the curvature shows a peak at u = 0.5 for the leading edge (Figure 5.7b). The Python function for the curvature is given below (5.2). The peak of the first derivative is more distinct compared to the peak of the curvature.

Listing 5.2: Calculating the line curvature

```
def curvature(x,y):
    tck,u = sci_i.splprep([x,y],s=0)
    u_new = pointspacing(.0001,.05,855,1726)
    dx,dy = sci_i.splev(u,tck,der = 1)
    ddx,ddy = sci_i.splev(u,tck, der = 2)
    k = (dx*ddy - dy*ddx)/(dx**2 + dy**2)**1.5
    return k
```

When both functions are applied to a known shape, the desired result is obtained. To test the robustness of this method, noise is added to the profile. Noise is observed in the real foil sections and should thus be considered. This noise is added to the profile using the `off_set_noise` function (5.3). The random noise is created using numpy's random normal distribution function [6]. This random noise is added perpendicular to the profile direction using the offset functions described in subsubsection 5.2.2.

Listing 5.3: Creating data noise on a line

```
def off_set_noise(x,y,stddev):
    d_off = np.random.normal(0,stddev,len(x))
    tck, u = sci_i.splprep([x,y],s = 0)
    x_spl, y_spl = sci_i.splev(u,tck)
    dx_spl, dy_spl = sci_i.splev(u,tck,der = 1)
    ddx_spl,ddy_spl = sci_i.splev(u,tck,der = 2)

    # u_new = np.append(np.sin(np.linspace(0,.5*np.pi,int(len(x)/2))),1+(1-np.cos(np.linspace
        (0,.5*np.pi,int(len(x)/2))))/2
    # u = u_new

    b_vector = np.vstack((splev(u,tck,der = 0),np.zeros(len(x_spl))))
    t_vector = np.vstack((splev(u,tck,der = 1),np.zeros(len(x_spl)))).T
    n_vector = np.cross(t_vector,np.array([0,0,1]))

    bb_vector = (b_vector + d_off*(n_vector.T/np.linalg.norm(n_vector,axis=1))) #calulating
        the off_set line
    return bb_vector[:2].T
```

[6] numpy.random.normal:https://numpy.org/doc/stable/reference/random/generated/numpy.random.normal.html, (visited on: 07/18/2023)

Max Radius from Centroid from $.5\pi$ to 1.5π

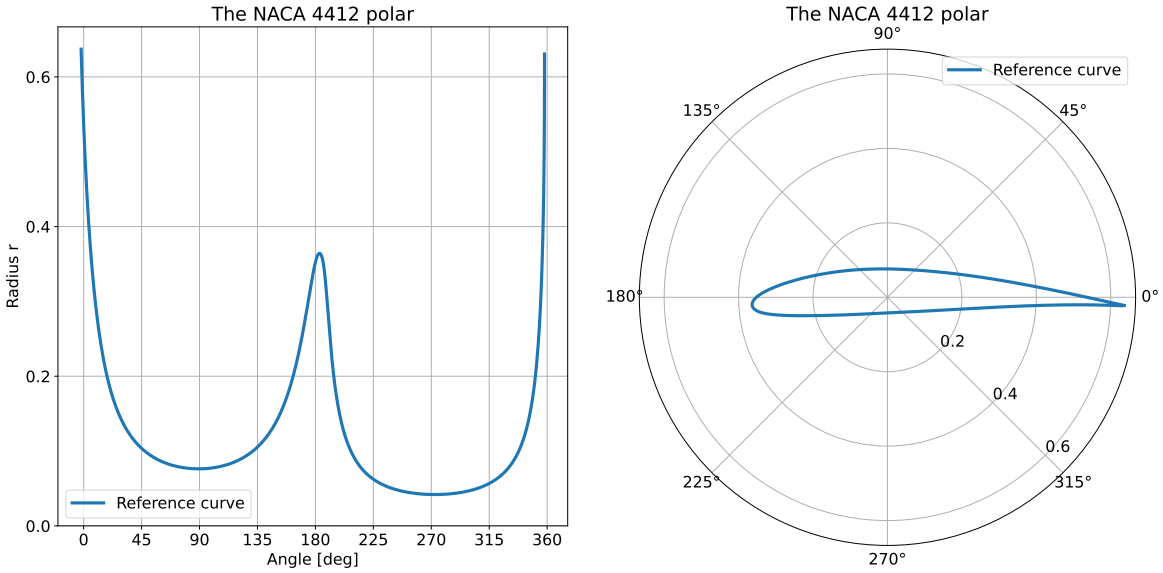

(a) Polar coordinates expressed in a Cartesian plot

(b) Polar coordinates expressed in a polar plot

Figure 5.8: The profile defined in polar coordinates showing distinct peaks at the leading and trailing edge.

The shape of a foil section is very rounded. This indicates that the use of polar coordinates might help to define the hydrofoil. This assumption is aided by the conformal mapping of an aerofoil to a cylinder using joukowski theory, as highlighted by Glegg and Devenport [62]. The result of transforming the Cartesian coordinates to Polar coordinates can be seen in Figure 5.8. Figure 5.8b shows the section in the polar coordinate scheme. While Figure 5.8a places these same coordinates in a Cartesian plot.

The origin of the coordinate system needs to be moved to obtain usable polar coordinates. The origin is placed at the mean of the x and y values. This places the origin in the middle of the profile. The polar radius is calculated using Equation 5.10. The polar angle is calculated using Equation 5.11.

$$r = \sqrt{(x - x_{\text{mean}})^2 + (y - y_{\text{mean}})^2} \tag{5.10}$$

$$\theta = \arctan \frac{(y - y_{\text{mean}})}{(x - x_{\text{mean}})} \tag{5.11}$$

The function `np.arctan2()` in Python keeps the result between positive and negative pi. In order to get a continuous curve, 2π is added to the point where theta flips sign. This produces the curve shown in Figure 5.8a. The peak at 180 deg, is the leading edge. This peak is found using scipy's `find_peaks` function [7]. This function identifies this peak and returns the highest data point. The code for this test is given in Listing 5.4. This method is tested using the same data noise used in subsubsection 5.2.1.

Listing 5.4: Changing to Polar Coordinates

```
x, y = Naca_points
x = x[:-1]
y = y[:-1]
xmean = np.mean(x)
ymean = np.mean(y)

r = np.sqrt((x-xmean)**2 + (y-ymean)**2)
theta = np.arctan2(y-ymean,x-xmean)
theta[20:][np.where(theta[20:]<0)] += 2*np.pi
```

[7] scipy.signal.find_peaks:https://docs.scipy.org/doc/scipy/reference/generated/scipy.signal.find_peaks.html, (visited on: 07/19/2023)

```
10
11 x_noiz,y_noiz = Naca_points_noizy
12 xmean_noiz = np.mean(x_noiz)
13 ymean_noiz = np.mean(y_noiz)
14
15 r_noiz = np.sqrt((x_noiz-xmean_noiz)**2 + (y_noiz-ymean_noiz)**2)
16 theta_noiz = np.arctan2(y_noiz-ymean_noiz,x_noiz-xmean_noiz)
17 theta_noiz[40:][np.where(theta_noiz[40:]<0)] += 2*np.pi
18
19 peaks, peakdict = sci_s.find_peaks(r_noiz, height = max(r_noiz)/2,distance = .25*len(r_noiz),
       width = 5)
20 LEpoint = np.argmin(abs(theta[peaks]))
21 TEpoint = np.argmax(abs(theta[peaks]))
22 TEid = peaks[TEpoint]
23 LEid = peaks[LEpoint]
```

5.2.2. Camber line Estimation

The following methods are used to define the Camber line. The mean camber line of a foil section is an important parameter in itself. The curve of the camber line dictates the lift created at an angle of attack of 0. The camber line intersects with the foil curve at the leading and trailing edges. Thus, these methods could be an accurate technique for obtaining the leading and trailing edge. There are two methods that have been analysed in this report that could extract the mean camber line from a set of points resembling a foil section. These are the offset of the foil surface inward and the use of voronoi points. Finally, this subsection will explore a method to extract the leading and trailing edge from the profile using the mean camber.

Camber line Data: Surface offset

The Camber line is the midpoint between the upper and lower surfaces, as shown in Figure 5.2. When two curves are offset perpendicular to itself by the same distance, the point of intersection will be the local midpoint between the two curves. This midpoint will be placed on the mean camber line if the curves are the top and bottom surfaces of a foil section.

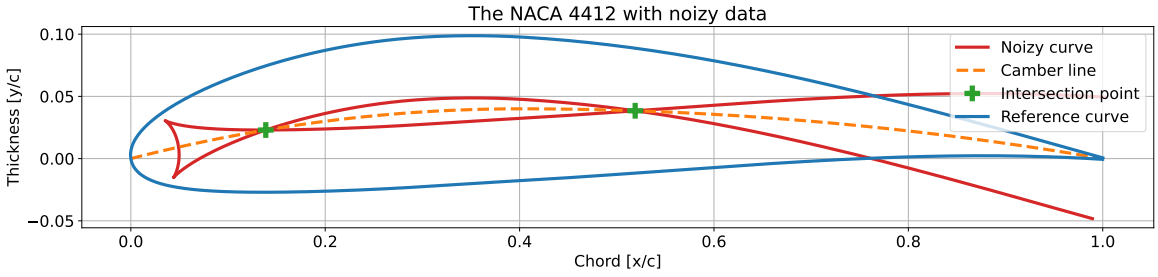

Figure 5.9: The NACA 4412 foil section with the curve offset by 0.05% of the chord length with the line intersecting on the camber line

Figure 5.9 shows how the curve offset intersects on the camber line. The camber line for the NACA 4412 is defined by a function. When intersection points of a wide range of curve offsets are found, the camber line can be estimated. The curve offset is found using Equation 5.12.

$$f(u) = P_p(u) + dN(u) \tag{5.12}$$

With ($P_p(u)$) the foil section curve. ($N(u)$) the normal vector at t, d the offset distance along the normal vector, and ($f(u)$) the offset curve. Equation 5.12 moves the curve by a distance d in the local frenet frame of reference. This reference frame is constructed from the velocity and acceleration vector of a curve. A continuous curve is needed to extract the velocity and acceleration vectors. This continuous curve is obtained from the data points using scipy's splprep function, as can be seen in Listing 5.5. The u value spans from 0 to 1 along the curve. The curve ($P_p(u)$) is the python variable C(u), ($P_p(u)$) is T(u),(P_p"(u)) is D(u). The normalised tangent or velocity vector of the curve is given by Equation 5.13.

$$T(u) = \frac{P'_p(u)}{||P'_p(u)||} \tag{5.13}$$

According to Gray, Abbena, and Salamon [63], the Normal vector can be calculated with Equation 5.14.

$$N(u) = B(u) \times T(u) \tag{5.14}$$

The Binomial vector (B(u)) is obtained from Equation 5.15.

$$B(u) = \frac{P'_p(u) \times P_p"(u)}{||P'_p(u) \times P_p"(u)||} \tag{5.15}$$

Listing 5.5: Offsetting a curve

```
tck_u, u = sci_i.splprep(Naca_points,s=0)
tck_u_up, u_up = sci_i.splprep(Naca_points[:,:int((npoints-1)/2)],s=0)
tck_u_low, u_low = sci_i.splprep(Naca_points[:,int((npoints-1)/2):],s=0)

offset = .05

C = lambda u,tck: np.array(sci_i.splev(u,tck)).T
T = lambda u,tck: np.vstack((sci_i.splev(u,tck,der = 1),np.zeros_like(u))).T
D = lambda u,tck: np.vstack((sci_i.splev(u,tck,der = 2),np.zeros_like(u))).T
B = lambda u,tck: abs((np.cross(T(u,tck),D(u,tck)).T/np.linalg.norm(np.cross(T(u,tck),D(u,tck
    )),axis=1)).T)
Tangent = lambda u,tck: (T(u,tck).T/np.linalg.norm(T(u,tck),axis=1)).T
Normal  = lambda u,tck: np.cross(B(u,tck),Tangent(u,tck))

offset_vector = C(u,tck_u) + offset * Normal(u,tck_u)[:,:2]
offset_vector_up = C(u_up,tck_u_up) + offset * Normal(u_up,tck_u_up)[:,:2]
offset_vector_low = C(u,tck_u_low) + offset * Normal(u,tck_u_low)[:,:2]
```

All values for Equation 5.12 are now defined. The next step is to identify the intersections. The top and bottom curves are separated into `offset_vector_up` and `offset_vector_low`. The Python function `interpolated_intercepts` will use the two curves to find the intersection points. The function shown in Listing B.1 needs two curves that are increasing in the x direction. Both x-axis values should be equal. The function will first find the point at which y2 crosses y1. At both sides of the intersection, linear interpolation between both data points will give an accurate estimation of the intersection. This results in a set of points that are located on the camber line. These points are checked for any duplicate points, as this will produce an error in the next step.

The points are fit by a 9th degree polynomial using a numpy poly1d function[8]. The 9th degree polynomial was found to be the best fit for the camber lines created by the NACRA 17 cross sections. This polynomial is used to filter out the data points from outliers. The (t/c or y) distance between the point and the polynomial is obtained and all points that fall outside the 99.5 percentile are deleted. From this new data set, a new polynomial is constructed and this method is repeated 10 times. After the final repetition, the new camber line is defined by the last polynomial. The code for the offset camber line is found in Listing B.2. A polynomial was selected to approximate the camber line, as it is a smooth continuous curve that typically does not display intricate shapes. The aim is to accurately capture the desired shape of the mean camber line.

The accuracy of this method is tested by taking a known shape: The NACA 4412. For the Naca series of foil sections, the camber line is given by a formula. This definition of the camber line will be the baseline. Both lines increase strictly on the x-axis. This allows comparison to be made using only the y-axis. The error is thus obtained by subtracting the y values of the estimated camber line from the baseline at the same x locations. Although this method is very simple, it will show the magnitude of the error and where the method is less accurate. This method will be compared with Camber line Data: Voronoi in section 9.2 to conclude which method provides a better result.

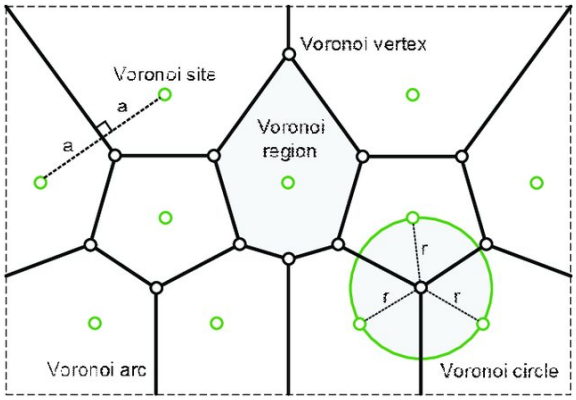

Figure 5.10: Voronoi diagram in a plane [64]

Camber line Data: Voronoi

The offset curve method showed the concept of the minimum distance between the two sets of points. This concept of finding the set of nearest points in a point cloud was developed by Voronoi [65]. A voronoi diagram of a set of points can be seen in Figure 5.10. Each data point is surrounded by a voronoi region. The region is enclosed by a set of voronoi arcs that separate two voronoi regions. The Voronoi arc is positioned at the midpoint between the data points. The point at which three voronoi arcs intersect is called the voronoi vertex. This vertex point is the midpoint of a circle through all three data points. When the data points are following the curve of a foil, the mid-section is the mean camber line. Because the circle is enclosed by the profile, the distance r from the voronoi point is equal to the thickness function (y_t) as can be seen in Figure 5.11.

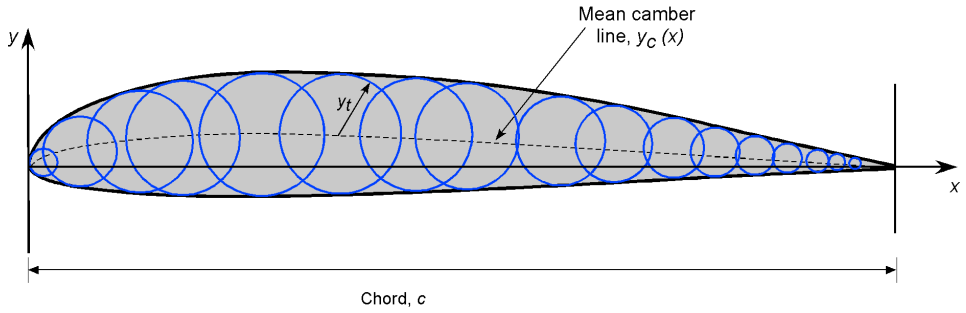

Figure 5.11: A graphical approach of estimating the mean camber line. Showing that the biggest enclosed circle for a given point on the profile surface has the centre located on the mean camber line [60].

Using this principle, the camber line is estimated using these Voronoi points. The Voronoi diagram in Figure 5.10 contains bounded and unbounded regions. The unbounded regions are located on the sides and are limited by the area of the diagram itself. For the foil sections, these unbounded regions could cause some distortion in the results. In order to prevent this, lines are placed on all sides of the profile. These lines can be seen in Figure 5.12. These lines are the data points projected in front, behind, above, and below the foil using the code in Listing 5.6.

Listing 5.6: Creating the box for the Voronoi

```
x, y = Naca_points
front = np.array([np.ones(len(y))*-.1,y]).T
back = np.array([np.ones(len(y))*1.1,y]).T
top = np.array([x,np.ones(len(y))*np.max(y)*2]).T
bot = np.array([x,np.ones(len(y))*np.min(y)*2]).T
foil_voronoi = np.delete(np.array([y,x]).T,[0,-1],0)
box =  np.vstack((front,back,top,bot,np.flip(foil_voronoi)))
```

[8]numpy.poly1d: https://numpy.org/doc/stable/reference/generated/numpy.poly1d.html, (visited on: 07/31/2023)

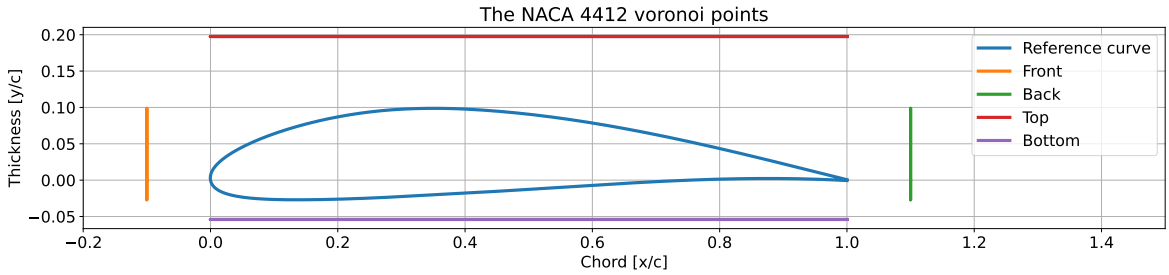

Figure 5.12: Voronoi Set up

This data set can be transformed into a voronoi diagram using scipy's voronoi function[9]. From this voronoi diagram, only the vertices are used. The resulting vertices are shown in Figure 5.13. The vertices created by the outside box are removed leaving only the points located within the profile with the code provided in Listing 5.7. It can already be observed that these points follow the camber line.

Listing 5.7: Creating the Voronoi vertex points and removing the outer points

```
vor = Voronoi(box)
camberline = vor.vertices
camberline_raw = camberline
#removing the outer points
camberline = camberline[(camberline[:,0] <= 1) * (camberline[:,0] >= 0) * (camberline[:,1] <=
     .5*np.max(y)) * (camberline[:,1] >= .5*np.min(y)),:]
```

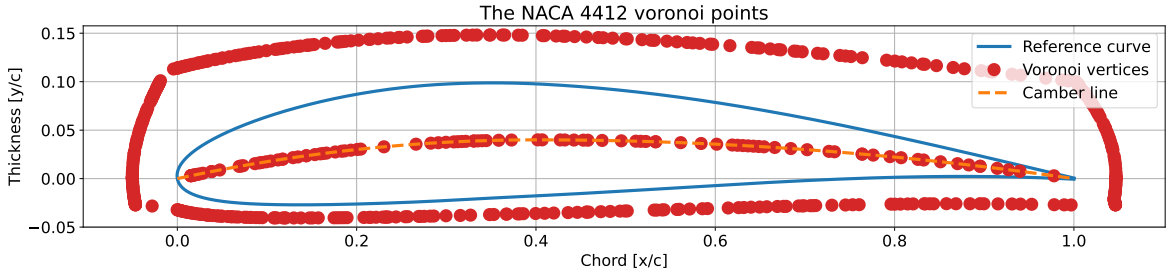

Figure 5.13: Voronoi vertex around the Naca 4412 foil

At this point there is a set of points that are estimated to be on the mean camber line. Due to the noise in the profile data and the inaccuracy of the method, the data needs to be filtered. This filtering is performed in a manner similar to that described in subsubsection 5.2.2. There are always two points located very close due to the voronoi vertex points forming an intersection of three regions. These are points located very closely and slightly offset from each other. This will create large differences in the gradient of the line. The Voronoi data points are, therefore, filtered by removing points with a large gradient. This method was inspired by the energy minimisation proposed by Li et al. [1]. Points with a gradient outside the 99th percentile are removed from the data. This will create a reduced data set. The point removal loop is repeated 15 times. A 9th degree polynomial is fitted over the data using the reduced data set to create the camber line. The precision of this method is tested in the same way as shown in subsubsection 5.2.2 and compared in subsection 9.2.3.

Polynomial fitted Camber line

The camber line can be approximated using the numpy function polyfit[10] and poly1d[11]. The poly fit function will create a set of coefficients for a polynomial of a specified degree. A polynomial of degree

[9] scipy.spatial.Voronoi:`https://docs.scipy.org/doc/scipy/reference/generated/scipy.spatial.Voronoi.html`, (visited on: 07/31/2023)

[10] numpy.polyfit:`https://numpy.org/doc/stable/reference/generated/numpy.polyfit.html`,(accessed at: 29/08/2023)

[11] numpy.poly1d:`https://numpy.org/doc/stable/reference/generated/numpy.poly1d.html`,(accessed at: 29/08/2023)

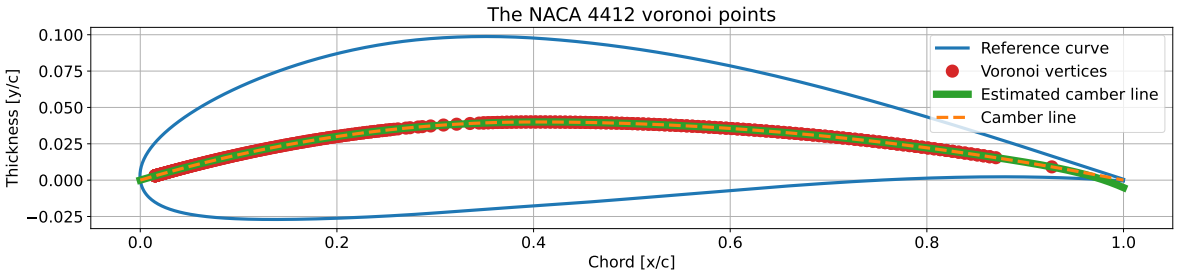

Figure 5.14: Mean Camber line with the voronoi vertex points

9 was found to be the best fit for the Nacra hydrofoil section camber lines. The polynomial coefficients are created as a function using the poly1d function.

The leading can be estimated using the mean camber line with the polynomial. These two points are located at the intersection of the camber line with the section curve. With the profile defined by a non-filtered cubic spline through all data points and the camber line as a polynomial. The intersection is determined to be the minimum distance between the two lines. The code in Listing 5.8 describes the creation of the splines from both data sources. The camber line is extended in front and behind the profile to ensure that there is an intersection between both curves.

Listing 5.8: Creating splines for the camber line intersect estimation

```
tck_profile,u_profile = sci_i.splprep(Naca_points,s=0)
x_spaced = np.linspace(-0.1,1.1,len(u_profile))
tck_camber,u_camber =  sci_i.splprep([x_spaced,test_poly_curve_offset(x_spaced)],s=0)
```

Using these spline lines, the distance between each line can be calculated using `spline_intersection` in Listing 5.9. This will create a minimum function at the leading and trailing edges. The function will only find the leading edge at this point. Using the least squares optimisation method from scipy, the minimum distance between both curves is found. The u and z values for the respective splines will be the output of this function. These values can be implemented in the spline to find the coordinates of these points.

Listing 5.9: Estimating the Leading edge using the camber line intersecting with the profile curve

```
def spline_intersection(u,z,tck_u,tck_z):
    C = lambda u: np.array(sci_i.splev(u,tck_u)).T
    P = lambda z: np.array(sci_i.splev(z,tck_z)).T
    return np.linalg.norm(C(u)-P(z))

Le_interesct = lambda inputv: spline_intersection(inputv[0],inputv[1],tck_camber,tck_profile)

result = sci_o.least_squares(Le_interesct,[0.,0.5])
```

The trailing edge is defined by a different method. The NACA 4412 foil section used before is calculated with an open trailing edge. There is a gap at the trailing edge, and there cannot be an intersection at the trailing edge because of this. For the actual profiles, the leading edge is again the only variable that can be estimated. This is affected by the finite trailing edge of the Nacra hydrofoils. The data do show points at the trailing edge. But the actual profile is cut to create a straight trailing edge. For the Nacra hydrofoils, the foil is shortened to 99% (0.9 x/c) of the chord length and the trailing edge is defined as the location of the point on the camber line at this cutoff location.

The leading edge and trailing edge can also be defined by a B-spline estimation of the camber line. This method will be explained in more detail in section "*B-spline fitting*" below.

B-Spline fitted Camber line

B-spline is a function that depends on a set of control points and the basis function of the B-Spline. A B-Spline is also a set of Bezier curves. For the following method, great inspiration came from the paramaterization preformed by Derksen and Rogalsky [2]. In their paper, the thickness profile and

camber line are parameterized using b-spline functions. Various foil parameters are used, such as the radius of the leading edge and the thickness position. Using those variables, the changes to the foil are relatively intuitive. The control points for the BP3333 parameterisation developed by Derksen and Rogalsky [2] is visualised in Figure 5.15.

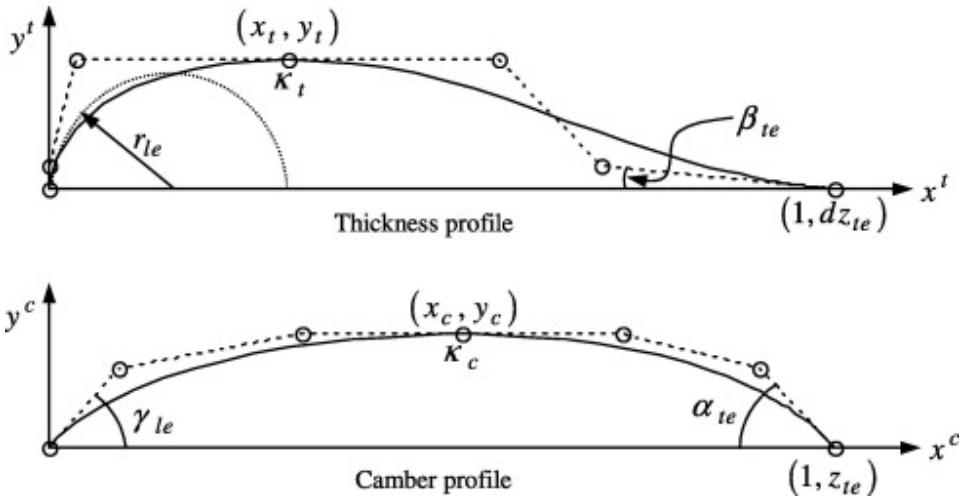

Figure 5.15: The control points for the BP3333 parameterization by Derksen and Rogalsky [2]

For the evaluation of the profile, the profile sections are not aligned with the coordinate system. The location of the control points will thus be fitted to the profile and will not yet be defined using the BP3333 parameterisation.

The B-spline needs a set of 2D control points and a matching knot vector (which will be denoted by t). The B-splines will be of the third degree. The maximum camber of the Nacra hydrofoils will be around 0.7% of the chord. The line will be mostly flat before this point. This requires the addition of a third knot before xc. The knot vector for the B-spline will be:

$$t = [0, 0, 0, 0, .25, .5, .5, .5, 1, 1, 1, 1] \tag{5.16}$$

The first four (0) knots clamp the curve to the initial position. Thus, the line will flow through the first point. The angle of the line is now defined by the angle of the line to the first control point. In subsubsection 5.2.3 this angle will be γ_{le}. The number of zero knots to clamp the line depends on the degree of the curve. The second point is controlled by the knot (0.25). This value must be between 0 and 0.5. When it is smaller, the leading edge points will provide more influence. When larger, the points near x_c will have greater influence. The (0.5) knots clamp the line at the middle point that will be placed on the maximum camber. The (1) knots follow the same principle as the knots at the leading edge.

The control points of the b-spline will be fitted using scipy's curve fit function [12]. This will fit the control points to the profile. This function requires that the output of the curve function be defined by an x-value. To aid in the convergence of the solution, the initial point (P_0) and the bounds can be defined. The values with subscript $_{pro}$ are located on the profile spline.

```
x_pro,y_pro = sci_i.splev(u_le,tck_profile)
```

The input is the variable u along the unfiltered spline and this will provide the coordinates using the `splev` function.

[12] scipy.optimize.curve_fit: `https://docs.scipy.org/doc/scipy/reference/generated/scipy.optimize.curve_fit.html`, (visited on: 08/07/2023)

$$x_0 = x_{pro} \qquad y_0 = y_{pro} \tag{5.17}$$
$$x_1 = x_c x_a \qquad y_1 = y_c y_a \tag{5.18}$$
$$x_2 = x_1 + (x_3 - x_1)x_b \qquad y_2 = y_c y_b \tag{5.19}$$
$$x_3 = x_c - (1 - x_c)x_d \qquad y_3 = y_c \tag{5.20}$$
$$x_c = x_c \qquad y_c = y_c \tag{5.21}$$
$$x_4 = x_c - (1 - x_c)x_d \qquad y_4 = y_c \tag{5.22}$$
$$x_5 = x_6 - (x_6 - x_4)x_e \qquad y_5 = y_6 + (y_c - y_6)y_e \tag{5.23}$$
$$x_6 = x_6 \qquad y_6 = y_6 \tag{5.24}$$

Equations (5.17) to (5.24) form the coefficient vector of the camber line B-Spline. Values denoted with a letter will be fitted by the curve fit function using the initial condition and the bounds given in Table 5.1.

Table 5.1: The initial guess (X_0) and the upper and lower bounds for the open variables of the Camber line B-Spline fit.

	u_le	**xa**	**xb**	**xc**	**xd**	**xe**	**ya**	**yb**	**yc**	**ye**	**y6**
X_0	0.5	0.5	0.5	0.5	0.5	0.5	0	0	0.06	0.5	0
Lower bound	0	0.05	0.1	0	0.05	0.1	-1	-1	0	0.1	-1
Upper bound	1	1	0.9	1	0.9	0.9	1	1	1	1	1

This curve fit is placed in a loop that has 5 iterations. In the first iteration x_6 is set to 1.2. This is the guess of the chord of the profile before the final rotation.

The upper and lower surfaces of the profile are extracted using this camber line. The fit of the thickness profile is explained in more detail in subsubsection 5.2.3. The B-Spline fit of the thickness profile provides the x position of the trailing edge. The variable x_6 is now updated to reflect the trailing edge.

Using the camber line fit, the (unfiltered) camber line data set is reduced. The root mean squared distance is found in the y direction for each data point. Data points less than 5E-05 from the camber line will be kept for the next iteration.

5.2.3. Data Smoothing

Error-calculation

To identify the accuracy of the filtered profiles, an error needs to be calculated between the original shape and the new shape. This error is calculated as the minimum distance between the original data set and the new curve. The error is calculated using *Squared Distance Minimisation* (SDM). The method was conceived by Wang, Pottmann, and Liu [3]. The previous methods:*Point Distance Minimisation* (PDM) and *Tangent distance Minimisation* (TDM) functions did not provide the necessary performance. The PDM error has a slow convergence, whereas the TDM tends to converge fast but unstable, reducing the accuracy. SDM uses the formulation of both methods to provide an error term based on ellipse-shaped iso-value curves.

PDM uses the Euclidean distance between two points as shown in Figure 5.16a. While TDM uses the distance (d) of the curve tangent to the data point, shown in Figure 5.16b.

The squared distance formulation is given by Equation 5.25.

$$g(x, y) = \frac{d}{d - \rho}x^2 + y^2 \tag{5.25}$$

Equation 5.25 is indefinite when $0 < d < \rho$, the expression thus becomes Equation 5.26. The $\hat{g}(x, y)$ now becomes the first order approximation to the squared distance function to the curve $\mathcal{C}$ in a neighbourhood of X_0

$$\hat{g}(x, y) = \frac{|d|}{|d| + \rho}x^2 + y^2 \tag{5.26}$$

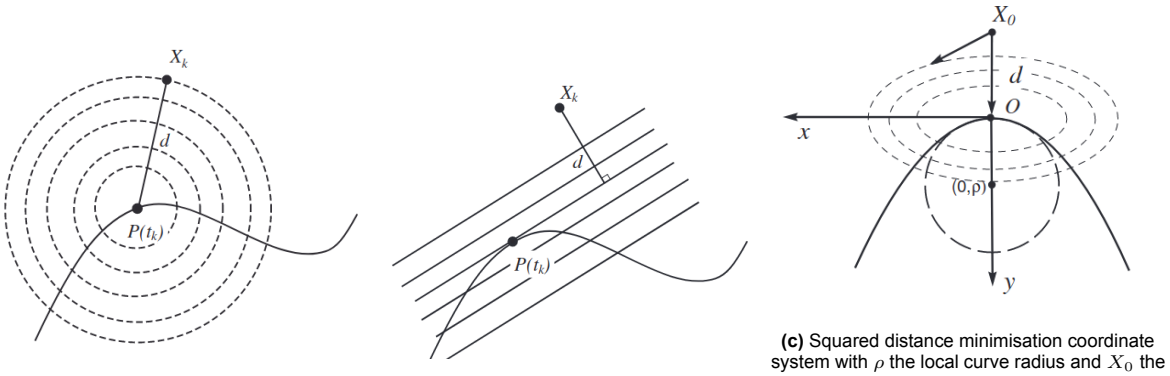

(a) Point distance minimisation with d the distance

(b) Tangent distance minimisation with d the distance between the points

(c) Squared distance minimisation coordinate system with ρ the local curve radius and X_0 the measurement point and d the distance between the point and curve $\mathcal{D}$.

Figure 5.16: Different distance minimisation methods visualised that are used for the error formulation of a B-spline by: Wang, Pottmann, and Liu [3].

The local point on the fitting curve will be denoted by $P_D(u_k)$. t_k is the spline parameter, T_k is the unit tangent vector, and N_k is the unit normal vector. The tangent and normal vectors of a curve are given by equations (5.13) and (5.14), respectively. The distance from a point on the curve to the data point is given by the Euclidean distance in Equation 5.6. For the vector notation, the formulation becomes Equation 5.27.

$$|d| = ||P_D(u_k) - X_k|| \tag{5.27}$$

The radius of a curve is equal to 1 over the curvature (κ). The curvature of a curve is given by Gray, Abbena, and Salamon [63] to be Equation 5.28.

$$\kappa(u_k) = \frac{1}{\rho(u_k)} = \frac{||P'_D(u_k) \times P_D"(u_k)||}{||P'_D(u_k)||^3} \tag{5.28}$$

$$x = (P_D(u_k) - X_k)^T T_k \tag{5.29}$$

$$y = (P_D(u_k) - X_k)^T N_k \tag{5.30}$$

$$e_{SD,k}(\mathcal{D}) = \begin{cases} \frac{|d|}{|d|-\rho} x^2 + y^2, & \text{if d<0,} \\ y^2, & \text{if 0<d<}\rho, \end{cases} \tag{5.31}$$

However, this is not what was found to be working in the code. Using the code in Listing 5.10, the problems with this method will be shown.

Listing 5.10: Code calculating the minimum distance between a curve and a data point.

```
tck_input , u_input = sci_i.splprep(Naca_points,s=0)

u = u_input
C = lambda u: np.array(sci_i.splev(u,tck_input)).T
T = lambda u: np.vstack((np.array(sci_i.splev(u,tck_input,der = 1)),np.zeros_like(u))).T
D = lambda u: np.vstack((np.array(sci_i.splev(u,tck_input,der = 2)),np.zeros_like(u))).T
B = lambda u: np.cross(T(u),D(u))/np.linalg.norm(np.cross(T(u),D(u)),axis = 1,keepdims = True
    )

R = lambda u: np.squeeze(1/(np.linalg.norm(np.cross(T(u),D(u)),axis = 1,keepdims = True) / np
    .linalg.norm(T(u),axis = 1,keepdims = True)**3))

Tangent = lambda u: (T(u)/np.linalg.norm(T(u),axis = 1,keepdims = True))[:,:2]
Normal  = lambda u: np.cross(B(u),Tangent(u))[:,:2]

x1j = lambda u: np.sum(Tangent(u)*(point-C(u)),axis=1) #dot product for a longer set of
    points old set
```

```
15 x2j = lambda u: np.sum(Normal(u)*(point-C(u)),axis=1)  #dot product for a longer set of
       points old set
16 x1 = lambda u: np.sum(Tangent(u)*(point-C(u)),axis=1) #dot product for a longer set of points
17 x2 = lambda u: np.sum(Normal(u)*(point-C(u)),axis=1)*B(u)[:,2]  #dot product for a longer set
       of points
18 d  = lambda u: np.linalg.norm(C(u)-point,axis = 1)
```

Figure 5.17 shows two different foil sections. These foil sections will be used to describe the problem encountered with the formulation defined in Equation 5.31. The red offset curve is a 110% scaled version of the blue curve and is translated to the right. This will cover the majority of scenarios that will be found in the real data. These are crosses of the curves, errors inside the profile, and errors outside the profile.

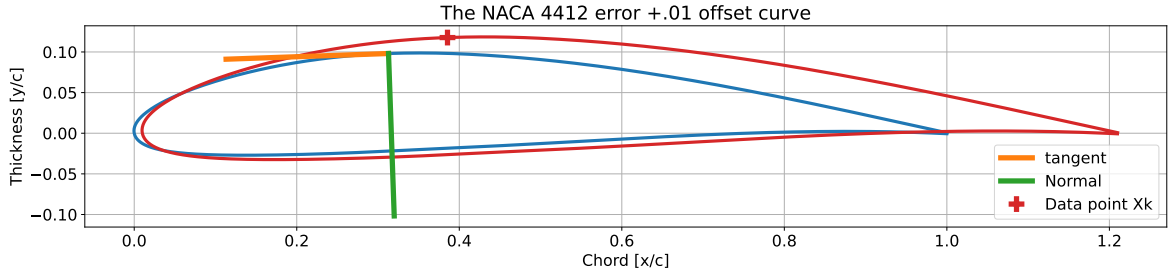

Figure 5.17: Two foil sections where the red curve substitudes for the raw data and the blue curve for the new curve $P_c(t_k)$, the corss a single data point and the arrow's the Frenet frame of reference.

The first problem can already be observed in Figure 5.7b. The curvature graph shows a discontinuity between u = 0.6 and u = 0.8. In a continuous function, these steps should not be present. These steps can be an artefact of the 4 formulas that are used to calculate the NACA 4 series aerofoils.

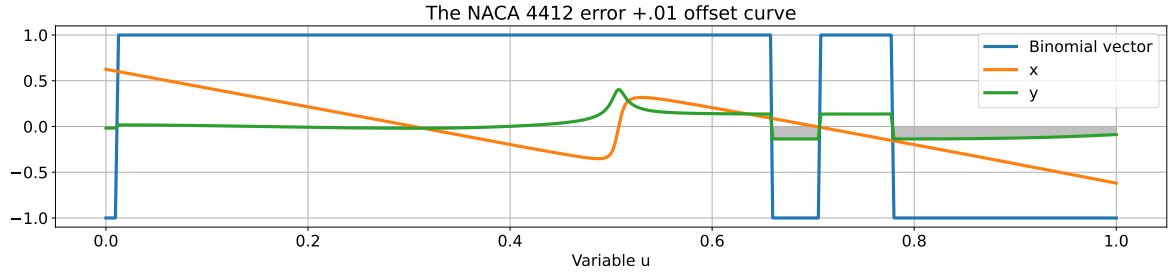

Figure 5.18: equations (5.15), (5.29) and (5.30) plotted over the variable u along the blue curve from Figure 5.17 and the point X_k from the same figure.

The binomial vector jumps from positive 1 to negative 1. This affects the results of Equation 5.30 with the same step. These steps influence the results due to the conditional formula. This is prevented by taking the absolute of the binomial vector from Equation 5.15. The normal vector now is always pointed inwards of the foil.

The condition set by Equation 5.31 sounds logical. When the y values cross the 0 axis, the squared values approach zero. This means that this intersection will always produce the lowest error. This is not the shortest distance between the profile and the data point, as shown by the distance line ($|d(u_k)|$) in Figure 5.19. This dependence on the normal distance from the curve should be reduced in order to find the correct minimum distance. The x and y values of Equation 5.26 should be reversed. This will find the point at which the distance to the normal axis is minimal. This changes Equation 5.26 to the following:

$$\hat{g}(x,y) = \frac{|d|}{|d|+\rho}y^2 + x^2 \tag{5.32}$$

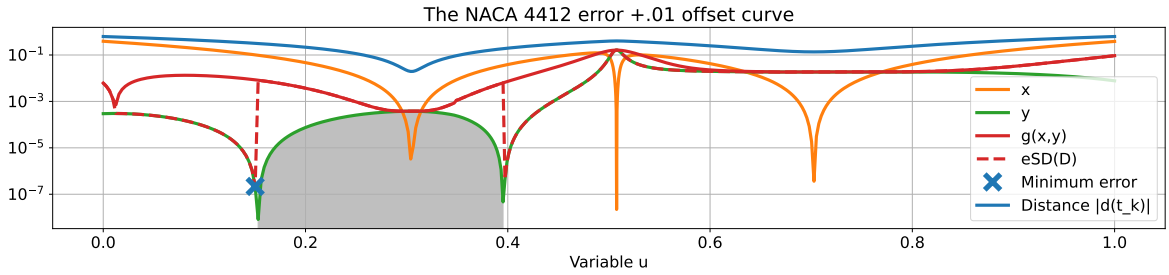

Figure 5.19: Plot of the different SDM equations plotted over variable u with x (Equation 5.29), y (Equation 5.30), ($|d(u_k)$) (Equation 5.27), g(x,y) (Equation 5.26) and eSD(D) (Equation 5.31) with the grey area showing the condition d<0.

The axis system in the paper was set with the y axis inward. With the equations for x and y, this will not be the case. The right coordinate system is achieved with $(X_k - P_D(u_k))$. This will transform the x and y equations into:

$$x = (X_k - P_D(u_k))^T T_k \tag{5.33}$$

$$y = (X_k - P_D(u_k))^T N_k \tag{5.34}$$

The final change is for the conditional formula for the error. With the x and y values now switched, the results for d<0 follow the minimisation of the distance to the normal axis or the value of x. While the case for the distance of points inside the profile is now inconclusive, as shown by the 3 different dips of the x value in Figure 5.19. The equation for the error is now transformed to:

$$e_{SD,k}(\mathcal{D}) = \begin{cases} x^2, & \text{if y<0,} \\ \frac{|d|}{|d|-\rho} y^2 + x^2, & \text{if 0<y and |d|<}\rho, \end{cases} \tag{5.35}$$

The results of these changes are shown in Figure 5.20. The minimum error now aligns with the minimum distance (d).

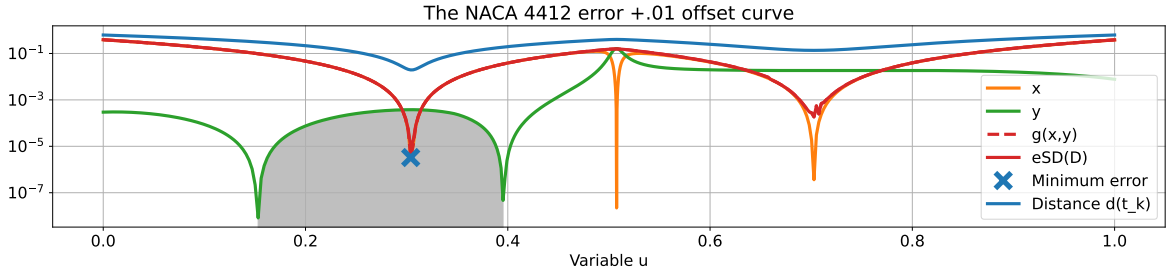

Figure 5.20: Plot of the different SDM equations plotted over variable u with x (Equation 5.33), y (Equation 5.34), $|d(u_k)$ (Equation 5.27), g(x,y) (Equation 5.32) and eSD(D) (Equation 5.35) with the grey area showing the condition y<0.

With the correct formulation for the minimum distance between a point and a curve. The final error between the original data set and a new curve can be formulated. The minimum distance is found using scipy's minimize function [13]. This function provides an accurate method of finding the global minimum of $e_{SD,k}(\mathcal{D})$.

With the use of numpy's "`apply_along_axis`" function [14], the miminum distance is found for each data point. The distance between the data points and the curve shows the local deviation. The sum of the distances will give the total error between the curves. When the error is calculated correctly, the

[13] scipy.optimize.minimize:`https://docs.scipy.org/doc/scipy/reference/generated/scipy.optimize.minimize.html`, (visited on: 07/31/2023)

[14] numpy.apply_along_axis:`https://numpy.org/doc/stable/reference/generated/numpy.apply_along_axis.html`, (visited on: 07/31/2023)

distance between the data point and the curve is perpendicular on the curve. An example of a correct error estimate can be seen in Figure 5.21. The function that will be used to calculate the error is found in section B.1,Listing B.3. The response to the error in the example in Figure 5.17 can be seen in Appendix B with Figure B.1 using the calculation method of the paper and Figure B.2 using the newly formulated calculation method.

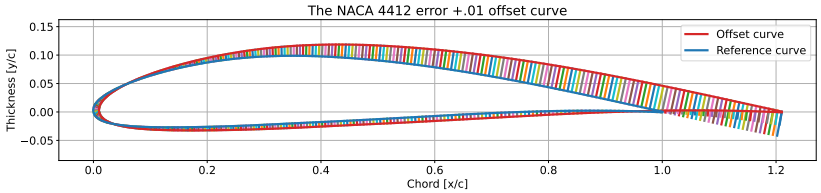

Figure 5.21: The method of the error visualised on the NACA 4412 foil with the coloured lines showing the minimum distance between the offset curve and the Reference curve. The method works when none of the lines intersect.

Filter using signal processing

It was noticed in paragraph "*First derivative or Curvature of the profile*" in subsection 5.2.1, that there is noise in the measurement data. In signal processing, noise is very common. Different methods have been developed to reduce this noise from signals. The foil shape is not a signal. Geometries can be expressed by Taylor series in the form of a large sum of sine and cosine functions. The parameterisation of the foil shapes using Taylor series was successfully examined by Chen et al. [66]. Although the parameterisation of the foil using Taylor series might not be useful to the current problem. The representation of a foil shape by different frequencies is useful.

Signals are analysed in the frequency domain, but are measured in the time domain. The time domain will present the time on the x-axis and the input signal on the y-axis. This transformation is performed using a fast Fourier Transform. The numpy environment in Python provides a fast Fourier function[15]. For the foil, there is no time domain. There is the spline variable u that spans the arc length of the foil. This is now defined as the time domain. The foil is made up of both the x and y coordinates. For the actual calculation the 2 dimensional Fast Fourier Transform is used[16].

In the frequency domain, the frequency is placed on the x-axis and the amplitude is placed on the y-axis. The results depend on the measurement frequency. The variable u is the distance between the points and is equally spaced along the foil. The distance between u is thus the measurement time. This results in a measurement frequency of $\frac{1}{du}$. To increase the measurement frequency, the point resolution is increased by a factor of 50. `u_sample = np.linspace(0,1,len(u_reduced)*50)`, with u_reduced the initial u vector and u_sample the sample set.

Listing 5.11: Transforming the foil to frequency domain.

```
1
2  tck_reduced, u_reduced = sci_i.splprep(data_dat_c1.T,s=0)
3  k = adj_func.curvature(data_dat_c1[:,0],data_dat_c1[:,1])
4  u_sample = np.linspace(0,1,len(u_reduced)*50)
5  time_step = u_sample[1]
6  x_spl,y_spl = sci_i.splev(u_sample,tck_reduced)
7  k  = adj_func.curvature(x_spl,y_spl)
8
9  fhat = np.fft.rfft2([x_spl,y_spl],norm = 'ortho')
10 freq = np.fft.rfftfreq(len(x_spl),d = 1/len(x_spl))
```

The code in Listing 5.11 shows the steps in the transformation. The input data is data_dat_c1. The frequency response of a NACA 4412 foil can be seen in Figure 5.22a. The frequencies are on the low side due to the rounded corners of a foil. This slowly reduces to the final measurement frequency on the right. The result of the noise can be seen in the Fast Fourier of an actual foil in Figure 5.22b.

[15] numpy.fft.fft:`https://numpy.org/doc/stable/reference/generated/numpy.fft.fft.html`,(visited on: 08/07/2023)
[16] numpy.fft.fft2:`https://numpy.org/doc/stable/reference/generated/numpy.fft.fft2.html`,(visited on: 08/07/2023)

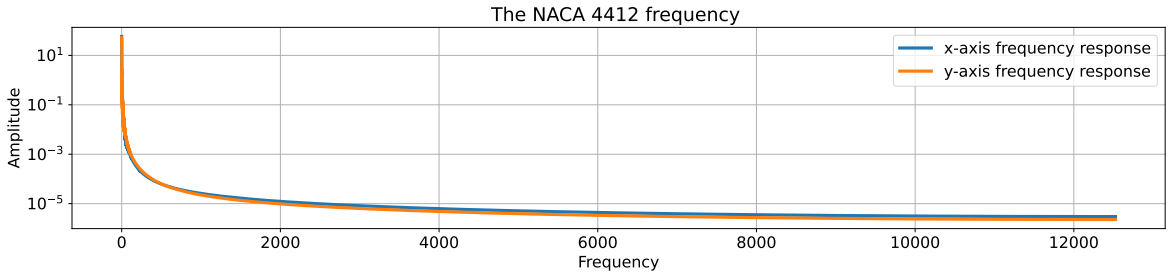

(a) NACA 4412.

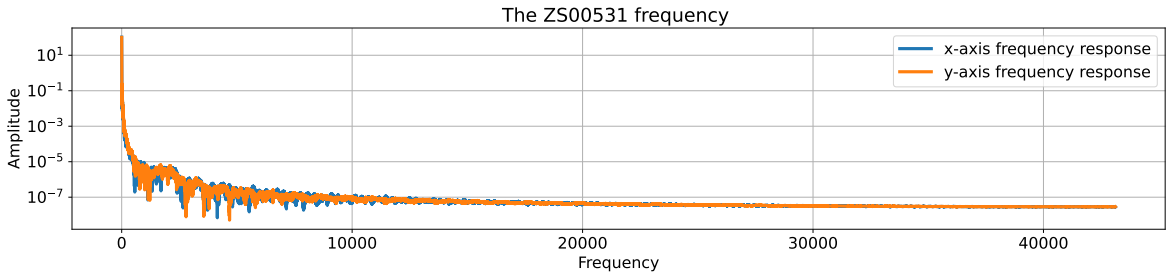

(b) ZS00544 at section 30.

Figure 5.22: The fast Fourier transform result foil sections.

From this point on, two simple methods can be applied: Low-pass frequency filter of high-pass amplitude filter. As stated before, the major frequencies are on the low side of the foil, and thus the noise will influence the higher frequencies. These high noise frequencies could be observed in the derivative (Figure 5.7b) and curvature (Figure 5.7c) analyses. With the low-pass filter applied using the code snippet from Listing 5.12:

```
fhat_cleaned1 = fhat*(abs(freq)<freqfilt)
```

The resulting x and y values need to be scaled to the correct chord length after this process by dividing by the maximum x value.

Listing 5.12: Low pass Frequency filter test code

```
def Frequency_filteringerror(freqfilt):
    fhat_cleaned1 = fhat*(abs(freq)<freqfilt)
    x_f1,y_f1 = np.fft.irfft2(fhat_cleaned1)
    x_f1,y_f1 = x_f1/max(x_f1), y_f1/max(x_f1)
    k1 = adj_func.curvature(x_f1[1:],y_f1[1:])
    data_dat_c1_fftf = np.array([x_f1,y_f1]).T

    RMSerror_fftf,RMSerror_x_fftf, varif_fftf = RMS_error(data_dat_c1,data_dat_c1_fftf)
    return [freqfilt,np.sum(np.abs(np.gradient(k1))),RMSerror_fftf]
```

The low pass filter The second method would filter all the low amplitude frequencies from the result. This could work because the high-amplitude frequencies apply the greatest influence on the final result. The high pass amplitude filter is applied using the following code snippet from Listing 5.13:

```
fhat_cleaned2 = fhat*(abs(np.conj(fhat))>amplfilt)
```

Listing 5.13: High pass amplitude filter test code

```
def Amplitude_filteringerror(amplfilt):

    fhat_cleaned2 = fhat*(abs(np.conj(fhat))>amplfilt)
    x_f2,y_f2 = np.fft.irfft2(fhat_cleaned2)
    x_f2,y_f2 = x_f2/max(x_f2),y_f2/max(x_f2)

    k2 = adj_func.curvature(x_f2,y_f2)

```

```
    data_dat_c1_ffta = np.array([x_f2,y_f2]).T

    RMSerror_ffta,RMSerror_x_ffta, varif_ffta = RMS_error(data_dat_c1,data_dat_c1_ffta)
    return [amplfilt,np.sum(np.abs(np.gradient(k2))),RMSerror_ffta]
```

To determine which method produces the best results, a test is envisioned that compares both methods. The test compares the error between the filtered profile and the actual profile. This error was previously described and is shown in the code as RMS_error. This error is compared to the potential of the curve. The potential is described as the sum of the first derivative of the profile curvature. With a profile that contains noise, the potential is high due to the large number of oscillations. While with a filtered profile, these oscillations get reduced and thus the potential of the curve reduces.

B-spline fitting

A B-Spline fit can approximate an aerofoil. This is proven by different parameterisation methods, of which the BP3333 [2] method is one. Most problems are not suitable for a non-aligned section. Therefore, the current method is proposed to aid in this function.

The thickness profile first requires a data set. The thickness is extracted using the B-Spline fit of the camber line. The thickness profile is perpendicular to the camber line. This is similar to the problem of finding the minimum distance between a line and a point in subsubsection 5.2.3. The point in the profile that corresponds to a position in the camber line is thus found by minimising Equation 5.36.

$$e_{SD} = (P_D(u_k) - X_k)^T T_k \tag{5.36}$$

With $P_D(u_k)$ a unfiltered spline of the profile data and X_k,T_k a point on the camber line and the local tangent.

The upper surface is found when the minimisation is within the limits ($u_{le} > u_k > 0$) and the lower surface ($u_{le} < u_k < 1$). Data points that are equal to the bounds must be removed. Using the following data set, the thickness B-Spline can be fitted.

$$x_0 = 0 \qquad y_0 = 0 \tag{5.37}$$
$$x_1 = 0 \qquad y_1 = y_q \tag{5.38}$$
$$x_2 = x_s \qquad y_2 = y_t \tag{5.39}$$
$$x_3 = x_t \qquad y_3 = y_t \tag{5.40}$$
$$x_4 = 2x_t - x_s \qquad y_4 = y_t \tag{5.41}$$
$$x_5 = x_u \qquad y_5 = y_u \tag{5.42}$$
$$x_6 = x_v \qquad x_6 = 0 \tag{5.43}$$

The coordinates of the spline coefficients are given in equations (5.37) to (5.43) These are fitted using the initial guess and bounds given in Table 5.2.

Table 5.2: The initial guess (X_0) and the upper and lower bounds for the open variables of the Thickness B-Spline fit.

	x_s	x_t	x_u	x_v	y_q	y_t	y_u
X_0	0.2	0.35	0.9	1.001	0.01	0.06	0.01
Lower bound	0	0	0.5	1	0	0	0
Upper bound	x_t	1	1	2	0.1	0.1	y_t

The trailing edge is not fixed in the x direction, but is the variable x_v. This variable is used to estimate the profile with a closed trailing edge. Thus, it can be used to compare the Nacra sections with different foil sections like the NACA series. The maximum thickness is now given by the variable y_t at the location x_t.

6

Geometric deviation analysis: Method

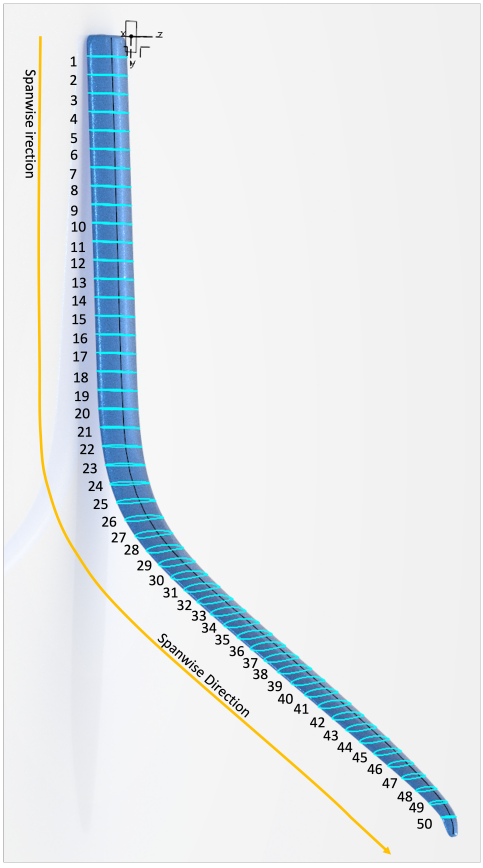

Figure 6.1: An overview of the Nacra hydrofoil showing the location of the different sections that need to be accurately orientated in a 2D reference frame.

In the literature review, the manufacturing of the hydrofoils was analysed. The chapter discussing the possible impact of the different manufacturing processes is provided in Appendix E. It was found that, from the different processes, moulding has a great impact on the final geometry.

The moulds of the hydrofoil could be slightly spaced apart, creating a thicker profile. This spacing can affect the misalignment of the mould halves. The offset of the moulds allows for the run out of resin at the mould line. The lack of resin causes the formation of voids (Figure 6.2a). The fact that the mould halves are not completely closed can be seen in Figure 6.2b. The leading edge of the hydrofoil can be seen with a large plate of resin still attached. The impact of especially the orientation of the mould will be analysed using the digitised sections.

The different methods for the foil processing were validated and verified. These methods can now be used to analyse hydrofoils. The hydrofoils will be analysed for their differences using the profile parameters.

The assumption of geometric variations between the hydrofoils is validated in chapter 12. The raw results of the 3D scan were not accurate enough to make a clear comparison. That is what is presented in ”*Geometric deviation analysis*”. This chapter will discuss the final method for extracting profile sections from the raw data obtained in Catia. The profile sections are defined in the global coordinate system of the hydrofoil shown in Figure 6.1.

The results of this method will be presented in chapter 10. Geometric differences between hydrofoils will be expressed in the various shape parameters of the profiles. The polynomial fit will be analysed in these sections as well. In chapter 9, it was found that the polynomial sometimes deviates upward. This is assumed to be caused by the misalignment of the mould halves during production.

The results will be able to answer the hypothesis formed in the following. The hypothesis will finally be tested in chapter 14.

Hypothesis 3: ***Manufacturing defects can be identified by the differences in the shape parameters of the different hydrofoil sections.***

H. 3.1: *The profile thickness can be an indicator for improper mould closure.*
H. 3.2: *The polynomial camber line can indicate a miss alignment of the mould halves*
H. 3.3: *A correlation can be found between the different parameters that could indicate improper mould closure or miss alignment.*

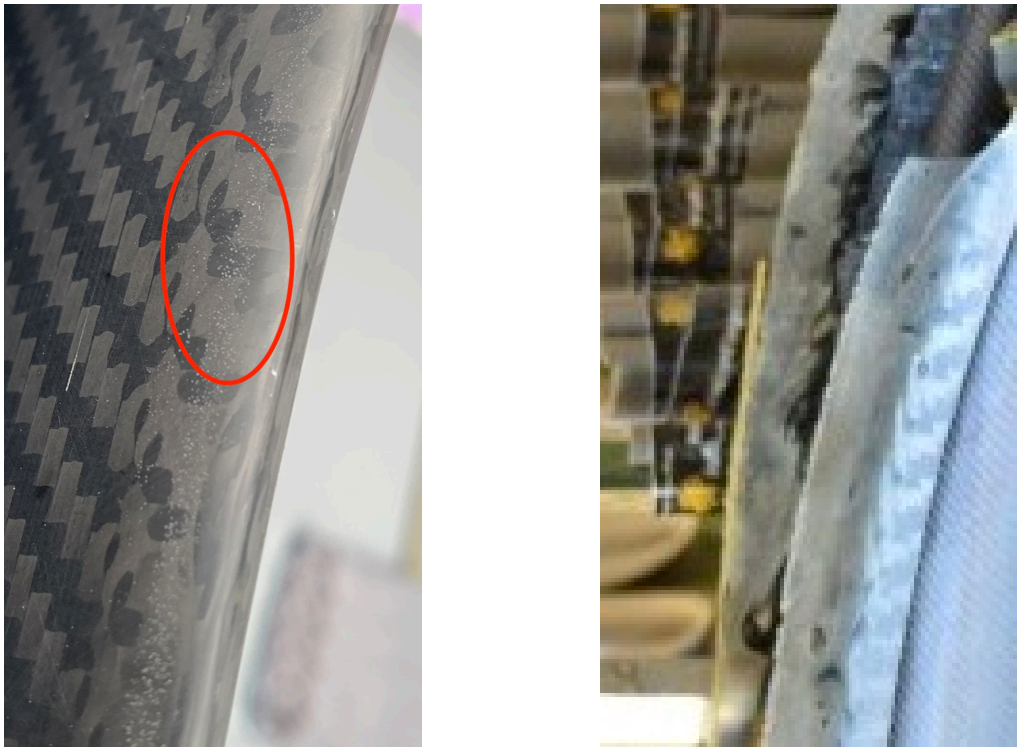

(a) Showing voids (white dots) and sanded carbon (change in pattern) at the leading edge.

(b) A close-up of the leading edge during production showing the pinched fibres and the resin run-out at the leading edge [67].

Figure 6.2: The different production errors that can be observed in the Nacra hydrofoils.

6.1. Theory

The literature identified that mould closure is a possible cause of geometric differences. Figure 6.2b is showing that the hydrofoils do have additional material after consolidation, with the white part sticking out. The maximum thickness is assumed to indicate the differences in mould closure between hydrofoils. The polynomial camber line is assumed to be affected by slight changes in leading edge placement due to mould misalignment.

6.1.1. Polynomial camber line fit as a indication for the mould misalignment

The polynomial camber line fit proposed in subsubsection 5.2.2 did not prove to be a good estimation of the camber line. This was found because of the large divergence at the leading and trailing edges. The polynomial showed a divergence upward at either the leading or trailing edge. This chapter assumes that this divergence is due to mould misalignment.

The misalignment of the moulds only adds a small part of the final impact. Hydrofoils need to be post-processed because of the run-out of the resin. The sanding and shaping of the leading edge is what contributes to the eventual differences between the hydrofoil. The misalignment will affect how this shaping is preformed, and thus the final shape of the hydrofoil.

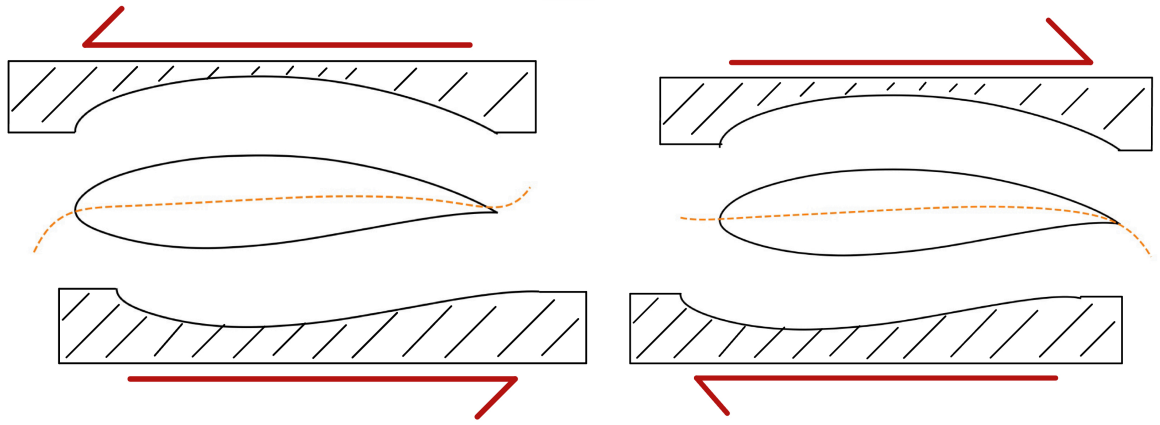

(a) Anti clockwise misalignment causing the trailing edge camber to deviate upwards.

(b) Clockwise misalignment causing the leading edge camber to deviate upwards.

Figure 6.3: Showing how the misalignment of the different mould halves could affect the fit of the polynomial camber line with the mould halves shown below and above the profile.

6.2. Methodology

6.2.1. Importing the files in python

The files are exported in the 3D global coordinate frame of the Catia model. This needs to be converted to a system that can be used by Xfoil. Xfoil needs the leading edge to be placed at the origin of the coordinate system. The trailing edge should be placed on the x axis at x = 1. For comparison of sections, this placement is critical. As the orientation will affect the profile parameter values.

Importing the Data The data from Catia is defined in the third-degree global Catia coordinate system. There is, however, a file that contains the local coordinate system for each section, defined in the same global coordinate system. This file will be used to transfer the coordinates from a 3D system to a 2D system. A file named `axissystems.txt` contains the translation ($\vec{R}_A$) and rotation ($\boldsymbol{R}_A$) of the section reference frame defined in the global coordinate system (A). The transformation vector ($\vec{R}_A$) has the shape shown in Equation 6.3. The rotation matrix ($\boldsymbol{R}_A$) is given in the shape shown in Equation 6.2. The translation vector in the section coordinate system (C) is calculated using Equation 6.1.

$$\vec{R}_C = \boldsymbol{R}_A \times \vec{R}_A \tag{6.1}$$

$$\boldsymbol{R}_A = \begin{bmatrix} 0 & \cos\theta & \sin\theta \\ 0 & -\sin\theta & \cos\theta \\ 1 & 0 & 0 \end{bmatrix} \tag{6.2}$$

$$\vec{R}_A = \begin{bmatrix} \text{Chord} \\ \text{Span} \\ \text{Thickness} \end{bmatrix} \tag{6.3}$$

$$\vec{R}_C = \begin{bmatrix} \text{Span} \\ \text{Thickness} \\ \text{Chord} \end{bmatrix} \tag{6.4}$$

The global coordinate system for the sections is not equal to the global coordinates in which the profile data ($\boldsymbol{D}$) is defined. Equation 6.3 can be seen in a different order than the values in Equation 6.6. The data only need to be rotated as the order of the axis in Equation 6.6 is equal to Equation 6.4. The rotation matrix $\boldsymbol{R_A}$ must be transformed to the correct coordinate system using the extra transformation matrix ($\boldsymbol{R}_B$) given in Equation 6.7. The final transformation of the data $\boldsymbol{D}_B$ to $\boldsymbol{D}_C$ is shown in Equation 6.5.

$$\boldsymbol{D}_C = ((\boldsymbol{R}_A \times \boldsymbol{R}_B) * \boldsymbol{D}_B^T)^T - \vec{R}_C \tag{6.5}$$

$$\boldsymbol{D} = \begin{bmatrix} \text{Span}_1 & \text{Thickness}_1 & \text{Chord}_1 \\ \text{Span}_2 & \text{Thickness}_2 & \text{Chord}_2 \\ \vdots & \vdots & \vdots \\ \text{Span}_{j-1} & \text{Thickness}_{j-1} & \text{Chord}_{j-1} \\ \text{Span}_j & \text{Thickness}_j & \text{Chord}_j \end{bmatrix} \tag{6.6}$$

$$\boldsymbol{R}_B = \begin{bmatrix} 0 & 1 & 0 \\ 0 & 0 & 1 \\ 1 & 0 & 0 \end{bmatrix} \tag{6.7}$$

The data in the axis system file contains the solved matrix for $\boldsymbol{R}_A$. Combined with the floats of the data, it is important that the number of digits of the Catia export is high. A reduction in digits from Catia will directly result in errors within the Python code. The axis system file uses 14 significant digits, while the profile coordinates are exported with a 12 digit significance. With this significance there are residual values in the span-wise direction (for each section) of $1e-5$. This should be 0 in the ideal case, as it is a 2D image that will be used in further analysis.

First orientation The set of coordinates obtained from Catia is now somewhere in a 2D space. They need to be rotated in order for the leading edge to be placed at the origin, and the trailing edge on the x-axis. To perform this rotation, a first guess of the leading and trailing edge needs to be made. This guess is made using the method described in subsection 5.2.1, Sect.*Max Radius from Centroid from .5π to 1.5π*". This method uses the foil defined in polar coordinates to identify the extremes.

The origin of the polar coordinates is defined to be at the midpoint of the data set. After translating the coordinates to the appropriate position. The Cartesian coordinates are transformed to the polar coordinates. This transformation is performed with Equation 5.10 and 5.11.

The order of the coordinates is important for the import in Xfoil. Data should start at the upper surface trailing edge and finish at the lower surface trailing edge. This is a counterclockwise rotation. Some section coordinates follow a clockwise direction. This is corrected by checking if the values of theta are decreasing in value. To remove the uncertainty of a non-constant increase or decrease theta value. The fact that `np.arctan2()` presents values between π and $-\pi$ is used. Due to this range, a large step is observed in the data. If this step is negative, the values of theta are increasing. The following code identifying this step and flips the data when the wrong direction is found.

Listing 6.1: Creating usable polar coordinates

```
transitionpoint = np.argmax(abs(np.diff(theta)))
if  np.diff(theta)[transitionpoint] < 0:
    print('works')
    r = np.flip(r)
    theta = np.flip(theta)

new_ids = (np.arange(len(r)) + np.argmin(r))%len(r)
theta = theta[new_ids]
r = r[new_ids]
```

The code will identify the leading and trailing edges by finding the peaks in the data. This peak function is affected when the profile ends at the leading or trailing edges. To create a repeatable solution, the end of the array is placed at the position where the distance to the origin is minimum. These points coincide with the top or bottom of the profile. The last 3 lines of code in Listing 6.1 show this change in the theta and r arrays. With the following data set, the leading edge and trailing edge are estimated using the same principles as those described in subsection 5.2.1, Paragraph "*Max Radius from Centroid from .5π to 1.5π*". With the leading and trailing edges defined, the section can be rotated to the correct orientation. The profile needs to be mirrored around the y-axis because all leading edges are facing away from the origin. The profile needs to be translated in order for the leading edge to be positioned on the origin. Finally, the profile is rotated.

For the rotation and translation, the vector between the leading edge and trailing edge is used.

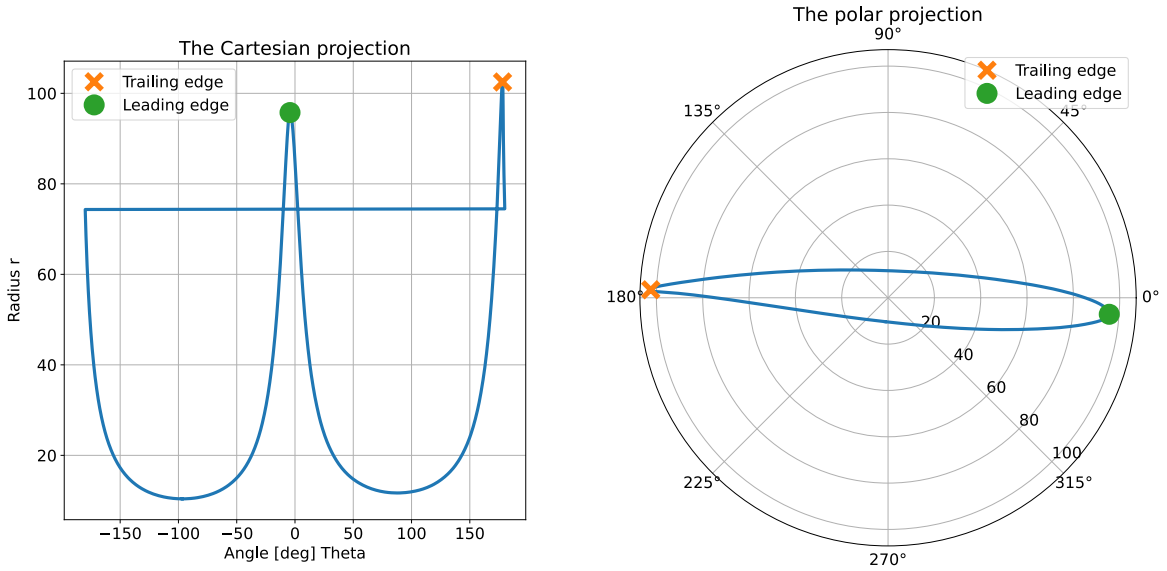

(a) The coordinates in a Cartesian plot

(b) The coordinates in a Polar plot

Figure 6.4: Showing how the leading edge and trailing edge can be found using the profile expressed in polar coordinates with the wide peak showing the leading edge and the sharp peak showing the trailing edge.

$$\begin{bmatrix} x_r \\ y_r \end{bmatrix} = \frac{\begin{bmatrix} x_{TE} \\ y_{TE} \end{bmatrix} - \begin{bmatrix} x_{LE} \\ y_{LE} \end{bmatrix}}{\left\| \begin{bmatrix} x_{TE} \\ y_{TE} \end{bmatrix} - \begin{bmatrix} x_{LE} \\ y_{LE} \end{bmatrix} \right\|} \tag{6.8}$$

$$\boldsymbol{D}_D^T = \begin{bmatrix} x_r & -y_r \\ y_r & x_r \end{bmatrix} * \left(\begin{bmatrix} x_1 & y_1 \\ x_2 & y_2 \\ \vdots & \vdots \\ x_{j-1} & y_{j-1} \\ x_j & y_j \end{bmatrix} - \begin{bmatrix} x_{LE} \\ y_{LE} \end{bmatrix}^T \right)^T \tag{6.9}$$

With the profile orientated correctly, it can be scaled in order for the chord length to equal 1. This will form the normalised raw data. The following versions of the data are created:

data_dat_cr Orientated data from Catia

data_dat_c1 Orientated data and scaled to a chord length of 1

data_dat_c99 Orientated data and scaled to a chord length of 1 and shortened to 0.99c in order to remove the trailing edge geometry.

6.2.2. Deriving the Camber Line from the data.

Camber line by offsetting top and bottom surfaces The method of creating the camber line by using the offset of the profile surfaces is discussed in subsection 5.2.1, section "*Camber line Data: Surface offset*".

This method finds the intersection between the offset of the upper and lower surface. This method has proven to be a reasonable assumption for the camber line. The data obtained using this method are combined with the data from the next step, which are the voronoi points.

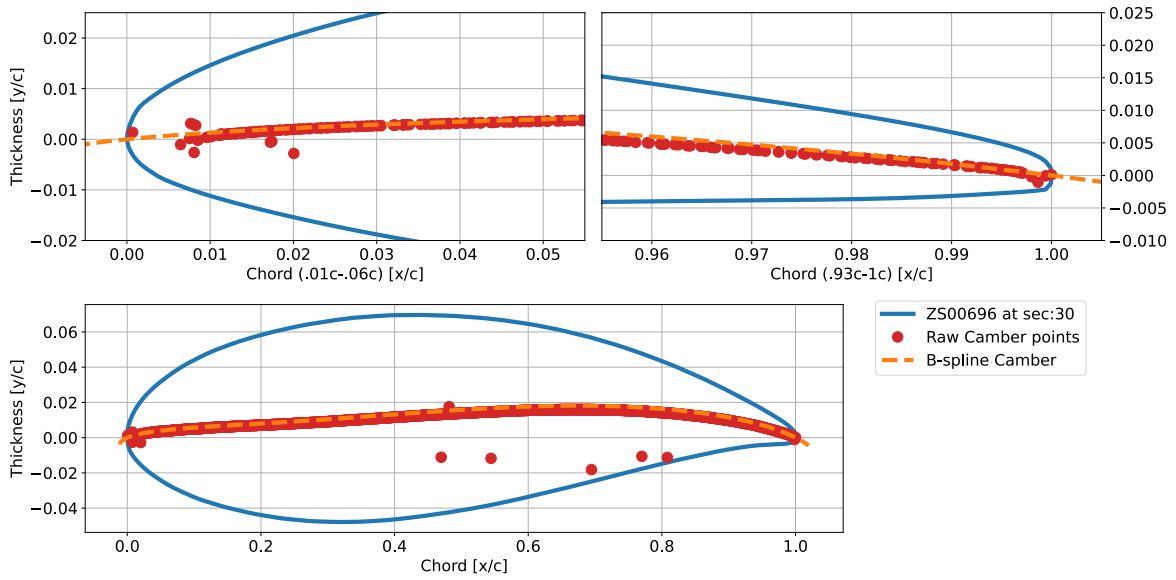

Figure 6.5: Showing the raw data from both the the Offset and Voronoi method.

Camber line by voronoi diagram The method of the voronoi point is explained in subsection 5.2.1, Paragraph "*Camber line Data: Voronoi*". A voronoi diagram finds the largest area that each data point can cover. This method is an analogy to cell growth. On the intersection of 3 voronoi area's a voronoi vertex is placed. For a data set that resembles a foil section, these vertex points are positioned on the camber line.

Filtering the camber line data set The data resulting from both methods contain some outliers as can be seen from Figure 6.5. Outliers are mostly located near the leading and trailing edges of the profile. These outliers are filtered using two different methods. The first method calculates the gradient to the next data point. If the points are placed far apart in the y direction, the gradient value will be high. Gradients that are larger as the 99th percentile are removed from the data. This method is repeated 15 times to reduce the data set.

The second method will identify the offset of the data with respect to a fitted polynomial. Using the reduced data to fit a 9 degree polynomial. It was found that a degree of 9 provided the best fit for the camber line. What the polynomial fit provides is a continuation of the line. If the spline function from scipy was used again, the last data points would influence the final result disproportionately.

Using this polynomial, the root-mean-squared distance on the y-axis is calculated for each data point. Data points that deviated more than the 99.5th percentile are removed from the data set. This method is repeated for 10 iterations.

After filtering the data, the values are similar enough to be fitted using the B-Spline method for the camber line, as explained in subsubsection 5.2.3. The resulting camber line will be used to find the thickness profile of the section. The thickness profile is a perpendicular distance from the camber line. To find this distance, the error formulation code is revisited as discussed in subsubsection 5.2.3. The point on the profile curve is on a vector perpendicular to the camber line when the tangent distance is 0. This tangent distance is given by Equation 5.33. Where the profile is defined as a set of points in subsubsection 5.2.3, it is a continuous curve in the current problem. The Camber line replaces the fitted curve ($P_D(t_k)$) of Equation 5.33.

$$x = (\vec{P}_D(u_k) - \vec{C}_k)^T \vec{T}_k \tag{6.10}$$

The matching locations are found using scipy's least squares minimisation. With the upper surface bounded by $0 \leq t_k \leq u_{le}$ and the lower surface by $t_{le} \leq u_k \leq 1$. The data from this minimisation

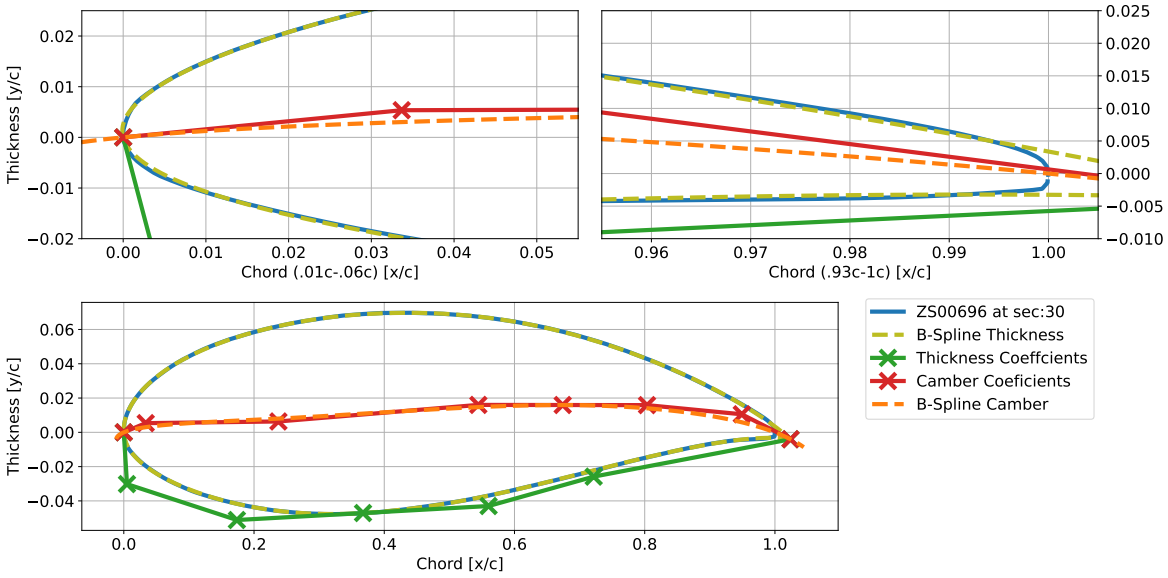

Figure 6.6: The fit of the B-spline camber line and Thickness on a Nacra hydrofoil section showing the B-spline coefficients with the crosses. It can be seen that it is a reasonable fit to the actual data.

needs to exclude all values equal to the bounds and non-increasing values. The resulting list of spline variables with matching camber positions follows the thickness profile.

The camber line should be the midpoint between the points on the top and bottom surfaces. The data set for the camber line is now replaced by finding the middle of the thickness profile points. This method is only possible now as it can be very unstable if the camber line used is not close to the final solution.

The data for the thickness profile will then be used to fit a B-spline to follow the thickness. The thickness profile is fitted using the method described in subsubsection 5.2.3. The use of the thickness profile fit is to estimate the profile with a closed leading edge. All sections have a finite trailing edge, as it is impossible to make an infinitely small trailing edge. In comparisons, all foils start with a closed leading edge in the analysis.

In order to comply with the design standard for profile sections, the same closed trailing edge foil needs to be reverse-engineered. The last knot on the B-spline is only locked in the y direction and set to 0. The x location of the thickness profile is fitted by the curve fit.

For the first iteration of fitting the camber line. The trailing edge is set at $x_{TE} = 1.2$. Using the last knot location of the thickness profile, this value is updated. The camber line and thickness profile are now terminating at the same location. This improves the fit of the camber line. If the camber line is fitted to be too long, the curve is too gentle and will deviate from the data set. With a short camber line, the last two knots can create a sharp curve that will create an error in the estimation of the chord length and trailing edge location.

The trailing edge location will be used for the final rotation of the profile. This error will impact the analysis in all fluid dynamic analysis.

The iteration will be repeated for 5 iterations. After these iterations, the leading edge will be given by the start of the camber line and the end of the camber line. Using Equation 6.8 and 6.9, the following data will be transformed:

- Data normalised with chord 1
- Data normalised to a chord of 1 and shortened to 0.99c
- Spline coordinates for the camber line
- The unfiltered Camber line points from the Offset and Voronoi methods

- The Final Camber line data set.

The spline coordinates for the thickness profile are divided by the length of the set thickness profile. The thickness is related to the camber and it does not need to be rotated in this case.

The important parameters can now be extracted from the B-spline fit. The location and height of the thickness are equal to the third B-spline coefficient. The camber B-spline consists of one more knot. The maximum camber location and thickness are thus given by the fourth B-spline coefficient.

The final step is to reverse engineer the profile using the B-spline data. This step will be used to calculate the accuracy of the fit in the following method and to validate the placement of both the camber line and thickness profile (Figure 6.6).

6.2.3. Validation and Verification of the previous orientation.

Error estimation The data that is generated needs to be validated and verified. This is achieved by calculating the error between the spline and the actual data set. The error is calculated with the method described in subsubsection 5.2.3. The data set of the imported profiles will be used to create the points X_k in equations (5.33) and (5.34). This method creates a distance between the B-spline profile and the data set. The error of the complete profile is given by Equation 6.11.

$$e_{SD} = \sum_{k=0}^{n} \frac{||\epsilon_{SD_k}||}{n} \tag{6.11}$$

e_{SD_k} was defined in Equation 5.35 to be the minimum error between a curve and a data point. The sum of the absolute difference divided by the length of the data set (n) will give the final error.

6.2.4. Estimating Profile Parameters

The thickness and camber parameters are already identified by the B-Spline fits. The 3 coefficient of the Thickness B-Spline is positioned on the maximum thickness location. The maximum thickness y_t and its location x_t are given by the python code: `cv\_thickness\_f[3,1]` and `cv\_thickness\_f[3,0]`. The `\_f` is used for the values after rotation. These are the final normalised foil parameters. The camber B-Spline added a extra coefficient before the maximum camber to provide a better fit. The maximum camber y_c and its location x_c are thus found with the python variable: `cv\_camber\_f[4,1]` and `cv\_camber\_f[4,0]`.

The leading edge radius was identified to be an important parameter for the hydrofoil performance. This variable is not found with the method described above. The leading edge radius is found using

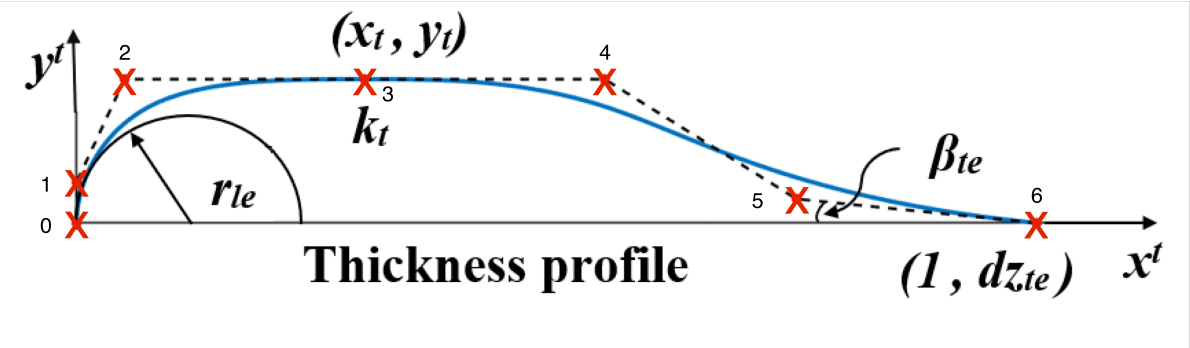

Figure 6.7: The 6 thickness B-Spline coefficients shown on a profile and identifying the the profile parameters: x_t,y_t,r_{le},κ_t,β_t and $d_{Z_{te}}$. With the figure modified from Tortora, Concilio, and Pecora [4].

the B-spline method proposed by Derksen and Rogalsky [2] (Figure 6.7). This method links the spline coefficients to specific profile parameters, such as the radius of the leading edge, the location of the thickness, and the angle of the trailing edge. Therefore, it is a good method for the parameterisation of foil sections. This dependency on these parameters is also the reason why this method was not used before.

The previous B-spline method allowed for more flexibility between the coefficient locations. This was important because the chord length was not yet equal to 1. The flexibility will add more room for a better fit on a more complex profile like the 3D scanned surfaces. Due to this reason, the maximum thickness y_t and its location x_t are not variables for the BP3333 optimisation. The equations for the spline coefficients are given in equations (6.12) to (6.18), creating the coefficient matrix Equation 6.20.

$$x_0 = 0 \qquad y_0 = 0 \tag{6.12}$$

$$x_1 = 0 \qquad y_1 = \frac{3\kappa_t(x_t - r_t)^2}{2} + y_t \tag{6.13}$$

$$x_2 = r_t \qquad y_2 = y_t \tag{6.14}$$

$$x_3 = x_t \qquad y_3 = y_t \tag{6.15}$$

$$x_4 = 2 * x_t - r_t \qquad y_4 = y_t \tag{6.16}$$

$$x_5 = 1 + (d_{Z_{te}} - \frac{3\kappa_t(x_t - r_t)^2}{2} + y_t)\cot\beta_{te} \qquad y_5 = \frac{3\kappa_t(x_t - r_t)^2}{2} + y_t \tag{6.17}$$

$$x_6 = 1 \qquad y_6 = d_{Z_{te}} \tag{6.18}$$

There are now additional parameters that describe the profile. κ_t is the curvature at the top of the profile and r_{le} the radius of the curvature at the leading edge. $d_{Z_{te}}$ is the thickness of the trailing edge. This value is set to 0 as the data have been scaled to a chord of 1 with a closed trailing edge. The final parameter is r_t. This is a variable that depends on all other variables. A suitable value for r_t is given as the smallest root of Equation 6.19, within the limits $\max(0, x_t - \sqrt{\frac{-2y_t}{3\kappa_t}}) < r_t < x_t$

$$\begin{aligned} \frac{27\kappa_t^2}{4} r_t^4 \\ -27\kappa_t^2 x_t r_t^3 \\ + \left(9\kappa_t y_t + \frac{81\kappa_t^2 x_t^2}{2}\right) r_t^2 \\ + \left(2r_{LE} - 18\kappa_t x_t y_t - 27\kappa_t^2 x_t^3\right) r_t \\ + \left(3y_t^2 + 9\kappa_t x_t^2 y_t + \frac{27\kappa_t^2 x_t^4}{4}\right) = 0 \end{aligned} \tag{6.19}$$

$$Cv_{\text{Thickness}} = \begin{bmatrix} x_0 & y_0 \\ x_1 & y_1 \\ x_2 & y_2 \\ x_3 & y_3 \\ x_4 & y_4 \\ x_5 & y_5 \\ x_6 & y_6 \end{bmatrix} \tag{6.20}$$

Identify whether the method provided an accurate fit. An error is calculated between the thickness profile data points and the new spline. Using the data points instead of the previously fitted spline ensures that the error from one is not propagated to the next profile. With all values plotted on the x axis, it is possible to define the error as the absolute difference in y divided by the number of points, as shown in Equation 6.21.

$$e_{SB} = \sum_{k=0}^{n} \frac{||y_{D_k} - y_{BP_k}||}{n} \tag{6.21}$$

The error will be defined as e_{SB}. The thickness points are y_{D_k} and the spline y_{B_k}. The number of data points is set to n.

7

2D section hydrodynamic analysis: Method

The final step in this thesis would be to analyse the differences between the hydrofoils with the fluid dynamic performance. Hydrofoils that are processed i section 6.2 can be used in the programme Xfoil.

Analysis of fluid dynamic performance will give the first indication of the impact of the differences. 2D analysis is only the first step in identifying how manufacturing impacts hydrofoil performance. The 2D analysis data can be used to estimate the performance of the complete lifting line method. With the hydrofoils simulated as a complete wing, only then a good comparison can be made between each hydrofoil.

In this step, the important areas will be analysed. What area of the hydrofoil is critical to the performance and what shape parameter this might be affected by. This question is addressed by challenging the following hypothesis.

Hypothesis 4: ***There is a difference in the hydrodynamic performance between the different hydrofoils.***

H. 4.1: *The difference in shape affect the location where ventilation can occur.*
H. 4.2: *The biggest impact on the performance is influenced by the leading edge radius.*
H. 4.3: *The high pressure side of the profile presents separated flow at positive angles of attack.*

7.1. Theory

In order to understand the input of the analysis and the final result, a basis of understanding needs to be established. A detailed explanation will be provided in the previously written literature review (Appendix F).

7.1.1. Fluid dynamics

A foil needs to produce lift. Lift is created by the flow around the profile. If there is a difference in pressure between the upper and lower surfaces of the profile, a resulting force is generated that points upwards instead of backward (Figure 7.1a). When the resultant force is deconstructed in its components, the lifting and pulling force can be found (Figure 7.1b). Drag around a profile is a combination of the pressure acting on the profile and the shear friction of the flow and the surface (Figure 7.1c).

The different fluids in fluid dynamics can be compared using the Reynolds number. The Reynolds number is a dimensionless value that predicts flow phenomena. Combining speed, object length, and

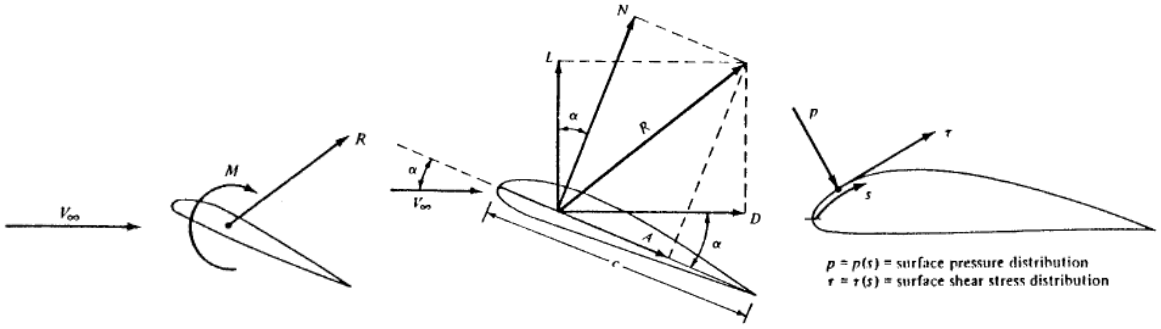

(a) The fluid flowing over an foil shape produces a moment and a resultant force in the direction illustrated.

(b) The resultant force can be deconstructed into its components lift and drag.

(c) The drag is a combination of the fluid pressure (p) and the shear friction (τ) on the surface.

Figure 7.1: Different figures showing the components of lift and drag of a foil shape as explained by Anderson [5].

fluid properties to calculate a value. Using the Reynolds number, different sized parts can be compared by matching the Reynolds number. The Reynolds number is given by Equation 7.1.

$$Re = \frac{\rho V l}{\mu} \tag{7.1}$$

With flow speed (V), chord length (l), density (ρ) and dynamic viscosity (μ). For the scaling of the profile sections, the lift and drag force are defined as unit less coefficients. These coefficients are called the lift coefficient (c_l ,Equation 7.2) and the drag coefficient (c_d ,Equation 7.3).

$$C_l = \frac{L}{\frac{1}{2}\rho_\infty V_\infty^2 c} \tag{7.2}$$

$$C_d = \frac{D}{\frac{1}{2}\rho_\infty V_\infty^2 c} \tag{7.3}$$

In fluid dynamics, there is laminar and turbulent flow. A flow is laminar when the fluid is flowing perpendicular to itself. This is often found in the wick of a candle when the air in the room is still. Not far from the wick, the smoke will start to form circles. This is the transition to turbulent flow, as can be seen in Figure 7.2a.

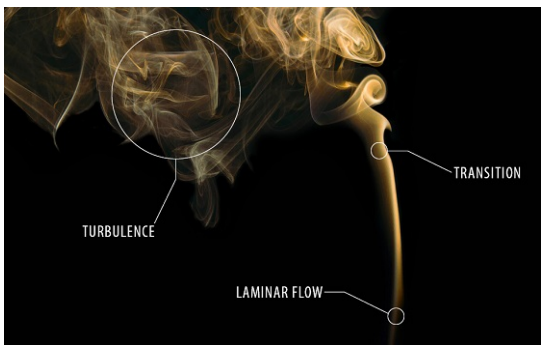

(a) Airflow visualised with smoke starting as a laminar flow and transitioning to a turbulent flow on the top. [68]

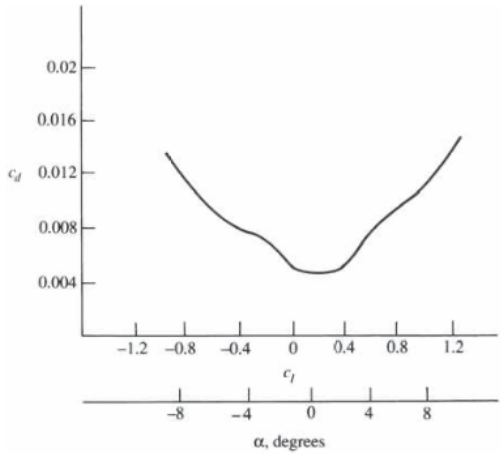

(b) The drag bucket shown as the small indentation in the middle with the of this lift over drag curve with the curves on the side showing the drag increase with turbulent flow. [69]

Figure 7.2: caption

Turbulent flow has the fluid particles moving around much more. This movement is rotational and is called vorticity. When laminar flow is flowing over a surface, the transition (*boundary layer*) to no speed at the surface and air speed is relatively small. This does not produce as much resistance. However, when the flow is turbulent, this transition is larger and the resistance of the flow greater. Therefore, laminar flow is desired.

The homogeneous nature of the laminar flow does result in a less effective ability to follow a curve. When it cannot follow the curve, it will separate. This separate flow creates a lot more drag than when it would have stayed attached.

When analysing a profile in fluid dynamics, there is a region where the flow is laminar. This region is called the drag bucket (Figure 7.2b). Outside the drag bucket the flow is fully turbulent.

The ability of the flow to remain attached to the surface is dependent on the Reynolds number. At higher Reynolds numbers, the flow transitions are earlier and contain more "*Energy*" which allows for better attachment of the flow.

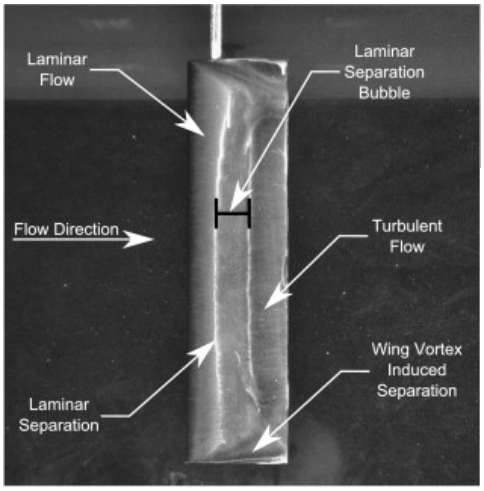

(a) Upper surface oil flow visualisation of major flow features on the Wortmann FX 63-137 rectangular wing with aspect ratio of 4 (α = 9 deg, Re = 90,000) by Ananda, Sukumar, and Selig [6]

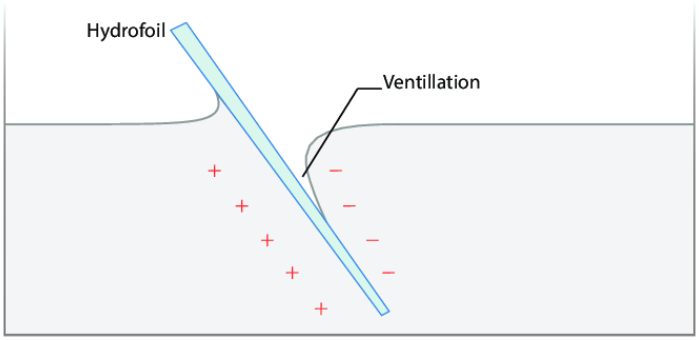

(b) Ventilation induced by a lifting hydrofoil piercing the free surface [70].

Figure 7.3: Visualising the laminar separation bubble on a wing and the effect of ventilation caused by this laminar separation bubble.

At low Reynolds numbers, it is common for the laminar flow to separate from the surface. Separation causes the flow to transition to a turbulent flow. This turbulent flow has a larger boundary layer and can still be attached to the surface. This causes a small region of separation called a laminar separation bubble. The separation bubble can be seen in the middle of the wing in Figure 7.3a.

The laminar separation bubble can make the transition from laminar to turbulent flow more abrupt. This results in a sudden increase in drag. The hydrofoil has a specific phenom that is related to this laminar separation bubble. If the pressure in a separated region falls below the ambient air pressure and a connection to the air is made, the hydrofoil will ventilate (Figure F.11). The pressure coefficient at which ventilation can occur is given by Equation 7.4.

$$c_{p_{cr}} = \frac{p_{\text{atm}} - hg\rho_{\text{water}}}{\frac{1}{2}V^2\rho_{\text{water}}} \tag{7.4}$$

The dynamic pressure at the bottom of the fraction is calculated by the density of the fluid (ρ_{water}, $\frac{\text{kg}}{\text{m}^3}$) multiplied by the cubed speed (V, $\frac{\text{m}}{\text{s}}$). The static pressure of the water is given by the depth of immersion (h), gravitational acceleration (9.81 $\frac{\text{m}}{\text{s}^2}$ and the density of the water.

A hydrofoil with ventilation produces significantly less lift than one without ventilation, leading to a decrease in the force of the sails. This can cause the boat to crash into the water, reducing its speed from 20 knots to 4 knots, or capsize the boat. Thus, this is a critical factor in hydrofoil performance.

7.1.2. Xfoil

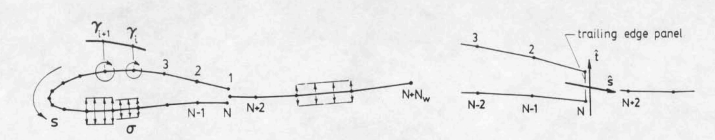

Figure 7.4: Airfoil and wake paneling with vorticity γ and source distributions σ, with trailing edge details on the right [38].

The programme Xfoil is used to analyse the hydrofoil sections in 2D. The programme was designed by Mark Drela in 1989[38]. The programme calculates the flow over the profile by reducing the shape in a set of vertices. Each vortex is connected by a panel. The method is thus called *panel method*.

In this simplification, the effects of viscosity are not taken into account. The viscosity of the flow is important when analysing laminar to turbulent transition and friction drag. The programme calculates the boundary layer using an integral function. The results of this method are very close in accuracy to the more complex models that are currently being used for this particular use case.

7.2. Methodology

7.2.1. Frequency optimisation

The optimal low pass frequency needs to be found before profile sections can be analysed in Xfoil. The data set created in chapter 5 is retrieved. The raw data with a chord length of 1 (**data_c1**) is used for the optimisation. These data are transformed into a periodic spline with no smoothing applied. The data is then recreated but now with a uniformly distributed spline parameter with a length a 1000 times longer. Multiplication is performed to make sure that the sampling frequency is high enough. The more accurate method would be to

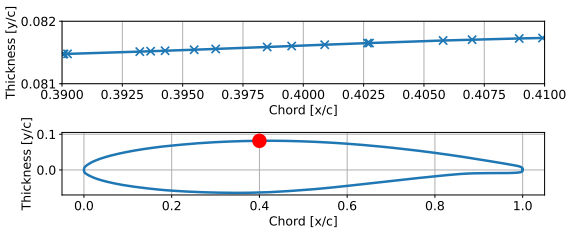

(a) The point spacing of the real data shown above and the location of set of points shown with the red dot in the profile below.

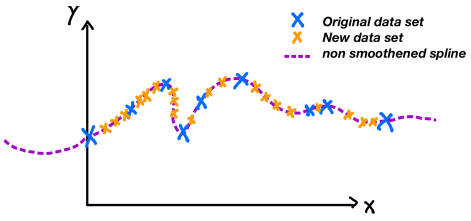

(b) Schematic representation of the profile sampling with the blue crosses showing the real data points, the purple dashed line the non smoothed spline and the small orange crosses the new data set. The new data set better follows the curves of the profile and will be able to find all the frequencies.

Figure 7.5: Showing the source of the noise in the data and how the increase of the sample size ensures that all the frequencies are captured.

The Fast Fourier Transform (FFT) is performed using the numpy.rfft2 function [1]. This function returns 2 dimensional FFT for a real array. The data used for the FFT is not imaginary in the mathematical sense. By using the 2 dimensional data, the noise in the y-axis (up and down) and the x-axis (spacing) can both be smoothed.

The FFT is calculated as orthogonal. The FFT can be calculated in the forward, backward, or orthogonal direction. The orthogonal direction produces the best results because the profile is periodic. This method does affect the scaling of the profile when transforming it back. The profile is scaled equally in

[1] Numpy.rfft2:`https://numpy.org/doc/stable/reference/generated/numpy.fft.rfft2.html`,(visited on: 09/07/2023)

both the x and the y directions. As the leading edge is positioned on the origin of the axis system, the profile can be scaled back to its original size by dividing by the maximum x value.

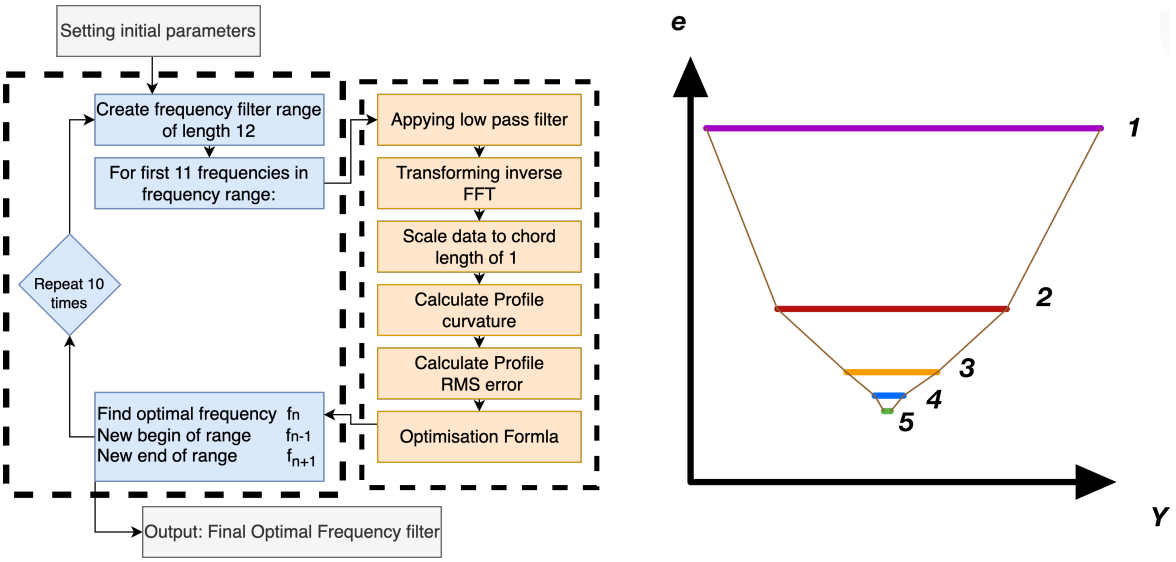

(a) The different steps in the optimisation of the low pass filter for each profile section

(b) Showing the decrease of the error and the smaller range for each iteration with the numbers showing the different iterations.

Figure 7.6: Showing how the optimisation of the low pass filter frequency is performed.

Optimisation of the low-pass filter frequency is shown in the schematic presented in Figure 7.6a. A optimisation function is calculated for 10 frequencies that are spaced logarithmically. For each frequency, the orange block on the right is evaluated in the order presented. The corresponding code can be found in Listing D.2. The low-pass filter is applied by multiplying, all values with a frequency past the low-pass filter, by zero. The inverse FFT function from numpy can be applied to the data to return them to normal coordinates. When these coordinates are scaled back, the curvature (Equation 5.9) and the profile error (explained in subsubsection 5.2.3) can be estimated. The function used for the optimisation is given in Equation 7.5.

$$e_S = \left(\sum_t = 1^n \kappa_t \right)^{e_{SD}} \tag{7.5}$$

The function uses both the potential and the error to find the best frequency. If only the error is used, some frequencies would converge on the sample frequency because the small reduction was missed by the frequency range. The curvature does not show an optimum throughout the curve, as can be seen in Figure 9.12a. Using the increased potential with higher frequencies and the reduction of error, the optimisation point is thus the lowest value on the curve, as can be seen in Figure 7.7.

Figure 7.7: Showing the used optimisation function verses the real error and potential curve.

The final results are saved in a file to be retrieved for the Xfoil analysis.

7.2.2. Xfoil analysis

The Xfoil analysis is performed for sections 15, 20, 24, 30, 35, and 40. These sections are chosen to provide a good spread of the different shapes of the hydrofoil that are identified in chapter 10.

The range of Reynolds numbers was chosen to be linked to the different boat speeds. The minimum liftoff was assumed to be around 10 knots. The maximum boat speed is assumed to be 35 knots. The water is assumed to be fresh water at 20 degrees Celsius. five different speeds are used for the analysis with an even spacing. The speeds used are: 10, 16.25, 22.5, 28.75, 35 knots. The units of knots are

not compatible with Equation 7.1. A knot is about 0.51444 m/s. The speed used for the analysis is therefore 5.14, 3.36, 11.57, 14.79, and 18.01 metre per second.

Table 7.1: The Reynolds number in different water conditions for a minimum boat speed of 10 knots and a maximum of 35 knots.

	Temperature degree [°C]	Density [kg/m3]	Dynamic viscosity [N s/m2]	Re min	Re max
Fresh water [71]	10	999.7	1.31E-03	7.87E+05	2.75E+06
	20	998.2	9.79E-04	1.05E+06	3.67E+06
Salt water [72]	10	1027	1.41E-03	7.49E+05	2.62E+06
	20	1025	1.09E-03	9.68E+05	3.39E+06

The water conditions also affect the final results. In Table 7.1 the Reynolds numbers for 10 and 20 degree water temperature in fresh and salt water. The water temperature of 10 degrees is around the minimum for safe operation of the boat. While 20 degrees is a very common water temperature to go sailing at. The sailors observe more ventilation on fresh water compared to salt water. Fresh water at 20 degrees Celsius is chosen to be used for the analysis.

The settings used to configure the Xfoil analysis are shown in the appendix (section D.2). The settings for the flow conditions are given in Table D.1. The settings used for the foil paneling are given in Table D.2.

An important setting for flow is the critical amplification factor (N_{crit}). The location of the transition point is defined by the point where N reaches the user specified N_{crit} Drela [38]. With a lower N_{crit} the separation bubble forms closer to the leading edge and the transition point will move up the chord.

In the paper presented by Patterson and Binns [73], the N_{crit} was estimated at 7 for the America's cup hydrofoiling boats. It is hard to validate this number to be correct for the America's cub boats. The question of whether this value would work for the Nacra 17 is still unsure. For this reason, the more common number of 9 was chosen as N_{crit}.

In the analysis, every section is evaluated for angle of attack between -20 and 20 degrees. The angle is changed with a step of 0.1 degree. The programme uses the previous boundary layer for the start of the analysis of the next angle. This would affect the results if the hydrofoil starts at stall with an AOA of -20. The angle is thus calculated from 0 to -20 and 0 to 20 degrees, with the boundary layer reinitialised between each analysis.

From each analysis the the following values are saved:

- Lift coefficient (c_l)
- Drag coefficient (c_d)
- Top transition point ($x_{tr_{\text{top}}}$)
- Bottom transition point ($x_{tr_{\text{bot}}}$)
- Pressure coefficient along the chord (c_p)
- Friction coefficient along the chord (c_f)

The friction coefficient is used to visualise the separated flow on the foil. When the coefficient is negative, the flow is in the opposite direction. When the flow separates, the flow starts to rotate in this region locally, changing the flow direction.

It is important to know the pressure coefficient in these separated regions. These are the regions where ventilation can occur. Using Equation 7.4, the critical region will be highlighted in the friction coefficient graph. The height of 0.4 m was chosen as the immersion depth. At this depth, the surface no longer influences the flow.

Using this information in Xfoil results in the analysis presented in chapter 11.

III

Results

8

Digitisation of the Nacra 17 Hydrofoil: Results

The results of the digitisation of the Nacra 17 will be discussed in the following chapter. The section 8.1 will discuss the deviations observed between the hydrofoils using the programme VXelements. This comparison is used for the initial identification of the geometric variations. The VXelement comparison will be used to discuss the observed differences compared to the accuracy stated by the 3D scanner in chapter 12. The data was transferred to Catia. section 8.2 will discuss the results of this process. It will present the absolute differences. These can be used to identify the success of the processing performed in Catia in chapter 12. The final section (8.3) will present the differences between a flat metal plate and the corresponding measurement. This can show the real accuracy of the scanner when scanning a thin object. The differences found between the hydrofoils will be the validations that there are indeed differences in the shape of the hydrofoils. The following chapters will analyse in detail what these differences actually are.

8.1. VXelement results

Table 8.1: The maximum variations that are found in VXelements by calculated by adding up the values from both sides.

Reference Foil	Comparison Foil	Highest Value [mm]		Lowest Value [mm]	
ZS00696	ZS00544	0.297	Between daggerboard casing supports	-0.127	Above Elbow
ZS00696	ZS00664	0.131	In Elbow	-0.321	70% of the chord at 70% of the span
ZS00531	ZS00691	0.271	Trailing edge above Elbow	-0.389	At bottom clamping location boat
ZS00531	ZS00663	0.124	Trailing edge below elbow	-0.369	Mid chord above tip

The hydrofoils could be compared within the programme VXelement. The visual results of these comparisons are shown in figures A.9 and A.8 in the appendix, and one set is shown in Figure 8.1. Using these comparisons, the maximum values for each comparison could be determined. These values are summarised in Table 8.1. These values seem to vary between 0.1 and 0.3 mm for thicker variations. The spots that are less thick are around -0.3 and -0.4 mm, with the ZS00544 hydrofoil being the outlier with only -0.127 at the thinnest point.

When observing the Hydrofoil figures, it is important to realise that the wide part is the root of the hydrofoil with a small chord at the tip. The leading edge of the hydrofoil can be identified by the curved side. In all pictures, the trailing edge is relatively straight along the span. The leading edge is curved, especially when approaching the tip.

Looking at figures 8.1a and A.9c a thicker part can be observed at the elbow of the hydrofoil. The other side of the hydrofoils does not show a thinner part: ZS00544 (figure 8.1b),and ZS00664 (figure A.9d). This shows that there is some difference in shape around the elbow that affects the entire chord.

There is a variation along the chord that is visible in most hydrofoils. Figure 8.1a shows an increased thickness of the leading edge up to 50% of the chord length below the elbow on the low pressure side. The opposite side (figure 8.1b shows a good fit with the ZS00531 foil it is compared with and is mostly thinner after 50% chord near the elbow.

The ZS00664 hydrofoil is comparable to the reference foil at the leading edge in figures A.9c and A.9d. For this foil, the trailing edge thickness seems to be less thick compared to the reference along the majority of the span. The ZS00691 is different again by showing a thinner profile at mid chord along the span. The leading and trailing edge are comparable to the reference foil ZS00531 in figures A.8c and A.8d.

The hydrofoil ZS00663 shows a high area in the elbow at the low pressure side and high areas at the tip and root on the high pressure side (figures A.8a and A.8b). This could indicate a different angle at the elbow or a slight bend along the span. This can also be observed in the hydrofoils ZS00544 (figures 8.1a and 8.1b) and ZS00664 (figures A.9c and A.9d) to a lesser extend.

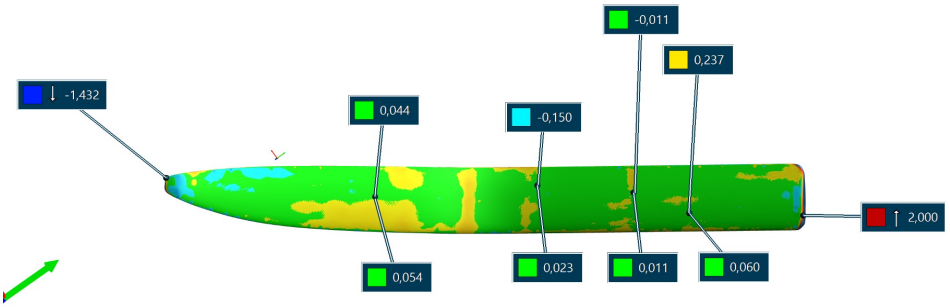

(a) Hydrofoil ZS00544 compared with ZS00696, low pressure side.

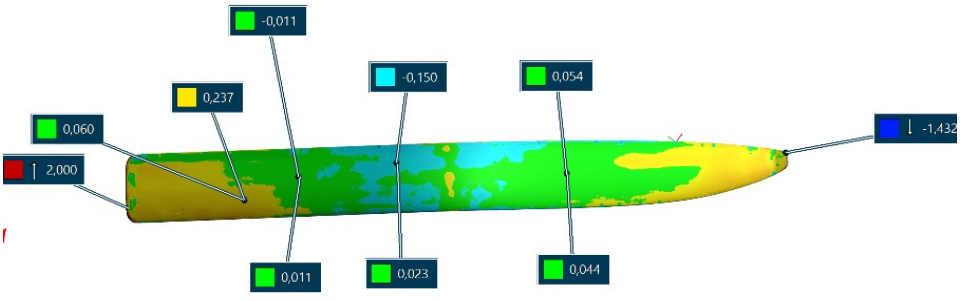

(b) Hydrofoil ZS00544 compared with ZS00696, high pressure side.

Figure 8.1: Nacra 17 Port Hydrofoil compared using VXelement

Table 8.2: The maximum absolute variations found using Catia according to the Catia deviation analysis.

Reference Foil	Compared Foil	Boat side	Max value [mm]	Location
ZS00531	ZS00544	SB	2.220	Tip, extending the lenght
ZS00531	ZS00664	SB	39.919	Bend Point Tip
ZS00531	ZS00691	BB	4.616	Bend Point Tip
ZS00531	ZS00663	BB	4.330	Trailing edge .8 span
ZS00531	ZS00696	SB	1.995	Tip and root extending the length

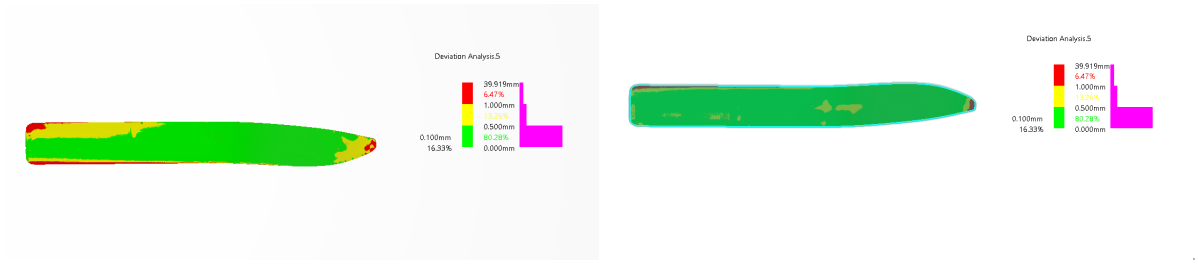

(a) ZS00664: High pressure side **(b)** ZS00664: Low pressure side

Figure 8.2: The deviation analysis of the hydrofoils using Catia and compared with ZS00531

8.2. Catia Results

The results in Catia show less detail compared to VXelements. The full set of comparison figures are shown in Figure A.10. The bending of the hydrofoil along the span, discussed in section 8.1, can be seen again in figures A.10g and A.10i. ZS00664 (figure 8.2a) shows some twist of the hydrofoil at the root trailing edge. The sensitivity on the deviation is not sensitive enough to make more distinctions between the hydrofoils.

The deviation analysis for all hydrofoils in Figure A.10 shows that the hydrofoils are aligned with a minimal deviation. The maximum deviation from the original hydrofoil ZS00531 given in Table 8.2. The hydrofoils show a general deviation between 2 and 5 mm. This deviation is mostly located at the tip and root of the hydrofoil. Hydrofoil ZS0664 is the outlier with 39.9 mm maximum deviation.

8.3. 3D scanner accuracy test results

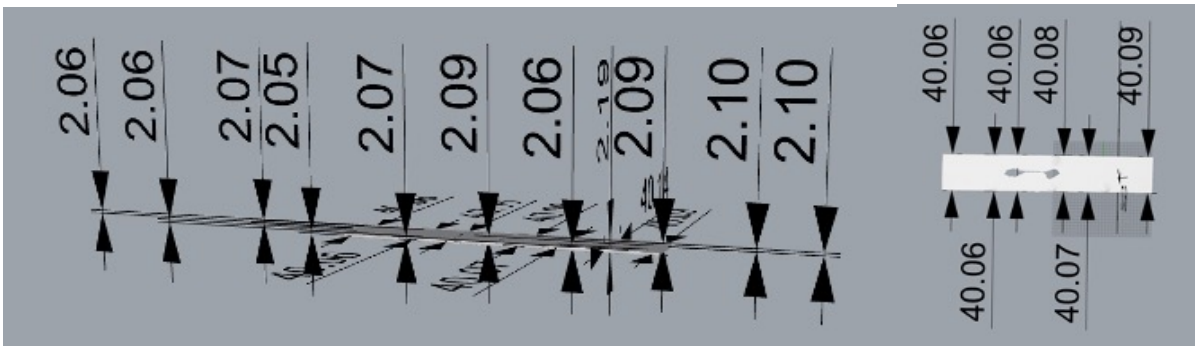

(a) Thickness measurements **(b)** Width measurements

Figure 8.3: Digital measurements of the metal strip used for accuracy validation of the HandySCAN 3D scanner

A metal strip was used to test the accuracy of the 3D scanner results. Digital measurements of the plate are shown in Figure 8.3.

The width measurements of the plate as shown in Table 8.3, are relatively accurate. The error between the physical mean (40.08 mm) and the digital mean (40.07) variate by 0.01 mm. This is an error of

Table 8.3: The manual and digital measurements of the metal plate shown in Figure 8.3 as compiled by Alex Ashworth Briggs.

	Measured dimensions [mm]		**Mesh dimensions [mm]**	
	Thickness	Width	Thickness	Width
	2.04	40.05	2.06	40.06
	2.04	40.1	2.06	40.06
	2.04	40.1	2.07	40.08
	2.06	40.05	2.05	40.09
	2.06	40.05	2.07	40.06
	2.06	40.1	2.09	40.07
	2.06		2.19	
	2.06		2.10	
	2.06		2.10	
Mean	2.05	40.08	2.09	40.07
ST Dev	0.01	0.03	0.04	0.01

-0.01%. The thickness deviated a bit more. The physical mean thickness (2.05 mm) and digital mean thickness (2.09 mm) vary by 0.04. This is with the scanner accuracy stated to be 0.02 mm and the volumetric accuracy estimated to be 0.026 mm. The error between the physical and digital thicknesses is thus 1.68% according to the measurements.

9

Research Method Validation for 2D Section Processing: Results

This chapter will present the results of the methods proposed in chapter 5. Table 9.1 shows a summary of the different methods that are assessed in this chapter. Highlight if a method passes past the first validation. If this is the case, the error of the chord is given to assess the method. This chapter will be structured summarily as to how the methods are presented in the methods.

Table 9.1: The success of the different methods described in chapter 5

Method	**Validation**	**Verification** Error of chord length %	**Applied in code**
Furthest points method	✓	0.131%	X
X and Y axis intersections	X	X	X
First derivative or Curvature of the profile	X	X	X
Max Radius from Centroid from $.5\pi$ to 1.5π	✓	-0.0201%	✓
Polynomial fitted Camber line	X	X	X
B-Spline fitted Camber line	✓	-1.588e-6%	✓

9.1. Alignment using the Profile data: Result

9.1.1. Furthest points method: Result

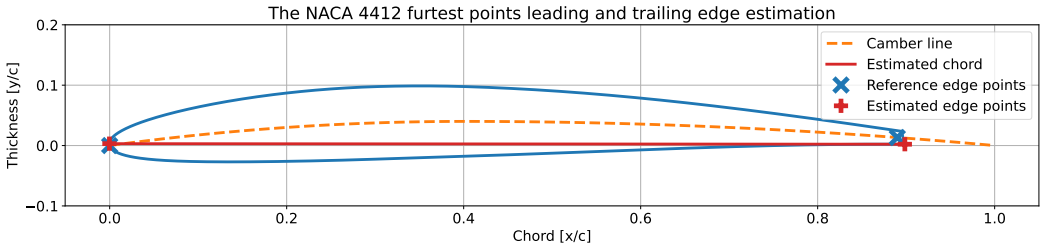

Figure 9.1: Showing the maximum distance compared between all points

The furthest points are calculated using the method described in paragraph "*Furthest points method*".Figure 5.5 showed that the method can estimate the approximate location of the leading and trailing edge. When the method is applied to a known aerofoil shape, the limitations of the method become apparent. To

test the robustness of the method, the NACA 4412 section was shorted to 0.9 chord length as shown in Figure 9.1.

Validation The Naca 4412 aerofoil in Figure 9.1 has a finite trailing edge. That means that there is a small gap between the upper and lower surfaces. The chord line is now estimated between the lowest-most point of the trailing edge and the corresponding furthest point on the leading edge. The deviation of the estimated and real leading edge location can be seen by the offset of the red plus and the blue cross in Figure 9.1.

Verification The distance over chord (d/c) to the actual trailing edge is 0.014 d/c or 1.401e-02 d/c. The leading edge is closer with 0.00314 d/c or 3.144e-03. The resulting chord length was 0.8988 x/c. The difference in length in the estimation of the chord length is thus 1.181e-03 x/c. This results in an error of 0.131% of the chord.

Although the actual numbers will not be significant, the magnitude of the error will be an important parameter to compare the different methods.

9.1.2. X and Y axis intersections: Result

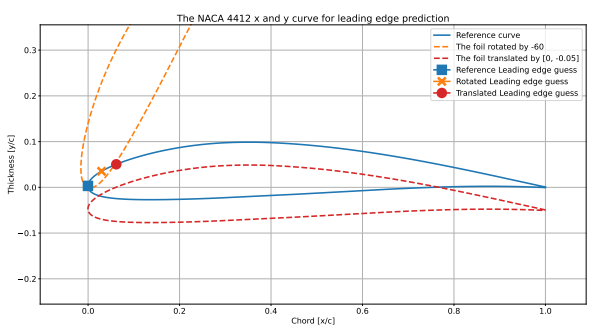

(a) NACA 4412 section with the location changes identified.

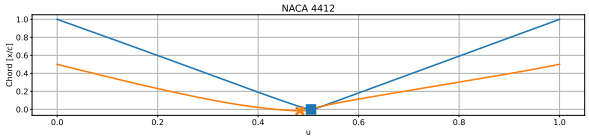

(b) The effect of rotation using the x values

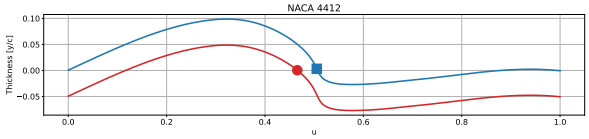

(c) The effect of translation using the y values

Figure 9.2: The estimation of the leading edge using the x and y axis of the NACA 4412 profile

Validating the x-coordinate method The x values of the foil coordinates could be used to identify the leading edge. Figure 9.2b shows that thee x coordinates show a valley at 0.5 u. This u is an independent variable that spans the curve of the profile. The x coordinates are very sensitive to the rotation of the foil. This dependency can be seen by the second orange line that is shifted to the left. This moves the minimum x-value and thus the leading edge estimation. Figure 9.2a visualises the magnitude of this change. The orange cross is the new leading edge estimation and it is located far above the actual leading edge.

Validating the y-coordinate method The y coordinates could also be used for leading edge estimation. The y coordinate change sign at the leading edge. When the profile is translated into the y axis, this point moves. The red curve and the circle in Figure 9.2c visualises this change. The same red circle is placed on the actual profile in Figure 9.2a. The circle is now offset to the left of the foil coordinates. This method is only valid if the foil coordinates are already perfectly aligned. This is not the case for the Nacra sections.

9.1.3. First derivative or Curvature of the profile

The derivative of the curve at the leading edge should approach infinity as the line approaches vertical. This point should also show the highest curvature of the foil. The validation of this theory was already given in Figure 5.7b for the derivative and Figure 5.7c for the curvature.

The problem with the 3D scanned surfaces is the addition of noise. The sections are defined by around 2000 points. These points are not perfectly spaced and located on the exact profile. This is the limitation

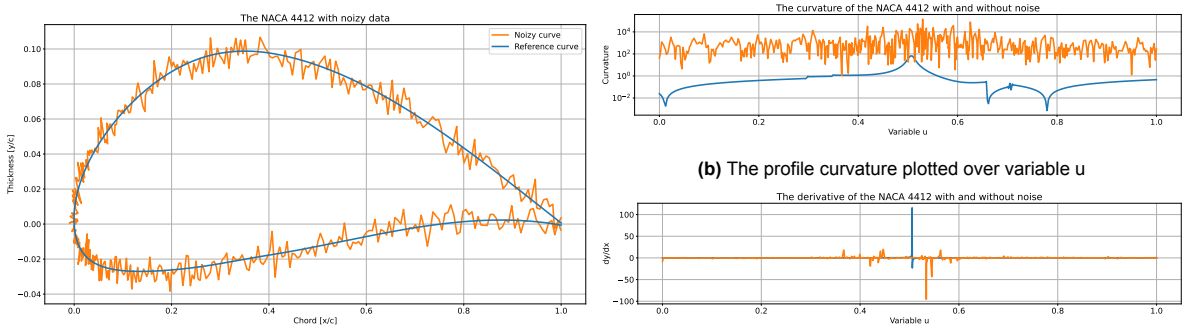

(a) The corresponding profile with added noise

(b) The profile curvature plotted over variable u

(c) The profile first derivative plotted over variable u

Figure 9.3: A comparison between a normal and noisy data set for using the derivatives to find the leading edge

of measurements, in general. But the result is that noise is added to the data. A exaggerated version of this noise is applied to the NACA foil in Figure 9.3a.

Validating the derivative method When observing the derivative of this profile. The peak at the leading edge is completely disappeared. The noise derivative is plotted above the original derivative. From this data it is impossible to determine the leading edge.

Validating the Curvature method The curvature is given in Figure 9.3c. The clean response is changed in a very noisy line from which no distinct peak at the leading edge can be observed.

9.1.4. Max Radius from Centroid from $.5\pi$ to 1.5π: Result

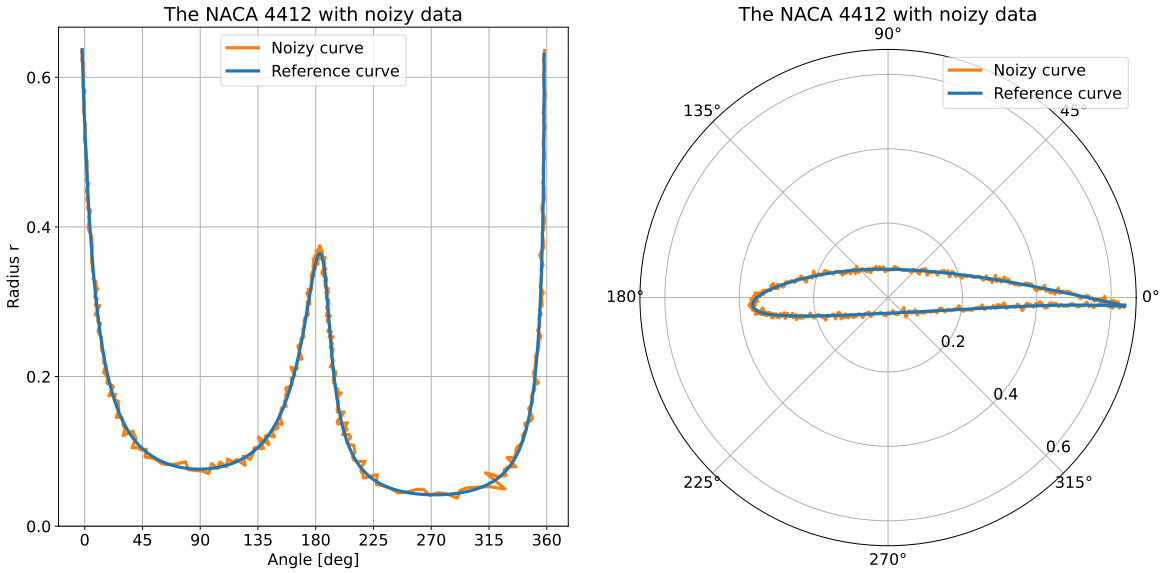

(a) Polar coordinates expressed in a Cartesian plot

(b) Polar coordinates expressed in a polar plot

Figure 9.4: The profile defined in polar coordinates comparing the reference profile with a noisy variant

Validation The shape of an aerofoil is very curved. This makes it suited to be plotted in a polar coordinate frame. The polar coordinates plotted in a Cartesian plot are used to determine the leading and trailing edges. The leading edge is clearly visible by the peak in the middle of the graph. While the trailing edge is located at the two ends on either side of the plot in Figure 9.4a.This method is independent of the rotation and translation of the profile. It can even be used to automatically identify

what the leading and trailing edge would be. The leading edge is usually a lower and wider peak. The trailing edge can be a higher and more narrow peak.

Verification The difference in distance over chord (d/c) between the actual leading edge and the peak found in Figure 9.4a is 0.00393 d/c.

In order to test the robustness of this method, the same noise is added as observed in the method using the derivative and curvature. The distance to the actual leading edge when noise is applied to the profile is 0.00848 d/c. Both values seem close to the actual leading edge. When extending the analysis to the final chord length. The chord length for the noise-free profile is found to be 1.0002c. When the noise is added to the profile, the chord length changes slightly to 1.0074c. Thus, the error for this method without noise is found to be -0.0201%. The error for the profile with noise is less significant. The addition of noise will affect the chord length in addition to the fit of the leading edge.

9.2. Camber line Estimation: Results

9.2.1. Camber line Data: Surface offset: Result

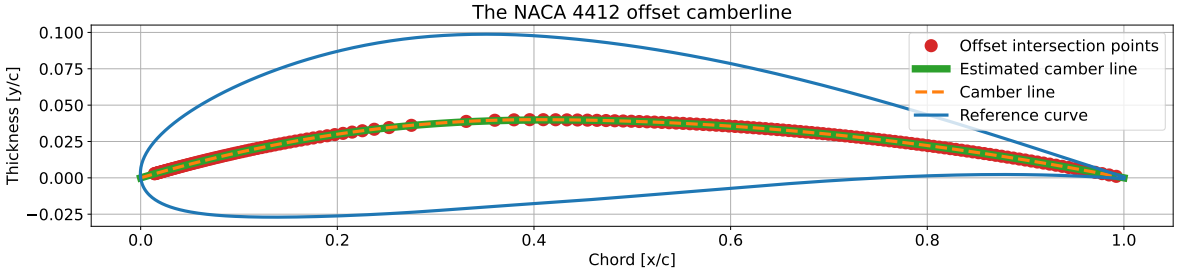

(a) The offset intersection points and camber line estimation polynomial

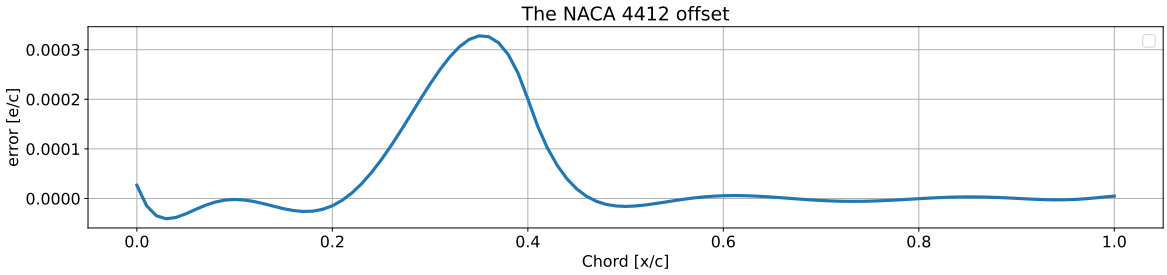

(b) The error of the offset derived polynomial

Figure 9.5: The results of the offset method on the NACA 4412 profile

Validation The offset of the surface created a set of points. These points are located at the camber line. This could already be observed in Figure 5.9. When this surface offset is applied several times at increasing distances, a set of points is created. This set of points can be seen as red circles behind the two lines in Figure 9.5a. The points are hidden behind the two camber lines. This is a very good sign. When a polynomial of degree 9, is fitted through these points. This line also follows the camber line. This polynomial estimation is shown as the green line in Figure 9.5a. The actual camber line of the profile is given as the dashed orange line.

Verification That the lines are similar is evident. But the degree of similarity is shown in Figure 9.5b. That figure shows the normalised distance in y between the actual camber line and the estimation. The largest error between the lines is 0.0003 % of the chord at around 0.35 of the chord length. Looking at the points in Figure 9.5a, the spacing between the points increases at the same location. The offset

method is thus accurate at the leading and trailing edge and decreases in accuracy at the highest camber location.

9.2.2. Camber line Data: Voronoi: Result

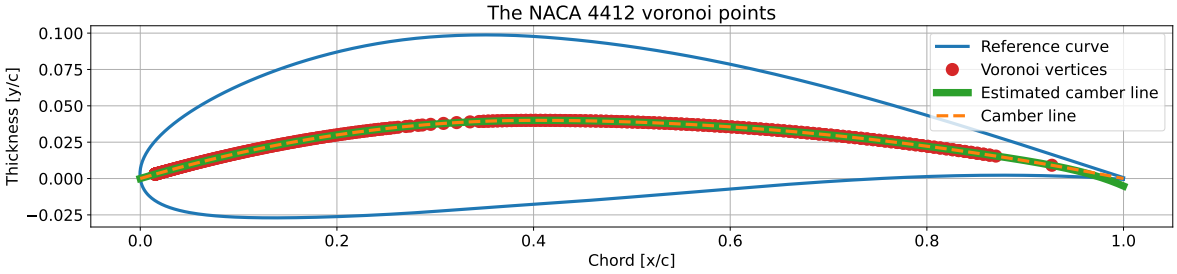

(a) The voronoi points and camber line estimation polynomial

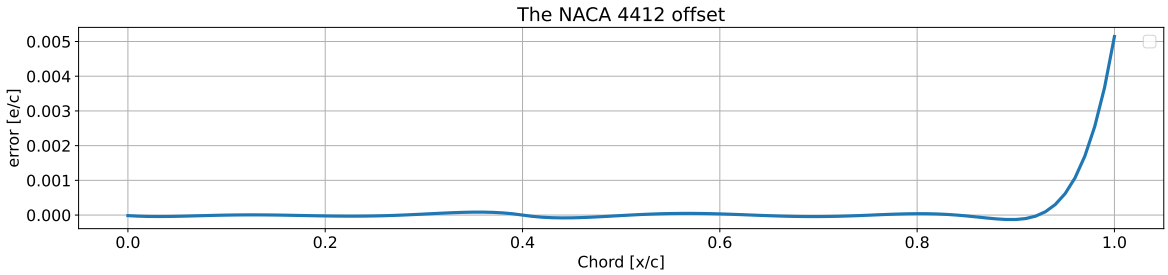

(b) The error of the voronoi derived polynomial

Figure 9.6: The results of the voronoi method on the NACA 4412 profile

Validation The set of voronoi points are shown to follow the camber line in Figure 5.14. The same image is again given in Figure 9.6a. When comparing the spacing of the red data points with those in Figure 9.5a. It is clear that the spacing at the maximum camber is more dense. However, the number of points at the trailing edge is very minimal. All points do seem to follow the camber line.

Verification When comparing the fitted polynomial with the actual camber line, the error shown in Figure 9.6b is found. The lack of points at the trailing edge resulted in a larger error. This has the effect that the error is magnitude higher compared to Figure 9.5b. The results seem to accurately follow the camber line apart from the trailing edge.

9.2.3. Polynomial fitted Camber line: Result

A polynomial fit is used to filter the camber line data points. It would be logical that this fit would accurately represent the entire camber line.

Validation In Figure 9.7, the polynomial fit (red) is fitted using the camber line points estimated with the previous tested methods. This method provided accurate results for the NACA 4412. As this method is used to calculate the error in sections 9.2.1 and 9.2.2. When the polynomial is used on the Nacra Hydrofoil data, the polynomial deviates significantly. With the green markers (x) indicating the leading and trailing edge, a difference can be seen in the top two images in Figure 9.7. In the bottom image, the deviation is seen more clearly. The current section is not the worst deviation observed using the polynomial fit.

Due to this deviation, this method cannot be used to estimate the full camber line and thus can be used for the final orientation.

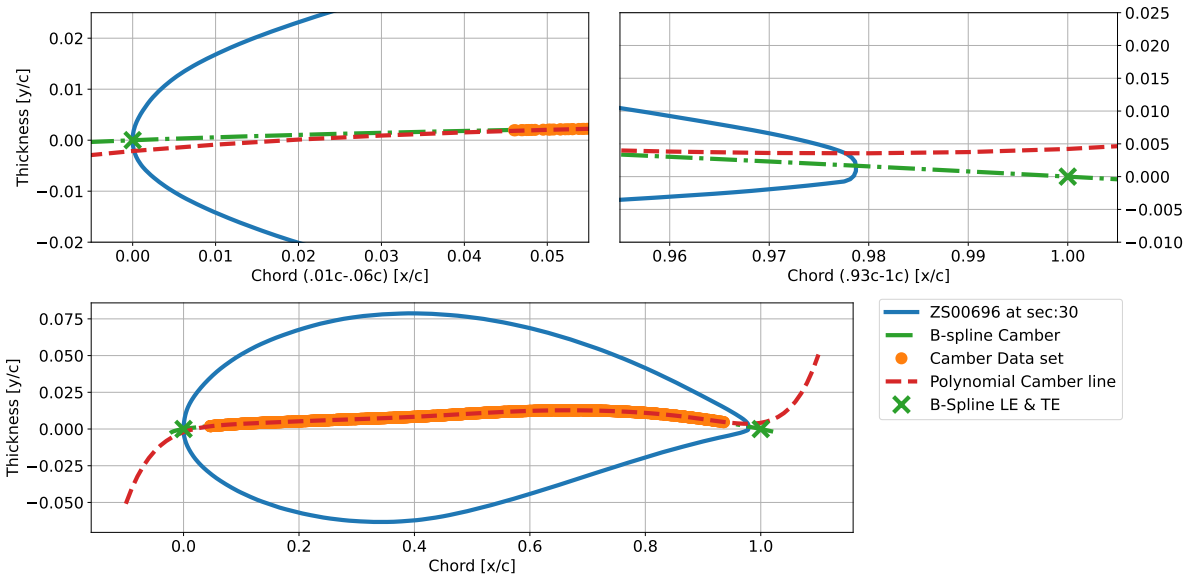

Figure 9.7: The fit of the Polynomial camber line (red) curves away from the camber line when extrapolating beyond the data set.

9.2.4. B-Spline fitted Camber line

The B-spline method is tested by applying the method on the NACA 4412 foil.

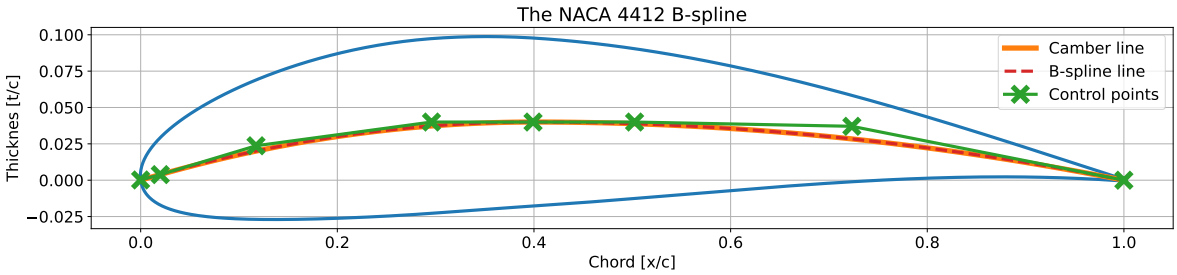

Figure 9.8: The B-spline camber line control points fitted to a NACA 4412

Validation: Camber line Spline The resulting B-spline fit can be seen in Figure 9.8. The control points follow the profile of the camber line. The red dashed camber line seems to match the camber line exactly. It does look like the B-spline can be fitted over the camber line.

Verification: Camber line Spline When subtracting the B-spline camber Y values from those of the actual camber line, the error shown in Figure 9.9 is obtained. The largest deviation is found at the leading edge of the profile. The error oscillates along the camber line between 3.0E-05. The error of the leading edge is given in Table 9.2 below.

The largest error is found in the estimation of the maximum camber position of a half-percent of the chord. The estimated camber location was determined to be 0.399 x/c while the actual point is set at 0.4 x/c.

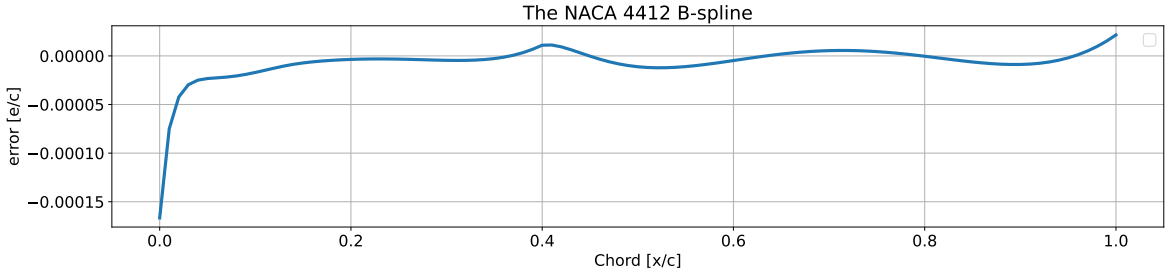

Figure 9.9: The B-spline camber line fit error for the NACA 4412

Table 9.2: The Camber B-spline error for the NACA 4412

Variable	Difference [d/c]	**error in % chord**
Leading edge	1.639e-04	-
Trailing edge	-3.579e-05	-
Chord Length	-1.588e-08	-1.588e-06 %
Maximum Camber	-1.093e-05	6.029e-03 %
Maximum Camber location	-9.452e-04	0.236 %

9.3. Data Smoothing

9.3.1. Error-calculation: Result

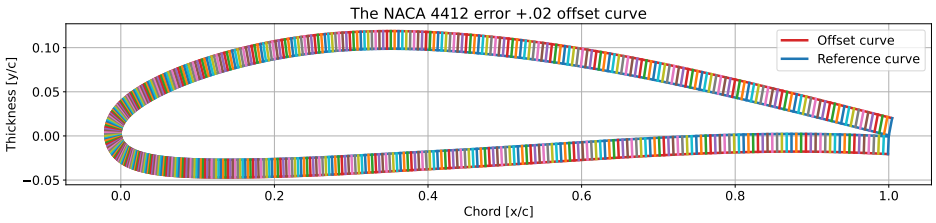

Figure 9.10: The error calculated on a curve that is offset by 0.02 in order to validate that no lines overlap and to calculate the accuracy of the method.

The error is calculated as the sum of all the lines shown in Figure 9.10. The red curve is off-set by 0.02% of the chord from the surface of the blue curve. This problem is comparable to the integral of the two surfaces. The result of the error should therefore be 0.02. The actual error is 0.02. When taking into account the whole value, the error of this method is 0.03323%.

9.3.2. Filter using signal processing: Result

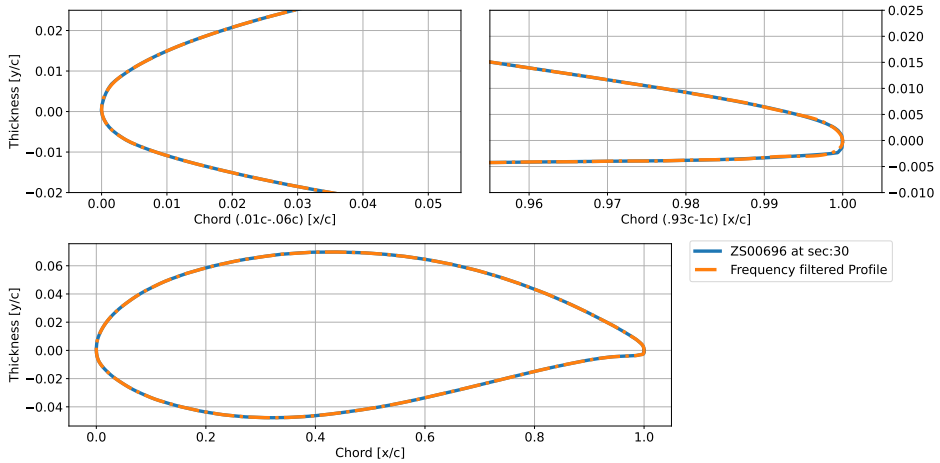

Figure 9.11: A Nacra Hydrofoil filtered with the low-pass filter (dash dot line) compared with the actual profile. With only a small deviation visible at the trailing edge.

Validation The profile data can be filtered by transforming the data to the frequency domain and filter by frequency or amplitude. That this is possible can be seen in Figure 9.11. The orange enclosed profile is filtered at a frequency of 197 Hz. The data in the frequency domain for this profile were shown in Figure 5.22b. The maximum frequency of the data was 46 kHz. The low pass filter at 197 Hz is placed just before the amplitude changes significantly. The filtered profile does seem to fit the actual profile fairly well.

Verification The filter location is a variable that needs to be optimised. If the filter is too aggressive, there is no data left to produce the foil section. If only a small part is filtered, the noise is still present and will affect the results of the solution. To show that there is an ideal filter frequency, the error and potential of the profile are plotted at different filter locations. The results of this analysis can be seen in Figure 9.12. For both the amplitude and the frequency filter a dip in the error result can be observed. For the frequency, the error of the profile dips to 0.0208 at 197 Hz. The error of the amplitude is lower

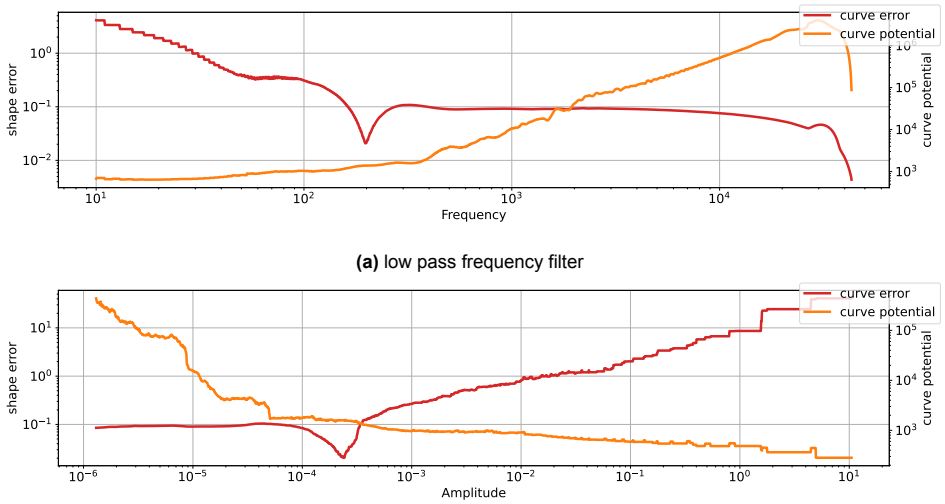

(a) low pass frequency filter

(b) high pass amplitude filter

Figure 9.12: The error and the curvature potential plotted over the low pass frequency and high pass amplitude filter

with 0.0204 at an amplitude of 2.407e-04. The potential of the curve at the optimum frequency filter location is 1389 while the amplitude reaches 1575 at this point.

It should be noted that the frequency,amplitude, error, and potential values are all arbitrary values that are highly dependent on the number of points and data locations in the profile. But for this one profile they can be compared. Thus, it seems that the frequency filter produces the smoothest profile with a small variation in the error. The results from the amplitude filter showed residual oscillations in the results. This can be the reason for the stepped results in both the error and the potential of the amplitude filter results in Figure 9.12b. The reduction of frequencies removed sharp corners from the results. This is likely the cause of the smooth curve seen in Figure 9.12a and the lower potential value.

9.3.3. B-spline fitting: Result

The profile can be estimated with B-spline interpolation. A small set of control points will be placed to form an equation that fits the data. The B-spline is first applied to the camber line.

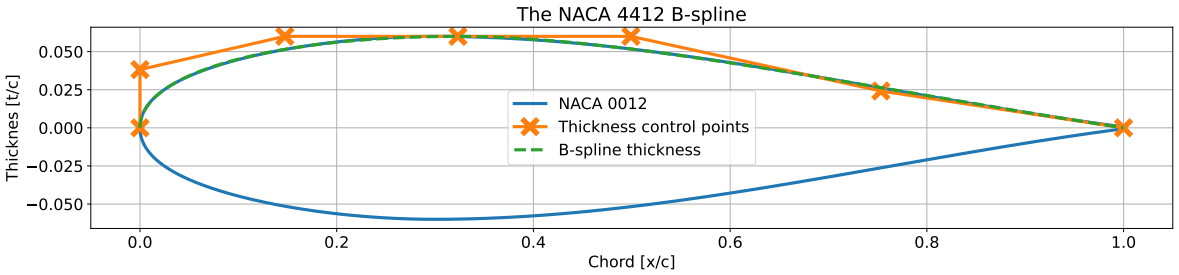

Figure 9.13: The B-spline Thickness profile control points fitted to a NACA 4412

Validation: Thickness Spline The B-spline can also be implemented for the thickness profile. The resulting fit of the B-spline to the extracted thickness of NACA 4412 can be seen in Figure 9.13. The symmetric version of the NACA 4412 foil is the NACA 0012 foil. This version is thus plotted in Figure 9.13 and will be used to further evaluate this spline fit.

At first site, the fit seems to follow the curve of the reference foil. The trailing edge point is used to fit the chord length in the Nacra Hydrofoils. This point seems to be positioned short of the actual chord length. The maximum thickness does seem to fit the actual point.

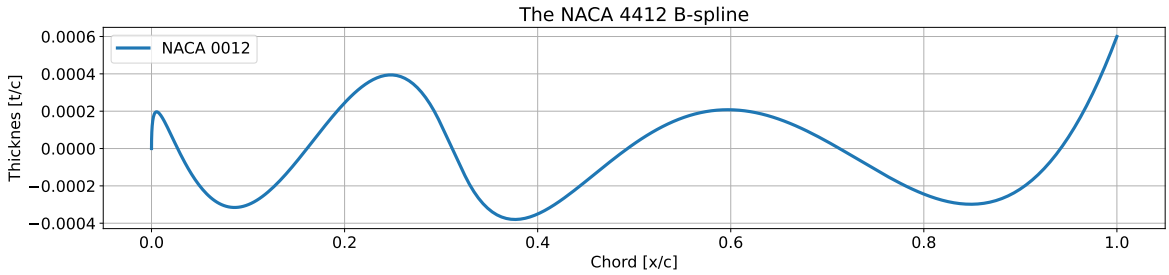

Figure 9.14: The error of the B-spline thickness fit plotted over the chord length showing small oscillation indicating a small reduction in complex shape, and a larger deviation at the trailing edge showing a reduction in fit accuracy.

Verification: Thickness Spline .0008 When normalising the y values, like the previous comparisons, the error is a bit higher compared to the other fits. The error oscillates around 8.0e-4 with a large increase at the trailing edge of 2.0e-3.

The control points are fitted to the shape variables. The X position of the last control point is free and will fit the chord length. While the control point at the maximum thickness point is fitted using the data extrapolated from the camber line. The error of these variables to the reference foil are given below (Table 9.3).

Table 9.3: The Thickness B-spline error for the NACA 4412

Variable	Difference [d/c]	**error in % chord**
Trailing edge	-3.579e-05	-
Chord Length	-2.220e-16	-2.220e-14 %
Maximum Thickness	6.166e-07	1.028e-03 %
Maximum Thickness location	0.0232	-7.740 %

These values are larger than those found before. The estimated chord length was found to be approximately 1 x/c. While the actual chord length is exactly 1. The maximum thickness for the reference was set to be 0.06 t/c or 0.12 t/c for both sides. The maximum thickness found for the reference foil was 0.06 t/c. While the spline found the maximum thickness of 0.06001. The maximum thickness location for the NACA foils is approximately 0.3 x/c. The maximum thickness location found for the reference foil was 0.302. The maximum thickness location fitted with the B-spline was 0.322.

The B-spline seems to provide accurate estimations of the NACA 4 series profile.

10

Geometric deviation analysis: Results

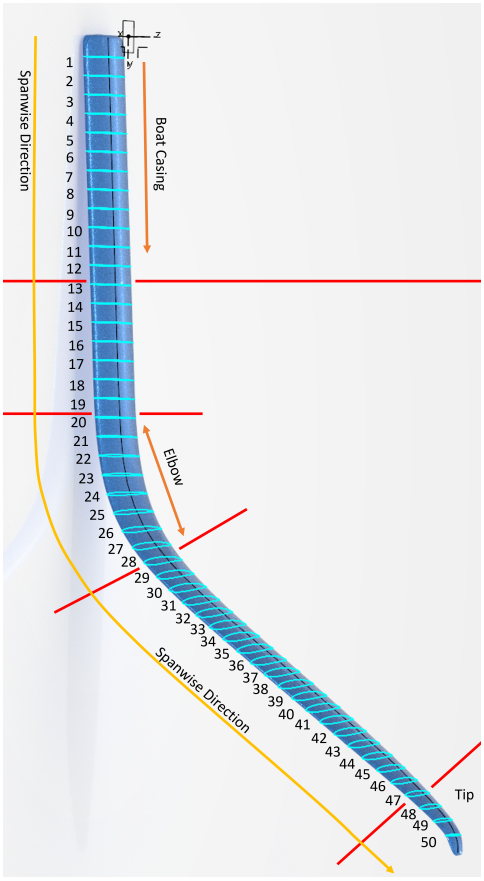

Figure 10.1: An overview of the Nacra hydrofoil showing the location of the different sections combined with the terminology that is used to describe the different parts of the Hydrofoil.

This chapter will evaluate the results obtained using the methods described in section 6.2. The goal of the chapters describing the "*Geometric deviation analysis*" is to identify the magnitude of the differences in shape between the hydrofoils. Before a comparison can be made. The method needs to be validated if the output is obtained. This validation is described in section 10.1. section 10.2 identifies if the methods produced accurate results by means of verification. The methods are confirmed to provide good results, so they can be compared in the next steps.

In order to compare the hydrofoils, the shape is deconstructed into different parameters. These parameters are the maximum camber (y_c) and its location (x_c), the maximum thickness (y_t) and its location (x_t), and the leading edge radius (r_{le}). After comparing each parameter, the correlation between the parameters is evaluated.

Finally, the theory that the polynomial camber line fit can identify mould misalignment is analysed in the final section (10.4).

10.1. Validation

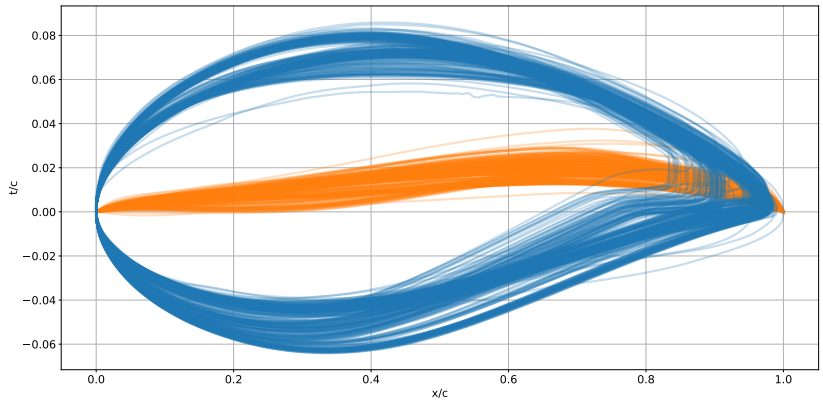

Figure 10.2: Macro validation of the foil placement to identify large placement errors, plotting the profile data in blue and the camber line in orange.

The first validation of the processing is shown in Figure 10.2. The figure shows all the hydrofoil sections plotted in the same plot. If there was a foil that did not align properly, it would show up in this graph. All camber lines properly intersect the t/c = 0 line at the 0 and 1 x/c points. All leading edges are positioned on the origin with the trailing edge at the right-hand side. This indicates that the process performed correctly.

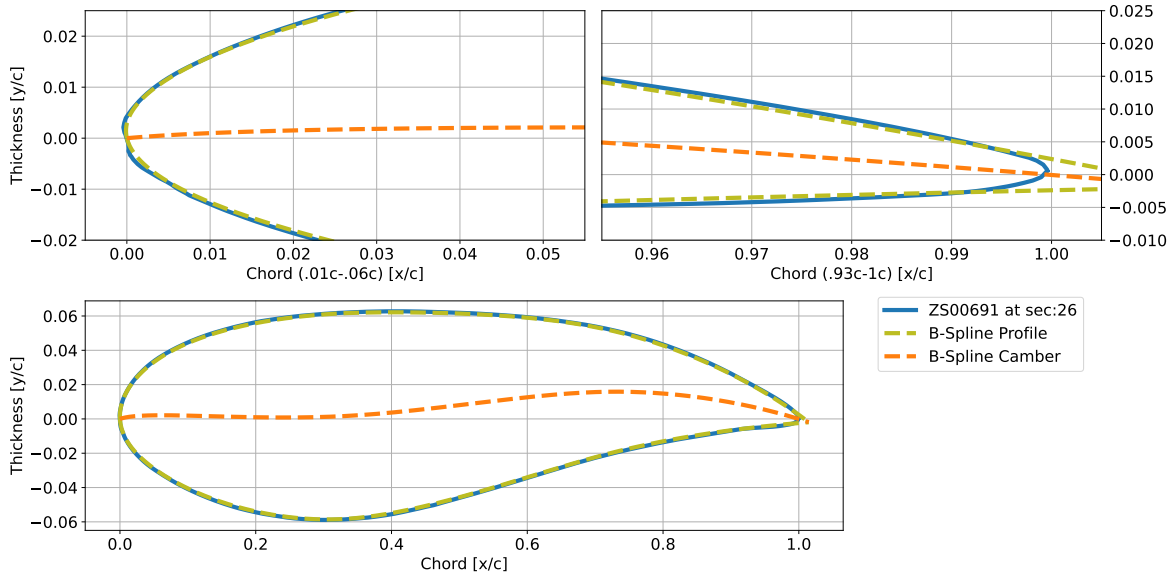

Figure 10.3: The profile ZS00691 at section 26 with the mean camber B-Spline (orange) and the B-Spline profile (green) overlaid of the profile data extracted from Catia.

When observing the B-Spline fit of the profile ZS00691, section 35. The fit of the B-spline produced a relatively good approximation of the profile. There is a slight shift visible at the trailing edge in the top right image. The trailing edge is more rounded compared to the B-Spline fit. The two curves match when observing the complete profile in the bottom image. Even the fit at the leading edge (top left) seems to follow the curve accurately. The B-Spline fit seems to fit the profile. Especially since this is a profile is the outlier with respect to accuracy according to Figure 10.4a.

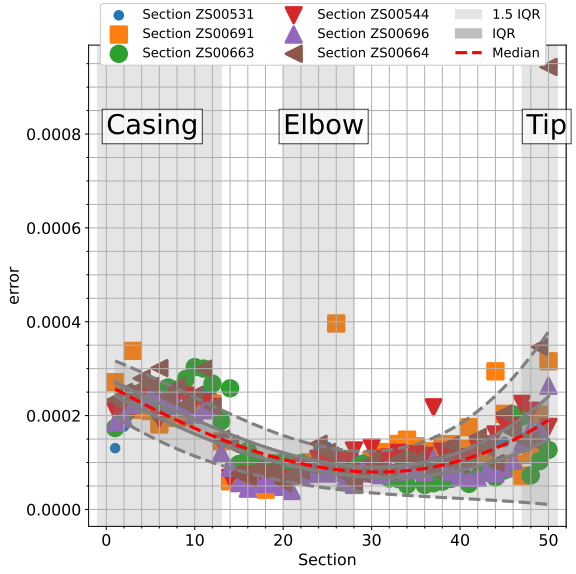

(a) Error of the B-spline fit plotted along the chord, identifying the the accuracy of the fit and possible outliers.

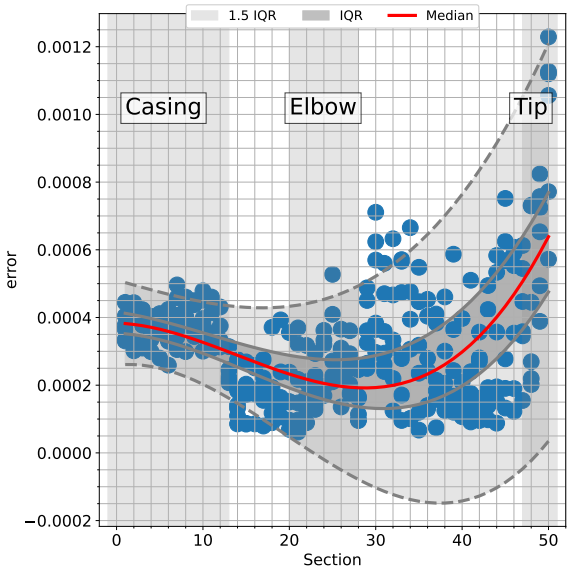

(b) Error of the BP3333 B-spline fit along the span showing the accuracy and precision of the fit.

10.2. Verification

For a better understanding of the accuracy of the program, the B-spline fit error is plotted in Figure 10.4a along the span. The plot shows that the accuracy of the fit seems to be good. With the average error not exceeding 0.0004c. When converting this accuracy to the actual profile. The fit error is (0.0004c * 200mm =) 0.08 mm. There are two sections that produced an error that exceeded 4e-4c. These are ZS00691, Section 26 and ZS00664, Section 50. When observing the ZS00691 foil section, in Figure 10.3 the error seems to be located primarily at the trailing edge. This area is not as critical compared to the leading edge for the alignment and fluid dynamic analysis.

A distinct step in the produced errors can be observed in Section 12. This step in error is likely caused by the change in shape in Section 12. Before this section, the trailing edge is widened to provide good support against the casing of the boat that holds the hydrofoil in place. The sections above are hard to fit as the trailing edge widens and distorts the results of the thickness profile fit.

Figure 10.4a show's the 25th percentile range in dark grey and the 1.5 quartile range in light grey. The line indicating this range is smoothed to provide an understanding of how it progresses along the pan. The quartile and 1.5 quartile ranges for the following comparisons are not filtered as a comparison. The error can be seen to be stable after Section 12 up to Section 40. After Section 40 the error starts to increase again. The increase in error seems to follow the reduction in the chord length that starts at Section 35. The chord length slowly reduces from 200 mm at Section 35 to 80 at Section 50. This reduction in chord length could increase the impact of the accuracy of the scanner. The same increase in uncertainty can be seen in the error of the BP3333 spline fit (Figure 10.4b).

The leading edge is fitted with a separate spline using the B-Spline parameterisation method BP3333. The resulting error from this method is shown in Figure 10.4b. The resulting error is slightly higher compared to the fit shown in Figure 10.4a. The method for calculating the error is also different. The difference cannot be directly compared. The spread of the error appears to be higher with the BP3333 spline, indicating a reduced precision.

The accuracy and precision of the results are found to be good for further analysis.

10.3. Results of the Shape Parameters

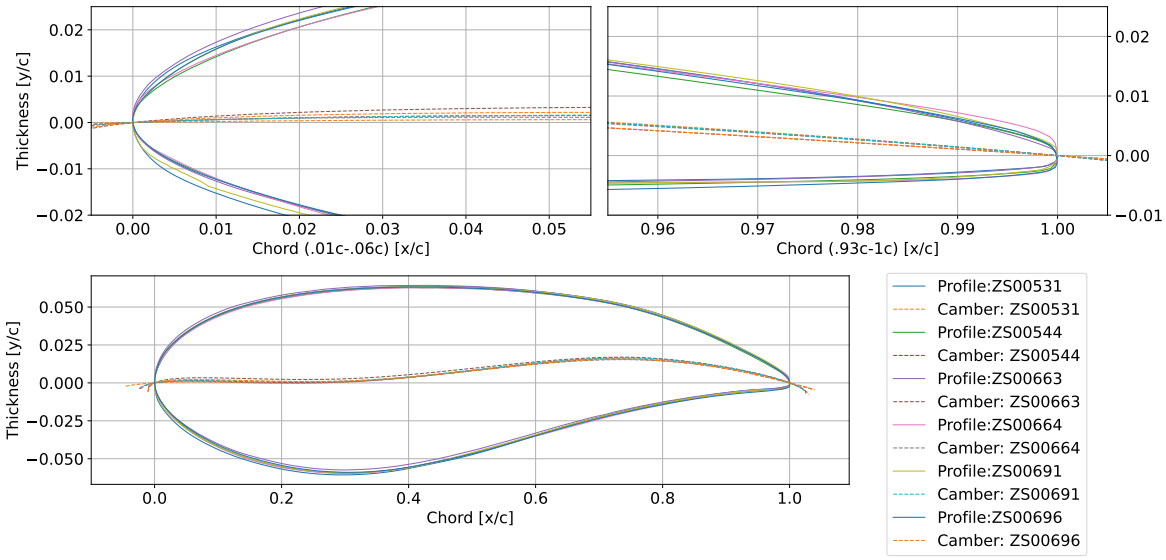

Figure 10.5: A picture showing all 6 different hydrofoils at section 35. It visualises the differences in shape at the leading edge (top-left), trailing edge (top-right), and the general shape (bottom).

With the foil sections correctly aligned, the differences between the sections can be seen in Figure 10.5. The leading edges differ in curvature as can be seen in the top left image. A variation in trailing edge thickness resulted in a slight change of the length from the leading edge to the end of the profile data (top right image). The sections themselves are very similar when compared in the overview image (bottom). A slight shift in the camber line can, however, be observed (bottom).

For a better comparison between the hydrofoils. The maximum thickness (y_t) and its location (x_t), the maximum camber (y_c) and its location (x_c), and the leading edge radius are compared between the hydrofoils along the span in the following sections. This is followed by checking if there is any correlation between a set of shape parameters of the hydrofoils.

10.3.1. Maximum Thickness location

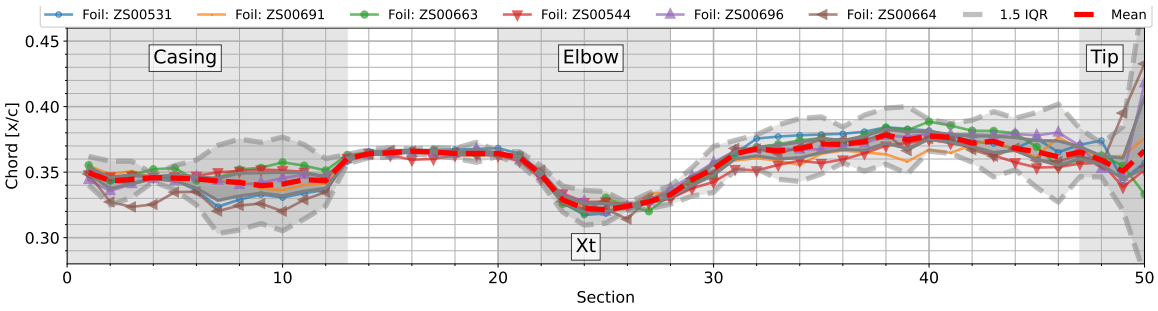

Figure 10.6: The variability of the Maximum thickness location (x_t) along the span showing that different shapes are used above the elbow (0.36/c), at the elbow (0.32/c) and below the elbow (0.37/c)

The variation in thickness along the hydrofoil span is plotted in Figure 10.6. The thickness location on the chord varies along the profile span. The part above the elbow is located at around 0.36 x/c. While this moves forward after Section 20. The most forward position of the thickness location is around 0.32 x/c. After Section 30 the location stabilises again at around 0.37 x/c. The standard deviation does start to increase after Section 28. The results finally start to deviate significantly at the last 2 sections (49-50).

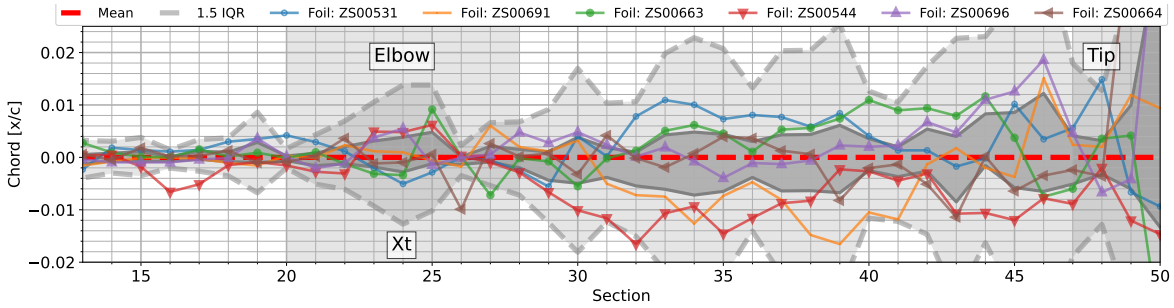

Figure 10.7: The difference between the Maximum thickness location (x_t) of each hydrofoil highlighted by normalising the data around the mean and plotted over the span by the sections.

Table 10.1: The sum of the deviation of the thickness location between section 13 (bottom of the boat) and 47 (start of tip) as shown in Figure 10.7. Highlighting the trend of a given hydrofoil.

Foil code	Plot colour	Side	Deviation as % of the chord [x/c]
ZS00531		Starboard	0.0940
ZS00691		Starboard	-0.0848
ZS00663		Starboard	0.0705
ZS00544		Port	-0.180
ZS00696		Port	0.0792
ZS00664		Port	0.0333

The comparison of the different hydrofoils over the span is better visualised in Figure 10.7. The first 13 sections are removed from the visualisation. These sections are located in the boat and do not affect overall performance. The location of each foil is normalised with the mean thickness location that was found in Figure 10.6. The increase in the standard deviation is now even more prevalent after Section 28. The interquantile range (light grey) seems to increase in area after section 28.

Observation of different hydrofoils, the ZS500544 (in red) hydrofoil can be seen deviating from the set at section 28. After this point, the thickness locations are more forward compared to the other hydrofoils. The thickness remains more forward along the span. The other hydrofoil that deviates forward is ZS00691 (in orange). This deviation is mostly between sections 31 and 44. After 44, the locations start to oscillate around the mean.

The hydrofoils ZS00664 and ZS00696 seem to be positioned closest to the mean along the span. The ZS00664 (in brown) results are more stable along the span. It starts to deviate significantly at the tip from Section 46. ZS00696 (in purple) fits in the interquantile range for most of the span. After Section 41 the thickness moves more aft over the chord compared to the mean. The hydrofoil ZS00531 (in blue) presents a less stable position compared to the mean. It is mostly positioned in the interquantile range along the span. It does tend to show a more aft location, especially after Section 32.

The position of ZS00663 (in green) seems to be the least stable of the set. This is mostly true up to Section 28. After this section, the location steadily moves aft compared to the mean.

If the sum of the deviations for each hydrofoil is taken between Sections 13 and 47, the following results can be observed (Table 10.1). The data contribute to the observation from Figure 10.7. The hydrofoils ZS00531 and ZS00664 are located more aft compared to the mean. The foil ZS00696 reports an even higher number, while this is not observed by visual inspection of Figure 10.7. The hydrofoil deviates backward after Section 42. This might be enough to skew the results. The ZS00544 and ZS00691 foils are normally lower compared to the mean. This can be observed in Figure 10.7.

10.3.2. Maximum Thickness

The results of the maximum thickness are multiplied by 2. This will make the results comply with the measurement scheme used to identify the foil parameters. For the maximum thickness in Figure 10.8, the same step can be seen as found in Figure 10.6. After section 20, the thickness decreases from

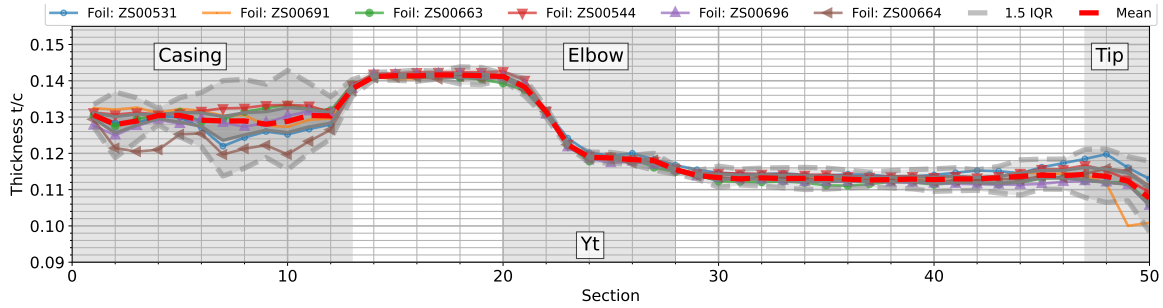

Figure 10.8: The variability of the Maximum thickness (y_t) along the span showing that different shapes are used above the elbow (0.142/c), at the elbow (0.119/c) and below the elbow (0.113/c)

around 14.2 % to 11.3 %. A small step can be observed between Sections 24 and 26. The thickness stabilises here around 11. 9%. The last two sections, at the tip, are more slender, as all hydrofoils decrease in thickness percentage. This is expected as a winglet like the tip of the Nacra Hydrofoil is usually a slender symmetric section. Its purpose is to reduce the tip vortex. This is created by the generation of lift.

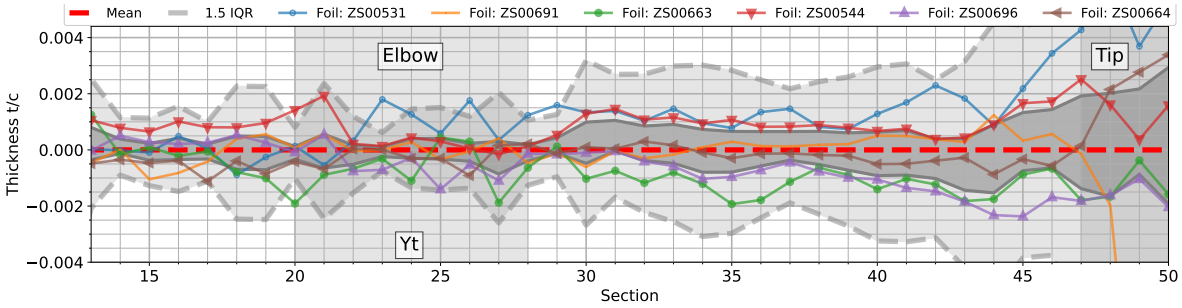

Figure 10.9: The difference between the Maximum thickness (y_t) of each hydrofoil highlighted by normalising the data around the mean and plotted over the span by the sections.

When normalising the data around the mean, the results look as shown in Figure 10.9. The widening of the interquantile range after section 28 is even more noticeable in this view. The results for the thickness are more stable for the individual hydrofoil compared to the thickness location in Figure 10.7. There is some variability before Section 28. But after this point, the different lines are more clearly separated.

The hydrofoil with the greatest thickness is found to be ZS00531. This is closely followed by ZS00544. They are approximately 0. 00175 % thicker compared to the mean at sections 30 and 31. The thickness of the mean at Section 31 is approximately 11.29 % of the chord. Therefore, these hydrofoils are 11.29175 % of the chord length thick. The chord length is approximately 200 mm of the sections. That means that the variation in thickness is 0.35 mm. Thus, these differences are very small on the actual hydrofoils.

The hydrofoils ZS00663 and ZS00696 are shown to be on the thinner side compared to the set of hydrofoils. When observing the results in Table 10.2. This difference is confirmed. The ZS00664 and ZS00691 are neatly in the middle of the range. The ZS00691 shows a higher value in Table 10.2, but this could be explained by the large deviation at the tip.

It is interesting to note that the hydrofoil ZS00544 showed the location of the thickness to be the most forward of the set of hydrofoils. While ZS00531 showed the location of the thickness to be moved more aft compared to the mean. This seems to indicate that there is no correlation with thickness and thickness location.

Table 10.2: The sum of the deviation of the thickness between section 13 (bottom of the boat) and 47 (start of tip) as shown in Figure 10.9. Highlighting the trend of a given hydrofoil.

Foil code	Plot color	Side	Deviation as % of the chord [t/c]
ZS00531		Starboard	0.0370
ZS00691		Starboard	0.0021
ZS00663		Starboard	-0.0293
ZS00544		Port	0.0305
ZS00696		Port	-0.0225
ZS00664		Port	-0.0101

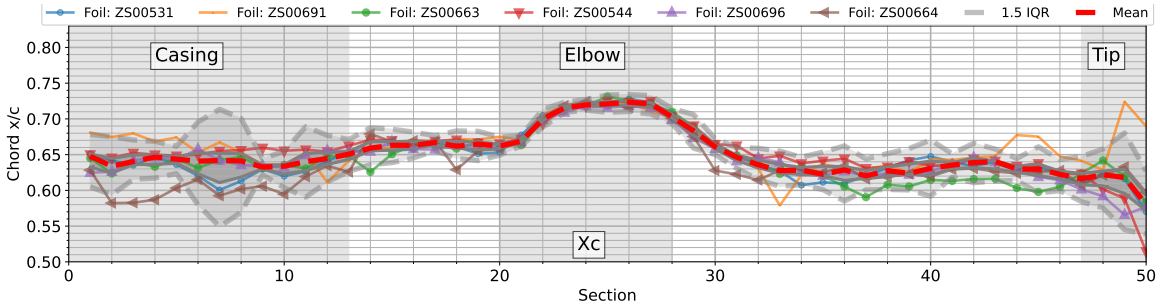

Figure 10.10: The variability of the Maximum camber location (x_c) along the span showing that different shapes are used above the elbow (0.66/c), at the elbow (0.72 x/c) and below the elbow (0.63/c)

10.3.3. Maximum Camber location

The same trends can again be observed in the location of the maximum camber plotted in Figure 10.10. There is a change in values between Section 20 and 28 (the elbow). The values in the top part between sections 14 and 20 stabilise at a chord location of 0.67 x/c. The value stabilises again after the elbow in Section 28. With uncertainty increasing at the tip. After Section 21 this increases in an arc up to 0.0.73 x/c at Section 25. After section 25 the arc continues downward up to section 32. After Section 32, the location of the hydrofoil varies between 0.62 x/c and 0.64 x/c.

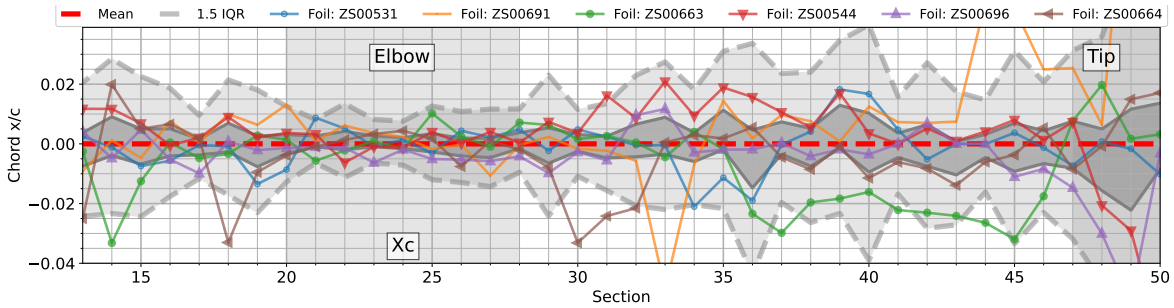

Figure 10.11: The difference between the Maximum camber location (x_c) of each hydrofoil highlighted by normalising the data around the mean and plotted over the span by the sections.

For the more detailed plot in Figure 10.11, the same increase in the IQR area can be observed. Unlike the data that were shown before, the camber location is very unstable and the differences are relatively small. According to Table 10.3, ZS00531 and ZS00696 are following the mean. The ZS00531 seems to follow the mean line along the entire span. ZS00696 does show the camber moving forward at section 47 (the tip) and onwards. These observations are verified by the results in Table 10.3.

ZS00664 and ZS00663 both show larger negative (forward) values in Table 10.3. When comparing these results with those shown in Figure 10.11. ZS00664 appears to follow the mean of the hydrofoils well along the span. It deviates forward at Sections 17 to 20, and 29 to 33. The ZS00663 hydrofoil appears to follow the mean along the span in Figure 10.11. The value in Table 10.3 shows a larger offset to the front. This deviation is generally observed in Figure 10.11 between Sections 35 to 47.

Table 10.3: The sum of the deviation of the thickness between section 13 (bottom of the boat) and 47 (start of tip) as shown in Figure 10.11. Highlighting the trend of a given hydrofoil.

Foil code	Plot colour	Side	Deviation as % of the chord
ZS00531		Starboard	-0.0263
ZS00691		Starboard	0.174
ZS00663		Starboard	-0.278
ZS00544		Port	0.214
ZS00696		Port	-0.084
ZS00664		Port	-0.179

However, this is the majority of the lower part of the hydrofoil. It is in part the section of the hydrofoil that is always providing the lift.

There are two hydrofoils that tend to have the camber located more aft on the sections. These are ZS00691 and ZS00544. The results of the ZS00544 follow the mean line for the first part along the span. The results tend to move aft between sections 30 and 40. The results of the ZS00691 hydrofoil show some significant outliers at sections 33, 44, 45 and after 49. The results apart from those values follow the mean relatively well. The values move slightly aft between Sections 34 to 43.

10.3.4. Maximum Camber

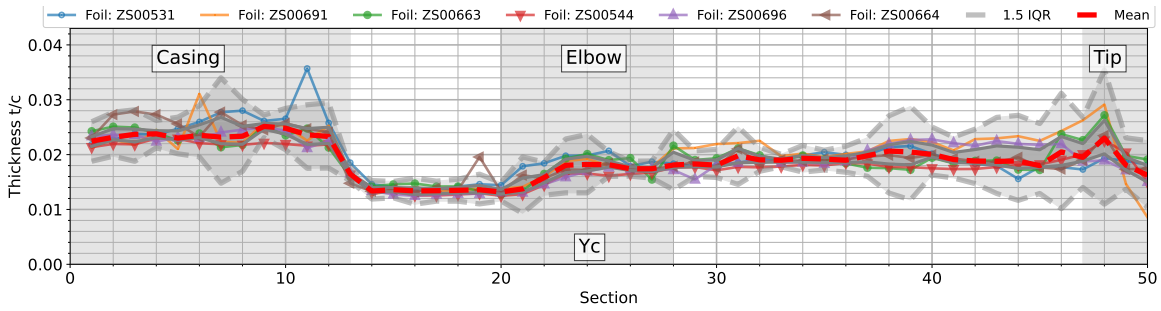

Figure 10.12: The variability of the Maximum camber (y_c) along the span showing that different shapes are used above the elbow (0.014/c), at the elbow (0.018/c) and below the elbow (0.02/c)

For the maximum camber, two distinct regions are visible in Figure 10.12. The camber before the elbow and after. Before the elbow the camber thickness is 0.013 t/c or 1.3%. While the camber thickness after the elbow variate between 0.021 t/c and 0.017 t/c. A larger camber is observed at the tip. This is surprising as wing tips are usually more symmetric in shape resulting in a lower camber thickness. It is clear that the uncertainty of the camber thickness starts to increase after the elbow, as was observed in all other metrics.

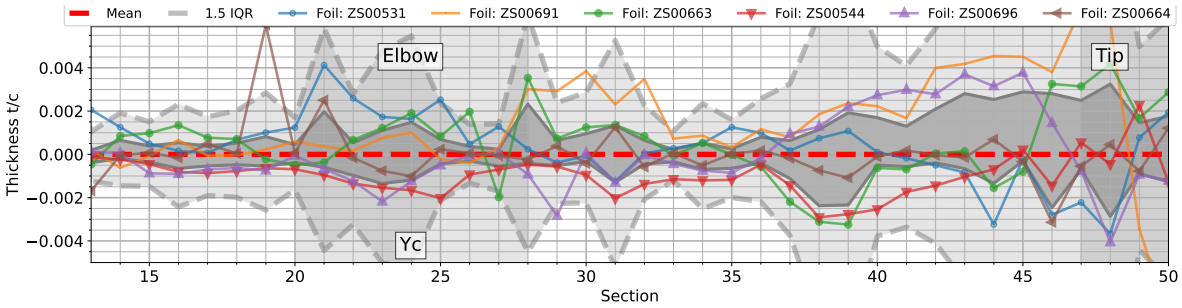

Figure 10.13: he difference between the Maximum camber (y_c) of each hydrofoil highlighted by normalising the data around the mean and plotted over the span by the sections.

When observing the normalised data in Figure 10.13. The hydrofoil ZS00544 stands out below the mean. This is influenced by the summarised data shown in Table 10.4. The highest maximum camber

Table 10.4: The sum of the deviation of the camber location as shown in Figure 10.13.

Foil code	Plot colour	Side	Deviation as % of the chord
ZS00531		Starboard	0.0151
ZS00691		Starboard	0.0582
ZS00663		Starboard	0.00965
ZS00544		Port	-0.0384
ZS00696		Port	-0.00744
ZS00664		Port	0.000246

can be seen in the hydrofoil ZS00691. This hydrofoil is significantly above the mean between sections 27 to 48. This results in a higher value in Table 10.4. The second foil with a higher maximum camber, according to Table 10.4, would be ZS00531. This hydrofoil can be seen mainly above the mean at the elbow. During most of the span, the maximum camber is around the mean value.

ZS00696 can be seen increasing in camber after section section 36 until section 45. Due to the lower camber at the root of the hydrofoil, the value in Table 10.4 is relatively small. The last two hydrofoils are all similar to the mean camber along the span of the hydrofoil.

10.3.5. Leading edge radius

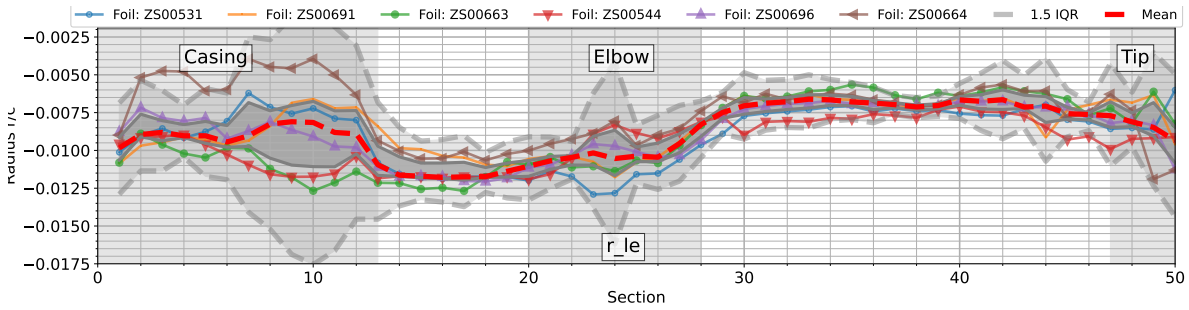

Figure 10.14: The variability of the leading edge radius (r_{le}) along the span showing that different shapes are used above the elbow (0.0124/c), at the elbow (0.0101/c) and below the elbow (0.0073/c)

The leading edge radius variability is shown in Figure 10.14. With every part the leading edge becomes sharper. As a smaller radius indicates a sharper leading edge. The radius starts at 0.0124 r/c and decreases to 0.0073 r/c. The uncertainty does not seem to increase as much as with the previous parameters. Although a larger spike of variability can be seen around section 26 in the elbow.

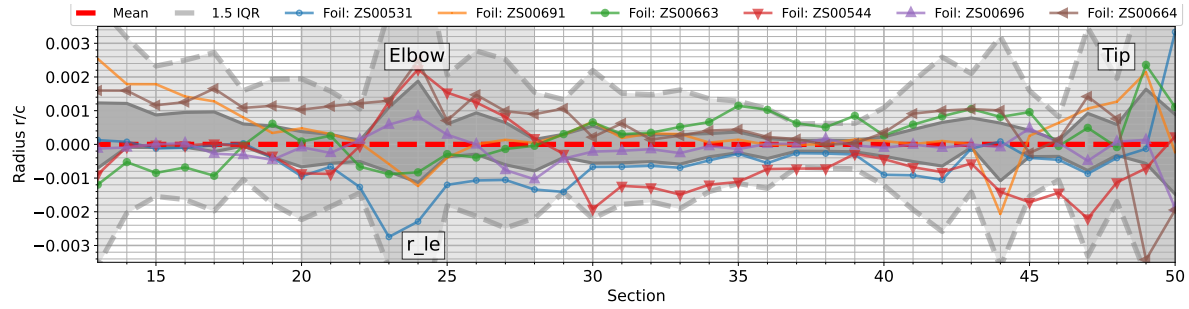

Figure 10.15: The normalised variability in the leading edge radius (r_le) along the hydrofoil span

For normalised data, ZS00554 and ZS00531 stand out as having a larger radius leading edge. This larger radius is particularly seen after Section 30 for the Hydrofoil ZS0544. The leading edge of the hydrofoil ZS00531 is more round at the elbow. These observations are complemented by the larger comparative negative values in Table 10.5.

Table 10.5: The sum of the deviation of the leading edge radius as shown in Figure 10.15.

Foil code	Plot colour	Side	Deviation as % of the chord
ZS00531		Starboard	-0.0107
ZS00691		Starboard	0.00610
ZS00663		Starboard	0.00993
ZS00544		Port	-0.0231
ZS00696		Port	-0.00664
ZS00664		Port	0.0283

The sharpest average leading edge, according to Table 10.5, should be ZS00664. The leading edge can be seen above the mean from the root to section 30 just past the elbow. The hydrofoils ZS00691 shows the same sharper leading edge at the root, but these differences are less distinct.

The subsequent hydrofoils are all similar to the mean leading edge values along the span.

10.3.6. Shape parameters Correlation

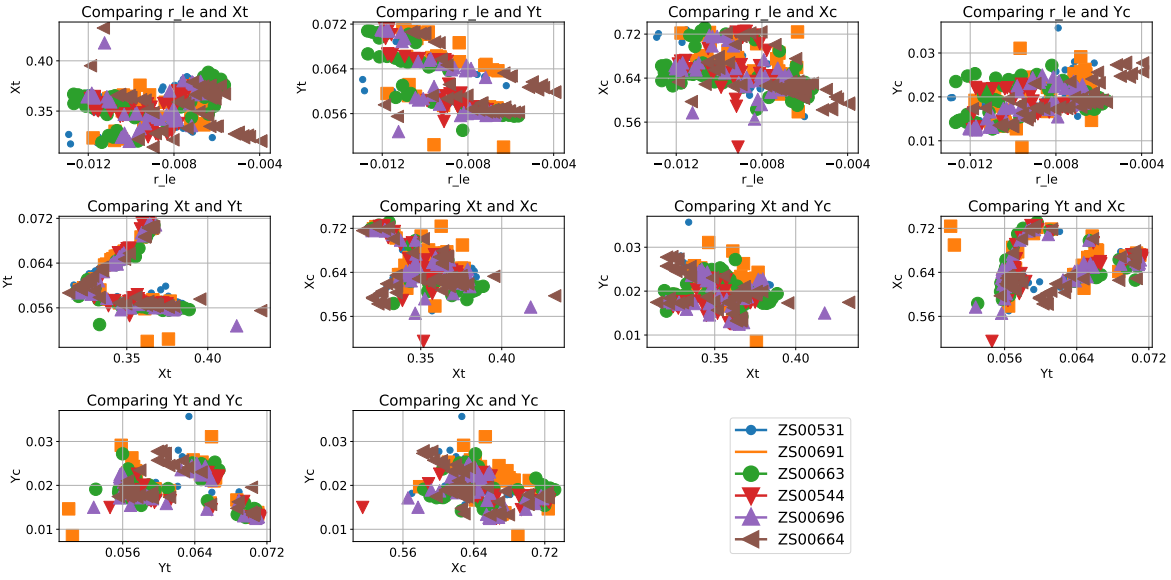

Figure 10.16: Different plots showing if a correlation between one of profile parameters exists.

When comparing each of the previously described shape parameters with each other. The scatter plots shown in Figure 10.16 are obtained.

In the comparison between the maximum thickness (y_t) and the maximum thickness location (x_t) a v shape can be observed. The maximum thickness (y_t) and the location of the camber (x_c) are formed into two curved lines. There could be a linear correlation between the radius of the leading edge (r_{le}) and the maximum thickness (y_t). In this plot, the data seems to be located on three different lines. The plots that are not yet mentioned, all seem to show one big cloud of points.

The three lines of the leading edge and maximum thickness plot seem to suggest that these shapes are a result of the 3 different profiles that are used in the hydrofoil design.

10.4. Results of polynomial camber line fit as an indicator for mould miss-alignment.

The polynomial fit was not found to be a good approximation of the camber line in subsection 9.2.3. When validating this approach, it was noticed that either the leading or trailing edge extended upwards.

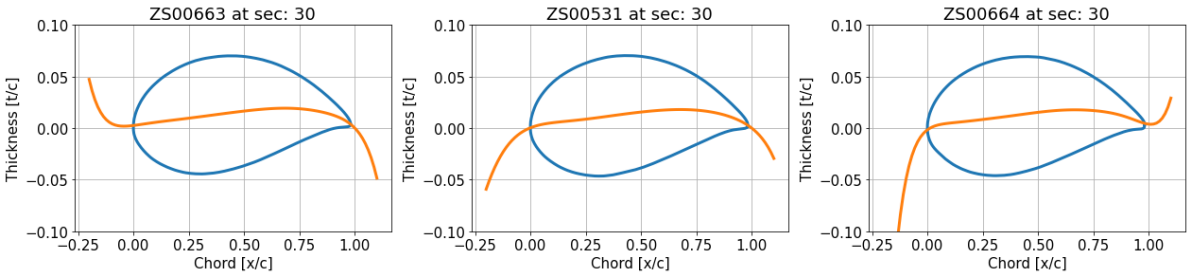

(a) Denoted by -1 **(b)** Denoted by 0 **(c)** Denoted by 1

Figure 10.17: Showing how the polynomial Camber line can deviate upwards at the leading edge (Marked by -1), upwards at the trailing edge (Marked by 1), or both extend downwards (Marked by 0).

Never did both extend upwards. Due to the positive camber, the camber line is expected to extend downwards at both ends.

With only one end that extends upward, this could be an indication of the misalignment of the moulds. The polynomial camber line was given a number using the method shown in Figure 10.17. When applying this to all sections, the table (Table C.1) shown in Appendix C. The first 13 sections, which are located in the boat, mostly show the trailing edge extending upwards. This could be explained by the thickened trailing edge that provides good support in the hydrofoil casing.

This tendency to move upward can be seen in the first row of Table 10.6. When averaging the data past Section 13, the data is approaching 0.

Table 10.6: The sum of the sections sections shown on the right with a section given (-1) with the leading edge extending upwards, (1) with the trailing edge upwards, and (0) with both extending downwards.

Section	ZS00531	ZS00544	ZS00663	ZS00664	ZS00691	ZS00696
0 - 13	0.92307692	1	1	0.84615385	0.38461538	1
13 - 50	0.02702703	-0.1081081	-0.1891892	0.18918919	-0.2702703	0.02702703

However, the data in section 13 is showing an interesting result. Both ZS00696 and ZS00531 show values close to 0. For hydrofoil ZS00531 most of the values are equal to 0 as well. The hydrofoil ZS00696 starts with a larger number of (1)'s, followed by an almost equal number of (-1)'s. While most values for ZS00691 are (0), all deviating camber lines deviate up at the leading edge.

It can be seen that the data do not show a clear trend. But it seems to be a slight indication that there are differences in this area between the hydrofoils.

11

2D section hydrodynamic analysis: Results

11.1. Results of the Friction Coefficient Analysis

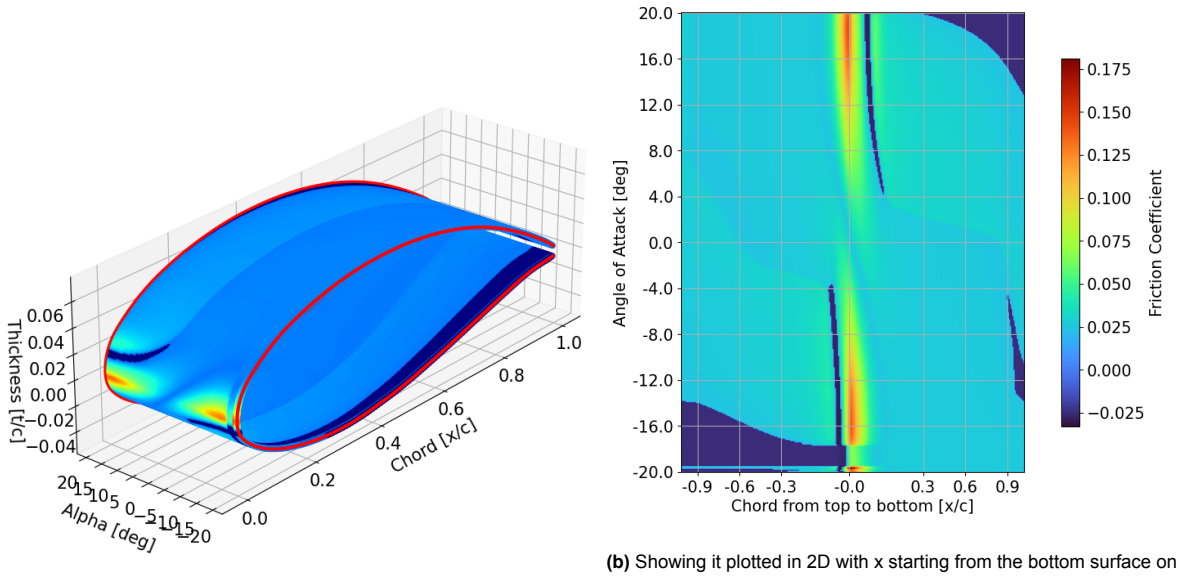

(a) Showing it Plotted on a foil section

(b) Showing it plotted in 2D with x starting from the bottom surface on the left.

Figure 11.1: The friction coefficient plotted for the Nacra hydrofoil ZS00544 at section 35. With the friction coefficient offset below zero, highlighting the location of the flow separation on the surface.

The friction coefficient (c_f) on top of a 3D profile is shown in Figure 11.1. The dark blue area's show the location where the friction coefficient is negative. This corresponds to the area of separated flow. Figure 11.1a shows how the separation at the leading edge moves forward when the angel of attack increases (right to left). The dark part on the bottom right shows the stall of the section at negative 20 AOA. The leading edge experiences high friction as the air curves past the leading edge. This would also be the area where the pressure coefficient is high.

The 3D representation helps to gain an intuitive understanding of where the separation of flow is occurring. It covers a large part of the section. This prevents one from observing the whole surface to see how the separation develops. The surface of the profile can be plotted on a flat plane using the same

colours. This representation is shown in Figure 11.1b. The angle of attack is now located on the y-axis and spans 20 degrees (top) to -20 degrees (bottom). The profile is not as clear in this representation. The bottom surface starts at the trailing edge at chord -1 (left). With the leading edge in the middle at chord 0 and finally the top trailing edge at 1 (right). In this representation, the development of the stall can be clearly seen as the separated flow moves from the trailing edge towards the tip at (alpha<-13 , lower surface)(alpha <12, upper surface).

Small areas of laminar separation visualised by the thin blue strips near the leading edge. The flow separates in the dark blue area and attaches to the surface again afterward. A small region of laminar separation can be seen on the top trailing edge surface after -4 AOA.

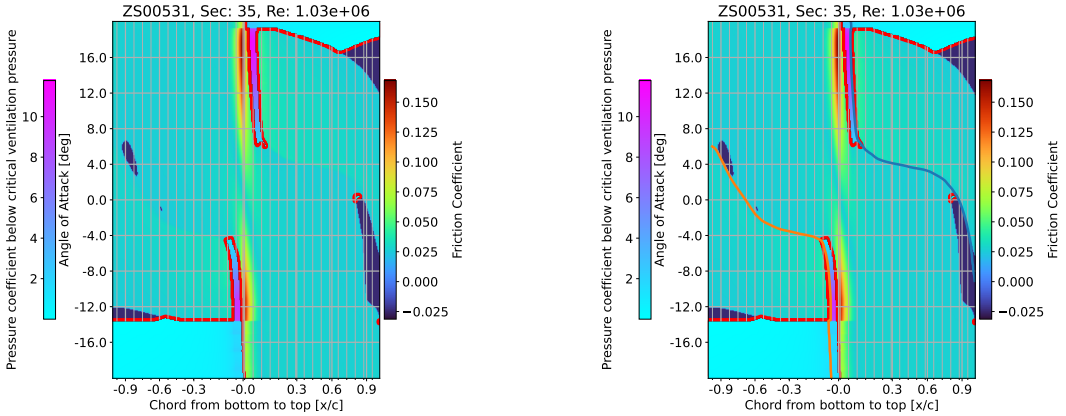

(a) The critical pressure region

(b) The critical pressure with the flow transition plotted on top

Figure 11.2: The Friction coefficient for ZS00531, Section:35 at Reynolds number 1.03e06 shown with the critical pressure for the onset of ventilation plotted in the red encircled area. The flow transition is plotted on top to show how the turbulent transition develops over different AOA

The figure can be enhanced with the addition of the critical ventilation pressure coefficient Figure 11.2. As ventilation requires both a separated flow and a pressure below ambient air pressure, this is the only area where the pressure is plotted. The area is highlighted by a red line (Figure 11.2a).

The flow region separated at the leading edge is critical. Pressure is always below ambient pressure, allowing ventilation. A small section of the separation at the trailing edge can also be seen. At 0 angle of attack, the section might ventilate at this Reynolds number linked to 10 knots of boat speed.

That these area's are laminar flow separation can be seen in Figure 11.2b. In this plot, the flow transition from laminar to turbulent is shown by the orange (lower surface) and blue (upper surface) lines. The lines are behind the separated region when looking from the leading edge. Therefore, the laminar flow separates, transitions to turbulent, and reattaches to the surface.

The figures 11.3a to 11.3c shows the surface at the different Reynolds numbers. The speed of the flow does affect the separation significantly.

When observing the stall of the foil, shown by the large separated regions on the top and bottom of the figures in Figure 11.3, the region decreases in size with increasing Reynolds numbers. Higher speed flow can adhere better to the surface. The same observation can be seen in the thin strips of separated flow at the leading edge. The width (along the chord) of this region decreases with increasing Reynolds numbers. However, the initial AOA of initiation does not change with the Reynolds number. It can only be seen to move away from 0 AOA by approximately a degree.

The separated flow at the trailing edge almost disappears at the highest Reynolds number. The region moves more aft on the chord. The initiation of the separated region only appears at higher angles of attack with increasing Reynolds numbers.

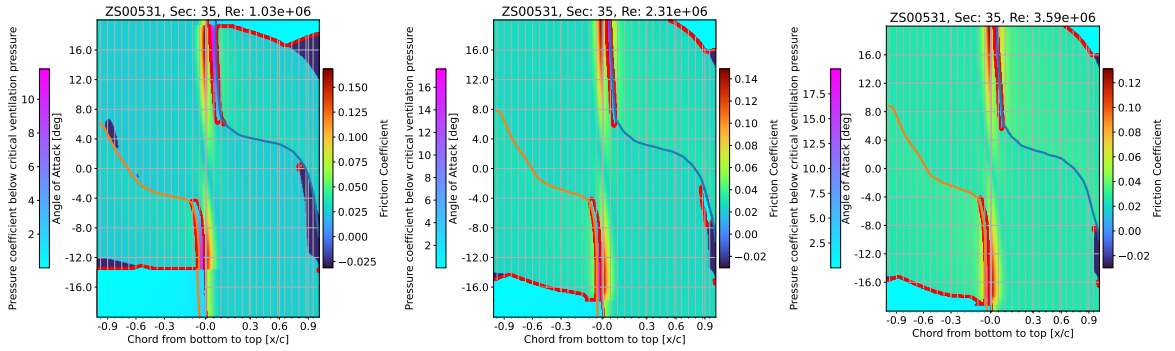

(a) Reynolds number: 1.03 e6 or a speed of 10 knots

(b) Re of: 2.31e6 or 22.5 knots

(c) Re of: 3.59e6 or 35 knots

Figure 11.3: The friction coefficient plotted for ZS00531, Section: 35 at different Reynolds numbers with the critical ventilation pressure highlighted in the red enclosed area and the laminar to turbulent flow transition shown with the blue (upper surface) and orange (lower surface).

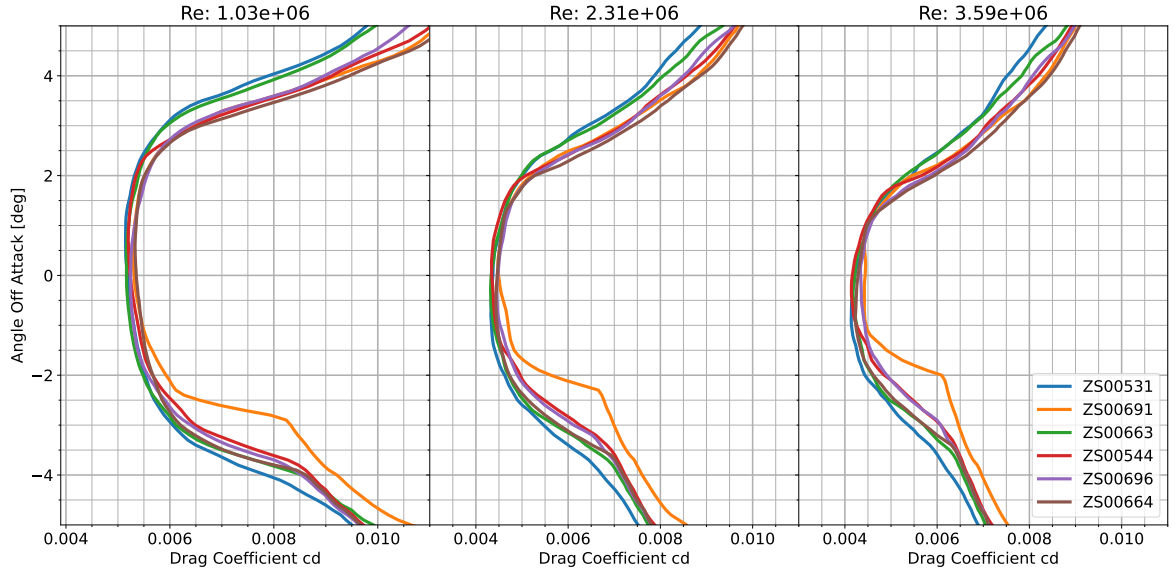

Figure 11.4: The angle of attack over the drag coefficient (c_d) for section 35, plotted at 3 different Reynolds numbers.

11.2. Results of the Drag Bucket analysis

The location of the regions of separation will affect the drag of the profile. A turbulent flow results in a higher resistance compared to a laminar flow. The presence of separated flow increases the profile drag. These effects can be seen in the drag bucket of the profile (Figure 11.4).

The size of the drag bucket can be seen to decrease with increasing speed. Mean while the drag itself decreases. The minimum drag can be seen in the right most image, just below zero AOA. The result from ZS00691 stands out from the data. The section of this profile presents more drag at negative angles of attack. The drag bucket is significantly smaller at these negative angels. Although ZS00691 starts to deviate at 2.5 degrees, most sections only do so between 3 and 3.5 degrees.

Comparing the friction coefficient distribution for both ZS00531 and ZS00691 identifies the reason for this decrease in the drag bucket size. The separation bubble at the leading edge starts closer to 0 for the ZS00691 hydrofoil section (Figure 11.5). The laminar flow transition line in orange (Figure 11.5b) starts to curve to the leading edge at approximately 0 degree of AOA. When the drag curve (Figure 11.4 far right) is observed at the same angle, the drag can be seen to increase. The sharp corner at -2 degrees

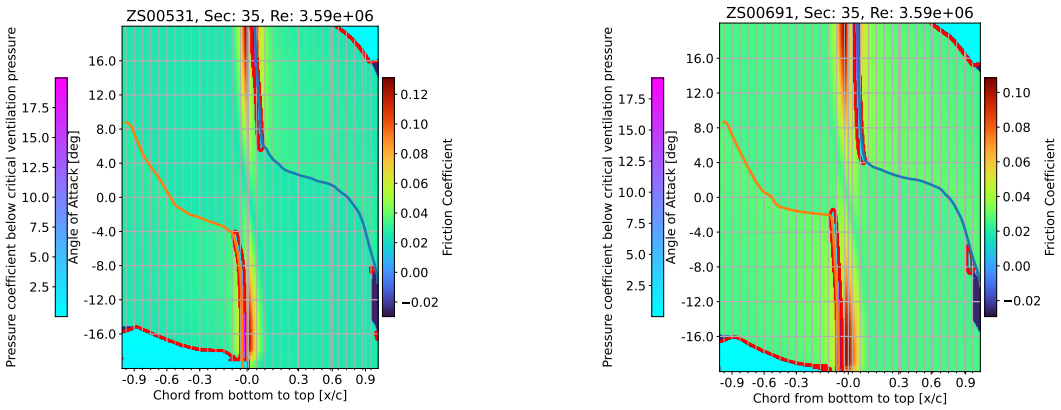

(a) ZS00531 section with the laminar separation bubble at angles smaller than -4 degrees and bigger than 5 degrees

(b) ZS00691 section with the laminar separation bubble at angles smaller than -2 degrees and bigger than 3.5 degrees

Figure 11.5: The Friction coefficient for ZS00531 compared to ZS00691 at section 35 and Reynolds number 3.59e 6

(Figure 11.4) corresponds to the start of the separation bubble on the lower surface of the ZS00691 section (Figure 11.5b).

The same connection can be made with the other profiles that deviated from the group. The AOA over drag graphs for the different span-wise sections are given in section D.3. From the sections that were analysed, the following outliers were detected with their corresponding section in the appendix.

- Section 15, ZS00663: Early separation at negative angles of attack (AOA over c_d, Figure D.1)(c_f graphs, Figure D.2)
- Section 24, ZS00664: Early separation at positive angles of attack (AOA over c_d, Figure D.3)(c_f graphs, Figure D.4)
- Section 30, ZS00544: Early separation at positive angles of attack (AOA over c_d, Figure D.5)(c_f graphs, Figure D.6)
- Section 35, ZS00691: Early separation at negative angles of attack (AOA over c_d, Figure D.7)(c_f graphs, Figure D.8)
- Section 40, ZS00691, ZS00696, ZS00664: Early separation at negative angles of attack (AOA over c_d, Figure D.9)(c_f graphs, Figure D.10)

11.3. Results of the performance impact on lift over drag

The impact of ventilation will probably be limited to the profiles with early separation at positive angles of attack. Negative angles of attack are found at the upwind hydrofoil. This hydrofoil needs to be in the water due to how the boat is constructed. It is common for hydro foiling sailboats to lift the upwind hydrofoil out of the water. The hydrofoil is producing upward and side-ways lift. The side-ways component is used to counteract the side-ways component of the wind. This balance is what makes a sailboat move forward.

When the downwind side ventilates, the loss of lift also results in the loss of sail pressure. This has the effect that the boat drops into the water and loses most of the speed.

Separation on the lower surface affects drag. For Figure 11.4, the increase in drag due to the separate flow is 0.0025 or 38% compared to 0.006 (c_d). The same magnitude of difference can be seen in the lift-versus-drag comparison (Figure 11.6).

The minimum drag between the different sections is practically the same. There is a slight difference in the size of the drag bucket and the rate of increasing the drag at the edges. Both ZS00531 (blue) and ZS00663 (green) show a slightly larger drag bucket. This results in a decrease in drag, at Reynolds number 2.31e 6, of 0.0006 c_d or 9% compared to the other profiles with a lift coefficient of -0.1. On the

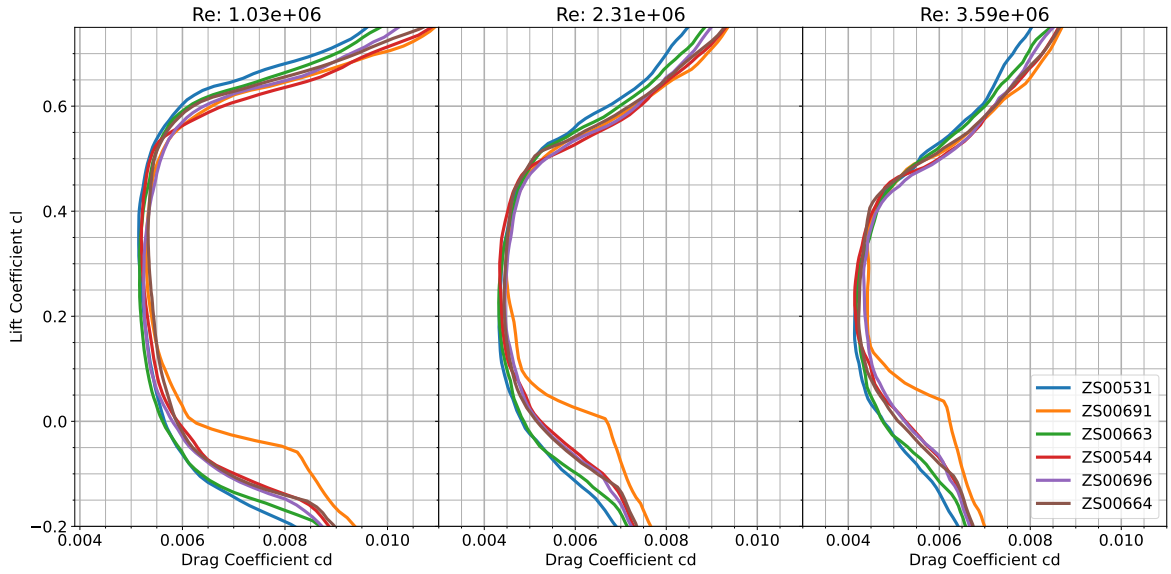

Figure 11.6: The lift coefficient (c_l) over the drag coefficient (c_d) for section 35

positive lift coefficients the difference is distributed more evenly. At a lift coefficient of 0.6 the difference between ZS00531 (0.0066 c_d) and ZS00544 (0.0075 c_d) is 0.0009 or 12 %. The drag can be calculated from the drag coefficient. The Reynolds number of 2.31e6 was calculated for an equivalent boat speed of 22.5 knots. The water was estimated to be fresh water at 20 degrees Celsius with a density of 998 $\frac{kg}{m^3}$. With the chord length of this section assumed to be 200 mm, the difference in drag can be calculated to be 13.4 Newton. This is equal to 1.4 kg.

The difference in the lift coefficient, with a drag coefficient of 0.0066, for ZS00531 (0.6 c_l) and ZS00544 (0.55 c_l) is a loss of.05 or 8% of lift for ZS00544. Using the same calculation as shown for the resonance. The loss of lift is 668 N or 68 kg. It should be noted that the differences for the full hydrofoil will likely cancel each other out and result in smaller differences.

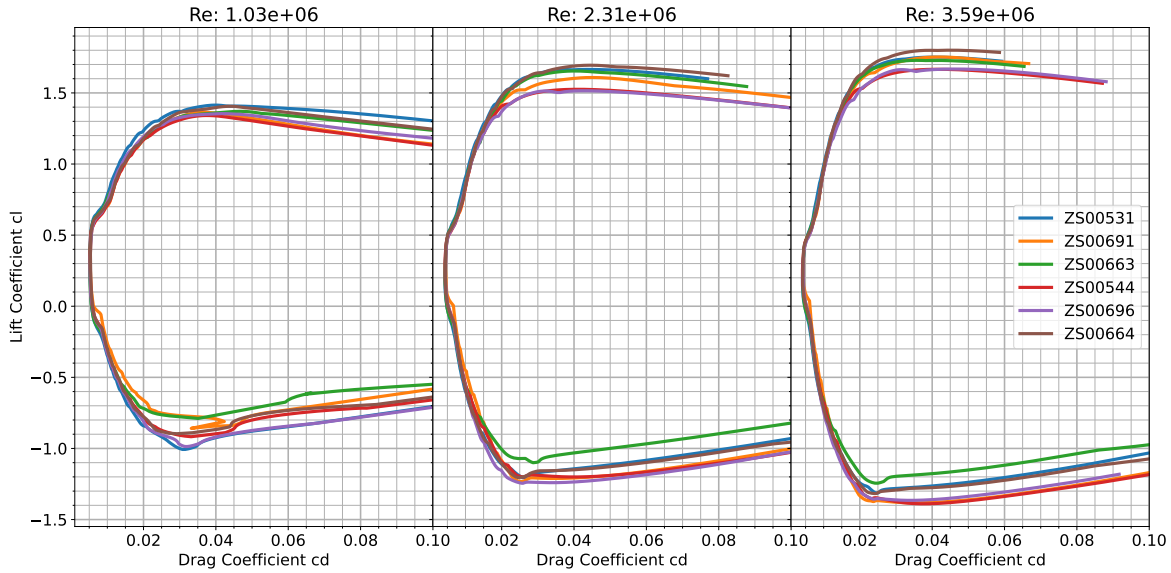

Figure 11.7: The lift coefficient (c_l) over the drag coefficient (c_d) for section 35 for the full range of lift coefficients

The complete range of the lift coefficient for the lift over drag comparison can be observed in Figure 11.7. When comparing the maximum lift coefficient with the maximum thickness identified in Figure 10.9, no

correlation can be found between the two. This is clear as both ZS00531 and ZS00663 are seen to have the highest maximum lift coefficient. While the ZS00531 hydrofoil has the largest maximum thickness, ZS00663 has the lowest.

The absence of a relationship between the maximum thickness or any of the shape parameters shown in chapter 10 is more evident when looking at the lift-to-drag ratio of the other sections in section D.4.

IV

Discussion

12

Digitisation of the Nacra 17 Hydrofoil: Discussion

12.1. Result discussion

There are a number of clarifications that need to be made after observing the results. These are the use of different measurement settings, apparent span-wise bending in the hydrofoil, and the use of Catia.

Different testing settings are used for the hydrofoils as shown in table 4.2. The shutter speed and resolution show a variation between the different hydrofoils. The variation in the shutter speed resulted due to different surface finish and room lighting. With glossy surfaces finishes, the shutter speed needs to be increased in order for the scanner to measure the surface. At lower shutter speeds, the scanner does not measure the surface correctly. This requires slower movements by the operator to achieve full scan coverage. With this difficulty to scan the surface, holes in the covered area could occur. This would result in measurement errors. The brightness of the surrounding light affected the shutter speed as well. A brighter room reduced the ability of the scanner to detect the lasers, and thus resulted in lower quality scans.

The shutter speed does not directly affect the accuracy of the scan and does not affect the final result. A lower shutter speed allows for higher resolution. The scan data rate is related to the shutter speed and resolution. At a very high resolution and/or shutter speed, the 16GB video memory of the laptop filled up and caused the programmeme to crash. This resulted in a loss of the complete scan. The 0.5 mm resolution was a suggestion by the support staff working with the 3D scanner. The resolution of 0.4 mm was found to be sufficient to produce a scan. A lower resolution would fill up the video memory. The author expects that the scans increase in quality with each successive scan. This results from the increase in the skill of operating on the hydrofoils. Combing the increase in resolution and the improvement of the operators skill does affect the final result. The effect of quality is mostly focused at the leading and trailing edges. This quality should be taken into account for further analysis. It is assumed that the hydrofoils can still be compared despite this change in accuracy.

The measurement setup chosen for the digitisation of the hydrofoils allowed for easy access to all sides of the hydrofoil. During the measurements, it was observed that the pressure of the foil on the wooden post varied between the hydrofoils. Combining this observation with those made in the results about the difference in span wise bending, one can conclude that this setup deformed the hydrofoils slightly. This difference in bending could distort the results in further investigations. For the current analysis made within this report, this difference is not noticeable. The hydrofoils are compared as 2D sections. These sections need to be aligned individually, thus removing effects of this bending on the final results.

The results obtained from Catia showed less detail compared to the comparison made using VXelements. For further analysis, VXelements would be the preferred program. The reason for the use of

Catia was mostly due to the limited availability of the required computer and licence usb. Without this usb, the programme did not allow for the necessary modifications needed for the processing of the foil. The PC and USB licence are part of the measurement setup. This made acquiring the computer and processing a timely process. Combined with the lack of experience with the program, resulted in the use of Catia for further processing of the hydrofoils.

12.2. Hypotheses

H. 1.1: ***The differences between the hydrofoil are greater than 0.1226 mm as calculated in equation* (4.2)** The difference in thickness observed in Catia, presented in Table 8.2, shows much higher numbers compared to the calculated volumetric accuracy. The values in Catia showed a range between 1.9 and 4.6 mm of absolute difference. The largest deviations observed in VXelemenets, presented in Table 8.1, are significantly smaller. That comparison showed a difference in thickness between 0.125 and 0.39 mm. The comparison in VXelements allowed the distinction between thinner and thicker parts of the hydrofoil. The deviation in thicker compared to reference hydrofoil was smaller (0.124 mm - 0.297 mm) compared to the deviation in thinner hydrofoils (-0.127 mm - -0.389 mm). These values are very close to the volumetric accuracy.

When comparing a 3D scan to an actual object in section 8.3. The problem becomes even more difficult. The test compared the width and thickness of a small metal plate with the 3D scan results. The width measurements showed a deviation of only 0.01 mm. Although the thickness deviated by 0.04, while the volumetric accuracy was estimated to be 0.026mm. This is a relatively large difference of 1.68%.

However, there was a problem with this measurement. On the scan of the plate, the position markers can still be seen. These remnants of the markers could also be seen in some of the hydrofoil scans. The current assumption is that these could not be removed by VXelements due to large curvatures. These bumps are only visible on the very leading and trailing edges of the hydrofoil. All the markers on the metal strip are located near a sharp edge. This could have easily changed the measurement by the 0.03 mm difference seen in the thickness.

The 3D scanner does seem to produce high detail that can be used to make objective conclusions from the data. It can still be the case that the hydrofoils vary in thickness due to the scanning method. This should be taken into account when drawing conclusions from the data.

H. 1.2: *The hydrofoil varies in shape along the span, requiring a scan of the complete surface*

The changes in geometry were best visualised by the comparison made in VXelements. The vxelement comparisons are shown in figures A.8 and A.9 in section A.3. The results noted the difference in thickness at the elbow of the hydrofoil. The magnitude of this difference varied with each hydrofoil. Using the colours of the deviation analysis, a difference in leading or trailing edge thickness was observed. These differences did not span the entire hydrofoil but changed along the span. This validates 1.2 and in turn the use of a noncontact reverse engineering solution.

H. 1.3: *The sanded resin layer provides a good measurement surface without the need for extra preprocessing for the scan*

The carbon wave pattern was slightly visible in the scan as highlighted in Figure 12.1. This can be due to the scanner looking through the resin surface. Or it could be due to insufficient post-processing by DNA composites. This pattern will show up, unless the surface is sufficiently sanded and coated multiple times. The pattern seems absent from the leading edge of the profile.

H. 1. *The Creaform HandyScan Black provides the necessary accuracy at high measurement speeds in order to digitise all hydrofoils in a timely matter.*

The Creaform HandyScan Black is suitable for measuring hydrofoils. Non-contact measurement techniques seem to be the better option due to the variations along the foil. The foil itself is tapered, changing sections, and there are definitely differences along the hydrofoil. The accuracy of the scanner is very close to the actual variations. The accuracy of the new 3D scanners will improve with time.

Figure 12.1: Showing the top of an Nacra 17 Hydrofoil scan, with the visible carbon weave highlighted by the black lines. A clear line is seen at the (presumed) boat support point showing a more detailed surface on the right side (below the boat) underneath the red line.

12.3. Conclusion

The hydrofoils seemed to be identical when observed with the naked eye. This required the use of reverse engineering to identify potential differences between the hydrofoil geometries. Using the literature, different reverse engineering options were identified. These were (as available for this project) optical and contact probing measurements. It was assumed that the deviations in shape were not constant along the hydrofoil. Therefore, this requires the measurement of the profile at different locations along the span. When using a contact method, this would take a significant amount of time. The results would only be of slightly higher accuracy. With the requirement for the most accurate method for scanning multiple sets of the complete hydrofoil, the Handy Scan Black was chosen to be the most suitable option.

After digitising the hydrofoils. It was found that the differences between the hydrofoils changed along the span. Although optical scanners are less reliable on mirror or transparent surfaces. It is concluded that the possible differences are insignificant to the final result.

Using a small plate as the reference geometry. A scan error of 1.68% was found for the thickness or the plate. This error is 50% higher than the stated accuracy of 0.02mm. The width of the plate was digitised with a standard error of only 0.01 mm. It seems that this error does not scale the size of the part. The difference in thickness could be contributed to the error introduced by the position markers close to the edge. As these markers could not be removed by the software in the post-processing.

The differences between the hydrofoils were found to be between 0.1 and 0.4 mm using VXelements and up to 4.6 mm in Catia. Differences between the different modelling programmes can be attributed to unfriendliness. The programme VXelement was, however, not able to extract the cross sections and thus Catia needed to be used. The differences in Catia validate the positioning of the different Hydrofoils along the same axis.

The hydrofoils are thus successfully digitised using the 3D scan programme VXelements and orientated using Catia. The 2D sections exported from Catia can now be used to analyse the Hydrofoils in detail.

13

Research Method Validation for 2D Section Processing: Discussion

13.1. Result Discussion

With the results of the hydrofoil processing shown in section 6.2. Some observation should be discussed.

The voronoi method (section 5.2.2) is limited to data sets that contain a large number of points. The voronoi vertex points are calculated with 3 data points. This results in a data set that resembles a saw tooth. These tooth are two points located very close to each other, one higher than its neighbour. When only a small number of points are used (100), the difference between these points becomes noticeable. When the number of points increases, the distance between these points decreases as well. With the 500 points used for the NACA 4412 foil, offset was no longer a problem. But it should be taken into account when applying this method to find the mean Camber.

The low-pass frequency filter on the profile data was found to be the optimum solution to reduce small variations in the surface while maintaining the actual shape of the profile. The method showed a high degree of accuracy for the ZS00696 foil at section 30. The creation of the data shown in Figure 9.6 needed to run for 14 hours. Therefore, it is not an optimised method of processing the data.

13.2. Hypothesis

Using the results presented in chapter 9, the hypothesis presented in chapter 5 can be answered.

The first step was to identify whether the profile itself could be used for accurate alignment, forming the hypothesis:
H. 2.1: *The Leading and trailing edges can be found consistently by using the raw data set.*
From the methods suggested that are capable of identifying the leading and trailing edge, hypotheses 2.1.2 to 2.1.5 did not provide a repeatable solution for the Nacra hydrofoils. There were two methods that were able to approximate the profile extreme points. These are the method based on the farthest distance between two points (hypothesis 2.1.1 in sec: section 5.2.1) and by using the polar coordinates (hypothesis 2.1.6 in sec: section 5.2.1). The method based on the furthest points showed a high sensitivity to the spacing and placement of the data points. In the provided example, the error in the chord length was calculated to be 0.131% (section 9.1.1). While the error for the method using polar coordinates estimated the chord length with an error of -0.0201% (section 9.1.4).

The polar method provided the extra benefit of the independence in orienting the profile and ordering the coordinates ([x,y] or [y,x]). These are both important characteristics. The coordinates are ([y,x]) after the first rotation to the local coordinate system as highlighted in subsection 6.2.1. The initial profile data are shown with the leading edge in the positive x direction (Figure 13.1). Using the angle theta, the

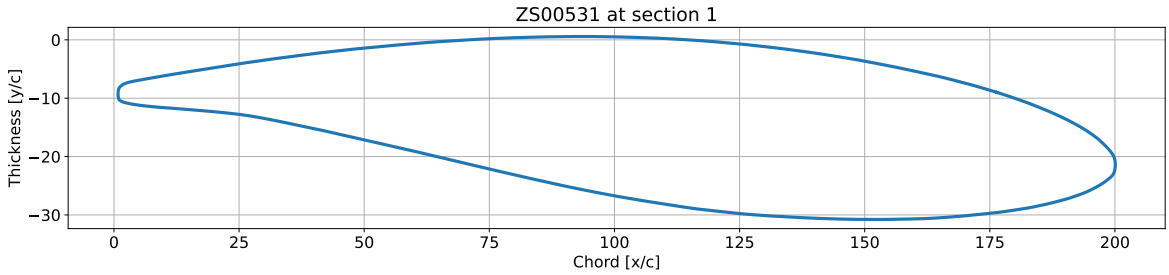

Figure 13.1: A Profile section as it is exported from Catia, showing that the leading edge is in the wrong direction

direction of the coordinates could be reversed to obtain the requirement that the data start at the top trailing edge and finish at the bottom trailing edge.

After the methods using just the profile itself. Methods using the camber line combined with the estimation of the camber line are presented. The question is if the camber line can be extracted from the raw data and thus evaluating the hypothesis:
H. 2.2: *The camber line can be extracted from the profile data*
Two methods are proposed that could create data that estimate the camber line. These methods are using the offset of the profile (hypothesis 2.2.1 at section 5.2.2) and using voronoi vertex points (hypothesis 2.2.2 at section 5.2.2). Both methods provided accurate data that followed the camber line of a NACA 4412 foil in section 9.2.1 (Offset) and section 9.2.2 (voronoi). The data for the offset of the surface lacked detail at the top of the camber line. The voronoi data did not extend to the leading and trailing edges.

The methods thus show a lack of accuracy in different areas. While the accuracy of the overall solution is very similar. This led to the use of both methods to estimate the camber line.

The camber line curve could be approximated using a polynomial (hypothesis 2.2.3 at section 5.2.2) or a B-Spline fit (hypothesis 2.2.4 at section 5.2.2). The polynomial fit was a promising option when applied to the NACA 4412 data. But when applied to the actual data. The extrapolated portion of the line curved significantly and missed the leading and trailing edge.

The B-spline method provided an accurate method of estimating the camber line using the data obtained with the offset and voronoi methods. The good performance of the B-Spline is likely due to the nature of how foil profiles are constructed. For the NACA four series, the camber line is split in a formula for before the maximum camber and a formula after the maximum camber. Therefore, the resulting curve might be too complex to be fitted by one polynomial. In order to fit both curves, the maximum camber point needs to be known. This is not the case in the Nacra hydrofoil sections.

The B-Spline will be used to estimate the camber line of the Nacra hydrofoils. This leads to the use of a B-Spline fit to estimate the thickness profile of the sections.
H. 2.3: *The Profile can be accurately approximated by applying a low pass filter on the data.*
Extraction of the thickness profile using the estimated camber line. Combined with the B-Spline fit through the data, this provided an accurate method of estimating the thickness profile. The B-spline fit could thus be used to estimate profile parameters such as the maximum thickness and maximum camber. The resulting profile allowed for an accurate method of aligning the different sections of the coordinate system.

The method did not fit the profile perfectly. The data were reduced to a less complex curve. This could be a problem in further fluid dynamic research. The curvature of the leading edge is a critical shape for the speeds at which the Nacra operates. So, while the hypothesis is technically invalid. The method is still used to obtain the profile parameters and to align the profiles in the same orientation.

The method of using a low-pass frequency filter was proposed to solve the problem with noise without losing the shape.
H. 2.4: *The profile can be accurately approximated using a B-spline function for the Camber line and the thickness profile.*

The method of filtering the profile data using a low-pass filter, proposed in subsubsection 5.2.3, showed great promise in subsection 9.3.2. A clear optimum was observed when filtering the profile data. When applying this optimal frequency as a low-pass filter on the profile. A good approximation of the profile was obtained. This profile followed the curve well at the leading edge. This method will be used to profile data to any further Fluid dynamic research.

13.3. Conclusion

This sections covering "*Research Method Validation for 2D Section Processing*" attempted to find a good approach to process the raw data from Catia, in order for the sections to be compared to each other, published foil sections, and to be used in fluid dynamic analysis. For the programme Xfoil, the leading edge must be placed at the origin ([x=0,y=0]), the trailing edge on the x-axis with a length of 1 ([x=1,y=0]), and the data should start at the top trailing edge following the contour of the section to the bottom trailing edge.

It started with identifying methods for finding the leading and trailing edge of the section. This could thus be used to orient the foils in the correct orientation. The best method was found to be by analysing the profile in polar coordinates. Both the leading edge and the trailing could be found with the foil placed in any orientation. However, this method was not accurate enough for the final orientation.

For the final orientation, the leading edge and trailing edge are estimated with the use of the camber line. This camber line is approximated by using voronoi and the offset of the surface to create a data set. The actual camber line is created with a B-Spline fit through that data set. This camber line could then be used to extract the top and bottom surfaces of the profile. These are subsequently fitted with a B-Spline representing the thickness profile. With these two B-Spline fits, the maximum thickness and camber could accurately be extracted of the profile.

Although the B-spline approximation provided an accurate representation of the profile. A lack of detail was found in the curve of the leading edge. For this reason, the last method was proposed. It attempts to filter the measurement noise from the data using a low-pass filter. This provided very promising results. The low-pass filtered data will be used for the analysis with fluid dynamics.

14

Geometric deviation analysis: Discussion

14.1. Result Discussion

The fit of the profiles on the boat casing produced some varying results. This was attributed to the increased trailing edge at sections 1 to 12. This thick trailing edge is used to create a good support against the boat. This part affected the thickness profile. The trailing edge will never converge at this part of the hydrofoil. While the fit of the thickness profile did assume that the top and bottom surfaces converge in a point. Because of this, the chord length was estimated to be much further away as to where it should be. This scaled the complete profile down. The camber line fit is less precise at larger distances from the last data point. This resulted in the camber line curving more. Combining both effects, rotated the foil more as it should have been. All data above Section 12 will thus not be useful for any analysis. It also does not affect the flow of water and thus will not affect the boat's performance.

The results of the maximum camber and its location are affected by the initial fit with the current method. The mean camber will be fitted on the orientation made with the polar coordinates. This was not the most accurate method. Because of this, the profile is rotated again after finding the leading and trailing edges with the B-Spline fit. After the rotation, the maximum location could change as a new spot is the highest point. The spline knots at the maximum are no longer horizontal. During the project, this was assumed to be acceptable. The rotations are very small, and thus the shift in location will be relatively small. This shift is assumed to be lower as the degree of accuracy is used in the plots. But the results are technically skewed because of the rotation.

Table 14.1: The different mean of the shape parameters of the hydrofoil at the sections above the elbow, at the elbow and below the elbow of the hydrofoil showing the different foil designs that are used.

	xt	yt	xc	yc
Above Elbow	0.36	0.14	0.66	0.14
At Elbow	0.32	0.12	0.72	0.018
Below Elbow	0.37	0.11	0.63	0.020

When observing the results of the different parameters. It is clear that the hydrofoil is designed using 3 different cross sections. The values of these sections can be seen in Table 14.1. There are three distinct sections. When observing the hydrofoil on the Nacra, all three sections fulfil different roles. The top of the board prevents the boat from drifting sideways. The elbow needs to connect the top and

bottom while experiencing an accelerated flow due to the curve. The bottom part of the hydrofoil lifts the boat out of the water.

14.2. Hypothesis 1

The hypothesis formulated for "*Geometric deviation analysis*" and set out in section 6.2.

H. 3. *Manufacturing defects can be identified by the differences in the shape parameters of the different hydrofoil sections.*

With the shape analysed in detail in these sections, the hypothesis stated in "*Digitisation of the Nacra 17 Hydrofoil*" (section 4.2), regarding the measurement accuracy should be re-evaluated. Therefore, the hypothesis related to the measurements will be evaluated before the interpretation of the geometric results. The important hypotheses related to accuracy and shape are hypotheses 1.1 and 1.2.

The first hypothesis (hypothesis 1.1) stated that the differences in the hydrofoils are greater as the volumetric accuracy is 0.1226 mm. When multiplying the results of the average deviation of the maximum thickness (table 10.2) by the average chord length of 200 mm. The largest value is 0.212 mm and the closest value to 0: 0.0120 mm. These are around the volumetric accuracy. The largest and smallest deviation for the other parameters are shown in Table 14.2

Table 14.2: Showing the maximum average Deviation for each hydrofoil in millimetres.

	Maximum average Deviation [mm]		Minimum average Deviation [mm]	
xt	-1.03	ZS00544	-0.19	ZS00664
yt	0.212	ZS00531	0.012	ZS00691
xc	1.22	ZS00544	-0.482	ZS00696
yc	0.333	ZS00691	0.00141	ZS00664
rle	0.171	ZS00664	-0.0174	ZS00696

The results are barley above the calculated volumetric accuracy. The actual accuracy of the hydrofoils could be better, as shown with the width measurements of a small plate in section 8.3. It does show that definitive conclusions cannot be made from the results of the hydrofoils.

The second hypothesis (hypothesis 1.2) stated that the shape varied along the span of the hydrofoil. This hypothesis can be confirmed using the plots in section 10.3. All parameters showed a variability in shape along the span. Three different shapes could be observed before the elbow, at the elbow, and after the elbow with some changes at the tip of the hydrofoil. When the data were normalised, some variability along the span between hydrofoils could also be observed. It is clear that the hydrofoils differ in shape and that this difference is variable at different points along the span.

With the accuracy of the measurements identified. The subhypothesis supporting hypothesis 3 can be evaluated. The first hypothesis is related to the closure of the mould, stating:

H. 3.1: *The profile thickness can be an indicator for improper mould closure.*

The results for the maximum thickness for each hydrofoil were relatively stable. The results (figure 10.9) after the elbow (section 28) were relatively linear. This supports the assumption that there is definitely a difference. If accuracy would affect the results. The thickness should change more as noise is added to the data.

The maximum thickness is located between 30 and 40 % of the chord. The camber line is relatively linear at this part of the section as can be seen in Figure 14.1. This was the reason why an additional knot location was needed for the B-Spline to create an accurate fit. The thickness is measured perpendicular to this camber line. This reduces any effect of sanding or mould misalignment on the thickness

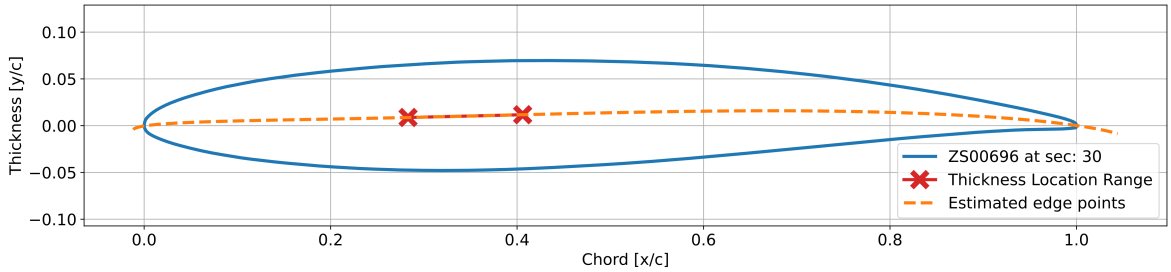

Figure 14.1: Showing that the camber line is approximately linear within the range of the Maximum thickness location (x_t).

value. Therefore, the thickness should be mostly affected by the spacing of the two mould halves. The maximum thickness is therefore likely an indication of the degree of closure of the two mould halves.

The second sub-hypothesis (hypothesis 3.2) was related to mould misalignment. The upward deviating polynomial camber line fit was hypothesised to be an indication of the moulds missing alignment. The camber line that points up at the leading edge indicates that the top halve shifted aft, and the trailing edge that points up indicates that the top mould shifted forward.

The data resulting in the fit of this polynomial did show a slight indication that this theory might be correct. The direction did not seem to be completely random for a single hydrofoil along the span. The deviations were seen in groupings. This indicates that the geometry did affect the fit and not outliers in the camber line data. However, with the current set of data, no conclusive results can be deduced from this metric. It could be worth investigating with a higher resolution data set for the camber line, or a foil where the production process was controlled in the same study. But with current data, hypothesis 3.2 is assumed to be incorrect.

The final sub hypothesis (hypothesis 3.3) theorised that a correlation between or more of the profile shape parameters that could indicate production variability with the mould closure. This could reinforce observations made using the polynomial camber line theory discussed before.

When comparing the different parameters, no discernible correlation could be found. The data did show distinct regions. These are attributed to the different foil shapes used in the hydrofoil. A clear difference was observed with the shape above the elbow, at the elbow itself, and below the elbow.

The hypothesis stated before that differences in shape can be used to identify manufacturing deviations is thus valid for the mould separation. It can be valid for mould alignment using the polynomial fit. This area needs more analysis to confirm the theory. No other set of variables was found to be an indication of manufacturing defects.

14.3. Conclusion

In *Research Method Validation for 2D Section Processing*, the best methods were identified to post-process the hydrofoils to compare them. Actual post-processing of the hydrofoil sections is discussed in the *Geometric deviation analysis*.

The post-processing produced results with high accuracy according to the validation and verification. Analysis of the different sections revealed that there are three different foil designs throughout the span. Differences between the hydrofoils could be observed when normalising the data. The thickness showed the most clear separation of the different hydrofoils. The other parameters varied more over the span. Although they varied more, a difference could still be observed.

An attempt was made to identify a correlation between the different parameters. This did not show a clear correlation between any of the parameters. The correlation graphs showed different shapes. These shapes are attributed to the three different profile shapes used in the hydrofoil design.

Due to the clear separation of the maximum thickness, this parameter can be assumed to be a good indication of the mould closure. The use of the polynomial camber line fit was identified as a possible

indication of mould misalignment. Although there is an indication that this is correct. It cannot be concluded using the current data set.

There are definitely differences between the different hydrofoils that are analysed. However, only the profile thickness can be identified to connect to a specific production process.

15

2D section hydrodynamic analysis: Discussion

15.1. Result Discussion

Correlation between the polynomial camber line and flow separation. From the results in chapter 11 no correlation was found between flow separation and one of the profile shape parameters. When comparing the separated foils with the result of the polynomial camber line fit Appendix C, explained in section 10.4. All foils with a different visible flow separation behaviour are shown to have the value -1. The -1 identified that the leading edge is pointing up to the leading edge. This was assumed to be caused by the top mould being shifted aft during production.

Table 15.1: The values for the polynomial camber line with the profiles that exhibited early separation highlighted in light grey.

Section	Hydrofoil					
	ZS00531	ZS00691	ZS00663	ZS00544	ZS00696	ZS00664
15	0	0	-1	1	1	1
20	0	0	0	0	0	1
24	-1	0	-1	-1	-1	-1
30	0	0	-1	-1	-1	1
35	0	-1	0	0	0	0
40	0	0	0	0	0	0

It is not the case that when the polynomial is pointed upward, the laminar separation bubble initiates at a lower angle of attack. There is also no distinction between the laminar separation bubble on the lower or upper surface related to this parameter.

It is evident from Table 15.1, the abbreviated form of Appendix C, that the likelihood of it being coincidental is not significant. There are two hydrofoils where it is the only negative value. It can be argued that all foils in section 24 show earlier separation.

In order to prove or disprove this finding. The polynomial method needs to be improved to produce reliable results. This will probably be achieved by increasing the number of sections. For each of these sections, the fluid dynamic analysis should be compared with the polynomial value. With the current data it is still inconclusive.

Designed Foil shape At most sections that were analysed, there was a profile that was significantly different from the group. This was always due to the laminar separation at the leading edge starting closer to an angle of attack of 0. This indicates that the shape of the leading edge is critical to the final performance of the profile.

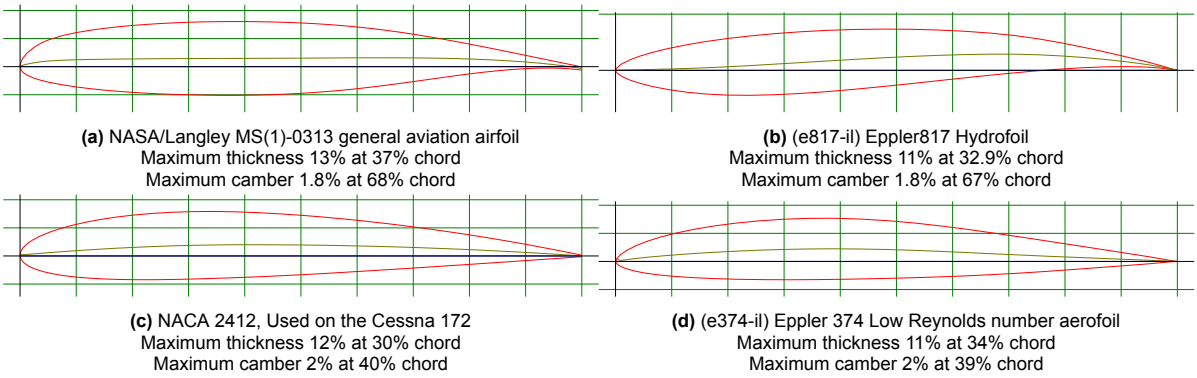

(a) NASA/Langley MS(1)-0313 general aviation airfoil
Maximum thickness 13% at 37% chord
Maximum camber 1.8% at 68% chord

(b) (e817-il) Eppler817 Hydrofoil
Maximum thickness 11% at 32.9% chord
Maximum camber 1.8% at 67% chord

(c) NACA 2412, Used on the Cessna 172
Maximum thickness 12% at 30% chord
Maximum camber 2% at 40% chord

(d) (e374-il) Eppler 374 Low Reynolds number aerofoil
Maximum thickness 11% at 34% chord
Maximum camber 2% at 39% chord

Figure 15.1: Two aerofoils comparible to the Nacra 17 hydrofoil shape and designed for transsonic speed or cavitating flow, with the camber behind 60% while the two foil shapes operating in the Nacra 17 reynolds number range have the camber before 35% of the chord.

The shape of the nacra 17 hydrofoil seems off when taking into account the range of Reynolds numbers that the hydrofoils operate. In chapter 10 it was identified that the maximum thickness is located at 35% of the chord and the maximum camber at 65% to 70%. Figure 15.1 shows different profiles, with the first two comparable to the Nacra 17 hydrofoil.

The MS(1)-0313 aerofoil is designed for a mach number of 0.72 according to McGhee, Beasley, and Somers [74]. The mach number indicates the speed of sound, and the aerofoil is designed for 72% of the speed of sound. The main challenge for the profile is the formation of shock waves at the top of the profile. These shock waves are created because the flow speed surpasses the speed of sound. These profiles are very flat on top to prevent the flow from reaching the speed of sound.

Although the speed of sound is not a problem in water, the same principle is the cause of ventilation. Ventilation is the phase change of water due to the pressure dropping below the triple point. The water starts to boil, and most of the lift is lost. By creating a flat upper surface, the pressure does not drop as low, allowing for higher speeds. The Eppler hydrofoil is relatively flat on top as can be seen in Figure 15.1b. Cavitation is usually reached at 50 knots. Therefore, this is not applicable to the Nacra 17.

"*The Eppler E817 was not intended for use at low Reynolds numbers*"-Speer [75]. The Naca 2412 (Figure 15.1c) and Eppler 374 (Figure 15.1d) are designed for low Reynolds numbers. The biggest difference between the sections is the location of the maximum camber. The two bottom profiles have the camber in the first 40% of the chord, whereas the two top profiles have the camber past 60%.

M. Selig conducted research on the formation of laminar separation bubbles. His research helps design an aerofoil section for the low Reynolds number range, with a good complete explanation found in his lecture notes [9]. In his lecture notes he describes the use of design angles such that there is a region where the velocity is constant. When these are too small for a given angle, the flow will separate. This theory is visualised in Figure 15.2. The left profile can be seen to exhibit laminar separation. while the right profile does not. The bottom set of pictures highlights the design angle. The red line symbolises the point at which the pressure becomes negative. If this region is very small, like the left profile, the laminar flow will separate. If this curve is more gentle, the region will be bigger and the laminar flow can remain attached to the surface.

15.2. Hypothesis

At the beginning of chapter 7, a set of hypotheses was presented. The main hypothesis of the *2D section hydrodynamic analysis* research was:

H. 4. *There is a difference in the hydrodynamic performance between the different hydrofoils.*

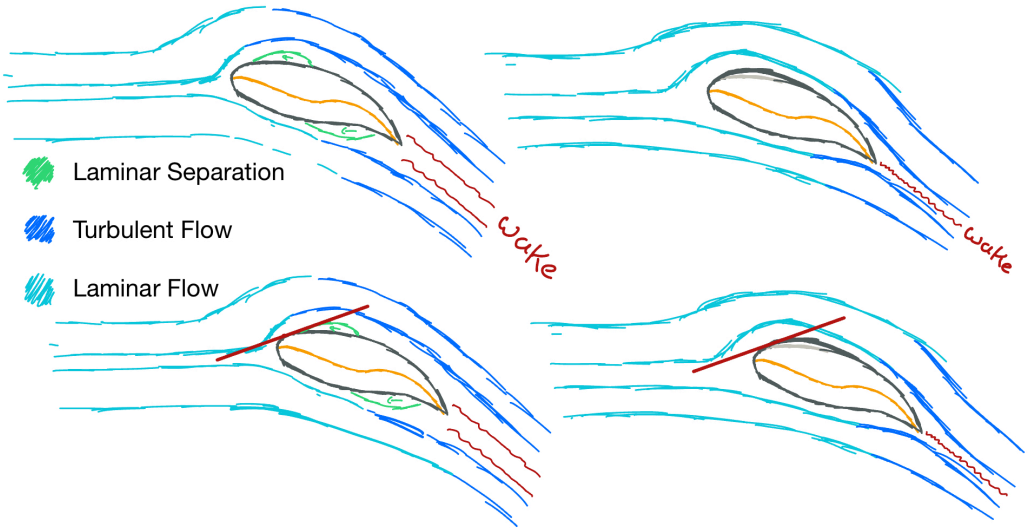

Figure 15.2: Showing the schematic flow around an aerofoil with the Nacra 17 on the left and a improved version on the right, the bottom pictures showing the design angle as explained by M. Selig in his lecture notes [9]

This hypothesis was divided into 3 sub-hypotheses, the first was defined as:
H. 4.1: *The difference in shape affect the location where ventilation can occur.*
This hypothesis has been proven to be correct. There are large differences in the critical angle at which the laminar separation bubble forms for the different profiles in the various span-wise sections. This is the effect of the curvature of the first part of the hydrofoil. Differences in the laminar to turbulent transition can be seen for the different sections. This transition is highly influenced by the geometry of the profile. It can be concluded that the difference in the shape of the hydrofoil influences the performance of the hydrofoils.

The second hypothesis (4.2) states that the greatest impact on performance is due to the radius of the leading edge. This is not the case, however, how likely this may seem given the previous conclusion. When comparing the radius of the leading edge with the separation of the different profiles, there are often contradictory results. For the observed separation bubble found at ZS00691, Section 35 (Figure 11.6), the radius of the leading edge was the median value.

The radius of the leading edge should be an indication of the performance, it should identify an outlier when the performance is an outlier. It is logical that the radius is not an indication for the separation and in turn the performance. It is the section of the profile between the leading edge and the maximum thickness that is affected.

The final subhypothesis (4.3) assumed that the concave trailing edge would show separation at small positive angles of attack. When observing the friction plots, one can see that there is indeed a small region of separated flow up to 70 % of the chord in Figure 11.3a. For the plots in the appendix, this separated region is visible between 30% and 60% of the chord for sections 15 (Figure D.2) and 24 (Figure D.4). It should be noted that these plots show the flow at a higher Reynolds number. This indicates that the region is larger at lower speeds. The resulting drag is only minimal due to this region, according to the drag over angle of attack graphs.

This validates the hypothesis "***H. 4.3:*** *The high pressure side of the profile presents separated flow at positive angles of attack.*" although the impact on performance is not seen as significant.

Returning to the original hypothesis (4) of this research step, there is in fact a difference in performance between the different hydrofoils. This difference can be best observed by the variation at which angle the laminar separation bubble initiates. Smaller differences, like the minimum drag and the maximum angle of attack, were not yet identified. This was mainly due to the small differences between the hydrofoils.

15.3. conclusion

The *2D section hydrodynamic analysis* attempted to identify the impact of geometric variations on the hydrodynamic performance for the two-dimensional case. Profile sections obtained in *Geometric deviation analysis* needed to be smoothed for the fluid dynamic results to be reliable. This smoothing step is performed with the use of a low-pass filter applied to the fast Fourier transform of the profile data. Therefore, these sections could be used in the Xfoil programme.

The Xfoil analysis looked at speeds between 10 and 35 knots for a fresh water temperature of 20 degrees. The speed range covers the assumed flight speeds of the Nacra 17.

From the results, the main focus was on the causation of ventilation. It was found that there is a significant difference at what angle the laminar separation bubble is initiated. This has the result of a significant increase in drag. The laminar separation bubble would facilitate the flow to ventilate. The possible impact of this phenomenon would be much greater than a small increase in drag would be.

The differences in profile shape, in fact, influence the performance of the Nacra 17 hydrofoils. There are significant differences in the possible start of ventilation. Minor variations in the lift and drag of the profile are observed. A more thorough investigation is necessary to determine the implications of these differences.

V

conclusion

16

Outlook

The Dutch Olympic Nacra 17 team sought help from TU Delft to gain understanding of what could influence the hydrofoils of a Nacra 17. They found that a foil that is stiff in the spanwise bending direction yields higher performance. To make the most of the hydrofoils in the 2024 Olympics, it is essential to comprehend their function. The team discovered that there is a disparity in stiffness, and thus performance, between the hydrofoils. Measurements conducted by the Nacra 17 class organisation [17] showed a difference in thickness between different hydrofoils.

Identifying the impact of different geometric variations and their resulting production process can help design and manufacture better hydrofoils. Focusing on the areas that have the greatest impact on performance will create a more uniform production. For the Olympic team, it will help identify which area of the hydrofoil needs to be maintained well to maintain a high performing hydrofoil.

16.1. Digitisation of the Nacra 17 Hydrofoil: Conclusion

The hydrofoils were observed to be identical with the naked eye, so reverse engineering was used to detect any potential discrepancies between the geometries. Literature was consulted to determine the available reverse engineering options, which were optical and contact probing measurements. It was assumed that the shape deviations were not uniform along the hydrofoil, so measurements had to be taken at various points along the span. Contact measurements would take a long time and the accuracy of the results would only be slightly higher. Differences between hydrofoils were found to be between 0.1 and 0.4 mm using VXelements.

There is still some uncertainty about the real accuracy of the 3D scanner. It was found that an optical 3D scanner like what was used is necessary for the digitisation of the hydrofoils. The difference between the hydrofoils vary along the hydrofoils. These differences will not be captured when using a contact method for the digitisation step. It is finally concluded that the data from the 3D scan were of high enough detail to continue with the analysis.

16.2. Research Method Validation for 2D Section Processing: Conclusion

This section attempted to find a suitable approach to process the raw data from Catia, so that the sections could be compared to each other, published foil sections, and used in fluid dynamic analysis. To do this, the leading edge was placed at the origin ([x=0,y=0]), the trailing edge on the x-axis with a length of 1 ([x=1,y=0]), and the data started at the top trailing edge following the contour of the section to the bottom trailing edge.

The leading edge and trailing edge were estimated with the use of the camber line, which was approximated by using voronoi points and the offset of the surface to create a data set. The camber line and the thickness profile were accurately fitted separately with the use of B-Spline curves.

This B-Spline allowed the maximum thickness and camber to be accurately extracted from the profile. However, a lack of detail was found in the curve of the leading edge. To address this, a low-pass filter was used to filter the measurement noise from the raw data set. This provided very promising results, and the low-pass filtered data will be used for the analysis with fluid dynamics.

16.3. Geometric deviation analysis: Conclusion

In *Research Method Validation for 2D Section Processing*, the best methods were identified to post-process the hydrofoils to compare them. The actual post-processing of the hydrofoil sections is discussed in the *Geometric deviation analysis*. The post-processing yielded results with great accuracy according to the validation and verification. Examining the various sections revealed that there are three distinct foil designs across the span.

When normalising the data, differences between the hydrofoils could be observed. The thickness showed the most obvious distinction for the different hydrofoils. The other parameters varied more over the span, yet a difference was still noticeable. An effort was made to identify a correlation between the different parameters, but this did not show a clear relationship between any of them. The correlation between the different parameters displayed various shapes. These shapes are attributed to the three different profile shapes used in the hydrofoil design.

Because of the clear separation of the maximum thickness between the hydrofoils, this parameter can be assumed to be a good indication of the mould closure. The use of the polynomial camber line fit was identified as a potential indication of mould misalignment. Although there is an indication that this might be a valid assumption, it cannot be concluded with the current data set.

It is evident that there are differences between the different hydrofoils that were analysed. However, only the profile thickness can be linked to a specific production process.

16.4. 2D section hydrodynamic analysis: Conclusion

The *2D section hydrodynamic analysis* aimed to determine the effect of geometric changes on the hydrodynamic performance for the two-dimensional case.

To ensure the accuracy of the fluid dynamic results, the profile sections obtained in *Geometric deviation analysis* were successfully smoothed. This was done by applying a low-pass filter to the fast Fourier transform of the profile data.

The smoothed sections were then used in Xfoil. The Xfoil analysis was conducted at speeds between 10 and 35 knots, with a water temperature of 20 degrees. This speed range covers the assumed flight speeds of the Nacra 17.

The main focus of the results was on the cause of ventilation. It was found that there is a significant difference in the angle at which the laminar separation bubble is initiated. This can have the effect of an unstable hydrofoil due to ventilation. In the results, this created a significant increase in drag. This laminar separation bubble would facilitate the flow to ventilate, which would have a greater impact than a small increase in drag.

In fact, variations in profile shape influence the performance of the Nacra 17 hydrofoils. There are significant differences in the potential start of ventilation, with minor variations in the lift and drag of the profile observed. Further investigation needs to be conducted to determine the implications of these differences.

16.5. Final Conclusion

The results of the different sections support the conclusion that this research provides a good basis for continued research on (Nacra 17) hydrofoils. The loss of information from the digitisation of the hydrofoils and the processing of the sections was found to be minimal. A difference in the shape of the different hydrofoils and their hydrodynamic performance has been observed.

Hydrodynamic analysis can identify the leading edge that is critical for the performance of the Nacra 17 hydrofoil. For the design of a hydrofoil, it is critical to keep the leading edge as accurate as possible. Small deviations that even after detailed analysis where not yet observed significantly affect the performance. The Olympic teams can use the results of this research to focus their maintenance efforts on the leading edge of the hydrofoil.

17

Revision and Perspective for future research

With the research finalised, there are several things that could be interesting for further research. There are certain steps that could be adjusted for an even better result.

17.1. Digitisation

With respect to the digitisation of the hydrofoil. The measurement setup can be significantly improved in usability. The hydrofoil was now loosely supported between a metal beam and a wooden post. This was considered to be the best method for full accessibility. A better method would have been to mount the hydrofoil bearings that support the hydrofoil in the boat, in an open structure. The hydrofoil can be placed in these bearings, providing a repeatable setup. The bearing could add a flat surface to the scan that can be used for the preliminary alignment. This will significantly speed up the process. The parts of the hydrofoil that are not yet digitised can be covered by starting a second scan using the same markers. The scanner will be able to fill in the missed area without loss of accuracy. This is only possible with the scanning technology used by the Creaform scanner.

17.2. 2D section analysis

The section analysis could be improved with a more complex B-Spline. Xfoil analysis showed a significant impact due to small variations in the leading edge. The shape parameters that were extracted from the profile did not capture the cause of these differences in hydrodynamic performance. A knot on the profile, in between the leading edge and the maximum thickness, might show a better conclusion.

Fixing the distance between the first two variables of the camber line B-Spline might provide a good solution as well. By fixing the distance between the spline coordinates the same, the result might be more sensitive to changes in the mean camber line data set. Thus, it could form a more reliable method of identifying the variations shown in the polynomial camber line fit.

17.3. Xfoil analysis

There are a large number of different tests that can be performed on the current Xfoil results. The first step would be to show the impact of tripping the flow at 50% of the chord.

On both the upper and lower surfaces of the different sections, laminar separation could be observed. It would be very interesting for the Olympic sailing team to know if tripping the flow before these separate regions results in an increase in performance.

The B-Spline version of the hydrofoils can be used to perform a parametric study of what affects the laminar separation bubble at the leading edge. This would provide a better understanding of what parameter influences this phenomenon.

The next step in the research was already outlined in the Research Scope. The xfoil data need to be used to construct a vortex lattice method. This method transforms the 2D data into a finite wing. The results from the vortex-lattice method can give a better insight in the impact of small differences in the analysed sections.

References

[1] Wen-long Li et al. “Section Curve Reconstruction and Mean-Camber Curve Extraction of a Point-Sampled Blade Surface”. en. In: *PLoS ONE* 9.12 (Dec. 2014). Ed. by Rongrong Ji, e115471. ISSN: 1932-6203. DOI: 10.1371/journal.pone.0115471. URL: https://dx.plos.org/10.1371/journal.pone.0115471 (visited on 09/05/2023) (cit. on pp. x, 6, 42).

[2] R.W. Derksen and Tim Rogalsky. “Bezier-PARSEC: An optimized aerofoil parameterization for design”. In: *Advances in Engineering Software* 41.7 (2010). Advances in Structural Optimization, pp. 923–930. ISSN: 0965-9978. DOI: https://doi.org/10.1016/j.advengsoft.2010.05.002. URL: https://www.sciencedirect.com/science/article/pii/S0965997810000529 (cit. on pp. xi, 43, 44, 51, 60).

[3] Wenping Wang, Helmut Pottmann, and Yang Liu. “Fitting B-spline curves to point clouds by curvature-based squared distance minimization”. In: *ACM Trans. Graph.* 25.2 (Apr. 2006), pp. 214–238. ISSN: 0730-0301, 1557-7368. DOI: 10.1145/1138450.1138453. URL: https://dl.acm.org/doi/10.1145/1138450.1138453 (visited on 05/04/2023) (cit. on pp. xi, 45, 46).

[4] Giancarlo Tortora, Antonio Concilio, and Rosario Pecora. “Airfoil Shape Morphing through a Novel Parameterization and Fitting Optimization Method Based on Uniform Non-Rational B-Spline Functions”. In: *Designs* 7.1 (2023). ISSN: 2411-9660. DOI: 10.3390/designs7010028. URL: https://www.mdpi.com/2411-9660/7/1/28 (cit. on pp. xi, 60).

[5] John D. Anderson. *Fundamentals of aerodynamics*. Sixth edition. McGraw-Hill series in aeronautical and aerospace engineering. New York, NY: McGraw Hill Education, 2017. 1130 pp. ISBN: 978-1-259-12991-9 (cit. on pp. xi, 64).

[6] G.K. Ananda, P.P. Sukumar, and M.S. Selig. “Measured aerodynamic characteristics of wings at low Reynolds numbers”. In: *Aerospace Science and Technology* 42 (2015), pp. 392–406. ISSN: 1270-9638. DOI: https://doi.org/10.1016/j.ast.2014.11.016. URL: https://www.sciencedirect.com/science/article/pii/S1270963814002612 (cit. on pp. xiv, 65, 178).

[7] J.S. Carlton. “Chapter 9 - Cavitation”. In: *Marine Propellers and Propulsion (Fourth Edition)*. Ed. by J.S. Carlton. Fourth Edition. Butterworth-Heinemann, 2019, pp. 217–260. ISBN: 978-0-08-100366-4. DOI: https://doi.org/10.1016/B978-0-08-100366-4.00009-2. URL: https://www.sciencedirect.com/science/article/pii/B9780081003664000092 (cit. on pp. xiv, 6, 179).

[8] Anthony F. Molland and Stephen R. Turnock. “Chapter 4 - Hydrofoils”. In: *Marine Rudders, Hydrofoils and Control Surfaces (Second Edition)*. Ed. by Anthony F. Molland and Stephen R. Turnock. Second Edition. Oxford: Butterworth-Heinemann, 2022, pp. 57–89. ISBN: 978-0-12-824378-7. DOI: https://doi.org/10.1016/B978-0-12-824378-7.00005-6. URL: https://www.sciencedirect.com/science/article/pii/B9780128243787000056 (cit. on pp. xiv, 180).

[9] Michael Selig. “Low Reynolds Number Airfoil Design Lecture Notes”. In: *VKI Lect. Ser.* (Jan. 2003) (cit. on pp. xv, 6, 118, 119, 186).

[10] Damien LeRoy. *Foilboarding Beginner’s Guide*. Aug. 6, 2015. URL: https://kitesurfingmag.com/foilboarding-beginners-guide/ (visited on 08/31/2023) (cit. on p. 1).

[11] Scuttlebut Sailing News. *Americas Cup Hydrofoils 101*. July 13, 2016. URL: https://www.sailingscuttlebutt.com/2016/07/13/americas-cup-hydrofoils-101/ (visited on 08/31/2023) (cit. on p. 1).

[12] JR MEyER and JR WILkIns. “Hydrofoil Development and Applications”. In: *High-Performance Marine Vehicles Conf., Arlington, HF1-24*. 1992 (cit. on p. 1).

[13] Popular Mechanics. “Sailboat ”stilts” Boost Speed”. In: *Popular Mechanics* 105.2 (Feb. 1956), p. 136 (cit. on p. 1).

[14] Matthew Sheahan. *Foiling: The history of the hydrofoiler*. Dec. 2021. URL: https://www.yachtingworld.com/features/foiling-the-history-of-the-hydrofoiler-135741 (visited on 11/10/2022) (cit. on p. 1).

[15] Norimitsu Onishi. "When Billionaire Sets Rules, It's an Exclusive Race". In: *The New York Times* (June 2013). URL: https://www.nytimes.com/2013/06/04/us/americas-cup-sailing-race-faces-challenges-in-san-francisco.html (cit. on p. 1).

[16] In: *Olympics* (June 2017). URL: https://olympics.com/ioc/news/tokyo-2020-event-programme-to-see-major-boost-for-female-participation-youth-and-urban-appeal (visited on 08/31/2023) (cit. on p. 2).

[17] *Measurement of Daggerboards for Nacra 17*. URL: https://nacra17.org/wp-content/uploads/2019/04/Palma-2019-Report.pdf (visited on 05/10/2023) (cit. on pp. 2, 123, 165).

[18] *NACRA 17 HYDROFOILS*. URL: https://dnaperformancesailing.com/hydrofoil-manufacturer/nacra-17-hydrofoils-manufacturer/ (visited on 10/13/2022) (cit. on pp. 5, 166).

[19] Laura Marimon Giovannetti et al. "Fluid-Structure Interaction of a Foiling Craft". In: *JMSE* 10.3 (Mar. 6, 2022), p. 372. ISSN: 2077-1312. DOI: 10.3390/jmse10030372. URL: https://www.mdpi.com/2077-1312/10/3/372 (visited on 01/24/2023) (cit. on pp. 5, 10).

[20] KD Potter. "Understanding the origins of defects and variability in composites manufacture". In: *International conference on composite materials (ICCM)-17, Edinburgh, UK*. 2009, p. 18 (cit. on pp. 5, 167, 168).

[21] A. Brient et al. "An Experimental Analysis of the Effect of Roughness Produced by Machining on Hydrodynamic Performance of Two-Dimensional Hydrofoil". In: *Third International Conference NSN'03*. Saint Petersbourg, Russia, June 2003. URL: https://hal.science/hal-01763046 (cit. on pp. 5, 167).

[22] Farbod Khameneifar. "Section-specific geometric error evaluation of airfoil blades based on digitized surface data". PhD thesis. University of British Columbia, 2015. DOI: http://dx.doi.org/10.14288/1.0221356. URL: https://open.library.ubc.ca/collections/ubctheses/24/items/1.0221356 (cit. on p. 5).

[23] Farbod Khameneifar and Hsi-Yung Feng. "Airfoil profile reconstruction under the uncertainty of inspection data points". In: *Int J Adv Manuf Technol* 71.1 (Mar. 2014), pp. 675–683. ISSN: 0268-3768, 1433-3015. DOI: 10.1007/s00170-013-5527-3. URL: http://link.springer.com/10.1007/s00170-013-5527-3 (visited on 05/04/2023) (cit. on p. 6).

[24] Farbod Khameneifar and Hsi-Yung Feng. "A new methodology for evaluating position and orientation errors of airfoil sections". In: *Int J Adv Manuf Technol* 83.5 (Mar. 2016), pp. 1013–1023. ISSN: 0268-3768, 1433-3015. DOI: 10.1007/s00170-015-7641-x. URL: http://link.springer.com/10.1007/s00170-015-7641-x (visited on 05/04/2023) (cit. on p. 6).

[25] Nilesh Salunke, Juned Ahamad, and S. Channiwala. "Airfoil Parameterization Techniques: A Review". In: *American Journal of Mechanical Engineering* 2 (Jan. 2014), pp. 99–102. DOI: 10.12691/ajme-2-4-1 (cit. on p. 6).

[26] R.W. Derksen and Tim Rogalsky. "Bezier-PARSEC: An optimized aerofoil parameterization for design". In: *Advances in Engineering Software* 41.7 (July 2010), pp. 923–930. ISSN: 09659978. DOI: 10.1016/j.advengsoft.2010.05.002. URL: https://linkinghub.elsevier.com/retrieve/pii/S0965997810000529 (visited on 01/24/2023) (cit. on p. 6).

[27] Otto Schrenk. "Systematische Unter-suchungen an Joukowsky-Profilen." In: *Zeitschrift fur Flugtechnik und Motorluftschiffahrt* 18 (May 1927), pp. 225–230 (cit. on pp. 6, 172).

[28] Bob Allen. *NACA Airfoils*. URL: https://www.nasa.gov/image-feature/langley/100/naca-airfoils (visited on 10/31/2022) (cit. on pp. 6, 172).

[29] Ira H. Abbott and Albert E. von Doenhoff. *Theory of wing sections: including a summary of airfoil data*. Correc. rep. of : McGraw-Hill Book, 1949. New York: Dover, 1959. ISBN: 978-0-486-60586-9 (cit. on pp. 6, 181, 184, 185).

[30] Sighard F. Hoerner. *Fluid-dynamic drag : practical information on aerodynamic drag and hydrodynamic resistance.* 2nd ed. Section: .. cm. Bakersfield: Hoerner Fluid Dynamics, 1992. ISBN: 978-99911-944-4-8 (cit. on pp. 6, 179).

[31] SF Hoerner. *Some Characteristics of Spray and Ventilation*. Tech. rep. GIBBS and COX INC NEW YORK, 1953 (cit. on pp. 6, 181).

[32] Anthony F. Molland and Stephen R. Turnock. "Chapter 6 - Rudder experimental data". In: *Marine Rudders, Hydrofoils and Control Surfaces (Second Edition)*. Ed. by Anthony F. Molland

and Stephen R. Turnock. Second Edition. Oxford: Butterworth-Heinemann, 2022, pp. 105–296. ISBN: 978-0-12-824378-7. DOI: https://doi.org/10.1016/B978-0-12-824378-7.00012-3. URL: https://www.sciencedirect.com/science/article/pii/B9780128243787000123 (cit. on pp. 6, 177).

[33] KA Morch. "Dynamics of cavitation bubbles and cavitating liquids". In: *Treatise on Materials Science and Technology* 16 (1979), pp. 309–355 (cit. on pp. 6, 177).

[34] Y. L. Young et al. "Ventilation of Lifting Bodies: Review of the Physics and Discussion of Scaling Effects". In: *Applied Mechanics Reviews* 69.1 (Jan. 2017). 010801. ISSN: 0003-6900. DOI: 10.1115/1.4035360. eprint: https://asmedigitalcollection.asme.org/appliedmechanicsreviews/article-pdf/69/1/010801/6075202/amr_069_01_010801.pdf. URL: https://doi.org/10.1115/1.4035360 (cit. on pp. 6, 181, 182).

[35] Michael S Selig, John Francis Donovan, and David B Fraser. "Airfoils at low speeds". In: (1989) (cit. on pp. 6, 172, 181).

[36] Michael S Selig and James J Guglielmo. "High-lift low Reynolds number airfoil design". In: *Journal of aircraft* 34.1 (1997), pp. 72–79 (cit. on pp. 6, 184).

[37] Michael S. Selig et al. "Systematic airfoil design studies at low Reynolds Numbers". In: *Fixed and Flapping Wing Aerodynamics for Micro Air Vehicle Applications* 1995 (2001), pp. 143–167. DOI: 10.2514/5.9781600866654.0143.0167 (cit. on p. 6).

[38] Mark Drela. "XFOIL: An analysis and design system for low Reynolds number airfoils". In: *Low Reynolds number aerodynamics*. Springer, 1989, pp. 1–12 (cit. on pp. 6, 66, 68, 182).

[39] Richard A Eppler and Dan M Somers. *A computer program for the design and analysis of low-speed airfoils*. Vol. 80210. National Aeronautics, Space Administration, Scientific, and Technical …, 1980 (cit. on pp. 6, 182).

[40] Ole Bergmann et al. "Comparison and evaluation of blade element methods against RANS simulations and test data". In: *CEAS Aeronaut J* 13.2 (Apr. 2022), pp. 535–557. ISSN: 1869-5582, 1869-5590. DOI: 10.1007/s13272-022-00579-1. URL: https://link.springer.com/10.1007/s13272-022-00579-1 (visited on 01/24/2023) (cit. on p. 7).

[41] Alec Bagué. "Dynamic Stability Analysis of a Hydrofoiling Sailing Boat using CFD." PhD thesis. June 2019 (cit. on p. 7).

[42] Kai Graf et al. "VPP-driven sail and foil trim optimization for the Olympic NACRA 17 foiling catamaran". In: *Journal of Sailing Technology* 5.01 (2020), pp. 61–81 (cit. on p. 7).

[43] Laura Marimon Giovannetti et al. "Fluid-Structure Interaction of a Foiling Craft". In: *Journal of Marine Science and Engineering* 10.3 (2022), p. 372 (cit. on pp. 7, 182).

[44] Alec Bagué et al. "Dynamic Stability Analysis of a Hydrofoiling Sailing Boat using CFD". In: *Journal of Sailing Technology* 6.1 (Mar. 22, 2021), pp. 58–72. ISSN: 2475-370X. DOI: 10.5957/jst/2021.6.1.58. URL: https://onepetro.org/JST/article/6/01/58/460849/Dynamic-Stability-Analysis-of-a-Hydrofoiling (visited on 01/24/2023) (cit. on p. 7).

[45] Nacra Sailing. *Flying an Olympic Powerhouse*. URL: https://nacrasailing.com/boat-portal/racing/nacra-17-olympic/ (visited on 03/22/2023) (cit. on p. 10).

[46] Nacra 17 Class. *Nacra 17*. URL: https://nacra17.org/nacra17/ (visited on 03/22/2023) (cit. on p. 10).

[47] Pipistrel. *Alpha trainer*. Apr. 2023. URL: https://www.pipistrel-aircraft.com/products/alpha-trainer/ (visited on 09/12/2023) (cit. on p. 10).

[48] Vinesh Raja and Kiran J. Fernandes, eds. *Reverse engineering: an industrial perspective*. Springer series in advanced manufacturing. OCLC: ocm86168229. London: Springer, 2008. 242 pp. ISBN: 978-1-84628-855-5 (cit. on pp. 18, 19).

[49] FARO. *FARO®Quantum Max ScanArms, The global standard in non-contact measurement arm technology*. URL: https://www.faro.com/en/Products/Hardware/ScanArms (visited on 06/09/2023) (cit. on p. 19).

[50] OLDBAC. *HANDYSCAN 3d™BLACK SERIES*. Feb. 2023. URL: https://oldbac.com/hardware-item/handyscan-3d/ (visited on 06/09/2023) (cit. on p. 19).

[51] Creaform. *Technical specifications*. URL: https://www.creaform3d.com/en/portable-3d-scanner-handyscan-3d/technical-specifications (cit. on p. 20).

[52] *HandySCAN 3D|BLACK Series technical specifications*. URL: https://www.creaform3d.com/en/portable-3d-scanner-handyscan-3d/technical-specifications (visited on 05/02/2023) (cit. on p. 20).

[53] *FARO QUANTUME FAROARM*. URL: https://euromarket.bg/js/tiny_mce/plugins/ajaxfilemanager/upload/Machine-Tools/TechSheet_QuantumE_FM_AM_EN.pdf (visited on 05/02/2023) (cit. on p. 20).

[54] George P. Pavlidis. *Laser scanning using a laser pointing device and a camera*. 2006. URL: https://georgepavlides.info/research/LaserScanningAndTriangulation.php (visited on 09/06/2022) (cit. on p. 21).

[55] Nicholas Adrian and Quang-Cuong Pham. "Locating Transparent Objects to Millimetre Accuracy". In: *arXiv e-prints*, arXiv:1903.02908 (Mar. 2019), arXiv:1903.02908. DOI: 10.48550/arXiv.1903.02908. arXiv: 1903.02908 [cs.RO] (cit. on p. 23).

[56] Paul Motley. *HOW TO SCAN DARK, SHINY, OR CLEAR SURFACES WITH A 3D SCANNER [WITH VIDEO DEMO]*. Mar. 19, 2021. URL: https://gomeasure3d.com/blog/scan-dark-shiny-clear-surfaces-3d-scanner-video-demo/ (visited on 07/14/2023) (cit. on p. 23).

[57] GISGeograpy. *How GPS Receivers Work – Trilateration vs Triangulation*. May 31, 2022. URL: https://gisgeography.com/trilateration-triangulation-gps/ (visited on 07/14/2023) (cit. on p. 24).

[58] Hiroshi Shintaku et al. "Three-dimensional surface models of autopsied human brains constructed from multiple photographs by photogrammetry". In: *PLOS ONE* 14 (July 2019), e0219619. DOI: 10.1371/journal.pone.0219619 (cit. on p. 24).

[59] Creaform. *REVERSE ENGINEERING OF PHYSICAL OBJECTS – TEACHING MANUAL*. Mar. 2014. URL: https://www.creaform3d.com/sites/default/files/assets/technological-fundamentals/teaching_manual_reverse_engineering_en_18032014_6.pdf (visited on 06/13/2023) (cit. on p. 25).

[60] J Gordon leishman. "Airfoil Geometries". In: *Introduction to Aerospace Flight Vehicles*. Embry-Riddle Aeronautical University, 2023 (cit. on pp. 32, 33, 41).

[61] Dale Crane. *Dictionary of Aeronautical Terms*. Aviation Supplies & Academics,Inc, 1991. ISBN: 1-56027-071-3 (cit. on p. 32).

[62] Stewart Glegg and William Devenport. "Chapter 2 - The equations of fluid motion". In: *Aeroacoustics of Low Mach Number Flows*. Ed. by Stewart Glegg and William Devenport. Academic Press, 2017, pp. 9–48. ISBN: 978-0-12-809651-2. DOI: https://doi.org/10.1016/B978-0-12-809651-2.00002-3. URL: https://www.sciencedirect.com/science/article/pii/B9780128096512000023 (cit. on p. 38).

[63] Alfred Gray, Elsa Abbena, and Simon Salamon. "Modern Differential Geometry of Curves and Surfaces with Mathematica, Third Edition (Studies in Advanced Mathematics)". In: Chapman & Hall/CRC, 2006. Chap. CHAPTER 7. CURVES IN SPACE, pp. 119–228. ISBN: 1584884487 (cit. on pp. 40, 46).

[64] Vera Galishnikova and Peter Pahl. "Constrained Construction of Planar Delaunay Triangulations without Flipping". In: *Structural Mechanics of Engineering Constructions and Buildings* 14 (Dec. 2018), pp. 154–174. DOI: 10.22363/1815-5235-2018-14-2-154-174 (cit. on p. 41).

[65] Georges Voronoi. "Nouvelles applications des paramètres continus à la théorie des formes quadratiques. Premier mémoire. Sur quelques propriétés des formes quadratiques positives parfaites." In: *Journal für die reine und angewandte Mathematik* 133 (1908), pp. 97–178. URL: http://eudml.org/doc/149276 (cit. on p. 41).

[66] Jin Chen et al. "A new direct design method of wind turbine airfoils and wind tunnel experiment". In: *Applied Mathematical Modelling* 40.3 (2016), pp. 2002–2014. ISSN: 0307-904X. DOI: https://doi.org/10.1016/j.apm.2015.09.051. URL: https://www.sciencedirect.com/science/article/pii/S0307904X15005855 (cit. on p. 49).

[67] *Custom Parts*. URL: https://dnaperformancesailing.com/custom-parts/ (visited on 10/13/2022) (cit. on pp. 54, 166, 168).

[68] Олег Жилко. *Smoke curling into the air*. URL: https://unsplash.com/photos/C5ayHUXMMX8?utm_source=unsplash&utm_medium=referral&utm_content=creditShareLink (visited on 10/11/2022) (cit. on pp. 64, 174).

[69] John Anderson. *Fundamentals of Aerodynamics*. 6th ed. Vol. SI edition. 2 Penn Plaza, New York, NY 10121: McGraw-Hill Education, 2017, pp. 5–496. ISBN: 9781259251344 (cit. on pp. 64, 172–175).

[70] Patrick Ploe. “Surrogate-based optimization of hydrofoil shapes using RANS simulations”. Theses. École centrale de Nantes, June 2018. URL: https://theses.hal.science/tel-02050026 (cit. on pp. 65, 181).

[71] *Water - Dynamic (Absolute) and Kinematic Viscosity vs. Temperature and Pressure*. URL: https://www.engineeringtoolbox.com/water-dynamic-kinematic-viscosity-d_596.html (visited on 09/11/2023) (cit. on p. 68).

[72] *Seawater - Properties*. URL: https://www.engineeringtoolbox.com/sea-water-properties-d_840.html (visited on 09/11/2023) (cit. on p. 68).

[73] Neil Patterson and Jonathan Binns. “Development of a Six Degree of Freedom Velocity Prediction Program for the foiling America’s Cup Vessels”. In: *Journal of Sailing Technology* 7 (1 2022), pp. 120–151. URL: http://onepetro.org/JST/article-pdf/7/01/120/2790895/sname-jst-2022-06.pdf/1 (cit. on p. 68).

[74] Robert J McGhee, William D Beasley, and Dan M Somers. *Low-speed aerodynamic characteristics of a 13-percent-thick airfoil section designed for general aviation applications*. Tech. rep. 1975 (cit. on p. 118).

[75] Thomas E Speer. “The BASILISCUS Project-Return of the cruising hydrofoil sailboat”. In: *Chesapeake Sailing Yacht Symposium*. 2001, pp. 1–22 (cit. on p. 118).

[76] addcomposites. *What are the Fundamental Steps of Composites Manufacturing?* 2022. URL: https://www.addcomposites.com/post/fundamentals-of-composites-manufacturing (visited on 03/22/2023) (cit. on p. 165).

[77] Lee Harper and Mike Clifford. “1 - Introduction”. In: *Design and Manufacture of Structural Composites*. Ed. by Lee Harper and Mike Clifford. Woodhead Publishing Series in Composites Science and Engineering. Woodhead Publishing, 2023, pp. 3–17. ISBN: 978-0-12-819160-6. DOI: https://doi.org/10.1016/B978-0-12-819160-6.00009-3. URL: https://www.sciencedirect.com/science/article/pii/B9780128191606000093 (cit. on p. 166).

[78] Pascal Hubert. “9 - Autoclave and out-of-autoclave processing of prepregs”. In: *Design and Manufacture of Structural Composites*. Ed. by Lee Harper and Mike Clifford. Woodhead Publishing Series in Composites Science and Engineering. Woodhead Publishing, 2023, pp. 209–236. ISBN: 978-0-12-819160-6. DOI: https://doi.org/10.1016/B978-0-12-819160-6.00020-2. URL: https://www.sciencedirect.com/science/article/pii/B9780128191606000202 (cit. on p. 166).

[79] Mark Bowkett and Kary Thanapalan. “Comparative analysis of failure detection methods of composites materials’ systems”. In: *Systems Science & Control Engineering* 5 (Jan. 2017), pp. 168–177. DOI: 10.1080/21642583.2017.1311240 (cit. on p. 167).

[80] M. Grabow et al. “Influence of the manufacturing process on the interlaminar tensile strength of thick unidirectional continuous epoxy/carbon fibre composites”. In: *Composites Part A: Applied Science and Manufacturing* 154 (2022), p. 106754. ISSN: 1359-835X. DOI: https://doi.org/10.1016/j.compositesa.2021.106754. URL: https://www.sciencedirect.com/science/article/pii/S1359835X21004668 (cit. on pp. 167, 169).

[81] Ismet Baran et al. “A Review on the Mechanical Modeling of Composite Manufacturing Processes”. en. In: *Archives of Computational Methods in Engineering* 24.2 (Apr. 2017), pp. 365–395. ISSN: 1134-3060, 1886-1784. DOI: 10.1007/s11831-016-9167-2. URL: http://link.springer.com/10.1007/s11831-016-9167-2 (visited on 05/15/2023) (cit. on p. 168).

[82] J Wang et al. “Experimental fabrication and characterization of out-of-plane fiber waviness in continuous fiber-reinforced composites”. In: *Journal of Composite Materials* 46.17 (2012), pp. 2041–2053. DOI: 10.1177/0021998311429877. eprint: https://doi.org/10.1177/0021998311429877. URL: https://doi.org/10.1177/0021998311429877 (cit. on p. 168).

[83] Artemis Technologies. *Amazon River - Artemis Technologies*. YouTube. Oct. 2018. URL: https://www.youtube.com/watch?v=q2il8Fagbyk (cit. on p. 171).

[84] Gary Anderson. *WHY SOME F1 DRIVERS THRIVE IN CARS THAT SINK THEIR TEAM-MATES*. The Race. URL: https://the-race.com/formula-1/why-some-f1-drivers-thrive-in-cars-that-sink-their-team-mates/ (visited on 09/06/2022) (cit. on p. 171).

[85] Michael Eckert. *The Dawn of Fluid Dynamics: A Discipline between Science and Technology*. en. 1st ed. Wiley, Dec. 2005. ISBN: 978-3-527-61073-0. DOI: 10.1002/9783527610730. URL: https://onlinelibrary.wiley.com/doi/book/10.1002/9783527610730 (visited on 05/05/2023) (cit. on p. 172).

[86] H. Schlichting and F.W. Riegels. *Grenzschicht-Theorie.* German. 8. Aufl. Section: 843 blz. ; .. cm. Karlsruhe: Braun, 1982. ISBN: 978-3-7650-1011-8 (cit. on p. 172).

[87] Ira H Abbott and Albert E Von Doenhoff. *Theory of wing sections: including a summary of airfoil data*. Courier Corporation, 2012 (cit. on p. 172).

[88] Richard Eppler. “Some new airfoils”. In: *NASA. Langley Res. Center The Sci. and Technol. of Low Speed and Motorless Flight, Pt. 1* (1979) (cit. on pp. 172, 181).

[89] Theodore A Talay. *Introduction to the Aerodynamics of Flight*. Special Publication (SP) NASA-SP-367. NASA Langley Research Centre Hampton, Jan. 1975 (cit. on pp. 174, 175).

[90] E.L. Houghton et al. “Chapter 3 - Viscous Flow and Boundary Layers”. In: *Aerodynamics for Engineering Students (Seventh Edition)*. Ed. by E.L. Houghton et al. Seventh Edition. Butterworth-Heinemann, 2017, pp. 151–254. ISBN: 978-0-08-100194-3. DOI: https://doi.org/10.1016/B978-0-08-100194-3.00003-1. URL: https://www.sciencedirect.com/science/article/pii/B9780081001943000031 (cit. on pp. 175, 177).

[91] Heinz Heisler. “14 - Vehicle body aerodynamics”. In: *Advanced Vehicle Technology (Second Edition)*. Ed. by Heinz Heisler. Second Edition. Oxford: Butterworth-Heinemann, 2002, pp. 584–634. ISBN: 978-0-7506-5131-8. DOI: https://doi.org/10.1016/B978-075065131-8/50015-4. URL: https://www.sciencedirect.com/science/article/pii/B9780750651318500154 (cit. on p. 176).

[92] Michael Miller. “The Multi-Objective Design of Flatback Wind Turbine Airfoils”. Master of Applied Science. Ottawa, Ontario: Carleton University, 2017. DOI: 10.22215/etd/2017-11723. URL: https://curve.carleton.ca/8092922f-e0da-4c2e-a8c0-08478d940059 (visited on 05/16/2023) (cit. on p. 176).

[93] Guoyu Wang et al. “Dynamics of attached turbulent cavitating flows”. In: *Progress in Aerospace sciences* 37.6 (2001), pp. 551–581 (cit. on p. 177).

[94] Deyou Li et al. “Numerical study of the hydrofoil cavitation flow with thermodynamic effects”. In: *Renewable Energy* 169 (May 2021), pp. 894–904. ISSN: 18790682. DOI: 10.1016/j.renene.2021.01.073 (cit. on p. 177).

[95] J. S. Carlton. “Chapter 12 - Resistance and Propulsion”. In: *Marine Propellers and Propulsion (Fourth Edition)*. Ed. by J. S. Carlton. Fourth Edition. Butterworth-Heinemann, 2019, pp. 313–365. ISBN: 978-0-08-100366-4. DOI: https://doi.org/10.1016/B978-0-08-100366-4.00012-2. URL: https://www.sciencedirect.com/science/article/pii/B9780081003664000122 (cit. on pp. 178, 179).

[96] Kaoruko Onishi, Kunimasa Matsuda, and Kazuyoshi Miyagawa. “Influence of hydrophilic and hydrophobic coating on hydrofoil performance”. In: *International Symposium on Transport Phenomena and Dynamics of Rotating Machinery (ISROMAC 2017)*. 2017 (cit. on p. 178).

[97] Samuel M. Smith et al. “The influence of fluid–structure interaction on cloud cavitation about a stiff hydrofoil. Part 1.” In: *Journal of Fluid Mechanics* 896 (2020), A1. DOI: 10.1017/jfm.2020.321 (cit. on p. 178).

[98] Günter H Schnerr and Jürgen Sauer. “Physical and numerical modeling of unsteady cavitation dynamics”. In: *Fourth international conference on multiphase flow*. Vol. 1. ICMF New Orleans New Orleans, LO, USA. 2001 (cit. on p. 178).

[99] Jiafeng Hao, Mindi Zhang, and Xu Huang. “The influence of surface roughness on cloud cavitation flow around hydrofoils”. In: *Acta Mechanica Sinica/Lixue Xuebao* 34 (1 Feb. 2018). investigated cavitation with a smooth and rough hydrofoil. It found that the cavitation on a rough hydrofoil was experienced an additional step for the development of the cloud cavitation.
It also influenced the flow pattern where it ocured as subulate cavities. The cavity area was also larger. The cavitaion on a rough surface is more servere., pp. 10–21. ISSN: 16143116. DOI: 10.1007/s10409-017-0689-0 (cit. on p. 178).

[100] Moran Charlou and Jeroen Wackers. “Numerical simulation of bi-stable ventilated flows around surface-piercing hydrofoils”. In: *22th Numerical Towing Tank Symposium, NUTTS’19*. 2019 (cit. on p. 181).

[101] Casey M Harwood, Yin L Young, and Steven L Ceccio. “Ventilated cavities on a surface-piercing hydrofoil at moderate Froude numbers: cavity formation, elimination and stability”. In: *Journal of Fluid Mechanics* 800 (2016), pp. 5–56 (cit. on p. 181).

[102] Thilo Keller et al. “Numerical simulations of a surface piercing A-class catamaran hydrofoil and comparison against model tests”. In: *Journal of Sailing Technology* 2.01 (2017), pp. 1–24 (cit. on p. 181).
[103] Ivan U Vakarelski et al. “When superhydrophobicity can be a drag: Ventilated cavitation and splashing effects in hydrofoil and speed-boat models tests”. In: *Colloids and Surfaces A: Physicochemical and Engineering Aspects* 628 (2021), p. 127344 (cit. on p. 181).
[104] Monroe Conner. *Daedalus Human-Powered Aircraft*. 2017. URL: https://www.nasa.gov/centers/dryden/multimedia/imagegallery/Daedalus/EC87-0014-8.html (visited on 03/22/2023) (cit. on p. 181).
[105] JM Wetzel. “Ventilation of bodies piercing a free surface”. In: *Second Symposium on Naval Hydrodynamics-Hydrodynamic Noise/Cavity Flow*. 1960, pp. 447–467 (cit. on p. 181).
[106] Richard Stone Rothblum. “Investigation of methods of delaying or controlling ventilation on surface piercing struts”. PhD thesis. University of Leeds, 1977 (cit. on p. 181).
[107] Deniz Tolga Akcabay et al. “Cavity induced vibration of flexible hydrofoils”. In: *Journal of Fluids and Structures* 49 (2014), pp. 463–484. ISSN: 0889-9746. DOI: https://doi.org/10.1016/j.jfluidstructs.2014.05.007. URL: https://www.sciencedirect.com/science/article/pii/S0889974614001030 (cit. on p. 181).
[108] Deniz Tolga Akcabay and Yin Lu Young. “Parametric excitations and lock-in of flexible hydrofoils in two-phase flows”. In: *Journal of Fluids and Structures* 57 (2015), pp. 344–356. ISSN: 0889-9746. DOI: https://doi.org/10.1016/j.jfluidstructs.2015.06.004. URL: https://www.sciencedirect.com/science/article/pii/S0889974615001346 (cit. on pp. 181, 182).
[109] DT Akcabay et al. “Cavity-induced vibrations of flexible hydrofoils and their susceptibility to lock-in and parametric excitations”. In: *Proceedings of the 2014 Symposium on Naval Hydrodynamics*. Vol. 570. 2014 (cit. on p. 181).
[110] François Axisa and José Antunes. “Introduction”. In: *Fluid-Structure Interaction*. Ed. by François Axisa and Jose Antunes. Vol. 3. Modelling of Mechanical Systems. Butterworth-Heinemann, 2007, pp. xvii–xx. DOI: https://doi.org/10.1016/S1874-7051(07)80003-X. URL: https://www.sciencedirect.com/science/article/pii/S187470510780003X (cit. on p. 182).
[111] Yong Zhao and Xiaohui Su. “Chapter 1 - Introduction”. In: *Computational Fluid-Structure Interaction*. Ed. by Yong Zhao and Xiaohui Su. Academic Press, 2019, pp. 1–10. ISBN: 978-0-12-814770-2. DOI: https://doi.org/10.1016/B978-0-12-814770-2.00001-5. URL: https://www.sciencedirect.com/science/article/pii/B9780128147702000015 (cit. on p. 182).
[112] J Knight et al. “Fluid Structure Interaction of Hydrofoils”. In: Used Star-CCM+ to analys AC45 daggerboards found good correlation when comparing the results with a straight NACA0012 foil. The materials was assumed to by isotropic and solid. Institute of Marine Engineering, Science and Technology (IMarEST), Nov. 2019. DOI: 10.24868/icmet.oman.2019.015 (cit. on p. 182).
[113] Vanilla Temtching Temou et al. “An experimental and numerical study of FSI applied to sail yacht flexible hydrofoil with large deformations”. In: *FIV2018-9th International Symposium on fluid-structure interactions, Flow-Sound interactions, flow-induced vibration & noise. July 8-11, 2018, Toronto, Ontario, Canada*. 2018 (cit. on p. 182).
[114] Vanilla Temtching Temou. “Experimental and numerical study of fluid-structure interactions on flexible hydrofoils in composites”. PhD thesis. Université de Bretagne occidentale-Brest, 2020 (cit. on p. 182).
[115] RF Nicholls-Lee, SR Turnock, and SW Boyd. “Application of bend-twist coupled blades for horizontal axis tidal turbines”. In: *Renewable Energy* 50 (2013), pp. 541–550 (cit. on p. 182).
[116] L Marimon Giovannetti et al. “Toward the development of a hydrofoil tailored to passively reduce its lift response to fluid load”. In: *Ocean Engineering* 167 (2018), pp. 1–10 (cit. on p. 182).
[117] Laura Marimon Giovannetti. “Fluid structure interaction testing, modelling and development of passive adaptive composite foils”. PhD thesis. University of Southampton, Mar. 2017. URL: https://eprints.soton.ac.uk/412651/ (cit. on p. 182).
[118] Martin Hepperle. *JAVAFOIL user’s guide*. 2017. URL: https://www.mh-aerotools.de/airfoils/java/JavaFoil%20Users%20Guide.pdf (visited on 09/11/2022) (cit. on pp. 183, 184).
[119] Falk Götten. “A highly automated method for simulating airfoil characteristics at low Reynolds number using a RANS-transition approach”. In: (2020) (cit. on p. 183).
[120] Howard H. Hu. “Chapter 10 - Computational Fluid Dynamics”. In: *Fluid Mechanics (Fifth Edition)*. Ed. by Pijush K. Kundu, Ira M. Cohen, and David R. Dowling. Fifth Edition. Boston: Academic

Press, 2012, pp. 421–472. ISBN: 978-0-12-382100-3. DOI: https://doi.org/10.1016/B978-0-12-382100-3.10010-1. URL: https://www.sciencedirect.com/science/article/pii/B9780123821003100101 (cit. on p. 183).

[121] Donreid. *Aerofoilengineering*. [accessed: 23/01/2023]. Aerofoilengineering. URL: https://aerofoilengineering.com/Validation.php (cit. on p. 183).

[122] Vasile PRISACARIU. "AERODYNAMIC ANALYSIS OF THE CLARK YH AIRFOIL". In: (2021), p. 37 (cit. on p. 183).

[123] Joseph Katz and Allen Plotkin. *Low-speed aerodynamics*. Vol. 13. Cambridge university press, 2001 (cit. on p. 183).

[124] Ole Bergmann et al. "Comparison and evaluation of blade element methods against RANS simulations and test data". In: *CEAS Aeronautical Journal* 13.2 (2022), pp. 535–557 (cit. on pp. 183, 184).

[125] J. Morgado et al. "XFOIL vs CFD performance predictions for high lift low Reynolds number airfoils". In: *Aerospace Science and Technology* 52 (2016), pp. 207–214. ISSN: 1270-9638. DOI: https://doi.org/10.1016/j.ast.2016.02.031. URL: https://www.sciencedirect.com/science/article/pii/S1270963816300839 (cit. on pp. 183, 184).

[126] Danny Nguyen. *Validation and Improvement of the TNO Model for Trailing Edge Noise Prediction*. University of California, Davis, 2018 (cit. on p. 183).

[127] Onur Günel, Emre Koç, and Tahir Yavuz. "CFD vs. XFOIL of airfoil analysis at low reynolds numbers". In: *2016 IEEE International Conference on Renewable Energy Research and Applications (ICRERA)*. IEEE. 2016, pp. 628–632 (cit. on pp. 183, 184).

[128] Abu Bakar et al. "Multi-Objective Optimization of Low Reynolds Number Airfoil Using Convolutional Neural Network and Non-Dominated Sorting Genetic Algorithm". In: *Aerospace* 9.1 (2022), p. 35 (cit. on p. 183).

[129] Omer Kemal Kinaci. "A numerical parametric study on hydrofoil interaction in tandem". In: *International Journal of Naval Architecture and Ocean Engineering* 7.1 (2015), pp. 25–40. ISSN: 2092-6782. DOI: https://doi.org/10.1515/ijnaoe-2015-0003. URL: https://www.sciencedirect.com/science/article/pii/S2092678216300991 (cit. on p. 184).

[130] Akira Oyama et al. "Aerodynamic optimization of transonic wing design based on evolutionary algorithm". In: *Third international conference on nonlinear problems in aviation and aerospace*. 2000, pp. 537–546 (cit. on p. 184).

[131] Ava Shahrokhi and Alireza Jahangirian. "Airfoil shape parameterization for optimum Navier–Stokes design with genetic algorithm". In: *Aerospace science and technology* 11.6 (2007), pp. 443–450 (cit. on p. 184).

[132] Tim Rogalsky and R. Derksen. "Bézier-PARSEC parameterization for airfoil optimization". In: *Canadian Aeronautics and Space Journal* 55 (Dec. 2009), pp. 163–174. DOI: 10.5589/q10-002 (cit. on p. 184).

[133] Xiaoqiang Lu et al. "An improved geometric parameter airfoil parameterization method". In: *Aerospace Science and Technology* 78 (2018), pp. 241–247. ISSN: 1270-9638. DOI: https://doi.org/10.1016/j.ast.2018.04.025. URL: https://www.sciencedirect.com/science/article/pii/S1270963817304686 (cit. on p. 184).

[134] Brenda M. Kulfan. "Universal Parametric Geometry Representation Method". In: *Journal of Aircraft* 45.1 (2008), pp. 142–158. DOI: 10.2514/1.29958. eprint: https://doi.org/10.2514/1.29958. URL: https://doi.org/10.2514/1.29958 (cit. on p. 184).

[135] Zachary P Backas. "Parametric optimization of a kiteboarding hydrofoil using computational fluid dynamics". In: *International Hydrofoil Society Mandles Prize for Hydrofoil Excellence* (2016) (cit. on p. 184).

[136] Pierluigi Guida, Laura Marimon Giovannetti, and Stephen Boyd. "Three-dimensional variations of the NACRA 17 main foil for benchmarking shape optimizations". In: *Proceedings of the 5th International Conference on Innovation in hiugh Performance Sailing Yachts and Sail-Assisted Propulsion* (2020), pp. 15–17 (cit. on p. 184).

[137] Georgios Pechlivanoglou. "Passive and active flow control solutions for wind turbine blades". In: 2013 (cit. on p. 185).

VI

Appendices

A

Digitisation of the Nacra 17 HydrofoilAppendices

A.1. VXelement Output files

File types explained that can be exported by VXelements.

.dea A DAE file is a 3D interchange file used for exchanging digital assets between a variety of graphics programs. It may contain an image, textures, or most likely, a 3D model. The DAE format is based on the COLLADA (COLLAborative Design Activity) XML schema, which is now owned and developed by Autodesk. https://fileinfo.com/extension/dae

.fbx Developed by Kaydara and owned by Autodesk since 2006. It is used to provide interoperability between digital content creation applications. FBX is also part of Autodesk Gameware, a series of video game middleware. https://en.wikipedia.org/wiki/FBX

.ma Animation file type

.obj The OBJ file format is an open data-format that represents 3D geometry alone — namely, the position of each vertex, the position of each vertex in a coordinate system. OBJ coordinates have no units, but OBJ files can contain scale information in a readable comment line. As this format is widely used by 3D modeling programs, it can be transferred between programs and interpreted on its own by some slicing and host softwares for 3D printing without exporting as an STL file. https://www.core77.com/posts/67499/Understanding-the-Different-Types-of-3D-Files

.ply Ply is a computer file format known as the Polygon File Format or the Stanford Triangle Format. The format was principally designed by the Stanford Graphics Lab to store three dimensional data from 3D scanners. In some cases this can be used as alternative to STL files. https://www.core77.com/posts/67499/Understanding-the-Different-Types-of-3D-Files

.stl STL (STereoLithography) is a file format native to the stereolithography CAD software created by 3D Systems. STL is also known as Standard Tessellation Language. This file format is supported by many other software packages; it is widely used for rapid prototyping and computer-aided manufacturing. STL files describe only the surface geometry of a three-dimensional object without any representation of color, texture or other common CAD model attributes. An STL file describes a raw unstructured triangulated surface by geometries located within a standard Cartesian coordinate system. STL coordinates must be positive numbers, there is no scale information, and the units are arbitrary. https://www.core77.com/posts/67499/Understanding-the-Different-Types-of-3D-Files

.txt A very broad file format and it is not clear how vxelement would use this.

.wrl As we described earlier, VRML helps translate 3D objects and image sequences into language that websites can understand and interpret. This helps enable interactive web experiences, where

users can view, move, and rotate objects around to get an accurate picture of how they might render in real life. https://blog.spatial.com/wrl-file

.x3d Used chiefly by printing service bureaus, X3D files can store a vast amount of information related to 3D graphics and scenery. The format is XML-based, supporting complex renderings and visualizations across software platforms. X3D strives to become the 3D graphics standard for web-based content, as it is robust enough for viewing objects—whereas most other formats are largely useful only for modeling parts and interpreting surface data. https://www.core77.com/posts/67499/Understanding-the-Different-Types-of-3D-Files

.x3dz Compressed x3d file

.zpr No information

.3mf The 3D with other 3D file formats. The 3MF Consortium came into being to deliver to the additive manufacturing industry a file format that is. https://3mf.io/specification/

.IGES Old 3D modelling software file standard

.STEP New more modern 3D modelling software. Best fidality for the full model.

A.2. Catia Fuctions

These images show the different functions used in Catia for hydrofoil processing. The environment of the function is given in the caption of each image. The steps taken for the foil processing are explained in subsection 4.2.4.

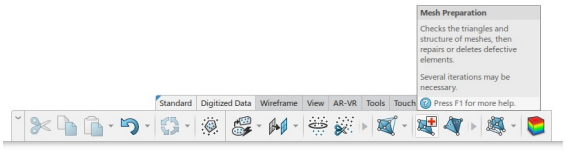

Figure A.1: Mesh pathologies in: Digitize shape preparation

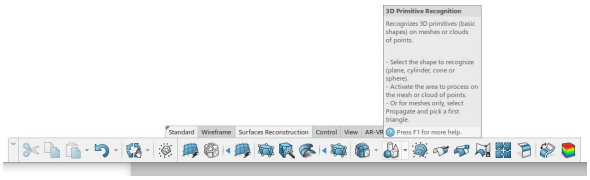

Figure A.2: 3D primative Recognitoin in: Digitize shape to surface

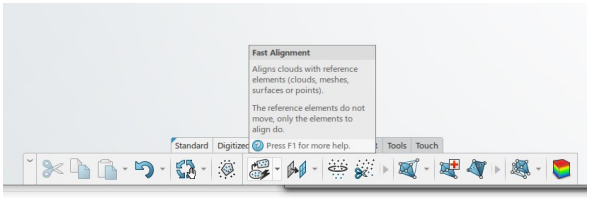

Figure A.3: Fast alignment: all named environments

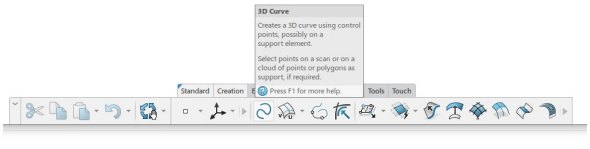

Figure A.4: 3D curve: Digitize shape to surface

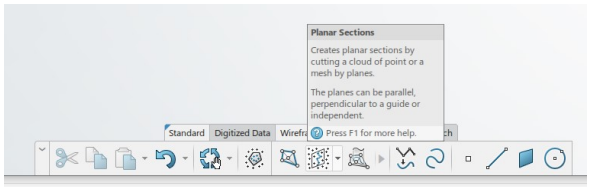

Figure A.5: Planer section in: Digitize shape preparation

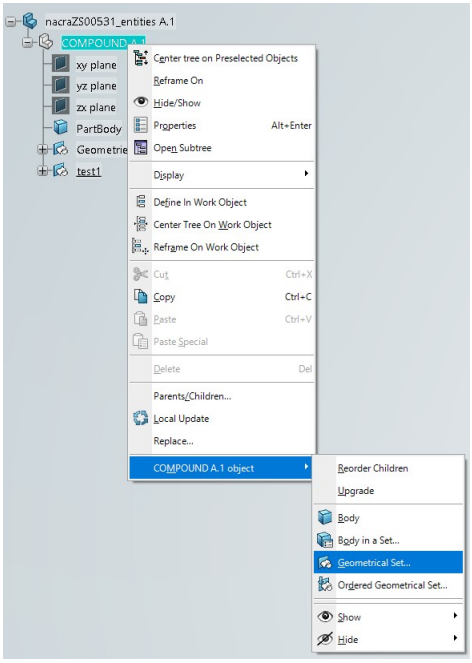

Figure A.6: Geometrical set in: all named environments

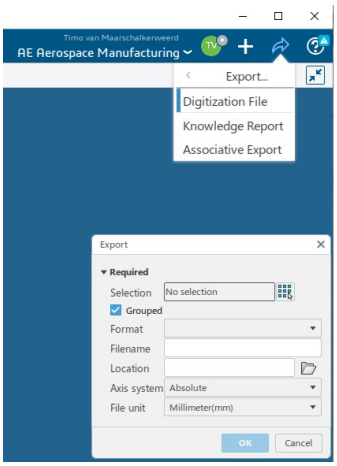

Figure A.7: Export digitised file in: all named environments

A.3. VXelement Comparison Figures

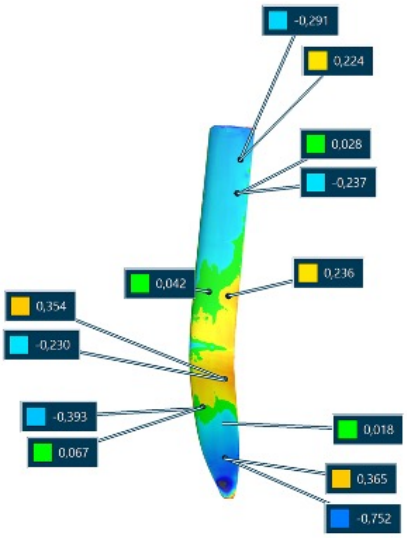

(a) Hydrofoil ZS00663 compared with ZS00531, low pressure side

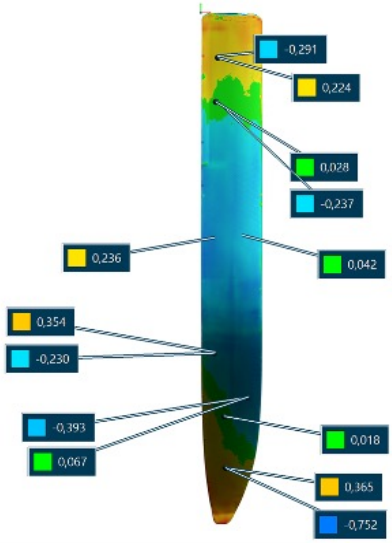

(b) Hydrofoil ZS00663 compared with ZS00531, high pressure side

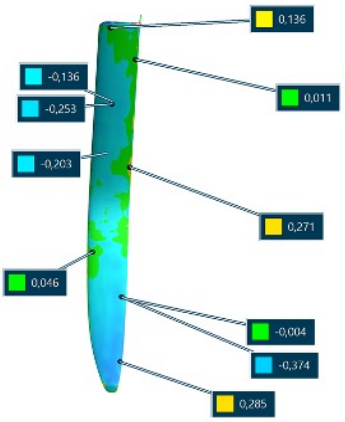

(c) Hydrofoil ZS00691 compared with ZS00531, low pressure side

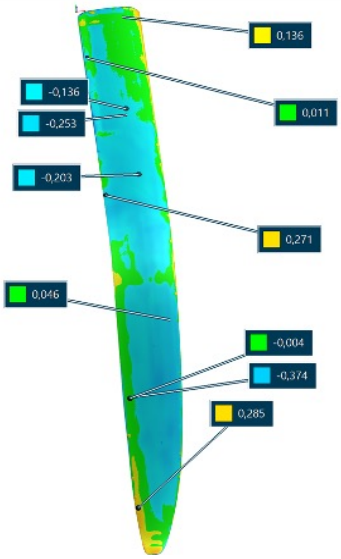

(d) Hydrofoil ZS00691 compared with ZS00531, high pressure side

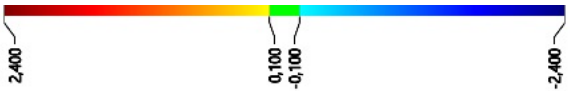

(e) gradient scale

Figure A.8: Nacra 17 Starboard Hydrofoils compared using VXelement

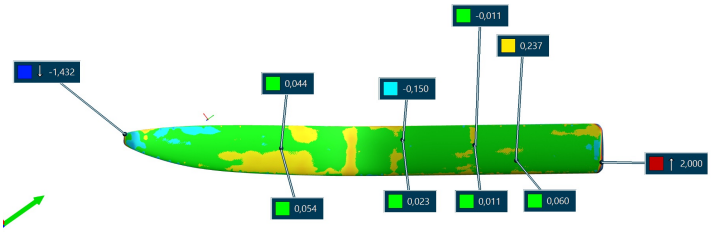

(a) Hydrofoil ZS00544 compared with ZS00696, low pressure side.

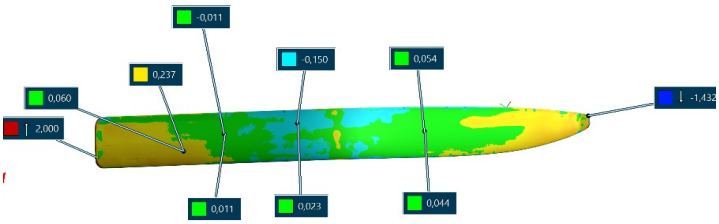

(b) Hydrofoil ZS00544 compared with ZS00696, high pressure side.

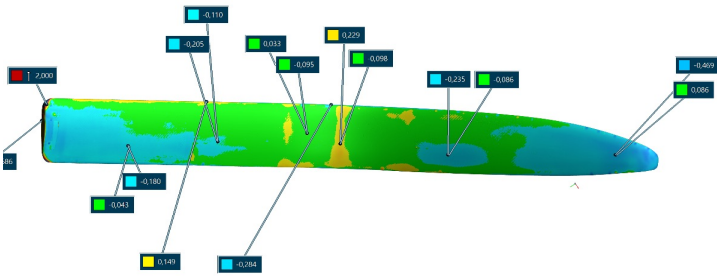

(c) Hydrofoil ZS00664 compared with ZS00696, low pressure side.

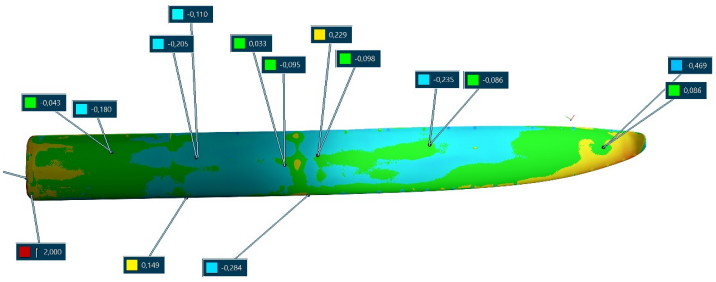

(d) Hydrofoil ZS00664 compared with ZS00696, high pressure side.

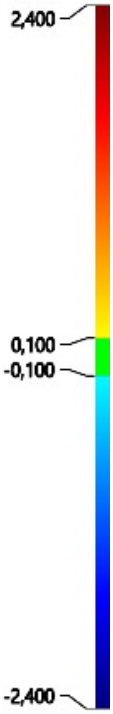

(e) gradient scale

Figure A.9: Nacra 17 Port Hydrofoils compared using VXelement

A.4. Catia Comparison Figures

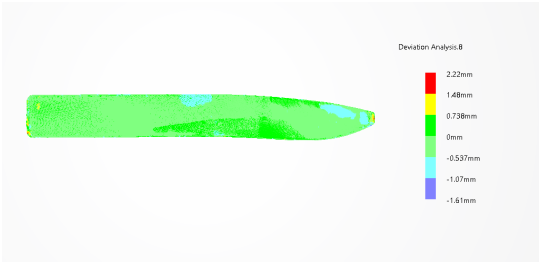

(a) ZS00544: High pressure side

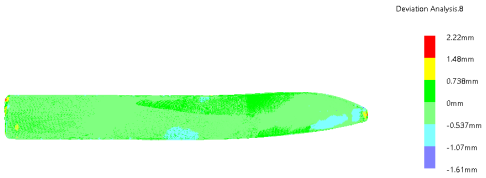

(b) ZS00544: Low pressure side

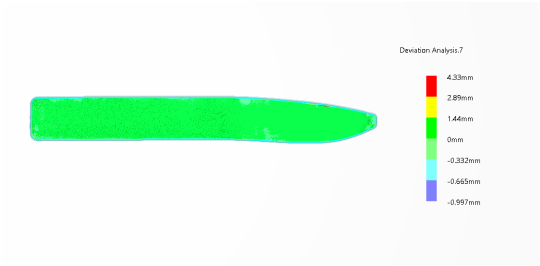

(c) ZS00663: High pressure side

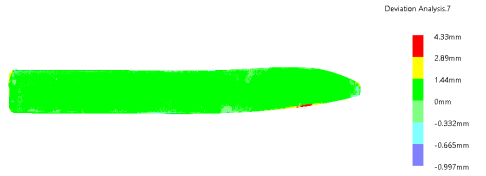

(d) ZS00663: Low pressure side

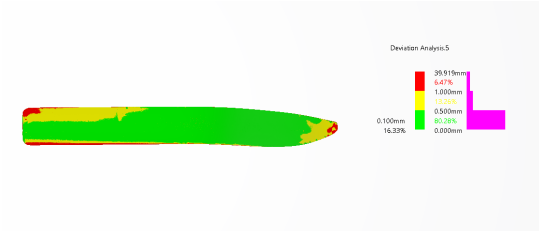

(e) ZS00664: High pressure side

(f) ZS00664: Low pressure side

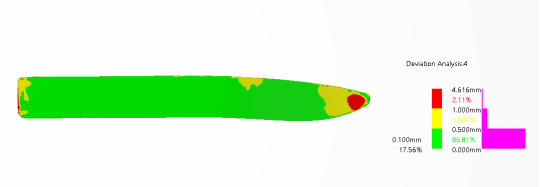

(g) ZS00691: High pressure side

(h) ZS00691: Low pressure side

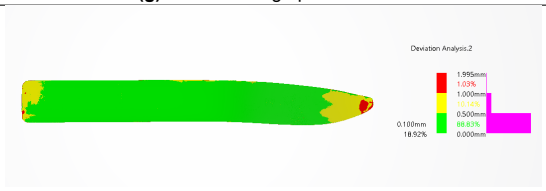

(i) ZS00696: High pressure side

(j) ZS00696: Low pressure side

Figure A.10: The deviation analysis of the hydrofoils using Catia and compared with ZS00531

B

Research Method Validation for 2D Section ProcessingAppendices

B.1. Code blocks

Listing B.1: intersection of two curves

```
    def interpolated_intercepts(x, y1, y2):
    """ TAKEN FROM THE INTERNET https://stackoverflow.com/questions/42464334/find-the-
        intersection-of-two-curves-given-by-x-y-data-with-high-precision-in"""
    """Find the intercepts of two curves, given by the same x data"""

    def intercept(point1, point2, point3, point4):
        """find the intersection between two lines
        the first line is defined by the line between point1 and point2
        the first line is defined by the line between point3 and point4
        each point is an (x,y) tuple.

        So, for example, you can find the intersection between
        intercept((0,0), (1,1), (0,1), (1,0)) = (0.5, 0.5)

        Returns: the intercept, in (x,y) format
        """

        def line(p1, p2):
            A = (p1[1] - p2[1])
            B = (p2[0] - p1[0])
            C = (p1[0]*p2[1] - p2[0]*p1[1])
            return A, B, -C

        def intersection(L1, L2):
            D  = L1[0] * L2[1] - L1[1] * L2[0]
            Dx = L1[2] * L2[1] - L1[1] * L2[2]
            Dy = L1[0] * L2[2] - L1[2] * L2[0]

            x = Dx / D
            y = Dy / D
            return x,y

        L1 = line([point1[0],point1[1]], [point2[0],point2[1]])
        L2 = line([point3[0],point3[1]], [point4[0],point4[1]])

        R = intersection(L1, L2)

        return R

    idxs = np.where(np.diff(np.sign(y1 - y2)) != 0)

    xcs = []
```

```
    ycs = []

    for idx in idxs:
        xc, yc = intercept((x[idx], y1[idx]),((x[idx+1], y1[idx+1])), ((x[idx], y2[idx])), ((
            x[idx+1], y2[idx+1])))
        xcs.append(xc)
        ycs.append(yc)
    return np.array(xcs), np.array(ycs)
```

Listing B.2: Camberline from offset of the curve

```
offset_line, _,_,_ = adj_func.off_set(Naca_points[0],Naca_points[1],-np.max(Naca_points[1])
    /3)
n_offsets = 101
n_curve_resolution = 1001
cos_spacing = True

LE_offset = int(n_curve_resolution/(2/3 *100))

x_up,y_up = Naca_points[:,:int((npoints-1)/2)]
x_low,y_low = Naca_points[:,int((npoints-1)/2):]

x_spacing = np.quantile([min(x_up),max(x_up)],df_Naca.half_spacing(n_curve_resolution,
    cos_spacing))
x_camber = []
y_camber = []
for d_off in np.linspace(0,(max(y_up)-min(y_low))/2,n_offsets):
    x_spacing = np.quantile([min(x_up)+d_off,max(x_up)-d_off],df_Naca.half_spacing(
        n_curve_resolution,cos_spacing = True))

    y_upper_offset = adj_func.off_set_line(x_up,y_up,x_spacing,-1*d_off)
    y_lower_offset = adj_func.off_set_line(x_low,y_low,x_spacing,-1*d_off)
    #finding the intersect points, Offset by a factor of LE_offset with respect to the
        resolution in order to avoid the incompatibility at the leading edge
    xcs,ycs = adj_func.interpolated_intercepts(x_spacing, y_upper_offset, y_lower_offset)
    x_camber.append(xcs[0])
    y_camber.append(ycs[0])



points_camber = np.array([np.concatenate(x_camber),np.concatenate(y_camber)])
points_camber = points_camber[:,np.unique(points_camber[0],return_index = True)[1]].T


#The points at the leading edge are not accurate thus these are removed by checking if they
    are deviate more than .0005 from a spline fitted through the points.
update_camber = points_camber
for itera in range(10):

    test_curve = update_camber
    test_poly_curve_offset = np.poly1d(np.polyfit(test_curve[:,0],test_curve[:,1],9))
    diff_array = abs(np.diff(np.vstack((update_camber[:,1],test_poly_curve_offset(
        update_camber[:,0])))),axis = 0))
    no_error_id = np.where(np.percentile(diff_array,99.5)>diff_array)[1]
    update_camber = update_camber[no_error_id]

""" Find a new value for .05 for a general solution"""
""" add filtering for gradient?"""
result_offset = update_camber
test_poly_curve_offset = np.poly1d(np.polyfit(result_offset[:,0],result_offset[:,1],9)) #
    final camber line

camberfunc = df_Naca.TwoPointCamberFormulation_Yc(M,P) #camberline function
XC = np.linspace(0,1,101) #camberline x coordinates
YC = camberfunc(XC) #camberline y coordinates

error_camber1 = YC - test_poly_curve_offset(XC) #camberline error
```

Listing B.3: RSMerror function

```
def RMS_error(Data_Original,Data_New):
```

```
    tck_input ,   u_input    = sci_i.splprep(Data_New.T,s=0)
    tck_original ,u_original = sci_i.splprep(Data_Original.T,s=0)

    def SDM_value(u, point):

        u = u[0]
        C = lambda u: np.array(sci_i.splev(u,tck_input))
        T = lambda u: np.array(sci_i.splev(u,tck_input,der = 1))
        D = lambda u: np.array(sci_i.splev(u,tck_input,der = 2))
        B = lambda u: np.cross(T(u),D(u))/np.linalg.norm(np.cross(T(u),D(u)))

        R = lambda u: 1/(np.linalg.norm(np.cross(T(u),D(u))) / np.linalg.norm(T(u))**3)

        Tangent = lambda u: T(u)/np.linalg.norm(T(u))
        Normal  = lambda u: np.cross([0,0,B(u)],Tangent(u))[:2]

        # print(f'u = {u}\npoint = {point}\nTangent = {Tangent(u)}\nRu = {R(u)}\nNormal = {
            Normal(u)}')

        x1 = lambda u: np.dot(Tangent(u),(point - C(u)).T)
        x2 = lambda u: np.dot(Normal(u),(point - C(u)))
        d  = lambda u: np.linalg.norm(point - C(u))

        # if x2(u) > 0:
        #     return d(u)**2
        # else:
        return (d(u)/(d(u)+R(u))*x2(u)**2)*(x2(u)>0) + x1(u)**2


    def minfunction(input_var):
        u = input_var[0]
        point = [input_var[1],input_var[2]]

        min_u = sci_o.minimize(SDM_value,u, args=(point))

        return min_u.x[0]

    input_arr = np.vstack((u_original,Data_Original.T)).T
    u_opt = np.apply_along_axis(minfunction,1,input_arr).T

    Data_New_fitted = np.array(sci_i.splev(u_opt,tck_input)).T
    RMSerror_x = np.linalg.norm(Data_Original-Data_New_fitted,axis = 1 )
    RMSerror = np.sum(RMSerror_x)

    verification_data = np.hstack((Data_Original,Data_New_fitted))

    return RMSerror, RMSerror_x, verification_data
```

B.2. Showing how the error formulation can go wrong

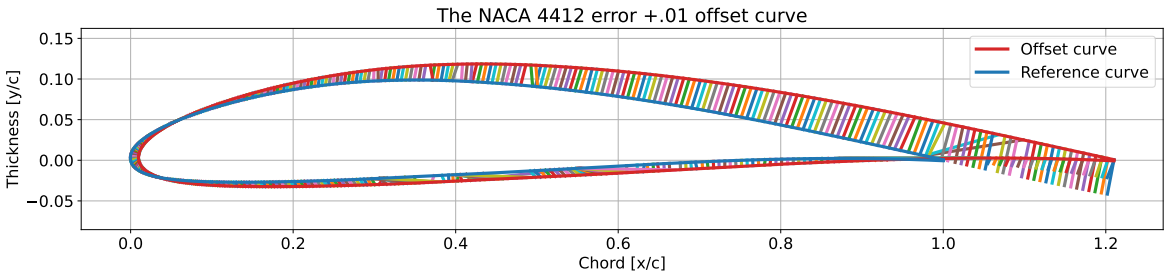

Figure B.1: The error visualised on the example shown in Figure 5.17 with: x (Equation 5.29), y (Equation 5.30), $|d(t_k)$ (Equation 5.27), and eSD(D) (Equation 5.31)

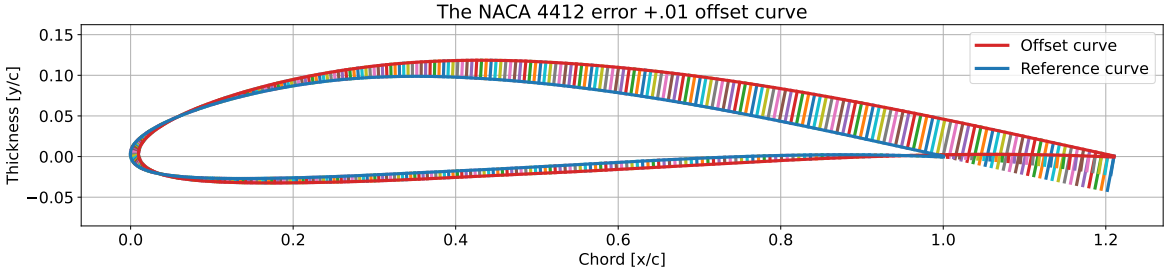

Figure B.2: The error visualised on the example shown in Figure 5.17 with: x (Equation 5.33), y (Equation 5.34), $|d(t_k)$ (Equation 5.27), and eSD(D) (Equation 5.35)

C

Geometric deviation analysis: Appendix

Table C.1: Showing if the polynomial camber line fit deviates upwards at the leading edge (white and -1), at the Trailing edge (dark grey and 1), or both down (light grey and 0). An attempt of identifying the miss alignment of the two mould halves as both ends should point downwards.

Section	ZS00531	ZS00544	ZS00663	ZS00664	ZS00691	ZS00696
1	1	1	1	1	0	1
2	1	1	1	1	0	1
3	1	1	1	1	1	1
4	1	1	1	1	0	1
5	1	1	1	1	0	1
6	1	1	1	1	0	1
7	1	1	1	1	1	1
8	1	1	1	0	0	1
9	1	1	1	1	1	1
10	1	1	1	1	1	1
11	1	1	1	1	1	1
12	1	1	1	0	1	1
13	0	1	1	1	-1	1
14	1	0	-1	1	-1	1
15	0	1	-1	1	0	1
16	1	0	1	1	-1	1
17	1	0	-1	1	0	1
18	0	0	-1	1	0	1
19	0	0	0	1	-1	1
20	0	0	0	1	0	0
21	0	1	-1	0	0	1
22	-1	0	1	1	-1	1
23	-1	0	-1	0	-1	0
24	-1	-1	-1	-1	0	-1
25	-1	-1	-1	-1	0	-1
26	-1	0	-1	1	0	-1
27	0	-1	1	-1	0	-1
28	0	0	-1	0	-1	-1
29	0	-1	-1	1	0	1
30	0	-1	-1	1	0	-1
31	0	-1	-1	0	0	-1
32	0	0	-1	0	0	-1
33	0	0	0	0	0	0
34	0	0	-1	0	0	0
35	0	0	0	0	-1	0
36	1	0	0	0	0	0
37	1	0	1	1	0	-1
38	0	0	0	1	0	0
39	0	0	1	0	0	0
40	0	0	0	0	0	0
41	0	0	1	0	0	0
42	0	0	1	0	0	-1
43	0	0	1	0	-1	0
44	1	0	1	-1	0	0
45	1	0	1	-1	-1	0
46	0	0	0	-1	-1	0
47	0	0	0	1	-1	0
48	-1	0	0	0	0	1
49	0	1	-1	0	1	1
50	0	-1	-1	-1	0	0

D

2D section hydrodynamic analysis: Appendix

D.1. Fast Fourier Transform: Code

Listing D.1: Applying the Fast Fourier Transform

```
    foil_code = data['Foilcode']
    sectionnumber = data['SecNumber']
    data_dat_c1 = data['data_c1']
    tck_reduced, u_reduced = sci_i.splprep(data_dat_c1.T,s=0,per=1)

    u_sample = np.linspace(0,1,len(u_reduced)*1000)
    x_spl,y_spl = sci_i.splev(u_sample,tck_reduced)

    fhat = np.fft.rfft2([x_spl,y_spl],norm = 'ortho')
    freq = np.fft.rfftfreq(len(x_spl),d = 1/len(x_spl))
```

Listing D.2: Calculating the Fast Fourier Transform Optimisation function

```
def Frequency_filteringerror(freqfilt):
    pointsreduction = int(len(data_dat_c1)/100)

    fhat_cleaned1 = fhat*(abs(freq)<freqfilt)
    x_f1,y_f1 = np.fft.irfft2(fhat_cleaned1)
    x_f1,y_f1 = x_f1/max(x_f1), y_f1/max(x_f1)

    k1 = adj_func.curvature(x_f1[1:],y_f1[1:])
    data_dat_c1_fftf = np.array([x_f1,y_f1]).T

    RMSerror_fftf,RMSerror_x_fftf, varif_fftf = RMS_error(data_dat_c1[::pointsreduction],
        data_dat_c1_fftf[::int(len(x_f1)/500)])

    potential = np.sum(np.abs(np.gradient(k1)))
    # print(f'tested filter {freqfilt}                giving the error {RMSerror_fftf}')
    return [abs(potential**(RMSerror_fftf)),RMSerror_fftf]
```

Listing D.3: The Optimisation loop for the Fast Fourier Transform

```
# Setting Up Pramaters
minval = 0.5 #frequency in base log 10
maxval = np.log10(freq.max())*.8 #frequency in base log 10 80% sample frequency
MinRMSerror = 10
minfreq = minval
lastfreq = minfreq
RMSvalues= []

for i in range(10):
```

```
    # print(f'iteration {i}')
    # print(f'iteration {i}   minval:{minval:.3g},    maxval:{maxval:.3g}     RMSmin error:{
        minfreq:.3g}')
    freqfilters = np.logspace(minval,maxval,12) #logspaced frequency range

    MinRMSerror = 10
    minfreq = lastfreq
    RMSerror = []
    for j in range(11):
        RMSerror_j,RMSeror_i = Frequency_filteringerror(freqfilters[j])
        RMSvalues.append([freqfilters[j],RMSerror_j,RMSeror_i])
        RMSerror.append(RMSerror_j)
        # print(f'RMSerror:{RMSerror[-1]:.4e},                    current:{freqfilters[j
            ]:.4e}')
    minfreq = freqfilters[np.argmin(RMSerror)]
    minval = np.log10(freqfilters[np.argmin(RMSerror)-1])
    maxval = np.log10(freqfilters[np.argmin(RMSerror)+1])

    if (maxval-minval)<0.001:
        break
```

D.2. Xfoil Settings

Table D.1: The Xfoil analysis settings that are used for the analysis of the different hydrofoil sections

Variable	Input	Explanation
ncrit	9	The
xtript	1	x/c location of tripping point to turbulent flow on the top surface
xtripb	1	x/c location of tripping point to turbulent flow on the bottom surface
viscous_mode	True	Adds viscosity effects to the flow. Necessary for modelling drag and flow separation
silent_mode	True	Blocks print statements from the original Xfoil code
maxit	2000	Maximum number of iterations for a converging solution
vaccel	0	Velocity acceleration, affects the convergence speed but should be 0 for best results

Table D.2: Xfoil geometry paneling settings used for the analysis of the different hydrofoil sections.

Variable	Range	Input	Explanation
npan	0-300	300	Number of panels to approximate the profile
cvpar	0-1	1	panel bunching parameter
cterat	0-10	0.2	Refined area/LE panel density ratio
ctrrat	0-10	.15	TE/LE panel density ratio
xsref1	0-1	1	Forward of the top refinement area
xsref2	xsref1-1	1	Aft of the top refinement area
xpref1	0-1	1	Froward of the bottom refinement area
xpref2	xpref1-1	1	Aft of the bottom refinement area

D.3. Identification of the cause of early separation

The following figures show the lift over drag for the different sections that are analysed using Xfoil and that showed one or more profiles with early separation. The corresponding friction coefficient graphs are attached to identify why the profile behaves differently from the majority.

D.3.1. Section 15

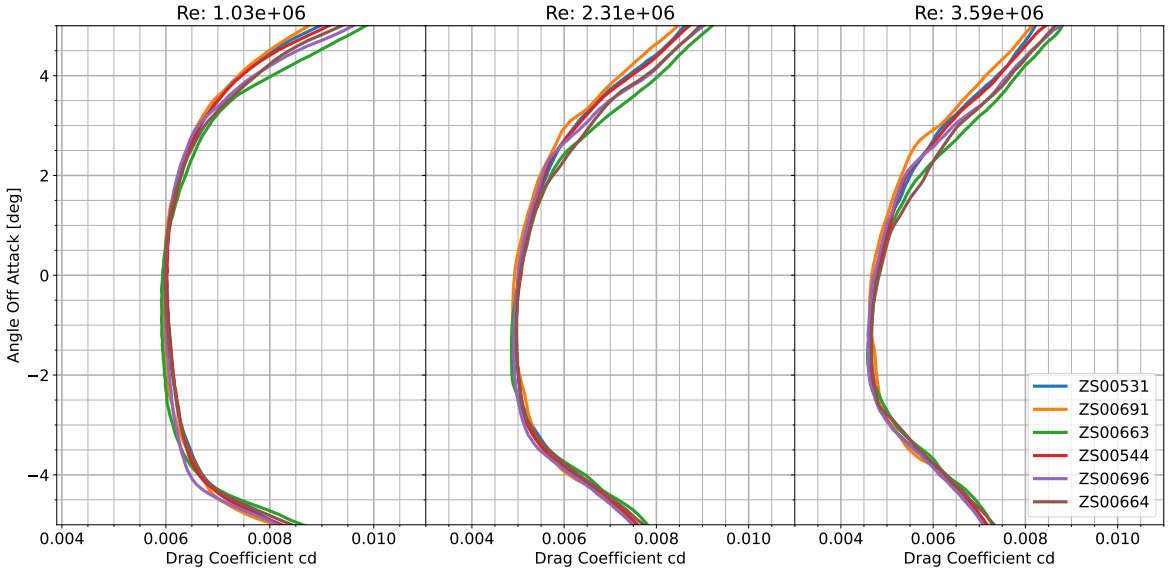

Figure D.1: The angle of attack over drag showing the early separation of section 15

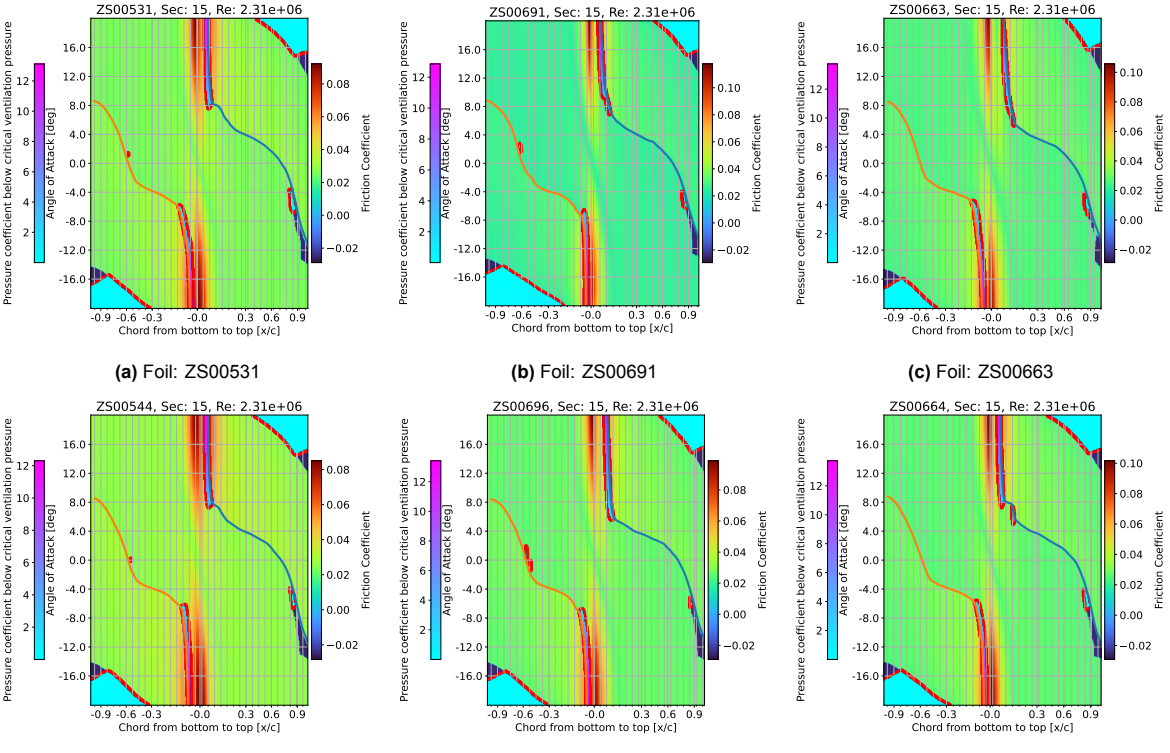

(a) Foil: ZS00531 **(b)** Foil: ZS00691 **(c)** Foil: ZS00663

(d) Foil: ZS00544 **(e)** Foil: ZS00696 **(f)** Foil: ZS00664

Figure D.2: These are the friction coefficient graphs for section 15 at Reynolds number: 2.31e6 equivalent to 22.5 knots of boat speed

D.3.2. Section 24

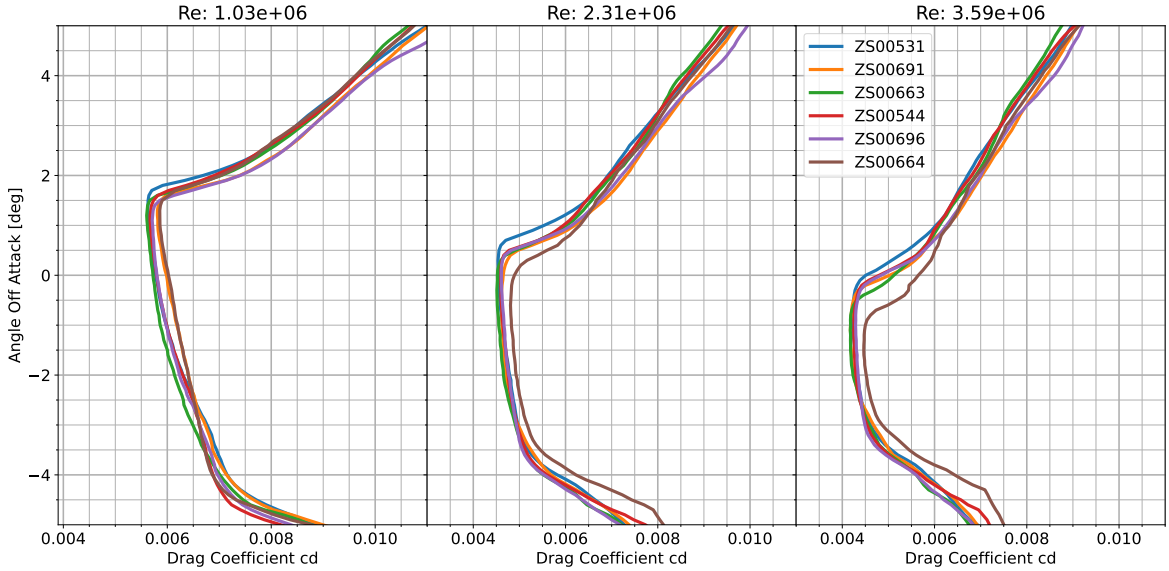

Figure D.3: The angle of attack over drag showing the early separation of section 24

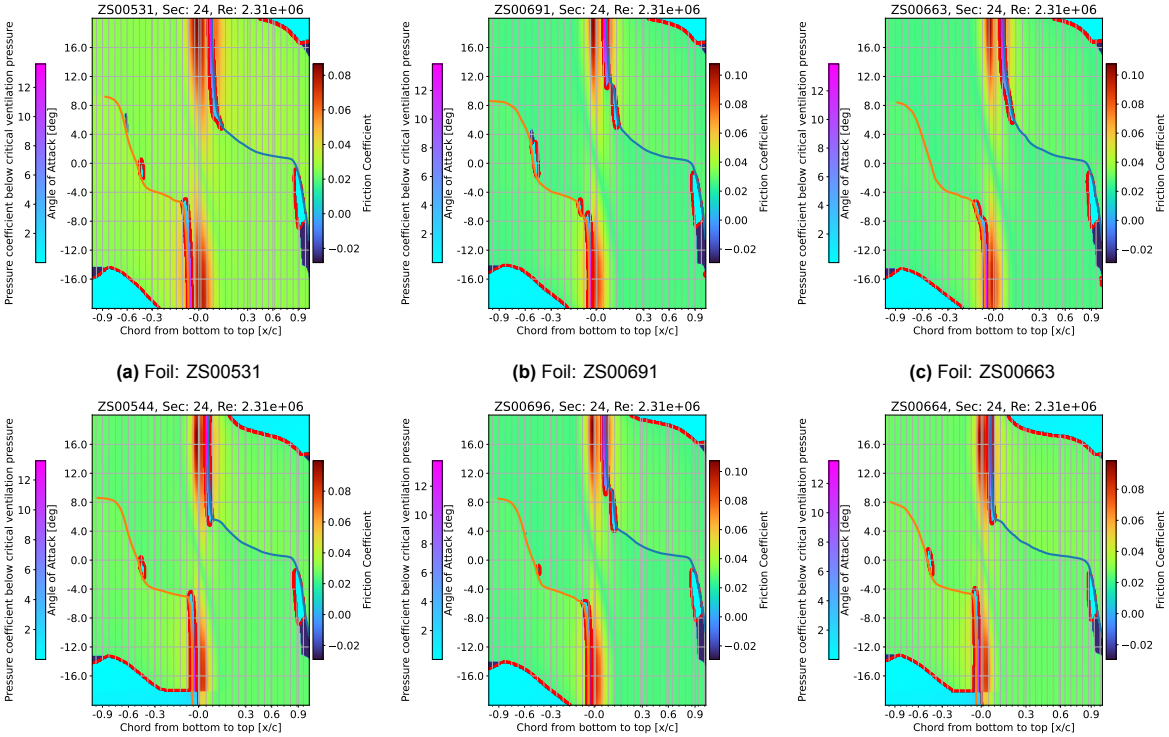

(a) Foil: ZS00531 **(b)** Foil: ZS00691 **(c)** Foil: ZS00663

(d) Foil: ZS00544 **(e)** Foil: ZS00696 **(f)** Foil: ZS00664

Figure D.4: These are the friction coefficient graphs for section 24 at Reynolds number: 2.31e6 equivalent to 22.5 knots of boat speed

D.3.3. Section 30

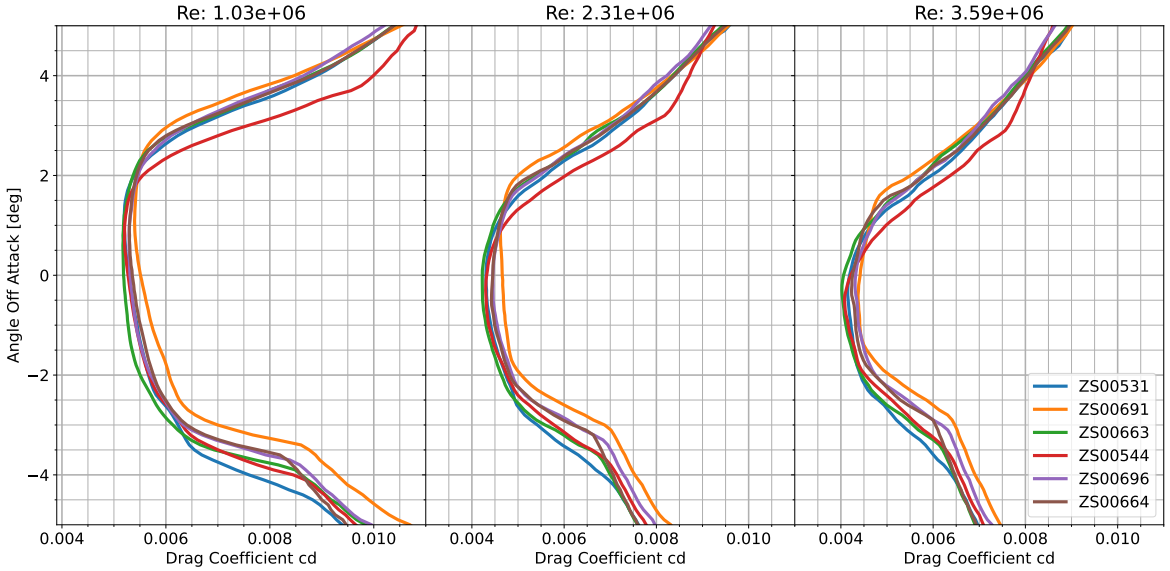

Figure D.5: The angle of attack over drag showing the early separation of section 30

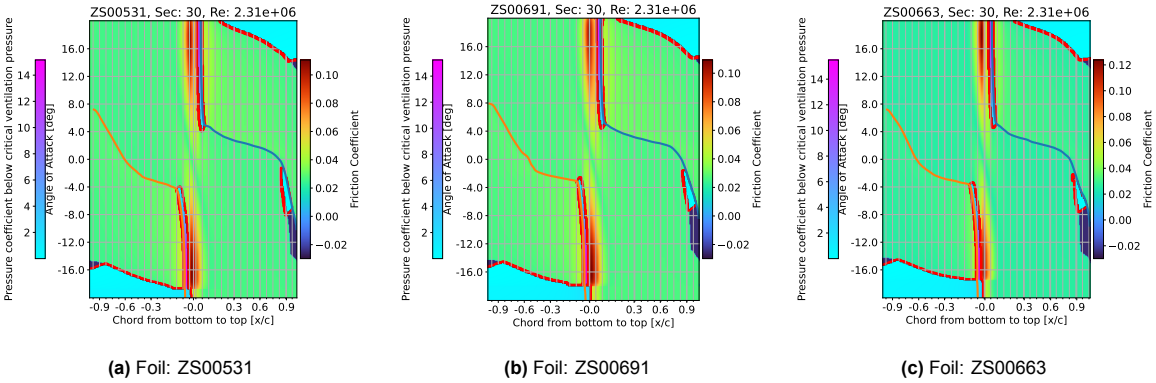

(a) Foil: ZS00531 **(b)** Foil: ZS00691 **(c)** Foil: ZS00663

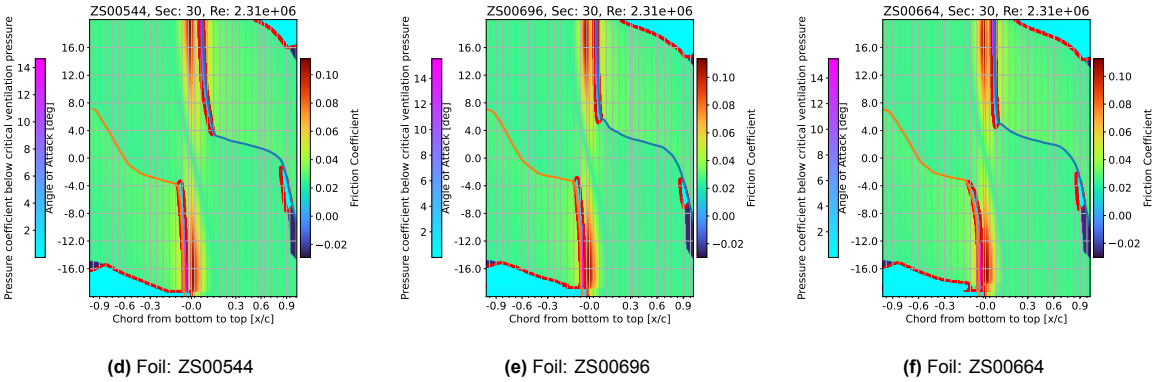

(d) Foil: ZS00544 **(e)** Foil: ZS00696 **(f)** Foil: ZS00664

Figure D.6: These are the friction coefficient graphs for section 30 at Reynolds number: 2.31e6 equivalent to 22.5 knots of boat speed

D.3.4. Section 35

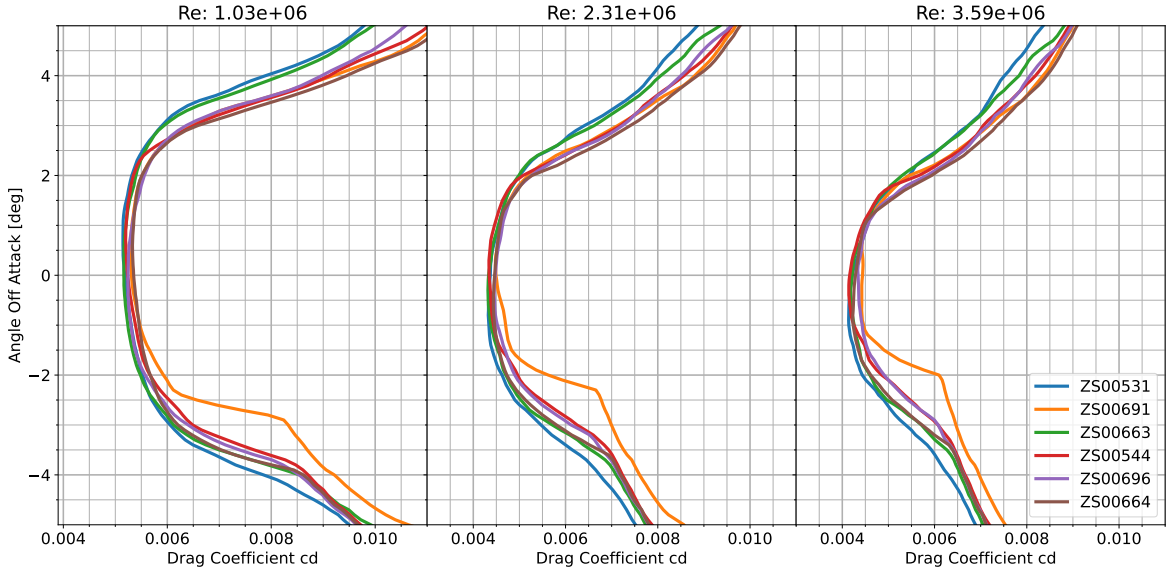

Figure D.7: The angle of attack over drag showing the early separation of section 35

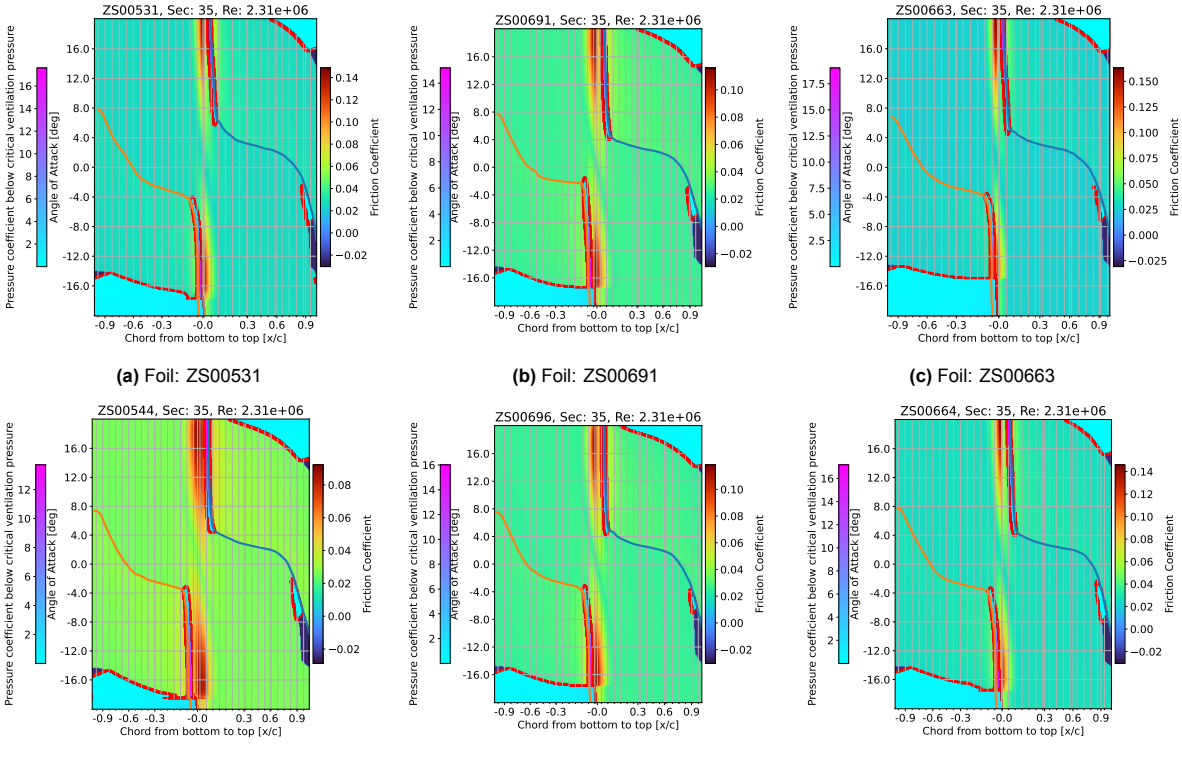

(a) Foil: ZS00531 **(b)** Foil: ZS00691 **(c)** Foil: ZS00663

(d) Foil: ZS00544 **(e)** Foil: ZS00696 **(f)** Foil: ZS00664

Figure D.8: These are the friction coefficient graphs for section 35 at Reynolds number: 2.31e6 equivalent to 22.5 knots of boat speed

D.3.5. Section 40

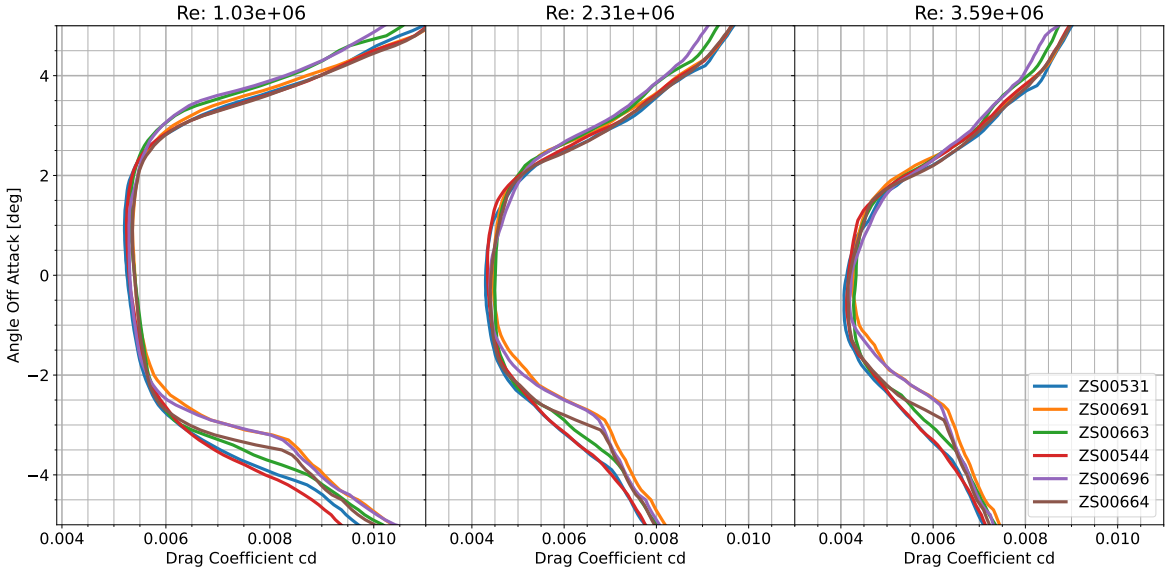

Figure D.9: The angle of attack over drag showing the early separation of section 40

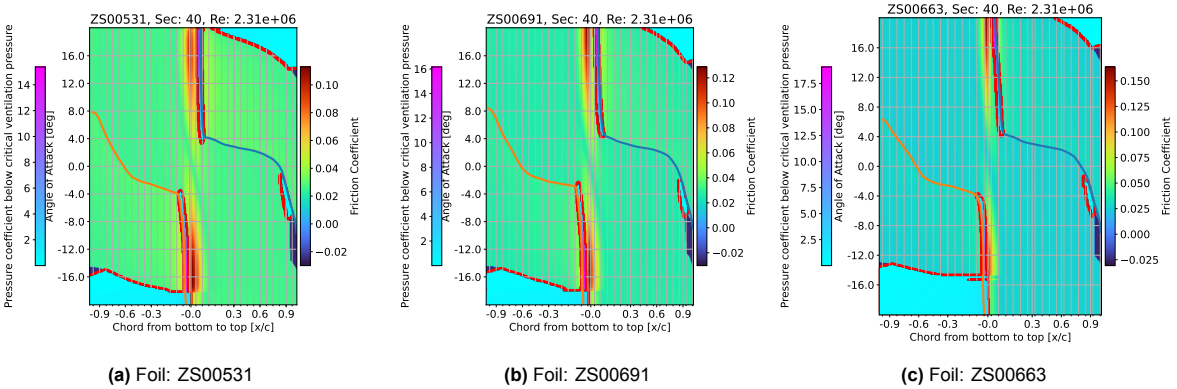

(a) Foil: ZS00531 **(b)** Foil: ZS00691 **(c)** Foil: ZS00663

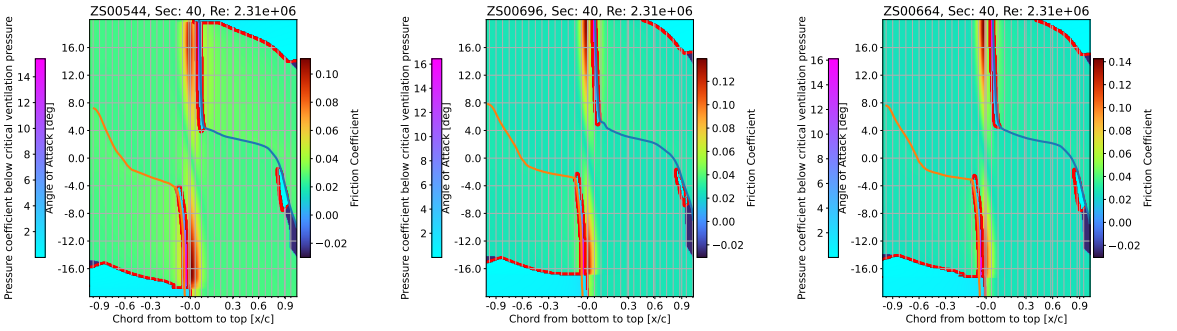

(d) Foil: ZS00544 **(e)** Foil: ZS00696 **(f)** Foil: ZS00664

Figure D.10: These are the friction coefficient graphs for section 40 at Reynolds number: 2.31e6 equivalent to 22.5 knots of boat speed

D.4. Lift over drag coefficient graphs

This section presents the lift-over-drag graphs for the analysed sections.

D.4.1. Lift over drag coefficient graphs for the full range of the lift coefficient.

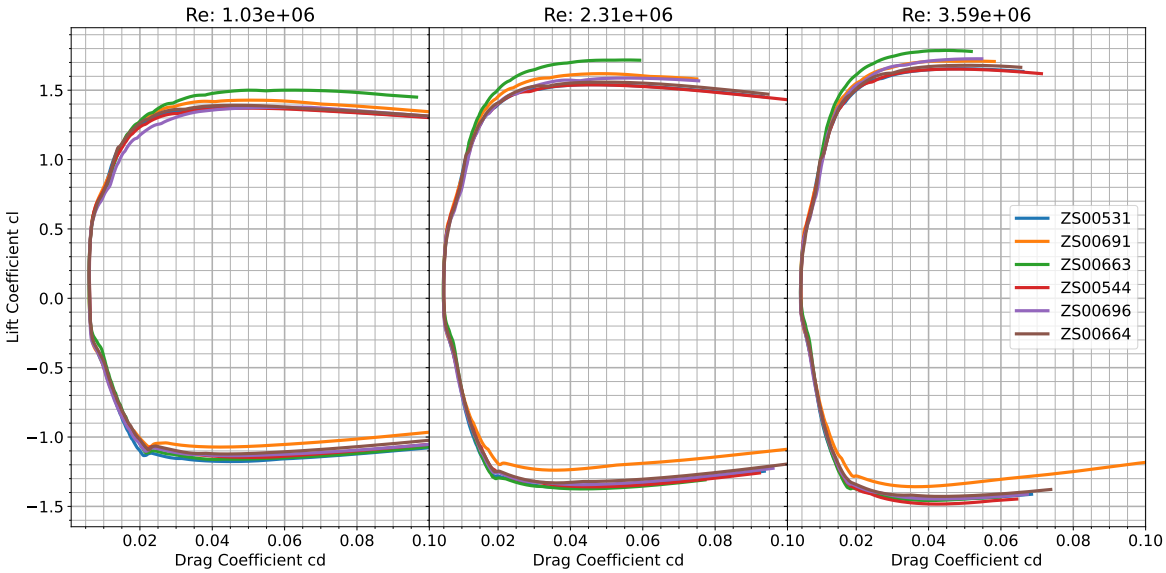

Figure D.11: The Lift over drag graphs at different Reynolds numbers for section 15

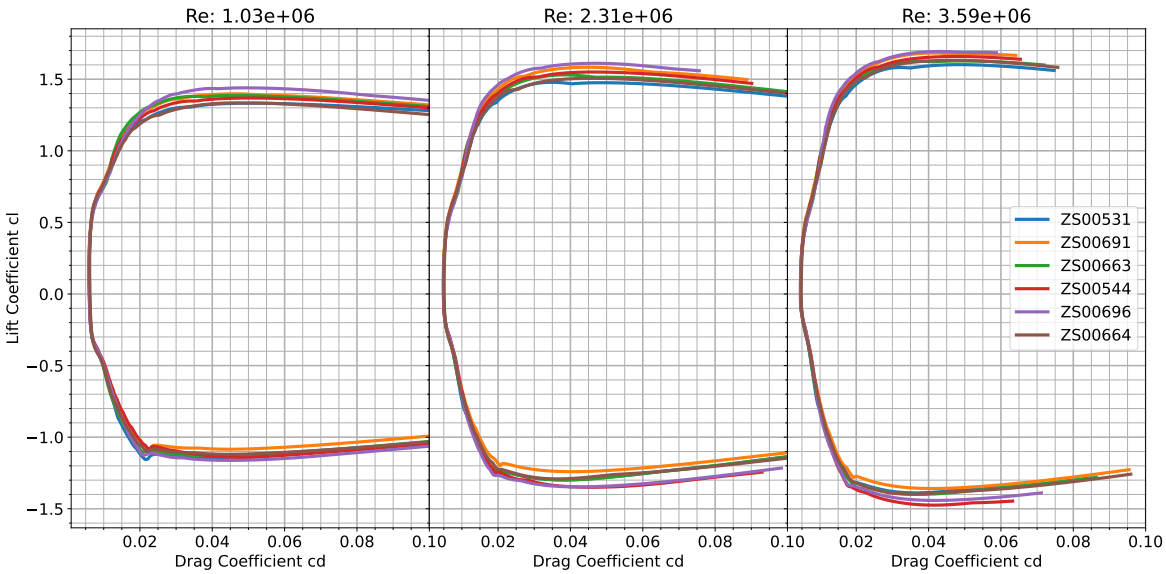

Figure D.12: The Lift over drag graphs at different Reynolds numbers for section 20

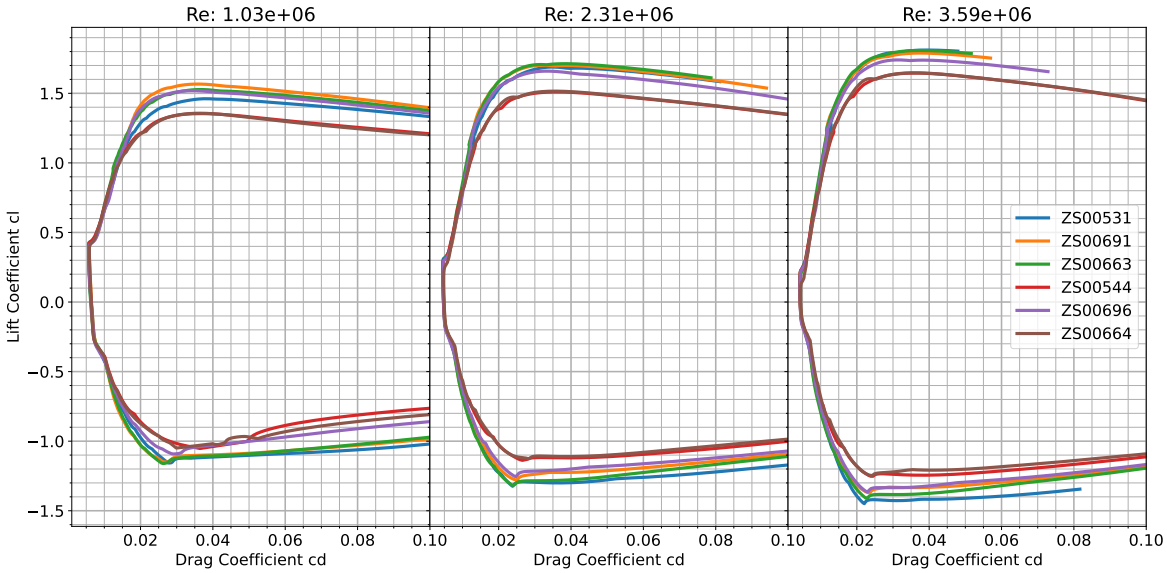

Figure D.13: The Lift over drag graphs at different Reynolds numbers for section 24

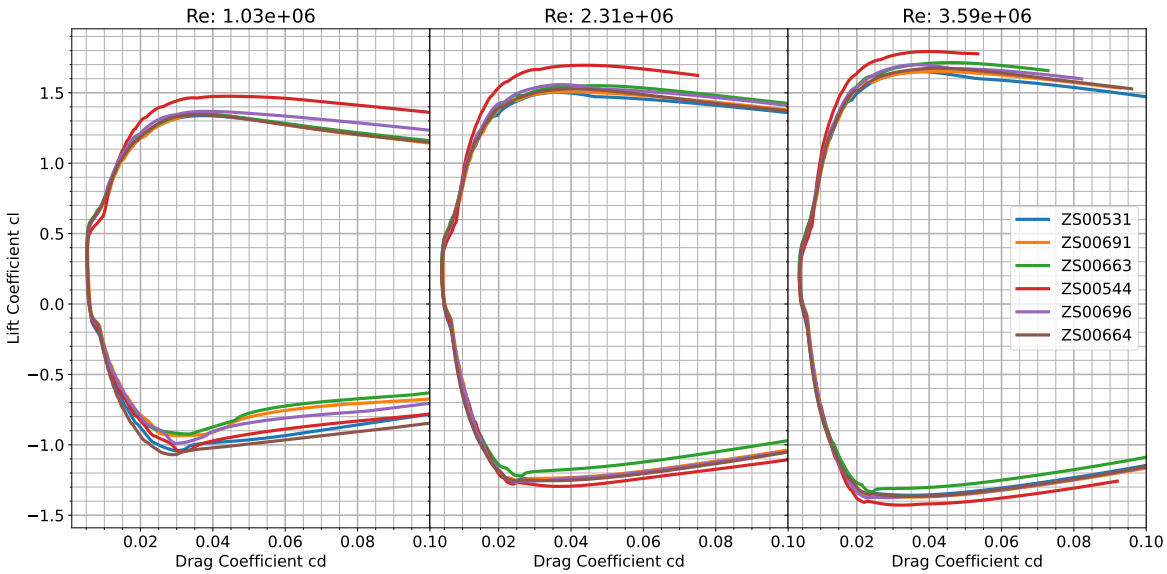

Figure D.14: The Lift over drag graphs at different Reynolds numbers for section 30

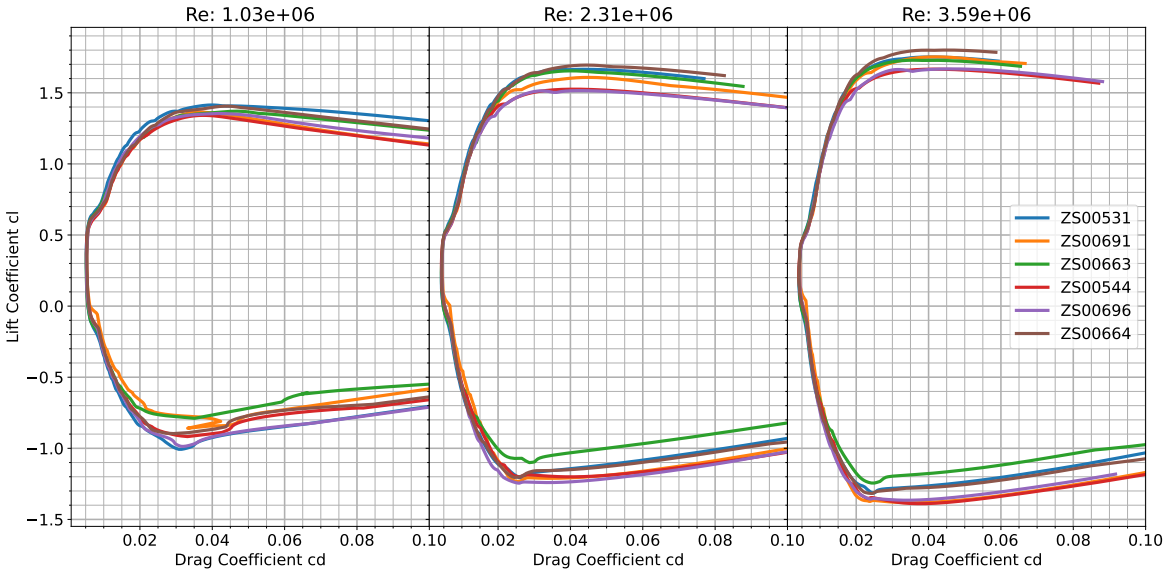

Figure D.15: The Lift over drag graphs at different Reynolds numbers for section 35

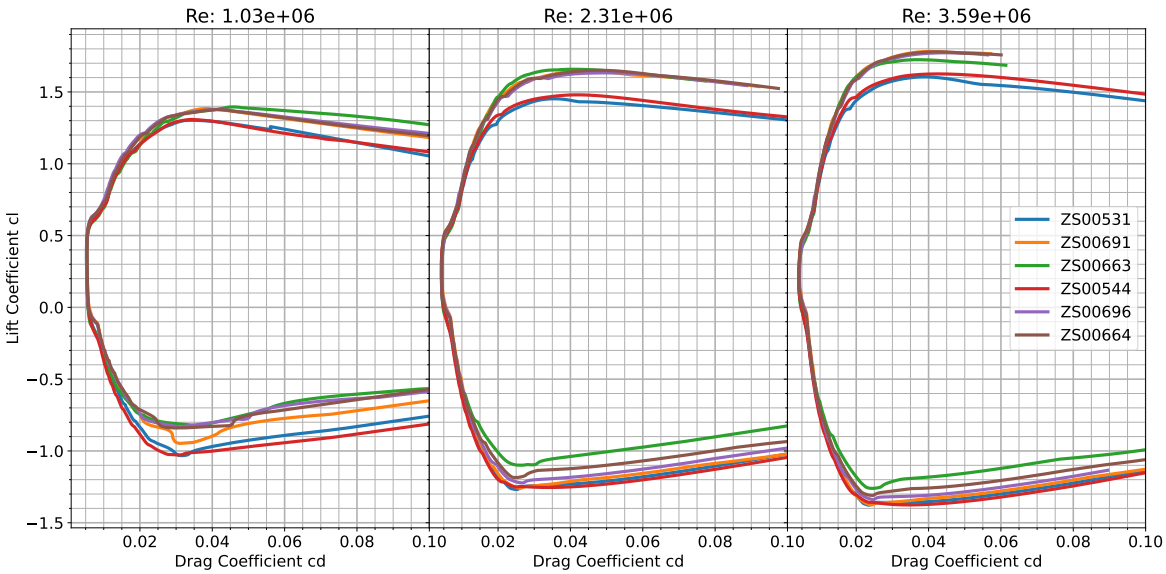

Figure D.16: The Lift over drag graphs at different Reynolds numbers for section 40

D.4.2. Lift over drag coefficient graphs for a reduced range of the lift coefficient showing the drag bucket.

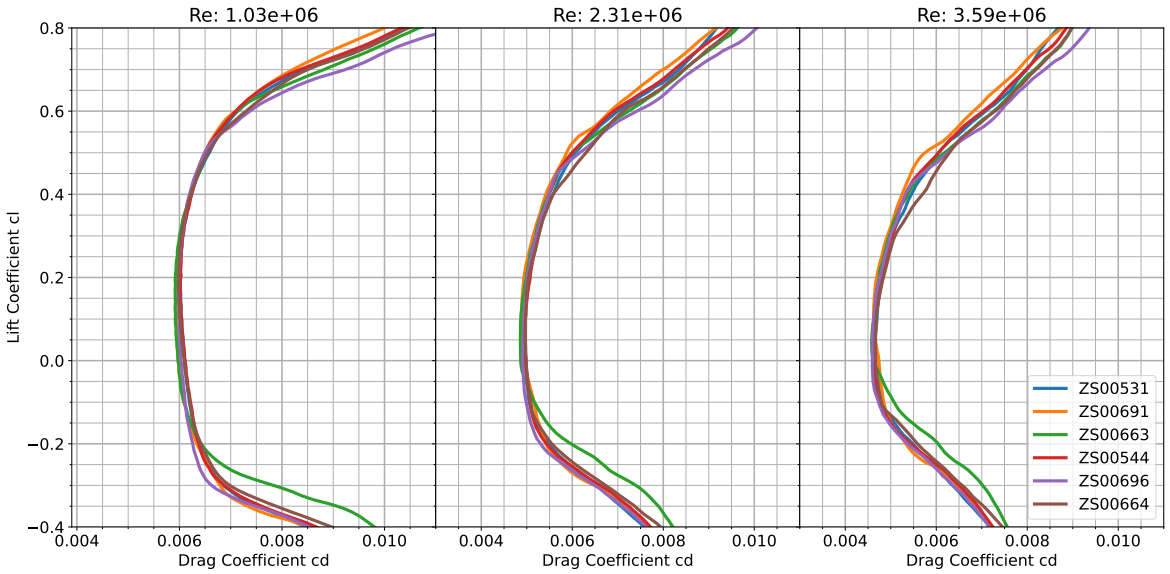

Figure D.17: Focused Lift over drag graphs at different Reynolds numbers for section 15

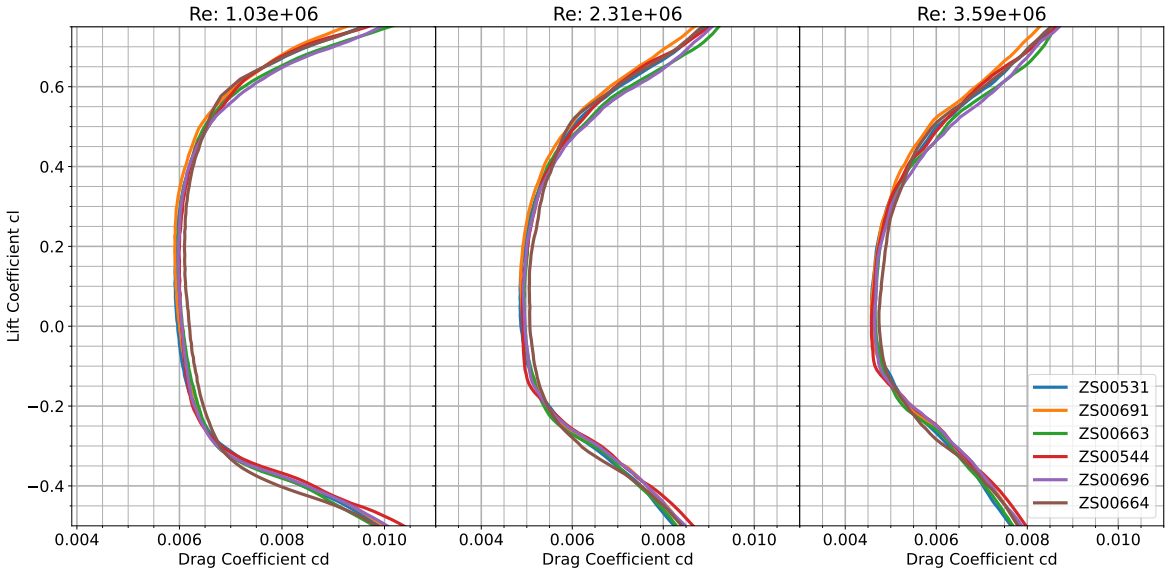

Figure D.18: Focused Lift over drag graphs at different Reynolds numbers for section 20

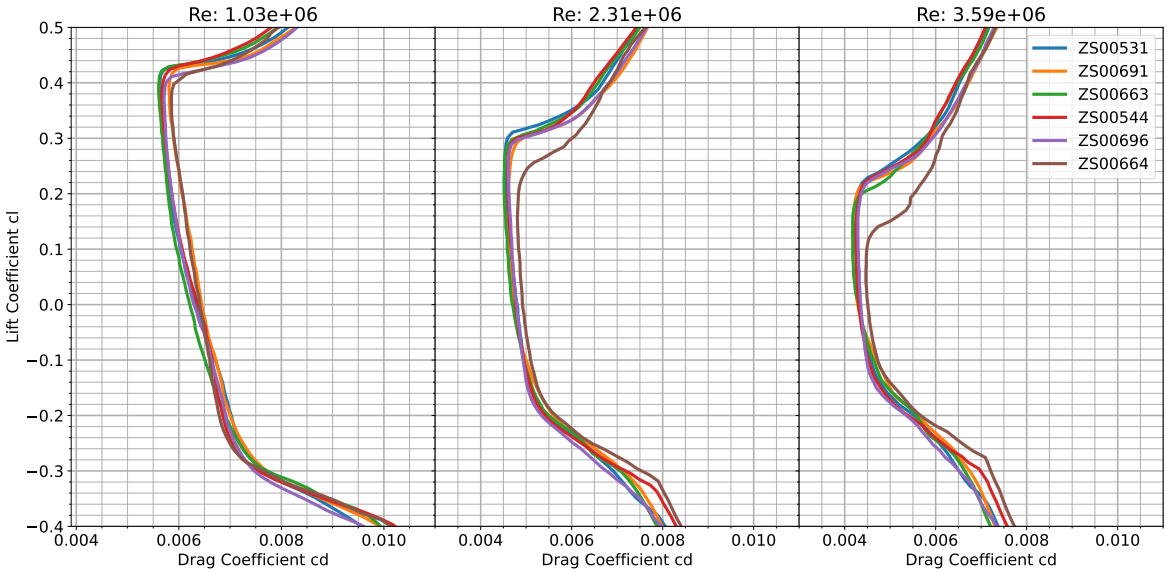

Figure D.19: Focused Lift over drag graphs at different Reynolds numbers for section 24

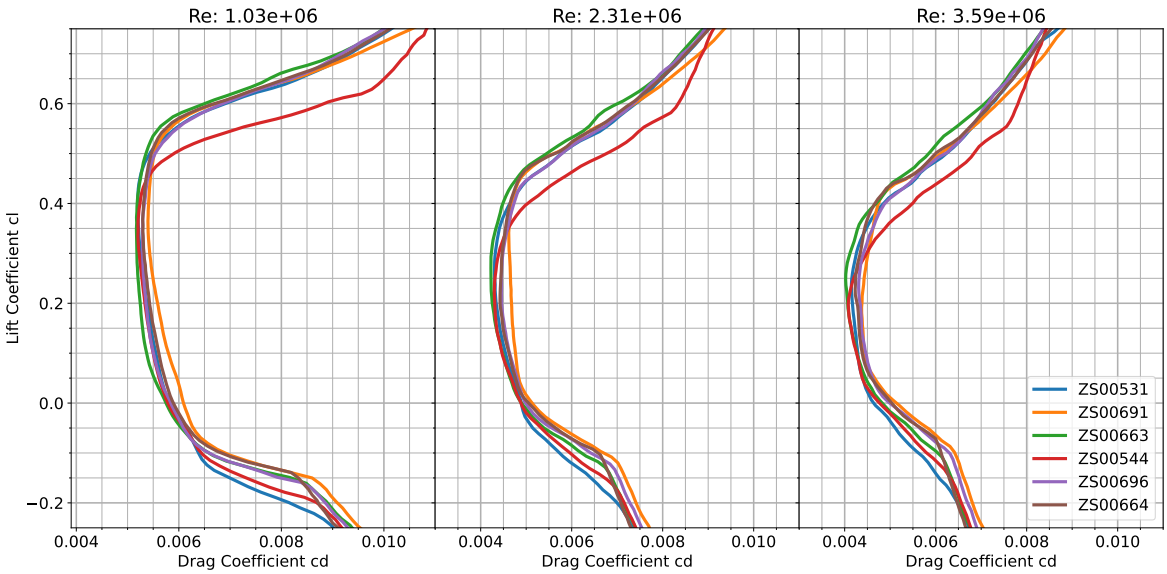

Figure D.20: Focused Lift over drag graphs at different Reynolds numbers for section 30

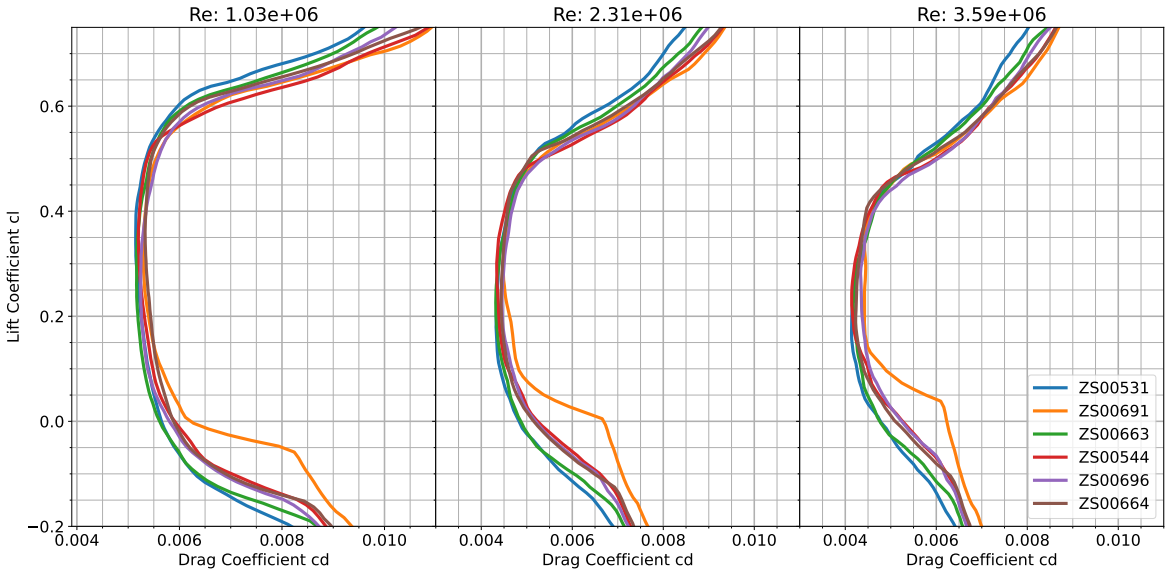

Figure D.21: Focused Lift over drag graphs at different Reynolds numbers for section 35

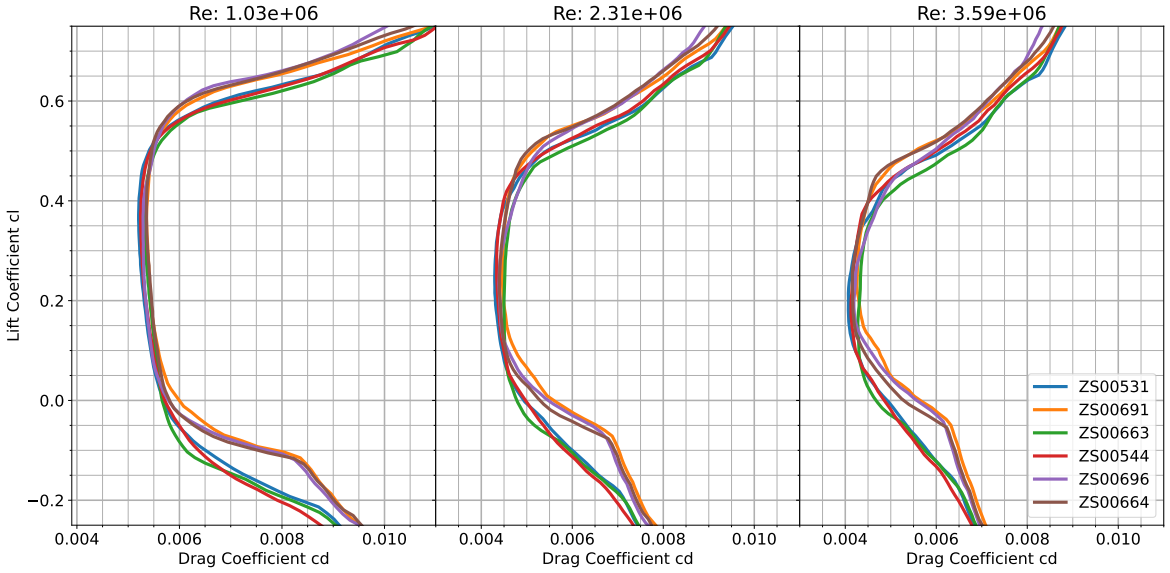

Figure D.22: Focused Lift over drag graphs at different Reynolds numbers for section 40

E

Defects in composite Hydrofoil Manufacturing

The NACRA 17 class adheres to a strict one-design rule, which requires all equipment to be identical. This rule aims to minimise development costs and emphasise the skill gap among the sailors. To ensure uniformity between parts, a single manufacturer, namely &DNA Composites, is assigned to produce the hydrofoils. Despite these measures, teams have reported discrepancies between hydrofoils, particularly in terms of bending stiffness. The differences in geometry have been found to be up to 0.31 mm, at an official measurement conducted by the class society [17][1]. The suggested class tolerances where stated to be 0.25 mm for the shape, -1 mm in thickness and the trailing edge ranging from 1.6 to 2.1 mm. During this test, the 3 brand new boards showed the biggest deviations from the measurement tools. This highlights the influence of the manufacturing process on the variation in shape. It further more shows that it is not caused by the sailors themselves.

Therefore, before delving into, quantification of hydrodynamic performance differences, it is crucial to explore the specific manufacturing factors of NACRA 17 hydrofoils by &DNA Composites that may contribute to variations in geometry and potentially impact hydrodynamic performance.

E.1. Nacra 17 Hydrofoil production techniques.

The Nacra 17 Hydrofoils have been produced by &DNA composites from when the Nacra 17 started flying in 2017 up to 2021. The hydrofoils are made using a carbon fibre reinforced polymer. The production is comparable to all combinations of (continuous) fibre reinforced polymers or FRP's. The production of FRP's can be summarised in the steps: impregnation,layup,consolidation, and solidification [76]. Combining the fibres and the polymer is called impregnation. Layup defines the placement of the fibres in specific orientations in/on a mould. This combination of fibre and polymer needs to be formed into one single structure using pressure in the process called consolidation. Concurrently as the consolidation the polymer is solidified while the pressure is maintained. This results in a mechanical structure that might need some removal of material after which it is suitable for use.

Impregnation and the method of production depend greatly on the length of the fibres and the type of polymer. The most common type of polymer for FRP structures is a thermoset polymer. A thermoset polymer starts as two different fluids that react with each other when combined and/or heat is added. The presence of the reactions makes the curing of the polymer non reversible. The second type of polymer is a thermo-plastic, that is solid at room temperature and melts at higher temperatures. The liquid state at room temperature of the thermosetting polymers makes it very easy to shape the material in a desired shape.

[1] *Measurement of Daggerboards for Nacra 17*. URL: `https://nacra17.org/wp-content/uploads/2019/04/Palma-2019-Report.pdf` (visited on 05/10/2023)

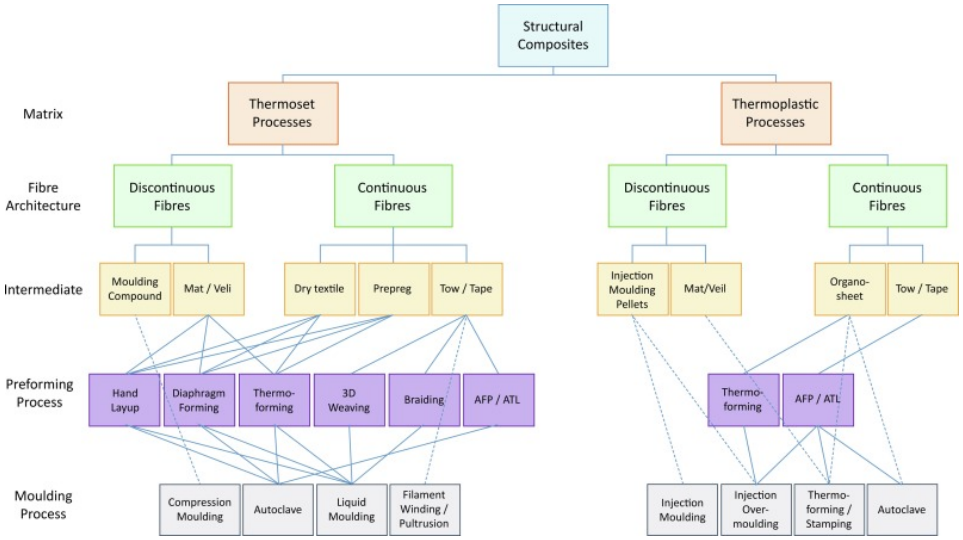

Figure E.1: Flow diagram showing different material options and processing routes for manufacturing structural fibre-reinforced composites [77].

The fibres in FRP are defined by size. It starts with small particles and chopped fibres that are added to the polymer. These types are usually orientated in random directions and add some support to the material. The third type is continuous fibres. These need to be applied in a certain direction adding significant improvements in the material properties in that direction . The continuous fibres can be woven into a cloth allowing to improvements into multiple directions.

(a) Two technicians laying up the fibres for a MOD 70 hydrofoil that is produced using the same production process as the Nacra foils

(b) The Nacra foils in different stages during the manufacturing process showing mould lines and resin that escaped the mould

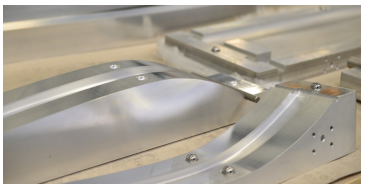

(c) Aluminium moulds that could be used to produce the nacra hydrofoils.

Figure E.2: Pictures showing different steps of production at &DNA composites as shown on their website [67].

On the website of &DNA it is mentioned that they use a carbon prepreg for the production of the hydrofoils [67]. The word '*prepreg*' means that the carbon fibres are already impregnated with the polymer. This is used for continuous fibre sheets with a thermoset polymer. The sheets of prepreg are cut using a pre-preg cutting machine [67] of the brand "*Zund*". The sheets of pre-preg are stacked on top of each other in a mould to create the rough shape of the product. The stacking of the fibre sheets can be seen in Figure E.2a.

The hydrofoils are buildup in two aluminium moulds with the mould on the outside, this is also called a *female mould*. The intersection between the two moulds is located at the leading and trailing edge. These aluminium moulds are aligned using small spherical alignment pins as seen in Figure E.2c.

In order to consolidate the plies of composite material, two plastic bags are placed on the inside of the hydrofoil with a composite spar separating the bags. The composite laminate is put under a vacuum in order to consolidate the plies. The Laminate is then placed in an autoclave to increase the pressure even further. A typical autoclave can reach 3-5 bar of pressure [78]. In the autoclave the part is cured.

The final product is a Nacra 17 hydrofoil with extruded resin and pinched fibres at the leading and trailing edges. These need to be removed by hand creating the final product. There is no assembly needed as the whole foil is made at once using &DNA unique "one-shot" technique [18].

E.2. Manufacturing Defects and their origin

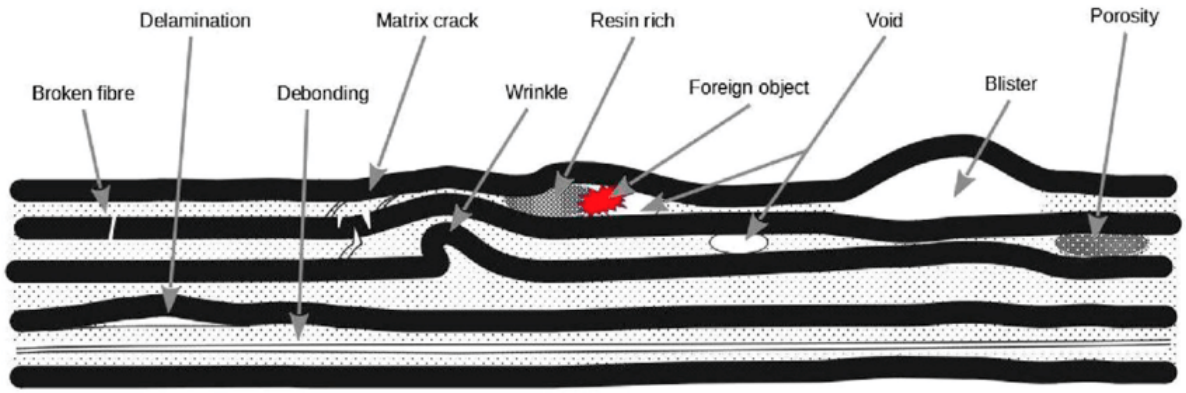

Figure E.3: Common defects that can occur in Fibre reinforced polymers visualised [79].

In the field of composite hydrofoil manufacturing, achieving consistent and high-quality products is essential for ensuring optimal performance. However, the manufacturing process itself can introduce variations that significantly impact the final performance of the hydrofoil. This chapter aims to explore the sources of manufacturing variations and their effects on the hydrofoil's performance using the technologies used by &DNA. Two notable studies, Grabow et al. [80] and Brient et al. [21], shed light on different aspects of this topic, emphasising the impact of manufacturing defects, machining quality, and shape deformations.

Brient et al. [21],tested the impact of milling direction and surface finish on the lift and drag performance. The surface roughness was found to increase drag and decrease lift. A bigger difference was found due to the direction of the tool path. The spanwise direction increased the drag coefficient from .01 to 0.015 compared to the chordwise direction.

During the production process, various types of product defects can occur. Defects that occur in composited parts can be: Voids, Delamination, Fibre misalignment and spring in or residual stress. Trough thickness defects like: voids, delamination and fibre wrinkling are shown in Figure E.3. These defects can appear on their own or be caused by a process related error like lay-up errors and curing errors. Potter [20] made an extensive summery on the different defects and errors that can occur in composite is found in **??** and Table **??**.

Layup errors, which occur during the layup stage of manufacturing, are typically caused by incorrect procedures. Examples of layup errors include using the wrong prepreg or layer count, incorrect ply size, and poor mould preparation or release. Most of these errors can lead to the formation of voids and delamination. **Delamination** refers to the separation of two connected plies, which significantly affects the stiffness and strength of a composite part, rendering it unusable. Delaminations can be caused by factors such as resin shrinkage, contamination, voids, and impact, as well as out-of-plane stresses resulting from demoulding or handling.

Voids are small air pockets within the material that can reduce the stiffness and failure strength of a part. They can be introduced by trapped air, volatiles in the resin or preform, bridging, resin shrinkage, and loss of resin due to excessive bleed or composite tool leakage. Preventing voids within a structure is challenging, but efforts should be made to minimize them through good tool design and proper manufacturing steps.

Cure errors occur when the curing process goes awry. The cure cycle involves specific pressure, temperature profiles, and duration necessary for the consolidation and solidification phases of production. If the specified values are not followed correctly, the properties of the resin deviate from the desired ones. Faults in the cure processes have a significant impact on the mechanical properties and can result in the rejection of the product for use.

"**Springback**" and **Residual Stresses** cause the part to deform and deviate from the design parameters, reducing its strength. When a part is not geometrically constrained, it is likely to warp or "spring

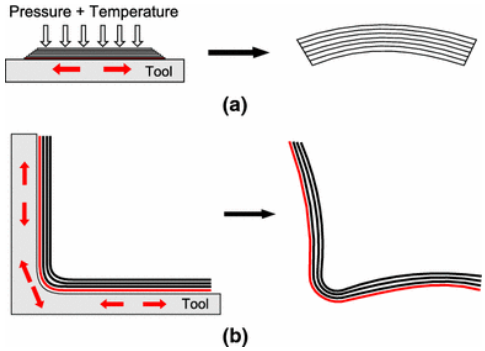

Figure E.4: Effect of tool–part interaction on distortion. a Flat parts. b Parts that have corner sections [81]

in", shown in Figure E.4. On the other hand, when a part is geometrically constrained, such as in a box shape, it experiences residual stresses that diminish its failure strength. These effects can be attributed in part to the interaction between the part and the tool. Large differences in thermal expansion coefficients between the part and tool or improper use of release agents can introduce stresses that lead to warping. Thickness defects like corner bridging and fibre wrinkling/misalignment, resulting from small bend radii and double curved surfaces, also introduce residual stresses and warping to the part.

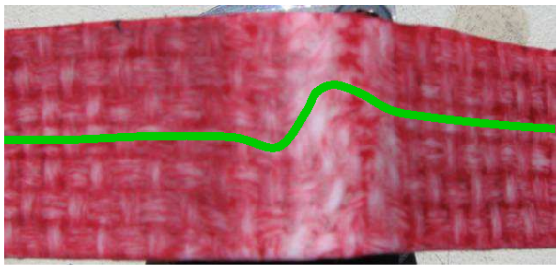

(a) In plane wavy fibre caused by consolidation [20].

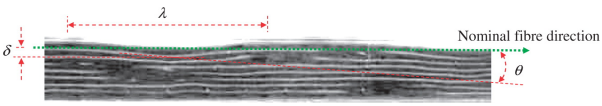

(b) Photograph of out-of-plane waviness in a Resin Transfer Moulding(RTM) component, showing waviness length λ, amplitude δ and misalignment angle θ as seen in Wang [82]

Figure E.5: Fibre wrinkling and waviness for in/out of plane waves

fibre Misalignment refers to errors in the direction of the fibres, including wrinkled and wavy fibres as shown in Figure E.5. Fibre direction errors typically arise from manufacturing processes where fibres are not aligned properly. Wrinkled and wavy fibres can be caused by layup errors, incorrect draping of double curved surfaces, ply drops or overlapping tape/plies, bridging, residual stress, or displaced fibres due to hydraulic compression. fibre waviness and wrinkling can occur in-plane or out of plane.

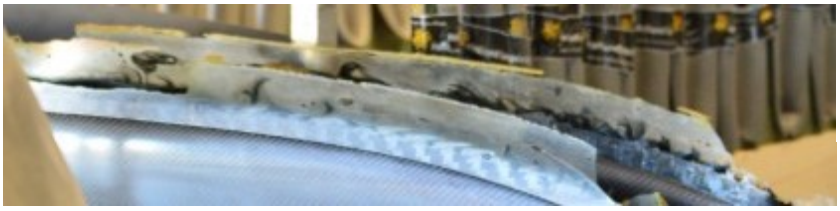

(a) The Nacra 17 hydorfoil showing the resin loss including lose fibres at the leading edge [67].

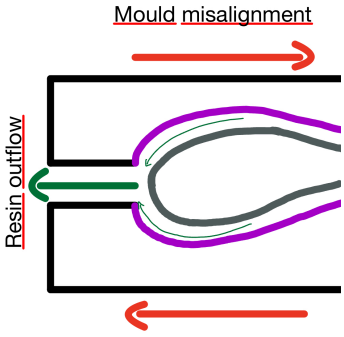

(b) A representation of the two female moulds that are not fully closed allowing the resin to flow from the leading edge in green.

Figure E.6: Mould induced defects for the Nacra 17.

Lastly, defects arising from the **mould line** can result in resin run-out or an incorrect shape. If the part is too thick, the mould may be misaligned (Figure E.6b) or fail to seal properly, leading to resin loss (Figure E.6a). Weakly constructed moulds can also deform under consolidation pressure, thereby distorting the part. Resin runout caused by defects in the mould-line requires post-processing that needs to be performed manually. These defects can result in improper resin distribution or an incorrect shape of the final product. When resin runout occurs, additional steps must be taken by hand to address and correct the issue. This post-processing is necessary to ensure the quality and integrity of the hydrofoils, requiring careful attention and manual intervention.

The product defects that influence the shape are voids, springback, and mould defects. When voids are located at the tool surface, in the case of the hydrofoil, it forms a dip that can affect the flow over the surface. Springback will make the geometry deviate form the intended shape and thus again affecting the hydrodynamic response. The defects related to the mould-line affect the shape as well. Using the aluminium moulds from Figure E.2c as an example. When the part is to thick, the mould will not be able to close completely, this might affect the alignment of the top and bottom mould, shifting the top and bottom shape from each other. The part will also change the overall shape as the hydrofoil has a greater thickness. The separation of the moulds allows for resin to flow out of the part and between the two moulds. That this happens can be observed in Figure E.2b. The flow of resin necessitates the post processing of the hydrofoils to shape the leading and trailing edge back into the original shape. It also means that with a reduction of resin, voids are likely to occur.

The strength of the part is influenced by all the given product defects. Stiffness is mainly affected by: Delamination, fibre misalignment, lay-up errors, cure errors, springback, residual stresses, and thickness variations. Especially the fibre misalignment affects the performance of an hydrofoil. Due to fibre misalignment, the coupling behaviour of the hydrofoil can be changed. This could create a bend-twist coupling that might lead to an unstable flight by twisting the foil to stall at an increased bending load.

In order to reduce the number of defects, it is important at what stage of the product life that the defects are introduced. Springback and residual stresses are controlled in the design stage. The removal of sharp corners and minimisation of double curved surfaces helps reduce these effects. When double curved surfaces are needed, like in a hydrofoil, the right type of weave can be chosen that is better equipped in following the complex shape. Choosing the right mould material to reduce the thermal coefficient variation has to be done during the design process. The mould design can help with resin run out and mould miss-alignment. These parameters are hard to change when production is set up. It should be noted that double curved surfaces form problems for open structures (hydrofoils when produced in two halves) and not closed structures like the one shot production of the Nacra 17 Hydrofoil. The weave type would still be an important parameter in order to follow the shape and prevent wrinkles.

The formation of voids is very dependent on the production itself. With a higher consolidation pressure, the voids can avoid being formed or pushed out of the part. The use of vacuum can pull gasses out of the part, thus reducing the voids or let resin flow to open regions that can become voids. This is the reason for the use of vacuum pumps and an autoclave. Grabow et al. [80] did research in the impact on manufacture techniques on the formation of voids with a special interest in hydrofoils. The many curves in a hydrofoil make the production of composites relatively difficult. They found that Automatic tape laying produced much higher quality parts with respect to hand layup. During hand layup, a much lower pressure is applied on the composite ply that reduces the compaction. Combining the lower precision of even skilled workers, small thickness variations, waviness and misalignment are introduced. This is supposed to be solved by applying a vacuum to the part for every 2 to 10 layers. Due to the nature of pressure, the force was applied normal to the material instead of normal to the mould. This error grows with an increase in plies. The effect of the variations only became clear after consolidation resulting in more variations of thickness. These irregularities during curing where interpreted as uncontrolled resin flow generated by a heterogeneous compaction. Although the porosity level where similar, larger areas of porosity's where observed.

The main impact on the geometry variations in composite hydrofoils are created by the mould design. Taking into account production steps that can improve the accuracy of the lay-up of a composite part. Minimising complex lay-up procedures and the need for post-processing while creating precise shapes

should be strived for. Adding fibre cutting machines, as is shown by &DNA, is an example of minimising variability within production parameters.

F

Hydrodynamic Analysis

The hydrodynamic performance be divided in two area's. The first area is the ultimate possible speed a hydrofoil can achieve at each wind speed and direction and the second is the ability of the sailors to get the most out of the foils. The drag is ultimately preventing the boat to go faster, but if the boat is unstable and it often crashes the sailors will still not win the race.

The reason for a foiling boat is to reduce the water resistance of the hull in order to increase the speed. The efficiency of foiling is best visualised by Artemis Racing when they sailed up the Amazon river without any wind [83]. They used their AC45 (flying sailing catamaran) on the amazon with a 10 knot current and no wind. The current generated enough airflow for the boat to move, lift-off and start sailing up the river. While sailing in displacement mode, with a hull in the water, boats barely surpass the wind speed and if they do it is almost always while moving away from the direction of the wind. This highlights the efficiency of the hydrofoils and the sails of the AC45 that allows the boat to move up wind at a higher speed as the current.

While a boat can be theoretically fast, it is up to the sailors to get the boat up to speed. To quote the formula 1 car designer Gary Anderson "I always tried to produce a consistent and useable car that wasn't too peaky aerodynamically to allow drivers to be confident" [84]. The same holds true for a sailor. If the optimal range for a boat is very small or close to crashing, it will be difficulty for the sailors to reach this point. There is thus a need to understand the impacts on the flow by small geometric deviations of the hydrofoils.

F.1. Hydrodynamic Theoretical Background

The section will explore the different concepts that are treated within hydrodynamics. In the following sections it will be discussed:

sec: F.1.1 Who provide the base for our hydrodynamics understanding?

sec: F.1.2 What flow is.

sec: F.1.3 Why for water we assume incompressible flow.

sec: F.1.4 Why viscosity is important.

sec: F.5 What the effect of the boundary layer is.

sec: F.1.6 What effects the 2D profile Drag.

sec: F.1.7 What effects the 2D profile Lift.

sec: F.1.8 What happens when the flow is not ideal.

sec: F.1.9 How the water surface influences the hydrofoil.

sec: F.1.10 What the impact of a structure can be on the Hydrodynamics.

F.1.1. Background

The study of wings emerged in parallel with the first controlled flights in the early 20th century. However, the understanding of flow principles was limited during this time, resulting in a significant gap between theoretical hydrodynamics, hydraulics, and aerodynamics around 1900 [85]. It took the publication of boundary layer theory by Prandtl to combine the different fields of fluid dynamics. "*It is the great merit of L. Prandtl, to have shown a way how both diverging trends of fluid mechanics could be combined again*"Schlichting and Riegels [86].

In the late 1920s and into the 1930s the National Advisory committee for aeronautics (Now NASA), developed a series of aerofoils denoted by 4 numbers. Together with the findings of Schrenk [27] that identified the correlation between curvature and thickness in the lift and drag, allowed a conceptual understanding of the shape of the aerofoil. The resulting graphs of these experiments were published and allowed engineers to quickly see the peculiarities of each shape [28]. These series were complemented by the 5, 6 and 7 series aerofoils. A large overview of the aerofoil data and the effect of different geometry/assumptions is presented by Abbott and Von Doenhoff [87]. This type of research was also performed by Richard Eppler [88] and Michael Seilg [35]. Using the collection of data, the effect of viscosity, perturbations, and smoothness of the aerofoil surface could be analysed using the pressure distribution, lift over angle of attack, and lift over drag. Due to the complexity with fluid dynamic flow, the combination of the research is not able to predict all types of shape variations.

F.1.2. Flow-types

Fluids are a large collection of molecules that are free to move. Good examples of this are the water and air around us. When studying the flow of molecules it is very difficult to keep track of every individual molecule as they move about in a random motion. It is not needed to calculate the position for every single molecule to analyse the aero- or hydrodynamic performance. Anderson (2017) explains it as follows: The distance for a molecule to move before it hits another molecule is called the mean-free path λ. If λ is magnitudes smaller compared to the scale of the body that is measured by diameter d, the flow appears to be a continuous substance. This is called a *continuum flow*. On earth, microscopic structures need to be analysed to take into account the individual molecules. The opposite of Continuum flow, Free Molecule Flow is usually observed when in space. The distance between the molecules is larger as the space craft and the space craft can distinguish each atom it hits. For the analyses in this report all flow will be a continuum flow.

F.1.3. Compressible vs incompressible

The distance between each molecule allows for the molecules to be compressed. All fluids can be compressed and this compression is caused by differences in pressure. When a flow hits an object there are differences of pressure around this object. In this report, hydrodynamics is analysed. Homogeneous liquids like water are already densely packed and do not really change in density when compressed. Accounting for the change in density when analysing the flow will make it more difficult. Thus for the analysis it is assumed the fluid is incompressible.

F.1.4. Viscosity

When the molecules move around they will transport mass, momentum, and energy. The transfer of these molecules will give rise to phenomena like mass diffusion, viscosity (friction), and thermal conduction. A flow exhibiting these behaviours are called *viscous flow* [69]. If these phenomena are not taken into account the flow is called an *inviscid flow*.

Just like incompressible flows, inviscid flows do not truly appear in nature. However, inviscid flow is approached when the Reynolds number goes to infinity. The Reynolds number (Equation F.1) is the ratio between the inertial and to viscous forces within a fluid which is subjected to relative internal movement due to different velocities within the fluid. With the flow speed (V), chord length (l), density

(ρ) and dynamic viscosity (μ).

$$Re = \frac{\rho V l}{\mu} \tag{F.1}$$

The Reynolds number allows for scaling of an object. A large cylinder with a relatively high flow velocity will react the same as a smaller cylinder with a lower velocity in the same fluid. At relatively high Reynolds numbers (>10^6), the fluid can be assumed inviscid for certain practical problem. At high Reynolds numbers the effects of a viscous fluid are limited to a small area around the body, this area is called the **boundary layer** [69].

Inviscid flows assumes no shear stress in the flow. Friction (shear stress) is a large part of aerodynamic drag. Thus an inviscid flow will not be able to correctly predict the total drag of the profile. For the analysis of the Hydrofoil a viscous flow is needed to analyse the different foils. Viscous flow requires the analysis of the boundary layer.

F.1.5. Boundary layer

The boundary layer is formed by the no slip condition at the object surface and the shear stress between the air layers. At the surface of a body the speed of the flow is zero with respect to the object (no slip). The speed of the flow will increase the further away from the surface. At a certain height the speed of the flow is equal to the speed of the flow far away from the object. The boundary layer is the region where the speed of the flow increases from zero to the bulk flow speed. The expanded view in Figure F.1b show this increase in speed. The change of speed is the cause of skin friction drag. The thickness of the boundary layer influences the the drag where a lower thickness creates less drag. The thickness of the boundary layer is dependent on the speed differential, caused by the surface friction and bulk flow speed, and the type of flow. There are two types of viscous flow as quoted from Anderson [69]:

- *Laminar flow*, in which the streamlines are smooth and regular and a fluid element moves smoothly along a streamline
- *Turbulent flow*, in which the streamlines break up and a fluid element moves in a random, irregular, and tortuous fashion

These types of flow can be observed in Figure F.1. The laminar flow in Figure F.1a, on the bottom moves fast and stays in the same shape. At a certain point this flow becomes unstable (**transition point**) and becomes turbulent. The region of flow is now increased as well. The point at which the flow transitions to a turbulent state is influenced by the roughness of the surface of an aerofoil as shown in Figure F.1c. A rough surface will increase the shear stress and will initiate the transition to a turbulent faster moving the transition point forward on the foil chord.

The friction on the skin differs between the two types of flow. A aerofoil with a laminar flow will experience less skin friction compared to an aerofoil with a turbulent boundary layer. The difference of the drag can be observed in Figure F.1d. It can be seen that after the transition the drag doubles in magnitude between the angles of -1 and 3 degree.

F.1.6. Drag

The Drag for a section is given by:

$$D = \frac{1}{2}\rho_\infty V_\infty^2 S C_D \tag{F.2}$$

The ρ_∞ is the freestream density of the fluid. While V_∞ is the freestream velocity. S is the area span of the object. The effect of drag for different shapes and different speeds is shown in Figure F.2. That S is independent of the drag coefficient can also be observed in Figure F.2a. The coefficient is comparable for the same shape at the same Reynolds number independent of size. When changing the Reynolds number the coefficient does change in value. When the airspeed increases the distribution between skin friction drag and pressure drag changes as the skin friction drag only increases slightly. This change in composition affects the C_D and shows that the skin friction drag is a big component at the Reynolds numbers where the Nacra hydrofoil operates in (up to $5 * 10^5$ with the average in the 10^4, sec**??**).

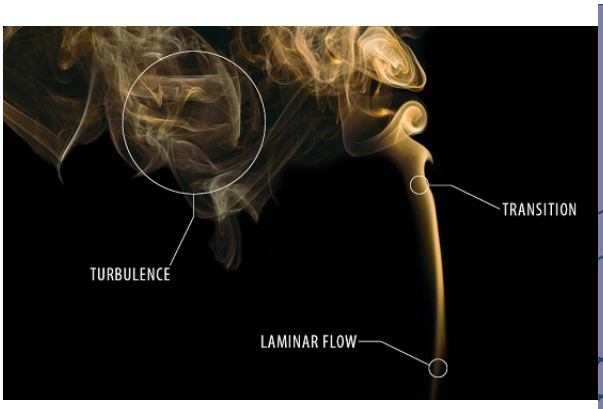

(a) Airflow visualised with smoke starting as a laminar flow and transitioning to a turbulent flow on the top. [68]

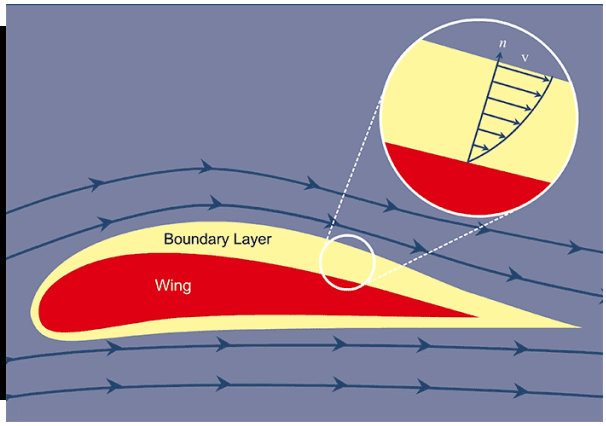

(b) An visualisation of the boundary layer around an aerofoil

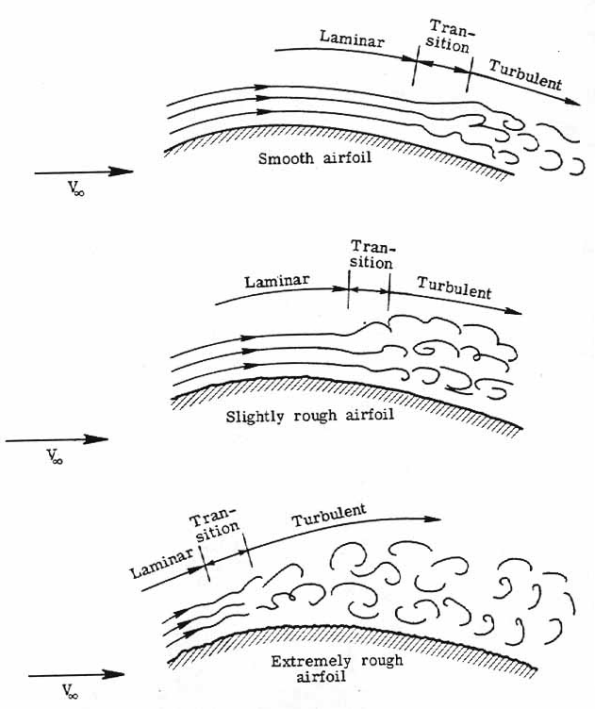

(c) The roughness of the aerofoil affecting the laminar to turbulent transition point from smooth to rough. [89]

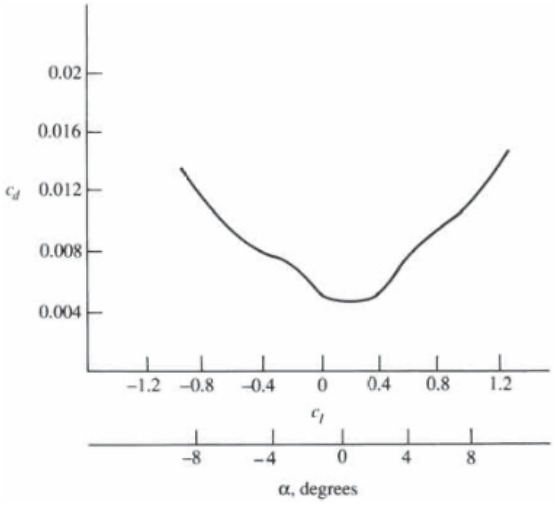

(d) Section drag coefficient for an NACA 63-210 aerofoil at Re = 3 x 10^6 [69]. The bump shows drag with laminar flow with an increase after the flow transitions to turbulant.

Figure F.1: The difference between laminar and turbulent flow.

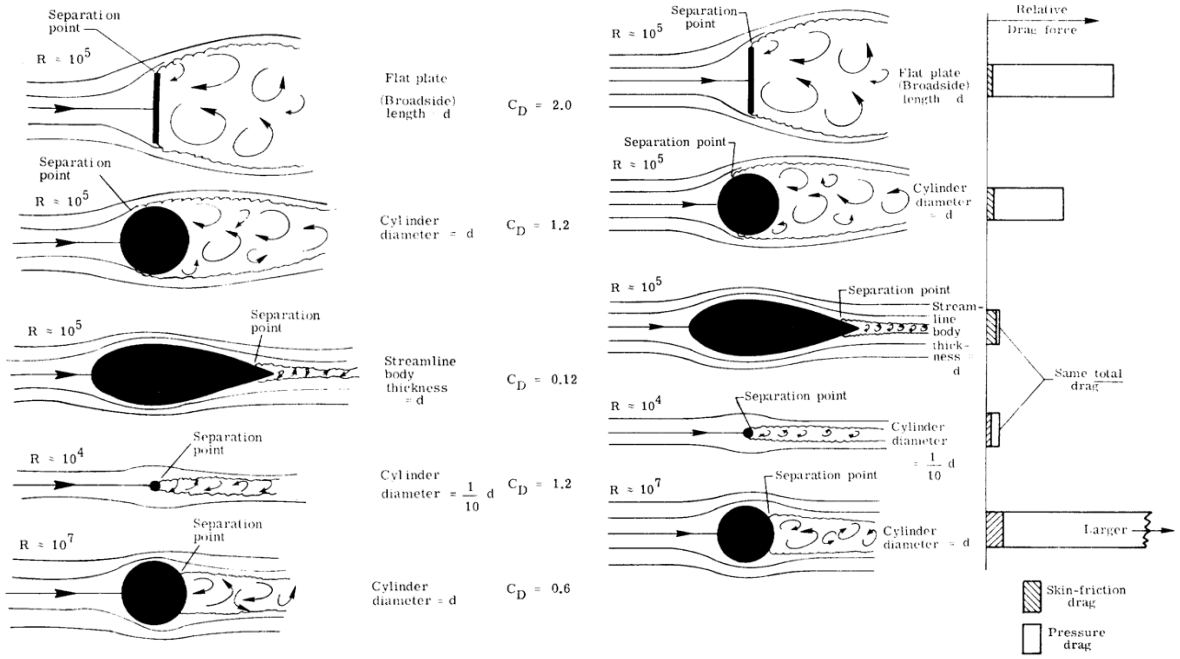

(a) Drag coefficients

(b) Composition of the drag component

Figure F.2: 2D flow visualised around various aerodynamic shapes, Reynolds numbers and frontal area 'd' [89]

Behind each shape there is a wake. This wake is created by the separation of the flow from the object. This wake consists of very turbulent air following the object. The velocity distribution across the wake will yield the drag of the measured object [69]. This shows that the size of the wake is an important contribution to the overall drag. Figure F.2b shows this connection as the drag force is equal for the teardrop shape and the cylinder one tenth its size but with the same cross section for the wake.

Some aerofoils are designed to have a laminar flow across the section to reduce the skin friction drag. While increasing the angle of attack the flow will transition from laminar to turbulent starting at the trailing edge. The laminar region reduces the skin friction drag visualised by the bump in Figure F.1d. This bump is called the drag bucket. The larger increase of drag after the drag bucket is caused by the separation of the flow from the surface, increasing the area of the wake.

Even though the turbulent flow generates more drag, it can be a desired type of flow in certain situations. Due to the larger size of a turbulent boundary layer and the smaller difference in speed across the boundary layer, the turbulent flow is said to stick more to the surface [90]. This reduces the wake and increases the angle of at which most lift is lost (stall).

F.1.7. Lift

The flow around an object can generate a perpendicular force known as lift. Lift is produced due to variations in the flow around the object's profile. In Figure F.3, the lift and the induced drag are depicted based on the reaction force acting on a flat plate. This example demonstrates a situation where the majority of lift is generated by the plate's impact. However, for a more streamlined shape, there are additional factors contributing to lift.

As the flow encounters the object, it must flow around it, causing the flow to curve. Initially, the flow is pushed away from the object and subsequently pulled back towards it at a specific point. This curvature is particularly noticeable when the flow remains attached to the object. The pressure difference around the object is both a cause and a result of this curvature. Figure F.4 illustrates the pressure distribution around a symmetric aerofoil at an angle of attack (AOA) of 0 degrees. It demonstrates the higher pressure at the front (positive cp and the arrows pointing to the profile), followed by negative pressure

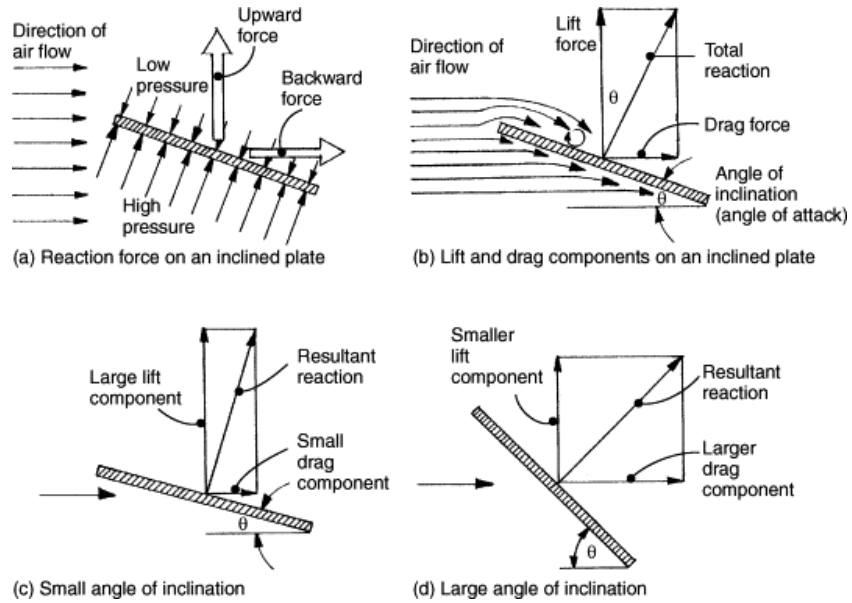

Figure F.3: The force components that result from an object moving through air.[91]

(negative cp and arrows pointing away) to curve the flow over the foil. At an angle of 10 degrees, the lower surface primarily pushes the flow away, resulting in positive pressure, while the top surface pulls the flow, creating negative pressure.

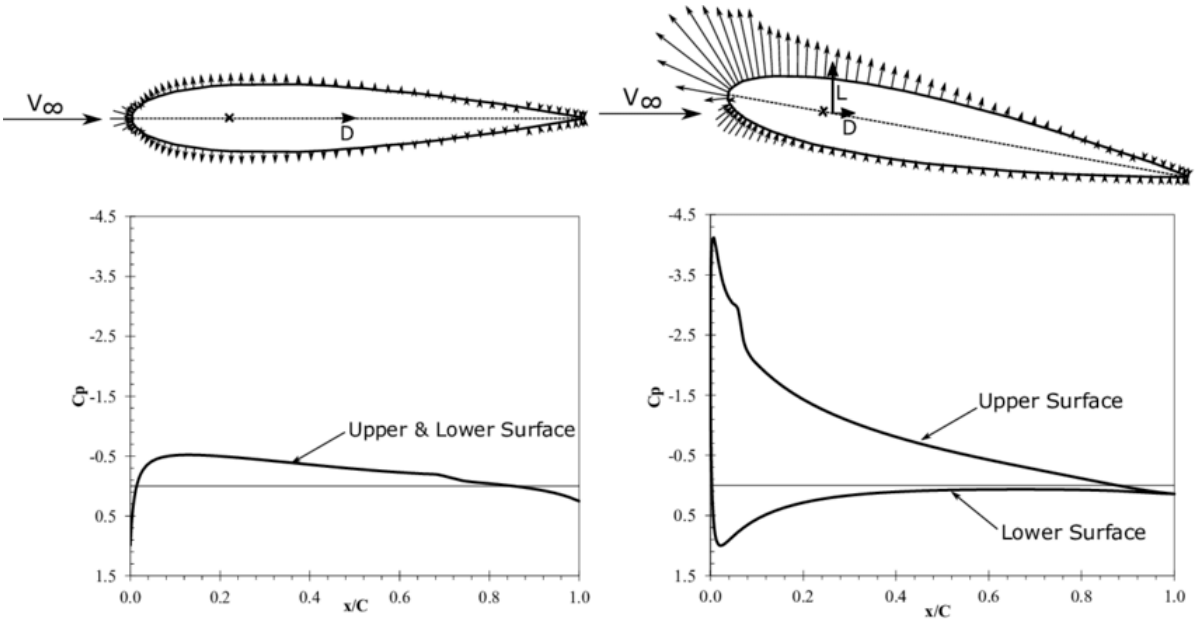

Figure F.4: Pressure distribution for a symmetric aerofoil at 0◦ and 10◦ angle of attack [92].

The pressure difference produces the same force vectors shown in Figure F.3. The graph represents the pressure in terms of pressure coefficient rather than absolute pressure. This dimensionless pressure coefficient is calculated using the following formula:

$$c_p = \frac{P - P_\infty}{2\rho_\infty V_\infty^2} \tag{F.3}$$

Here, P represents the local pressure, P_∞ is the freestream pressure, ρ_∞ is the freestream density, and V_∞ is the freestream velocity.

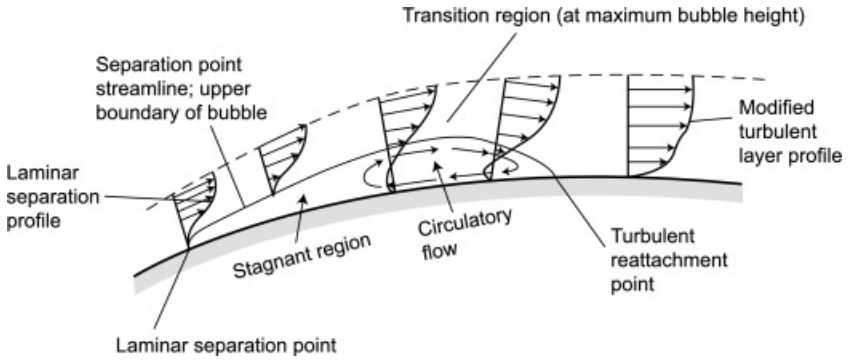

Figure F.5: Laminar separation bubble transition into turbulent layer [90].

To construct lift, drag, and moment, the pressure coefficient acting normal to the surface and the surface friction acting parallel to it are considered. These two factors together contribute to the normal and axial force components, which can then be transformed into lift and drag force vectors. The lift, drag, and moment coefficients are defined as follows:

$$C_L = \frac{L}{\frac{1}{2}\rho_\infty V_\infty^2 S} \tag{F.4}$$

$$C_D = \frac{D}{\frac{1}{2}\rho_\infty V_\infty^2 S} \tag{F.5}$$

$$C_M = \frac{M}{\frac{1}{2}\rho_\infty V_\infty^2 Sc} \tag{F.6}$$

In these equations, S represents the reference area. For a complete plane or wing, the reference area is the wing's total surface area, and the coefficients are denoted in capital letters. However, when considering a 2D section, S is equivalent to the chord length (c), and the coefficients are represented in lowercase letters (c_l).

F.1.8. Flow instabilities

Separation Bubbles As stated before, when separation occurs on the surface, this affects the thickness of the wake and thus the drag. While the separation of turbulent flow will generally not attach to the surface. A separation in the laminar flow can reattach back to the surface creating an laminar separation bubble, visualised in Figure F.5. This bubble can be between 1% of the chord to almost 100% of the chord. The transition to a turbulent flow allows for a large enough boundary layer that the flow can reattach to the surface. These bubbles are usually created at low pressure and large curvatures areas of the foil. The small bubbles appear at displacement-thickness Reynolds numbers ($Re_{\delta^*} = \frac{V_e \delta^*}{\nu}$) of 550 and higher. While the large separation bubbles appear at $Re_{\delta^*} > 400$. Between both numbers, both types can occur. The drop in pressure can be seen by comparing the inviscid and the viscous flow as seen in Figure F.6.

Cavitation When the pressure on the low side of the foil decreases far enough, the vapour saturation pressure of water can be crossed and the water will change its phase [33]. This phase change from liquid to gaseous is called cavitation. Within the field maritime engineering this is usually observed in small quantities at propellers and the rudders of very large ships. The formation and collapse of cavitation causes effects like noise, vibration, cavitation erosion and a unsteady interaction between liquid/vaper boundaries that affect the lift/drag of an aerofoil [32, 93].

The cavitation is analysed using the cavitation number (σ), calculated with Equation F.7 [94]. With P_v as the vapour pressure of the fluid and P_∞ the local water pressure. If the local pressure coefficient, calculated with Equation F.3, satisfies $C_p \leq \sigma$ cavitation will form on the surface.

$$\sigma = \frac{P_\infty - P_v}{0.5\rho V_\infty^2} \tag{F.7}$$

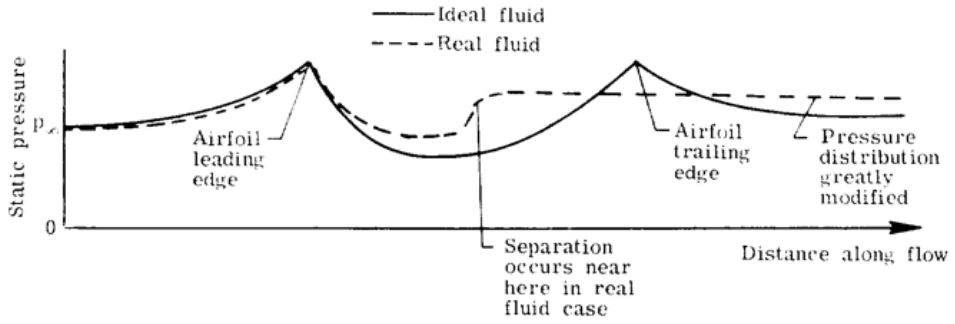

Figure F.6: Pressure distribution for the inviscid (ideal) and viscous (real) flow.

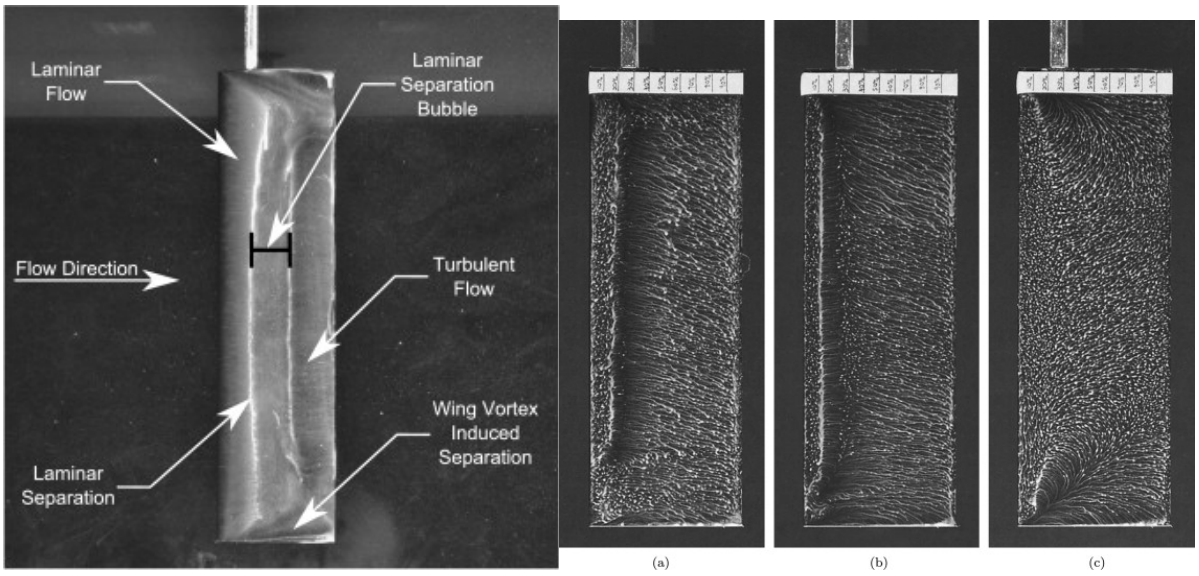

(a) Upper surface oil flow visualization of major flow features on the Wortmann FX 63-137 rectangular wing with aspect ratio of 4 (α = 9 deg, Re = 90,000).

(b) Upper surface oil flow visualization on the rectangular flat-plate, aspect ratio 3 wing at a Reynolds number of 60,000 at (a) α = 5 deg, (b) α = 7 deg, and (c) α = 10 deg.

Figure F.7: Visualisation of the laminar separation bubble on a flat plate by Ananda, Sukumar, and Selig [6]

There are 3 main types of cavitation as identified by Carlton [95].

1. **Vortex Cavitation**: This is usually the first type of cavitation that occurs. It starts when the pressure in the (tip) vertices drops below the vapour pressure. It often starts further away from the profile and looks like a mirrored rope.
2. **Sheet Cavitation**: Appears at the leading edge at higher angles of attack. With high suction pressures due to low leading edge curvature, sheet cavitation can occur. It is usually a stable blanket covering the first part of the profile
3. **Bubble Cavitation**: Is cavitation due to excessive camber/thickness and appears from mid span. It usually appears in non-separated flow and moves fast along the chord as bubbles.
4. **Cloud Cavitation**: Is found behind sheet cavitation and is usually a region of separated flow.

Cavitation can be influenced by a number of different parameters. Onishi, Matsuda, and Miyagawa [96] investigated the influence of hydrophobic coatings on the hydrofoil performance with respect to the cavitation. Together with the surface roughness, researched by citethao2018influence, are affecting the behaviour of the cavitation. They affect the forming, size and shedding frequency of the cavitation. Smith et al. [97] found that this shedding frequency affects and is affected by the natural frequency of the hydrofoil. The exact initiation of the cavitation is hard to model and predict, according to Schnerr and Sauer [98]. Hao, Zhang, and Huang [99] analysed cloud cavitation on the the Clark Y aerofoil section

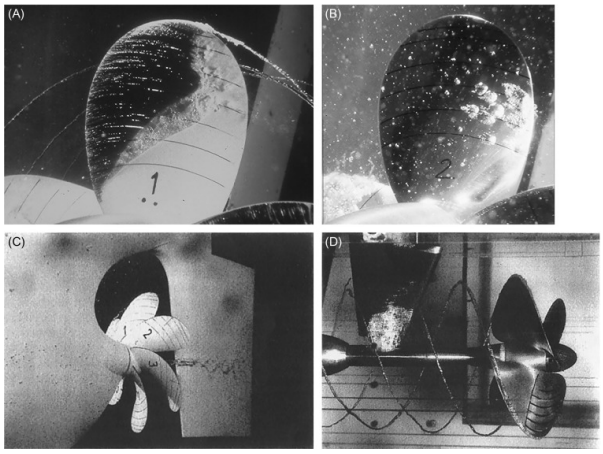

Figure F.8: Types of cavitation by Carlton [7]:(A) Sheet and Cloud cavitation with an attached tip Vortex, (B) mid-chord bubble cavitation, (C) Hub Vortex cavitation, (D) Tip vortex cavitation

at Reynolds numbers of $5.6 * 10^5$ and angles of attack of 8 degree. This is would indicate that cavitation needs to be accounted for during the analysis of the foil. The speed at which cavitation significantly affects the performance of the hydrofoils is usually found to be above 50-60 knots [95] (25-30 m/s). The Nacra 17 does not come close to these speeds, although it will be taken into account by evaluating the cavitation number σ.

F.1.9. Surface effects

Figure F.9a shows the creation of waves at the surface when the depth of submersion decreases. The interaction with the surface does create some complex interactions that need to be accounted for. The phenomenon can be split for vertical and horizontal surface-piercing hydrofoils. The values for each type can be projected on to the real angled hydrofoil. Using the chordwise froude number:

$$F_c = \frac{V}{\sqrt{gc}} \tag{F.8}$$

Vertical foil For vertical hydrofoils the following assumptions can be made using the example that is shown in Figure F.9a:

1. **effective aspect ratio**: decreases from twice its span to approximately .7 its original span with an increase in F_c (Figure F.9b).
2. **Wave drag**: can be neglected above a speed of $F_c = 3$. This is reached before the Nacra 17 lifts out of the water as measured by Hoerner [30] and collaborated in figures F.9c and F.9d.
3. **Spray drag**: Spray drag is approximately .24 for a thickness ratio of $\frac{t}{x_t} \leq .4$ and .12 for a thickness ratio greater than .4, found by [30] and in figures F.9c and F.9d.

Horizontal foil The case for the **horizontal foil** is more difficult. When the hydrofoil is submerged to a significant depth, the situation is comparable to a high flying aeroplane. When the distance decreases the pressure field of the hydrofoil will interact with the free surface. This effects the lift and drag by distorting the surface and creating waves. To calculate the speed, the depth froude number was devised as shown in Equation F.9. With (V) the flow speed, (g) the gravitation acceleration, and (h) the immersion depth. The effect of the lift and drag as shown in Figure F.10b can be estimated by the biplane theory proposed by Hoerner [30]. This is simulated by placing an identical foil 2 times the immersion depth away from the original foil. This holds true for an immersion depth less than 2 times the foil chord. For foils place at greater depth most impacts from the free surface can be neglected.

$$F_h = \frac{V}{\sqrt{gh}} \tag{F.9}$$

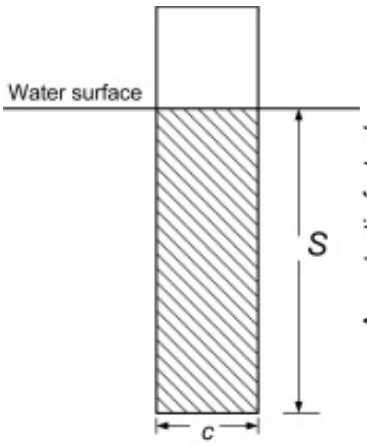

(a) Vertical surface-piercing foil.

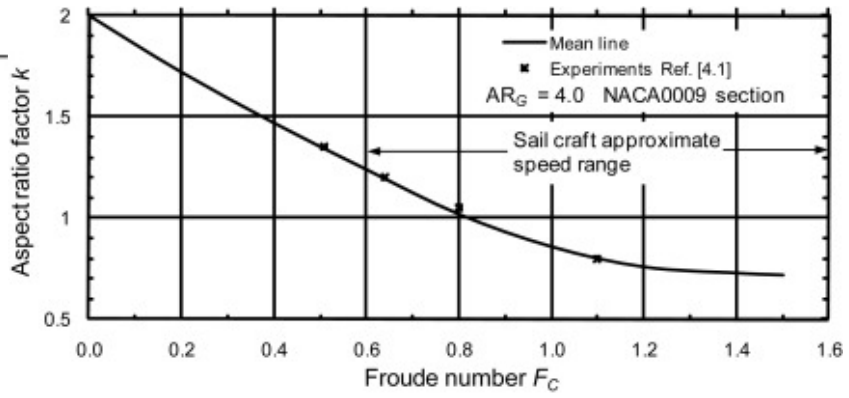

(b) Influence of speed on aspect ratio.

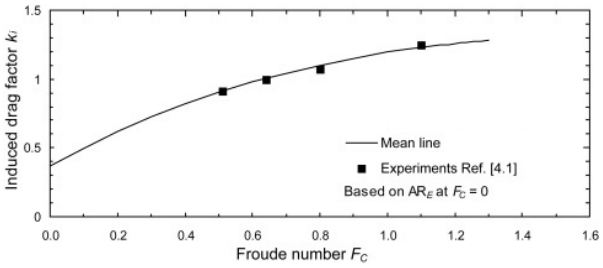

(c) Influence of speed on induced drag.

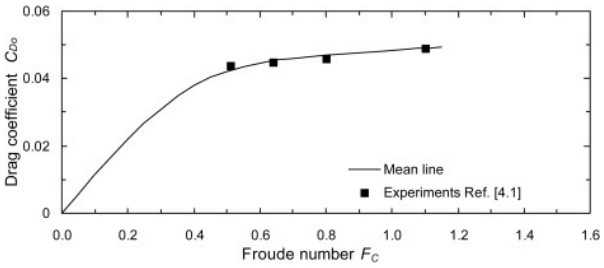

(d) Influence of speed on minimum drag.

Figure F.9: Showing the effects of speed defined by chord froude equation (F.8) as presented by Molland and Turnock [8].

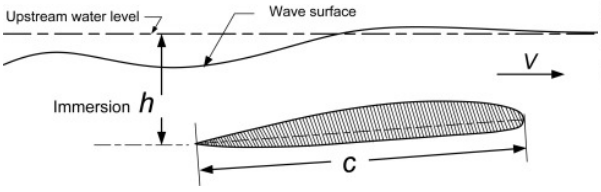

(a) Horizontal near free surface.

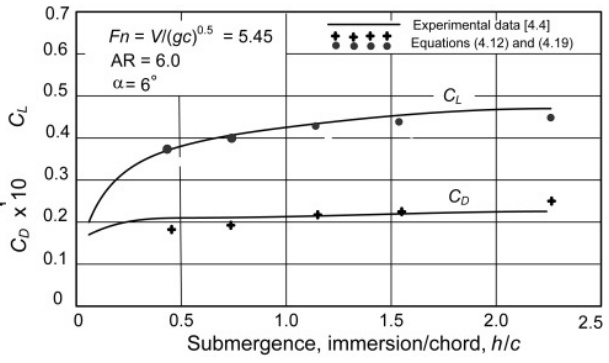

(b) Surface affect due to immersion depth.

Figure F.10: Showing the effects of a horizontal foil approaching the free surface as shown by Molland and Turnock [8]

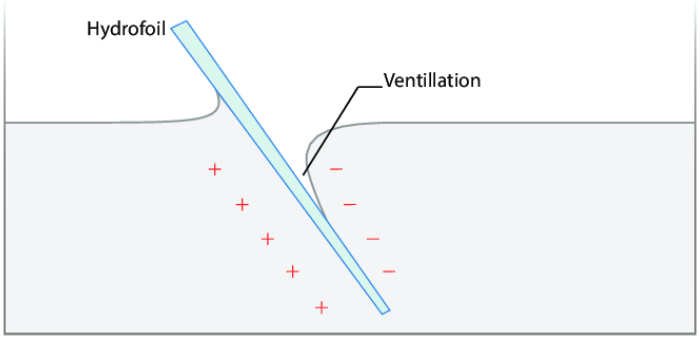

Figure F.11: Ventilation induced by a lifting hydrofoil piercing the free surface [70].

Ventilation When surface-piercing hydrofoils are considered, the presence of separation bubbles leads to the deformation of the foil shape, which affects suction at the leading edge. This low pressure separated flow gives rise to a phenomenon known as ”ventilation.” Ventilation, as explained by Hoerner [31], is the formation of a steady cavity connected to the atmosphere behind or past a surface-piercing body. To experience ventilation, two conditions need to be fulfilled, as discovered by [100]: a zone of low pressure, specifically lower pressure in the surrounding atmosphere on the suction side of the foil, and a separated flow on the suction side. In their study, the ventilated flow exhibited a 33% decrease in lift compared to the wetted flow. The Nacra 17 utilises these surface-piercing hydrofoils as its primary front hydrofoils. Unlike hydrofoils employing symmetric sectioned struts beneath the water surface, surface-piercing hydrofoils employ non-symmetric aerofoil sections at the water surface. This distinction is significant as it generates lift in close proximity to the water surface. Consequently, these types of foils are highly susceptible to ventilation phenomena. When ventilation occurs, the aforementioned reduction in lift often leads to the boat crashing.

The exact mechanics of ventilation are, as of now, hard to predict. Young et al. [34] and Harwood, Young, and Ceccio [101] investigated the initiation of ventilation. Harwood, Young, and Ceccio [101] set out to quantify the problem set by ventilation. They found that there is a critical region where ventilation can occur. If it does, it results in a large loss of lift. The effects that quantified by Harwood, Young, and Ceccio [101] are hard to scale according to Young et al. [34]. The scaling over froude or Reynolds number is critical in the application of the knowledge in new designs. The difficulty of modelling ventilation is highlighted by Keller et al. [102]. They set out to model the hydrofoil performance while ventilated but did not manage to match the test data to the CFD analysis. That ventilation is affected by the surface properties of the foils is highlited by Vakarelski et al. [103]. They tested how hydrofoils behave when coated in a hydrophobic coating. The results are that the hydrofoils are very susceptible to ventilation. As is stated before, ventilation can occur when a separated region at lower than atmospheric pressure exists. For the hydrophobic coating it could be separating the flow at an earlier stage or a smaller pressure difference was needed for the flow to propagate along the foil. According to Abbott and Doenhoff [29], Selig, Donovan, and Fraser [35], Eppler [88], and Conner [104] the separation bubbles form at Reynolds numbers ($60.000 < \mathrm{Re} < 500.000$), the same Reynolds numbers the Nacra 17 operates in. These laminar separation bubbles can facilitate ventilation according to Wetzel [105] and Keller et al. [102]. The methods of mitigating ventilation as suggested by Rothblum [106] are:

- Preventing propagation using a fence (obstacle).
- Preventing separation by boundary layer suction
- Preventing separation by boundary layer blowing

F.1.10. Fluid-Structure Interaction

Both Cavitation and Ventilation can be very dynamic phenomena. The change of fluid density affects the damping of the structure and the natural frequency. Research at the French Naval Academy [107–

109] found that as the relative mass ratio and stiffness of the hydrofoil decrease, there is an increasing tendency for the cavitation cavity shedding to lock-in to the foil resonance frequency and its subharmonics [108]. Young et al. [34] identified that the uncontrolled or unanticipated formation of ventilation cavities (or ventilation of vaporous cavities) can be very sudden and lead to control difficulties in addition to structural and/or hydro-elastic stability issues such as conduction, fluttering, transient (or parametric resonance). This is after considering the desire to create lighter structures with a minimum frontal area to reduce resistance. While still supporting the high loads created, as shown in **??**.

Axisa and Antunes [110] defined *fluid-structure interaction* as: "*dynamical coupling between a solid and a fluid in the absence of any permanent flow*" This is sometimes incorrectly combined with *flow-induced vibration* stated as: " *a permanent flow about a vibrating structure*"[110]. The dynamical behaviour obtained from the fluid-structure interaction forms the reference state for the dynamical response between the permanent flow and vibrating structure. Several methods for calculating the fluid-structural response are highlighted in the book written by Zhao and Su [111].

The significant impact of the material properties on the hydrofoil performance, analysed with FSI is highlighted by Knight et al. [112],Temtching Temou et al. [113] and Marimon Giovannetti et al. [43]. The goal to produce lighter and thinner structures can be achieved by utilising the an-isotropic nature of composite materials. This an-isotropic behaviour adds coupling behaviour that adds bend-twist coupling to the structure. Bend-twist coupling could unload the foil when a high bending moment is applied creating a stable system. Temou [114] did an extensive analysis to predict this behaviour. Nicholls-Lee, Turnock, and Boyd [115] investigated the possibility of these effects on tidal turbines. While for sailboats, the tuning of the mechanical behaviour was investigated by Giovannetti et al. [116] and elaborated on in her Ph.D. thesis Giovannetti [117].

F.2. Hydrodynamic Methodology

Using the knowledge of the flow around the foil. The flow needs to be analysed using a suitable program/calculation method.

The different tools that can be used for a 2D section analysis are first identified. Weighing their accuracy over the usability a solver will be chosen for the analysis in the thesis. This will tool will be used to answer the main question of this Chapter. Different critical parameters of a 2D hydrofoil will be investigated to narrow the scope of the possible variables that are introduced by the Manufacturing variability

F.2.1. 2D solvers

The following programs are found to calculate 2D aerofoil sections.

- Profil
- Xfoil 2 dimensional panel method
- javafoil 2 dimensional panel method
- Rfoil 2 dimensional panel method
- OpenFoam CFD
- TetrUSS CFD

Profile was the first panel code introduced by Professor Richard Eppler, University of Stuttgart, Germany [39]. Profil uses an 3rd order panel method and an integral boundary layer method. In contrast to Xfoil, PROFII does not couple the boundary layer and the external flow field. In order to predict transition it uses empirically derived transition relations. This method brakes down when some form of separation occurs.

Xfoil uses 2nd order panel method for the inviscid analysis. This results in a slightly worse prediction of both lift and drag. Xfoil does however couple the external flow field and the boundary layer, improving the results for separation within the aerofoils chord. This improves the transition prediction of xfoil. The transition formulation is based on the e^n method [38] and denotes the stability of the flow.

Java uses a third order panel method with the same boundary layer integral method used in the Eppler code [118]. Javafoil adds new stall and transition models to the boundary layer module.

Where all the panel methods use potential flow theory to solve the equations. CFD estimates the behaviour of the flow itself for discrete cells. The solution for one cell will update the solution for the other cells. There are different turbulence models for the calculations in these cells. These can all be present in each CFD program. The difference between these CFD programmes, is mainly focused on the user interface and the optimisation of the calculations to reduce the processing time while increasing resolution (accuracy).

CFD is a wide field of research. As discussed, OpenFoam and TrussUSD are only some of the many programs that perform CFD analysis. The main difference between these programs is the efficiency of calculation and the user interface. For CFD, the flow is apporoached from a more basic understanding. While all flow analysis is derived from the navier stokes equations, a panel method uses significant simplifications. The CFD allows for a better calculation of the navier stokes equations. For CFD there are a number of turbulent models that calculate the flow behaviour. In Figure F.12 these are $\kappa - \omega$ SST (Shear Stress Transport), $\kappa - \kappa l \omega$ transition model. Gotten et al. [119] also uses a $\kappa - \epsilon$ model. The different models use a difference theoretical assumption to calculate the flow. With most models it is true that a higher resolution leads to an increase in computational time. For more information on CFD analysis, Hu [120] discusses the computational method of CFD analysis.

F.2.2. 2D Solver accuracy

How accurate do these programs predict the flow around an aerofoil? The program ***Aerofoil*** is not open to the public. The only validation data is found on their website [121]. The tool shows a good prediction of the lift curve and the maximum lift, although lower as the experimental values. It over predicts the loss of lift after stall and stalls at a slightly lower angle of attack. The drag is over predicted near the drag bucket.

Xfoil and Javafoil are based/improvement on the theory of Profile and are thus considered more accurate [122]. While Profile and Xfoil use a second order panel method, Javafoil can apply even higher order panel method. The higher orders can be more sensitive to complex flows like separation resulting in an overall lower accuracy when there is more than one type of flow [123]. Bergman et. all [124] showed that Java foil predicted a separation bubble while xfoil, the CFD analysis and the experiment data did not show an significant separation event. This prediction resulted in a very high error for both the lift and the drag.

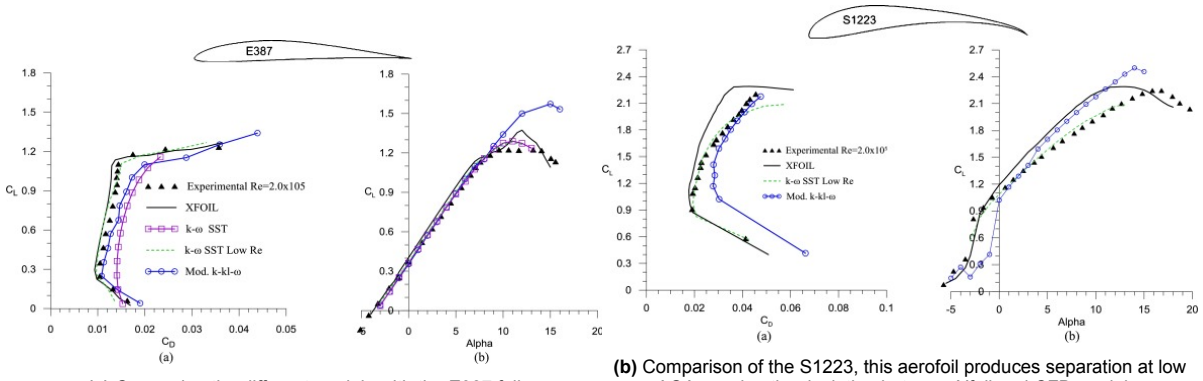

(a) Comparing the different models with the E387 foil

(b) Comparison of the S1223, this aerofoil produces separation at low AOA causing the deviation between Xfoil and CFD models.

Figure F.12: Comparison of Xfoil with experiments and 3 different turbulence models used in CFD [125]

Xfoil is a very common tool for the analysis of 2D aerofoil analysis or finite-wing analysis using its implementation in XFLR5. Xfoil faces the same problems as all the other panel methods. It does not correctly predict separated flows. Xfoil accurately predicts the lift slope but not the maximum lift or lift at stall [125–128]. The drag is usually slightly under predicted at low angles of attack. This can be seen in Figure F.12a. At High angles of attack the flow separation causes the experiment data to deviate from the prediction. A fully separated flow can cause problems in a xfoil analysis as seen in Figure F.12b.

The foil in Figure F.12b showed signs of separation bubbles at low angles of attack [36], resulting in an incorrect prediction of the lift and the and drag.

While CFD analysis out preforms Xfoil in accuracy. In a preliminary analysis of a 2d section xfoil will be a much quicker with minimal error. It can reduces the calculation time from days to minutes. This allows for more analysis to be performed. Xfoil is therefore a good analysis tool for preliminary analysis of 2D sections or optimisation workflow, according to: Bergmann et al. [124], Morgado et al. [125], and Günel, Koç, and Yavuz [127]. The data calculated by xfoil, can be used to calculate the forces for a finite wing using a program like XFLR5.

F.3. 2D section analysis

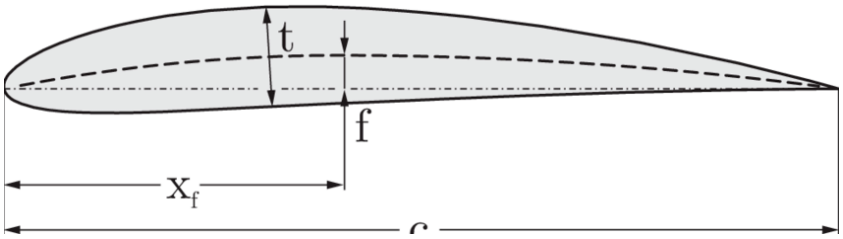

Figure F.13: The input Parameters for the NACA 4 series aerofoil NACA xf-f-t (2 values) xf (max camber/chord), f max chord thickness, t max thickness [118]

Just like the aerofoils, the effect of different parameters are imported to hydrodynamic analysis. These studies are called parametric studies. How two hydrofoils placed in tandem react to each other is investigated by Kinaci [129]. Showing the effects of different 2D foil parameters when two surfaces are placed in line with each other like the keel and rudder on most sailboats. The Naca series introduced parameterisation with the NACA 4 and 5 series aerofoils seen in Figure F.13. This still limits the control of the aerofoil shape. Therefore different 2D parametric aerofoil techniques are developt, namely: Parsec [130], Modified Sobieczky [131], BP3333 [132], BP3434 [132], IGP [133] and CST [134]. The use of parametric studies for optimisation within the field of hydrodynamics is shown by Backas [135], performing an optimisation on a kiteboard hydrofoil using CFD. The small differences of the NACRA hydrofoils make them very useful for investigating how small differences in geometry change performance, just as the studies for aerofoils described earlier. Guida, Marimon Giovannetti, and Boyd [136] investigated the Nacra 17 foils, but looked at differences in the overall shape and not at the cross-section level.

With those models the sections can be adjusted to fit a specific performance range. Before this adjustment is made it is important to connect the different goals of the sailors to different fluid dynamic properties, namely:

1. Start flying earlier: Maximize $C_{l_{max}}$
2. Minimise resistance in the water:
   (a) Minimum drag: Minimize $C_{d_{min}}$
   (b) Produce Lift at minimum drag: Maximize $\frac{C_l}{C_d}$
3. Improve the stability:
   (a) Increase the region with laminar flow: Optimise minimum drag (C_d) over α (AOA) range of the drag bucket
   (b) Reduce the presence of laminar separation bubbles
   (c) Minimise the change in moment: minimize $\frac{dC_m}{d\alpha}$

These functions are all dependent on the shape parameters of the hydrofoil. The extensive testing by Abbott and Doenhoff [29] resulted in a general understanding of how the different shape parameters affect the performance.

The impact of the general shape parameters of an aerofoil are given in Table F.1. It is interesting to note that the cl/cd found an optimum at a thickness of 12 percent of the chord. This is confirmed by Abbott

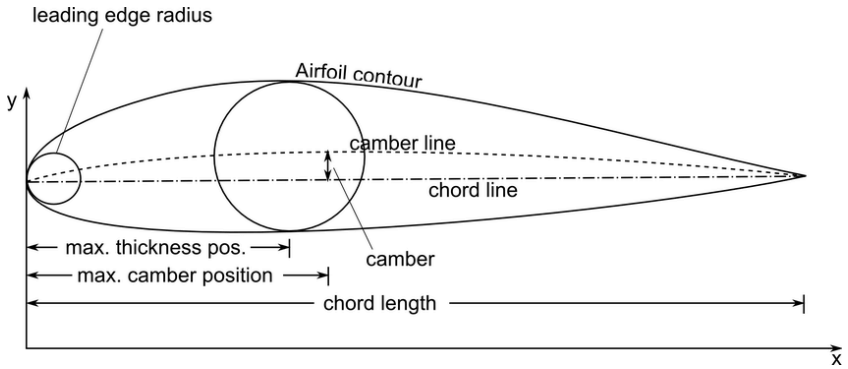

Figure F.14: The different shape parameters that are used to identify the general shape of an aerofoil [137].

Table F.1: Different aerofoil shape parameters and how they influence the performance parameters.

	Thickness	**Thickness position**	**Camber**	**Camber position**	**leading edge radius**
Cl max	increases	-	shift up-left	-	increases
Cd min	decreases	-	shift right	decreases	-
Cl/Cd slope	decreases	more shellow	shift left	-	-
Cl/Cd max	12% optimum [29]	-	increases	smoothing top curve	increases, smoothing top curve
dragbucket size	increases	-	-	-	increases
change moment	increases	increases	increases	increases	increases

and Doenhoff [29]. These values do not say anything about the laminar separation. More complex lift,drag and lift over drag optimisations optimisations require a more complex set of variables. Abbott and Doenhoff [29] found that for low Reynolds numbers the drag coefficient is lower for the 4 digit sections compared to the 6 digit sections. While the 6 digit aerofoil series is designed for a laminar flow meant to reduce the drag. The stall characteristics for the 4-5 digit sections is more favourably when the max camber is located more aft on the chord. The minimum drag can be reduced when taking the surface finish into account. A rough surface or bumbs, will make the flow transition to turbulent closer to the leading edge. As was identified in subsection F.1.5, the turbulent flow can delay separation.

Separation and laminar Separation bubbles increase the drag coefficient but are not specifically controlled by the shape parameters in Table F.1. To have an better understanding of the separation on the aerofoil the separation point should be plotted in a lift coefficient over chord plot. By combining the separation point with the lift over drag graph the effects of separation can be visualised.

By using the boundary layer shape factor H_{12} the trip point of the separation can be tuned. The boundary layer shape factor is dependent on the flow that came before and shows the potential that is asked for the flow. At high numbers the flow is asked to make a large shift and if it is not able it will separate from the shape. Using H_{12} to shape the leading edge and mid-chord of the foil. The foil can be made to reduce or prevent laminar separation. When the shaping of the foil is not an option, H_{12} can help place a trip point. This trip point is either a scratch, bump or other geometry on the foil that initiate turbulent transition. As the turbulent flow has more potential energy to follow the shape, separation is prevented. This reduces the overall drag of the foil and prevents early ventilation of the foil.

The general geometric shape parameters can be estimated without the use of Xfoil. These can thus give a good understanding of how the different sections of the Nacra 17 foils will perform. Using the polar's created by xfoil these performance differences can be validated. Xfoil can give a better understanding of the ventilation problem using the boundary layer shape factor. This will provide a better understanding of why the foils would show different performance.

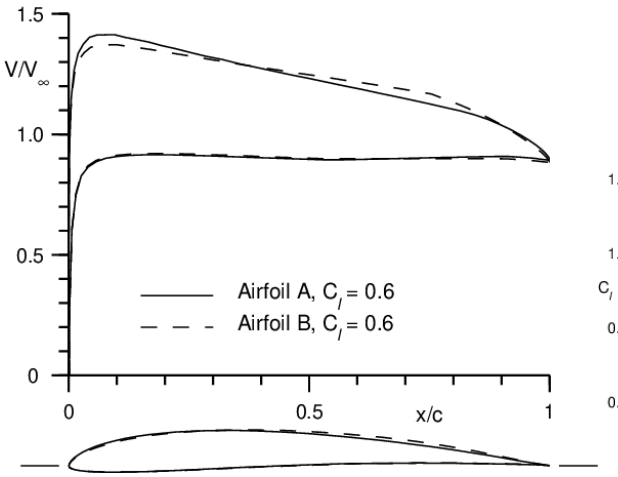

(a) Inviscid velocity distributions for airfoils A and B

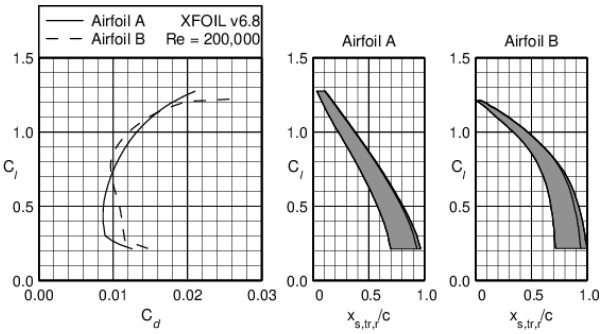

(b) XFOIL predictions for airfoils A and B to illustrate the effects of changes in the transition ramp on drag.

Figure F.15: Showing the connection of the transition ramp with the lift over drag performance for two very similar foil shapes, by Selig [9]

G

3D scanner spec-sheets

METROLOGY
SOLUTIONS

HandySCAN3D™

BLACK Series
THE TRULY PORTABLE METROLOGY-GRADE 3D SCANNERS

reddot award 2019
winner

WATCH PRODUCT VIDEO

CREAFORM

AMETEK®
ULTRA PRECISION TECHNOLOGIES

ASK OUR EXPERT

HandySCAN3D™

WHEN ACCURACY MEETS VERSATILITY AND PORTABILITY

The HandySCAN 3D™ line-up is the industry standard in portable metrology-grade 3D scanners and a proven and trusted patented technology. Optimized to meet the needs of design, manufacturing and metrology professionals, the BLACK Series provides the most effective and reliable way to acquire accurate 3D measurements of physical objects anywhere.

Portable, accurate and simple to use, the HandySCAN 3D | BLACK Series features unmatched speed that captures high-quality measurements. Since it performs regardless of environment changes or part movement, it represents the ideal tool for quality assurance and product development applications.

- **ACCURACY OF 0.025 mm (0.0009 in)**
- **SCAN-TO-MESH IN SECONDS**
- **CERTIFIED ISO 17025**
- **WORLDWIDE SUPPORT**
- **LARGE SCANNING AREA**
- **PATENTED TECHNOLOGY**

1. **High-performance optics**
   Optimal scan quality
2. **Extra single line**
   Easy capture of hard-to-reach areas
3. **Blue laser technology**
   High resolution capability
4. **Stand-off distance color indicator**
   Maximizes scanning performance
5. **Multifunction buttons**
   Quick access to frequently used software functionalities
6. **Highly ergonomic and sleek design**
   Provides outstanding user experience

ACCURACY & RESOLUTION

The HandySCAN 3D | BLACK Series delivers accurate, high-resolution and repeatable results, regardless of the measurement setup quality and no matter the user experience. Featuring dynamic referencing, both the scanner and part can move during measurement and still provide an accurate and high-quality scan.

Accuracy
0.025 mm (0.0009 in)

Volumetric accuracy
0.020 + 0.040 mm/m (0.0008 in + 0.0005 in/ft)

Reliable acceptance test
Based on VDI/VDE 2634 part 3 standard
ISO 17025 accredited laboratory

High resolution for fine details

High accuracy on large measurements
Integrated photogrammetry process and bundle adjustment optimisation

Integrated photogrammetry
High accuracy on large measurements with volumetric accuracy optimization

PORTABILITY

This handheld 3D scanner is a stand-alone device that does not require a tripod nor any external tracking device to operate. Fitting in a small suitcase, it can be brought anywhere and used in any environmental conditions without affecting its performance.

Lightweight
0.94 kg (2.1 lb)

Dynamic referencing
Both the object and scanner can be moved freely while scanning

Fits into a suitcase

Take it anywhere you need

SIMPLICITY & VERSATILITY

With its user-friendly interface and ergonomic design, this 3D measurement solution has a short learning curve. Highly versatile, it can be used to scan various object sizes and surface types in real time—all with the same device.

Plug and play

Simple user interface and real-time mesh visualization

Single device fits all needs

Masters complex and difficult surfaces

SPEED

The HandySCAN 3D | BLACK Series scanner features multiple laser crosses and an automatic mesh generation, enabling a faster workflow from the set-up to the scan and then to the file!

Instant mesh
Ready-to-use files

High measurement rate
Up to 1,300,000 measurements/s

11 laser crosses scanning area

Quick set-up
Up and running in less than 2 minutes

ASK OUR EXPERT

TECHNICAL SPECIFICATIONS

Innovating technology that provides accuracy, simplicity, portability as well as real speed to your metrology-grade applications.

	HandySCAN BLACK™	HandySCAN BLACK™|Elite
ACCURACY (1)	0.035 mm (0.0014 in)	0.025 mm (0.0009 in)
VOLUMETRIC ACCURACY (2) (based on part size)	0.020 mm + 0.060 mm/m (0.0008 in + 0.0007 in/ft)	0.020 mm + 0.040 mm/m (0.0008 in + 0.0005 in/ft)
VOLUMETRIC ACCURACY WITH MaxSHOT Next™|Elite (3)	0.020 mm + 0.015 mm/m (0.0008 in + 0.00018 in/ft)	
MEASUREMENT RESOLUTION	0.025 mm (0.0009 in)	
MESH RESOLUTION	0.100 mm (0.0039 in)	
MEASUREMENT RATE	800,000 measurements/s	1,300,000 measurements/s
LIGHT SOURCE	7 blue laser crosses	11 blue laser crosses (+ 1 extra line)
LASER CLASS	2M (eye safe)	
SCANNING AREA	310 x 350 mm (12.2 x 13.8 in)	
STAND-OFF DISTANCE	300 mm (11.8 in)	
DEPTH OF FIELD	250 mm (9.8 in)	
PART SIZE RANGE (recommended)	0.05–4 m (0.15–13 ft)	
SOFTWARE	VXelements	
OUTPUT FORMATS	.dae, .fbx, .ma, .obj, .ply, .stl, .txt, .wrl, .x3d, .x3dz, .zpr, .3mf	
COMPATIBLE SOFTWARE (4)	3D Systems (Geomagic® Solutions), InnovMetric Software (PolyWorks), Metrologic Group (Metrolog X4), New River Kinematics (Spatial Analyzer), Verisurf, Dassault Systèmes (CATIA V5, SOLIDWORKS), PTC (Creo), Siemens (NX, Solid Edge), Autodesk (Inventor, PowerINSPECT)	
WEIGHT	0.94 kg (2.1 lb)	
DIMENSIONS (LxWxH)	79 x 142 x 288 mm (3.1 x 5.6 x 11.3 in)	
CONNECTION STANDARD	1 X USB 3.0	
OPERATING TEMPERATURE RANGE	5–40°C (41–104°F)	
OPERATING HUMIDITY RANGE (non-condensing)	10–90%	
CERTIFICATIONS	EC Compliance (Electromagnetic Compatibility Directive, Low Voltage Directive), compatible with rechargeable batteries (when applicable), IP50, WEEE	
PATENTS	CA 2,600,926, CN 200680014069.3, US 7,912,673, CA 2,656,163, EP (FR, UK, DE) 1,877,726, AU 2006222458, US 8,032,327, JP 4,871,352, US 8,140,295, EP (FR, UK, DE) 2,278,271, EP (FR, UK, DE) 2,230,482, IN 266,573, US 7,487,063, CA 2,529,044, EP (FR, UK, DE) 3,102,908, US 15/114,563, CN 201580007340X	

(1) HandySCAN BLACK and HandySCAN BLACK|Elite (ISO 17025 accredited): Based on VDI/VDE 2634 part 3 standard. Probing error performance is assessed with diameter measurements on traceable sphere artefacts.

(2) HandySCAN BLACK and HandySCAN BLACK|Elite (ISO 17025 accredited): Based on VDI/VDE 2634 part 3 standard. Sphere-spacing error is assessed with traceable length artefacts by measuring these at different locations and orientations within the working volume. Results are obtained using integrated photogrammetry with volumetric accuracy optimization.

(3) The volumetric accuracy of the system when using a MaxSHOT 3D cannot be superior to the default accuracy for a given model.

(4) Also compatible with all major metrology, CAD, and computer graphic software through mesh and point cloud import.

CREAFORM

AMETEK® ULTRA PRECISION TECHNOLOGIES

Creaform Inc. (Head Office)
4700 rue de la Pascaline
Lévis QC G6W 0L9 Canada
T.: 1 418 833 4446 | F.: 1 418 833 9588
creaform.info@ametek.com | creaform3d.com

Authorized Distributor

FARO® QUANTUM^{E} FAROARM®

The New Standard for Cost-Effective Factory Inspection

The FARO Quantum^{E} FaroArm is a portable coordinate measuring machine (PCMM) that meets the most rigorous ISO 10360-12:2016 measurement standard in existence for articulated arms – an industry first. Available in a 7-axis configuration, Quantum^{E} offers an entry-level portable solution for organizations looking for a cost-effective factory inspection system.

Reliable and robust, Quantum^{E} has been tested to withstand the harshest shop-floor environments and enables manufacturers to have full confidence in their quality assurance processes and ensure high quality production. Additionally, the Quantum^{E} delivers market-leading portability, and ergonomics along with plug-and-play 3D laser scanning integration with optically-superior FAROBlu™ technology.

Most Common Applications

Alignment | Dimensional Analysis | CAD-Based Inspection | First Article Inspection | Incoming Inspection | In-Process Inspection | On-Machine Inspection | Part Inspection | Final Inspection | Reverse Engineering | Tool Building & Setup

Typical Industries

Aerospace: Part Inspection and Certification, Alignment, Tool & Mold Certification, Reverse Engineering

Automotive: Tool Building and Certification, Alignment, Part Inspection, Reverse Engineering

Metal Fabrication: First Article Inspection, Periodic Part Inspection

Molding/Tool & Die: Mold and Die Inspection, Prototype Part Scanning

Features & Benefits

Certified to Meet the Most Rigorous ISO 10360-12:2016 Measurement Standard

Quantum Arms are the first Arms in the market that are certified against ISO 10360-12:2016, setting a new industry performance bar, and ensuring maximum measurement consistency and reliability.

Innovative Design for Highest Performance and Factory Stress-Tested for Reliability

An all-new design ensures superior performance and confidence in measurement results in every working environment, while the FAROBlu, featuring blue laser technology, ensures best-in-class scanning capability. Every Quantum is tested for ruggedness and is factory-ready to ensure accuracy and performance.

Excellent Ergonomics and Usability

New ergonomic design, overall weight optimization, combined with new features such as tool-less quick-change, kinematic intelligent probes, provide unequaled freedom of movement and an unparalleled measurement experience.

High Speed Wireless Operation

New sophisticated and robust electronic design delivers superior reliability and guarantees optimal wireless operation for scanning and probing, allowing unmatched reach across the manufacturing floor.

Extended Battery Use

Dual hot-swappable batteries support prolonged cable-free operation of the device, making it easy to go to the part without the need for external power.

FAROBlu™ Laser Line Probe

The FAROBlu Laser Line Probe HD and FAROBlu Laser Line Probe SD leverage optically-superior blue laser technology. The blue laser has a shorter wavelength than a red laser, and delivers improved scanning results with higher resolution, enabling it to discover smaller details in an object. The blue laser also provides a 50% reduction in speckle noise compared to a red laser. Speckle noise is proportional to wavelength and degrades measurement accuracy.

Performance Specifications

Contact Measurement (Arm)*					
Measurement range	SPAT[1]	E_{UNI} [2]	P_{SIZE} [3]	P_{FORM} [4]	L_{DIA} [5]
	7 axis	7 axis	7 axis	7 axis	7 axis
Quantum^E 2.5m (8.2ft)	0.035mm (0.0014in)	0.050mm (0.0020in)	0.025mm (0.0010in)	0.050mm (0.0020in)	0.065mm (0.0026in)
Quantum^E 3.5m (11.5ft)	0.075mm (0.0030in)	0.095mm (0.0037in)	0.050mm (0.0020in)	0.075mm (0.0030in)	0.120mm (0.0047in)
Quantum^E 4.0m (13.1ft)	0.095mm (0.0037in)	0.120mm (0.0047in)	0.060mm (0.0024in)	0.100mm (0.0039in)	0.150mm (0.0059in)

FAROBlu HD Non-Contact Measurement (ScanArm)**	
Measurement range	L_{DIA} [5]
Quantum^E 2.5m (8.2ft)	0.075mm (0.0030in)
Quantum^E 3.5m (11.5ft)	0.110mm (0.0043in)
Quantum^E 4.0m (13.1ft)	0.130mm (0.0051in)

FAROBlu SD Non-Contact Measurement (ScanArm)**	
Measurement range	L_{DIA} [5]
Quantum^E 2.5m (8.2ft)	0.075mm (0.0030in)
Quantum^E 3.5m (11.5ft)	0.110mm (0.0043in)
Quantum^E 4.0m (13.1ft)	0.130mm (0.0051in)

All values represent MPE (Maximum Permissible Error)

* Contact Measurement (Arm):
In accordance with ISO 10360-12

**Non-Contact Measurement (ScanArm):
Full System performance in accordance with ISO 10360-8 Annex D

[1] SPAT – Single Point Articulation Test

[2] E_{UNI} – Sphere Probing Size Error comparing measured versus nominal values

[3] P_{SIZE} – Sphere Probing Size Error comparing measured vs nominal values

[4] P_{FORM} – Sphere Probing Form Error

[5] L_{DIA} – Sphere Location Diameter Error (Diameter of the spherical zone containing the centers of a sphere measured from multiple orientations)

Hardware Specifications

Operating temp range: 10°C - 40°C (50°F - 104°F)

Temperature rate: 3°C/5min (5.4°F/5min)

Operating humidity range: 95%, non-condensing

Power supply: Universal worldwide voltage; 100-240VAC; 47/63Hz

Laser Line Probe Specifications

	FAROBlu HD	FAROBlu SD
Accuracy	±25µm (±0.001in)	±25µm (±0.001in)
Repeatability	25µm, 2σ (0.001in)	25µm, 2σ (0.001in)
Stand-off	115mm (4.5in)	115mm (4.5in)
Depth of field	115mm (4.5in)	115mm (4.5in)
Effective scan width	Near field 80mm (3.1in) Far field 150mm (5.9in)	Near field 80mm (3.1in) Far field 150mm (5.9in)
Points per line	2,000 points/line	1,000 points/line
Minimum point spacing	40µm (0.0015in)	80µm (0.0031in)
Scan rate	300 frames/second, 300 fps x 2,000 points/line = 600,000 points/sec	120 frames/second, 120 fps x 1,000 points/line = 120,000 points/sec
Laser	Class 2M	Class 2M
Weight	485g (1.1lb)	485g (1.1lb)

Accuracy and repeatability specified at Full Field of View (FOV)

Meets OSHA requirements, NRTL TÜV SÜD C-US Listed, Complies with Electronic Code of Federal Regulations 47 CFR PART 15, 17 CFR Parts 240 and 249b – Conflict Material, 21 CFR 1040 Performance standards For Light-Emitting Products, and 10 CFR Part 430 – Department of Energy; Energy Conservation for External Power Supplies. Complies with the following EC Directives: 93/68/EEC CE Marking; 2014/30/EU Electrical Equipment; 2014/53/EU Radio Equipment Directive; 2011/65/EU RoHS2; 2002/96/EC WEEE; 2006/66/EC WEEE; 2006/66/EC Batteries and Accumulators; 2014/35/EU Low Voltage Directive; 2009/125/EC Ecodesign requirement. Conforms to the following standards: EN 61010-1:2010 / CSA-C22.2 No. 61010-1; EN 61326-1:2013 EMC; ETSI EN 300 328 V2.1.1; ETSI 301 489-1 V1.9.2; ETSI 301 489-17 V2.2.1; ETSI EN 62311:2008; IEEE 802.11 b/g; FCC Part 15.247 (WLAN and Bluetooth); Japanese Radio Law MPT No. 37 Ordinance (MIC classification WW); UN T1-T8; IEC 62133 2nd ed.; IEC 60825-1:2014 ed3.0; FDA (CDRH) 21 CFR 1040.10 / ANSI Z136.1-2007; EN 50581:2012; 21 CFR 1002 (Records & Reports); 21 CFR 1010 (Performance Standards).

Shock and Vibrations Testing per International Electrotechnical Commission (IEC) Standards: IEC 60068-2-6; IEC 60068-2-64; IEC 60068-2-27 Extreme Temperature Cycling (-20°C to 60°C). Based on: IEC 60068-2-1; MIL-STD-810G; ISTA

For more information, call 800.736.0234 or visit www.faro.com
FARO Technologies, Inc. | 250 Technology Park | Lake Mary, FL 32746

ISO 9001 BUREAU VERITAS Certification · ANAB ACCREDITED · GSA Contract Holder

SFDC_04MKT_493 Revised: 5/22/2018